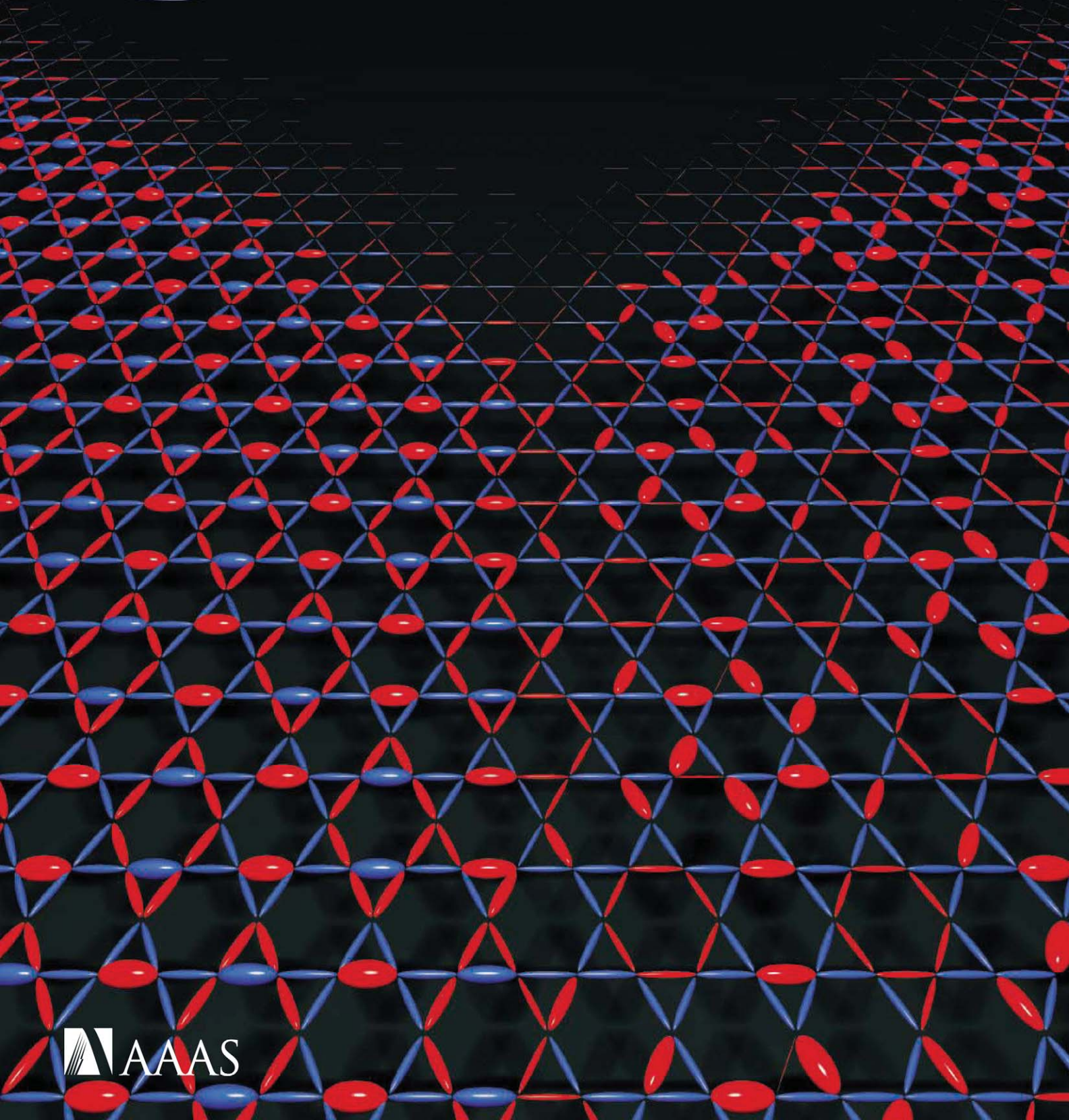


# Science

3 June 2011 | \$10





# How have these people contributed to the advancement of society?



Dr. John  
Pierce



Dr. Ephraim  
Katchalski-Katzir



Dr. David  
Turnbull



Dr. Willem  
Kolff



Dr. Theodore  
Maiman



Dr. Henry  
Beachell



Dr. Gurdev  
Khush



Dr. Georges  
Vendryes



Dr. Donald  
Henderson



Dr. Isao  
Arita



Dr. Frank  
Fenner



Dr. Luc  
Montagnier



Dr. Robert  
Gallo



Dr. Frank  
Rowland



Dr. Elias  
Corey



Dr. Marvin  
Minsky



Dr. William  
Morgan



Dr. Dan  
McKenzie



Dr. Xavier  
Le Pichon



Dr. Jacques-Louis  
Lions



Dr. John  
Wild



Prof. Dr. Gerhard  
Ertl



Prof. Christopher  
Polge



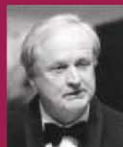
Dr. Frank  
Press



Dr. Kary  
Mullis



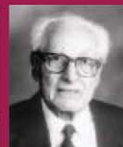
Dr. William  
Pickering



Dr. Arvid  
Carlsson



Dr. Nick  
Holonyak, Jr.



Dr. Edward  
Knipping



Dr. Charles  
Kao



Dr. Masao  
Ito



Dr. Joseph  
Engelberger



Dr. Hiroyuki  
Yoshikawa



Dr. Takashi  
Sugimura



Dr. Bruce  
Ames



Dr. Leo  
Esaki



Prof. Dr. Jozef  
Schell



Dr. Marc  
Van Montagu



Dr. W. Wesley  
Peterson



Dr. Jack  
Strominger



Dr. Don  
Wiley



Prof. Ian  
McHarg



Dr. Kimishige  
Ishizaka



Dr. John  
Goodenough



Dr. Timothy  
Parsons



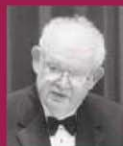
Dr. Timothy  
Berners-Lee



Dr. Anne  
McLaren



Dr. Andrzej  
Tarkowski



Dr. Benoit  
Mandelbrot



Dr. James  
Yorke



Dr. Seiji  
Ogawa



Dr. Kenichi  
Honda



Dr. Akira  
Fujishima



Dr. Keith  
Sainsbury



Prof. John  
Lawton



Dr. Makoto  
Nagao



Dr. Masatoshi  
Takeichi



Dr. Erkki  
Ruoslahti



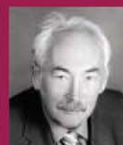
Sir John  
Houghton



Dr. Akira  
Endo



Prof. Albert  
Fert



Prof. Dr. Peter  
Grünberg



Dr. Peter  
Ashton



Dr. Vinton  
Cerf



Dr. Robert  
Kahn



Dr. Victor  
McKusick



Dr. Dennis  
Meadows



Dr. David  
Kuhl



Prof. Shun-ichi  
Iwasaki



Prof. Peter  
Vitousek

**This is an important consideration in our selection of Japan Prize recipients.**

This award, intended for international scientists and technologists, is given to people acknowledged as having attained outstanding and dramatic achievements, thus contributing to the advancement of science and technology, as well as to the peace and prosperity of mankind. From the first award in 1985 to the 27th award in 2011, 74 leading scientists from around the world have been honored.

## The 2011 (27th) Japan Prize Laureates



Dr. Dennis  
Ritchie



Dr. Ken  
Thompson



Dr. Tadamitsu  
Kishimoto



Dr. Toshio  
Hirano



# JAPAN PRIZE

THE JAPAN PRIZE FOUNDATION

WorldMags

Submission  
deadline  
**August 1**

# Your name here.



## The GE & Science Prize for Young Life Scientists. Because brilliant ideas build better realities.

Imagine standing on the podium at the Grand Hotel in Stockholm, making your acceptance speech for the GE & Science Prize for Young Life Scientists. Imagine having your essay read by your peers around the world. Imagine discussing your work in a seminar with other prize winners and Nobel Laureates. Imagine what you could do with the \$25,000 prize money. Now stop imagining. If you were awarded your Ph.D. in molecular biology in 2010, then submit your 1000-word essay by August 1, and you can make it a reality.

Want to build a better reality? Go to [www.gescienceprize.org](http://www.gescienceprize.org)



\* For the purpose of this prize, molecular biology is defined as "that part of biology which attempts to interpret biological events in terms of the physico-chemical properties of molecules in a cell".

(McGraw-Hill Dictionary of Scientific and Technical Terms, 4th Edition).

GE Healthcare Bio-Sciences AB,  
Björkgatan 30, 751 84 Uppsala, Sweden.  
© 2011 General Electric Company  
— All rights reserved.  
28-9402-06AB



GE Healthcare  
Life Science

# Confidence comes with the right interactions.

Join leading scientists from academia and industry at Developments in Protein Interaction Analysis (DiPIA), November 12-15, Boston, Massachusetts, USA.

This scientific conference offers opportunities to meet and discuss the latest developments in label-free interaction and stability analysis using Biacore™ Surface Plasmon Resonance (SPR) and MicroCal™ microcalorimetry systems.

Register at [www.gelifesciences.com/dipia](http://www.gelifesciences.com/dipia)

© 2011 General Electric Company – All rights reserved.  
GE Healthcare Bio-Sciences AB, Björkgatan 30,  
751 84 Uppsala, Sweden  
K11074. First published May 2011.



WorldMags





## EDITORIAL

- 1127 The Values of Science  
*Ismail Serageldin*

## NEWS OF THE WEEK

- 1132 A roundup of the week's top stories

## NEWS & ANALYSIS

- 1135 Quake Experts to Be Tried for Manslaughter  
*>> Editor's Note p. 1149; Research Article p. 1163*
- 1136 Concerns About Arsenic-Laden Bacterium Aired  
*>> Editor's Note p. 1149; Research Article p. 1163*
- 1138 Wellcome Puts Its Money on Elite Researchers
- 1139 Appraising U.K. Ecosystems, Report Envisions Greener Horizon

## NEWS FOCUS

- 1140 DNA Nanotechnology Grows Up  
Next Step: DNA Robots?
- 1144 Possible Sighting of Dark Matter  
Fires Up Search and Tempers

## LETTERS

- 1149 Editor's Note and Technical Comments on Wolfe-Simon *et al.*  
*B. Alberts*  
*>> News & Analysis story p. 1136; Research Article p. 1163*
- Zoos and Captive Breeding  
*A. Balmford et al.*
- Response  
*D. A. Conde et al.*

- 1150 CORRECTIONS AND CLARIFICATIONS

## BOOKS ET AL.

- 1152 An Empire of Ice  
*E. J. Larson, reviewed by V. B. Smocovitis*
- 1153 Little Eagles  
*R. Munro, directed by R. Silbert; Little Eagles*  
*R. Munro*

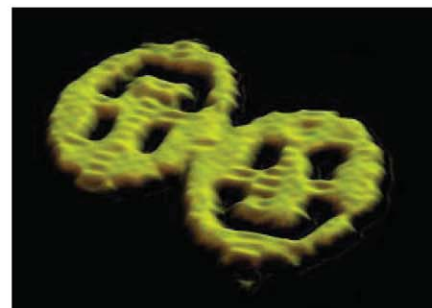
## POLICY FORUM

- 1154 Research Principles for Developing Country Food Value Chains  
*M. I. Gómez et al.*

## PERSPECTIVES

- 1156 Scaling Up DNA Computation  
*J. H. Reif*  
*>> Report p. 1196*
- 1157 Io's Tortured Interior  
*A. J. Coates*  
*>> Report p. 1186*
- 1158 Potential Solutions for Creating Responsive Materials  
*K. Sieradzki*  
*>> Report p. 1179*
- 1160 In Evolution, the Sum Is Less than Its Parts  
*S. Kryazhimskiy et al.*  
*>> Reports pp. 1190 and 1193*
- 1161 Behavior and the Dynamic Genome  
*A. M. Bell and G. E. Robinson*

CONTENTS continued >>



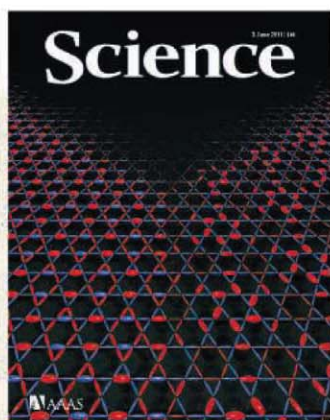
page 1140



page 1152



page 1161



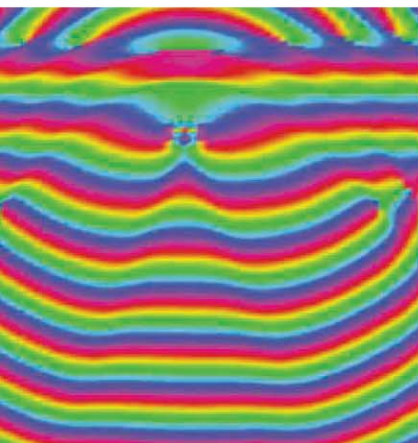
## COVER

Three possible phases of the kagome Heisenberg antiferromagnet, a model of geometrically "frustrated" magnetism: the diamond-pattern valence bond crystal (lower left), honeycomb valence bond crystal (lower right), and quantum spin liquid (upper empty wedge). Deviations of bond strengths from their average values are shown by bond widths and colors (red, stronger; blue, weaker). The simulations of Yan *et al.* (p. 1173) show that the true ground-state phase is the quantum spin liquid.

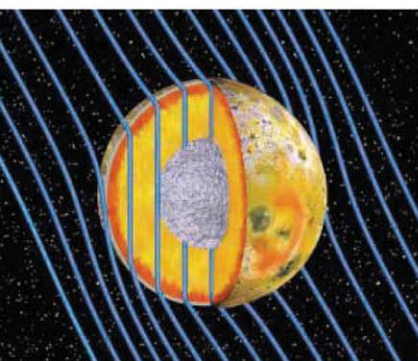
Image: Steven R. White, University of California, Irvine

## DEPARTMENTS

- 1124 This Week in *Science*
- 1128 Editors' Choice
- 1130 *Science* Staff
- 1217 New Products
- 1218 *Science* Careers



page 1167



pages 1157 & 1186



pages 1156 & 1196

## RESEARCH ARTICLE

- 1163 A Bacterium That Can Grow by Using Arsenic Instead of Phosphorus**  
*F. Wolfe-Simon et al.*  
 Evidence is offered for arsenate replacing phosphate as a molecular building block in a Mono Lake, California, bacterium.  
 >> *News & Analysis story p. 1136;*  
*Editor's Note p. 1149*

## REPORTS

- 1167 Polariton Superfluids Reveal Quantum Hydrodynamic Solitons**  
*A. Amo et al.*  
 A condensed-matter system is used to study superfluid dynamics.
- 1170 Observing the Average Trajectories of Single Photons in a Two-Slit Interferometer**  
*S. Kocsis et al.*  
 An experiment determined the trajectories of single photons through a two-slit interferometer.
- 1173 Spin-Liquid Ground State of the  $S = 1/2$  Kagome Heisenberg Antiferromagnet**  
*S. Yan et al.*  
 Numerical calculations reveal that the true ground state of a frustrated two-dimensional system is a gapped spin liquid.
- 1176 Two-Dimensional Mott-Hubbard Electrons in an Artificial Honeycomb Lattice**  
*A. Singha et al.*  
 A collective electron excitation displays an unusual dependence on applied magnetic field.
- 1179 A Material with Electrically Tunable Strength and Flow Stress**  
*H.-J. Jin and J. Weissmüller*  
 Changes in a layer of oxygen adsorbed onto nanoporous gold reversibly affect its mechanical properties.  
 >> *Perspective p. 1158*
- 1183 Magnetosphere Sawtooth Oscillations Induced by Ionospheric Outflow**  
*O. J. Brambles et al.*  
 Numerical simulations show that a class of magnetospheric disturbance can be generated by the outflow of ions from the ionosphere into the magnetosphere.

- 1186 Evidence of a Global Magma Ocean in Io's Interior**  
*K. K. Khurana et al.*  
 Magnetic field measurements made near Jupiter's moon Io strengthen the evidence for a magma ocean in its interior.  
 >> *Perspective p. 1157*
- 1190 Diminishing Returns Epistasis Among Beneficial Mutations Decelerates Adaptation**  
*H.-H. Chou et al.*
- 1193 Negative Epistasis Between Beneficial Mutations in an Evolving Bacterial Population**  
*A. I. Khan et al.*  
 Interactions between genes reduce the benefits of a mutation and decrease the rate of fitness gain during adaptation.  
 >> *Perspective p. 1160*
- 1196 Scaling Up Digital Circuit Computation with DNA Strand Displacement Cascades**  
*L. Qian and E. Winfree*  
 Scalability and noise control are demonstrated in a molecular computer built of DNA.  
 >> *Perspective p. 1156*
- 1202 Crystal Structure of the Maltose Transporter in a Pretranslocation Intermediate State**  
*M. L. Oldham and J. Chen*  
 An intermediate structure provides insight into how a transport substrate allosterically activates adenosine triphosphatase activity.
- 1206 Residue-Specific Vibrational Echoes Yield 3D Structures of a Transmembrane Helix Dimer**  
*A. Remorino et al.*  
 Vibrational spectroscopy coupled with isotopic substitution can probe protein structure.
- 1210 Interaction Between Notch and Hif- $\alpha$  in Development and Survival of *Drosophila* Blood Cells**  
*T. Mukherjee et al.*  
 Ligand-independent Notch signaling promotes blood cell survival during normal development and under hypoxic stress.
- 1214 Increased Structure and Active Learning Reduce the Achievement Gap in Introductory Biology**  
*D. C. Haak et al.*  
 A focus on problem-solving skills reduced achievement gaps in university classes.



## SCIENCEONLINE

## SCIENCEEXPRESS

[www.scienceexpress.org](http://www.scienceexpress.org)

### Detection of Convective Downflows in a Sunspot Penumbra

G. B. Scharmer et al.

Downflows detected near the edges of a sunspot's outer filaments provide a missing piece for convective models of sunspot motion.

10.1126/science.1206429

### Recombinant Origin of the Retrovirus XMRV

T. Paprotka et al.

Analysis of the origin of XMRV suggests that links between the virus and human disease are due to laboratory contamination.

10.1126/science.1205292

### No Evidence of Murine-Like Gammaretroviruses in CFS Patients Previously Identified as XMRV-Infected

K. Knox et al.

Chronic fatigue syndrome patients reported previously to be XMRV-infected show no signs of the virus in an independent evaluation.

10.1126/science.1204963

### Editorial Expression of Concern on Lombardi et al. Report

B. Alberts

10.1126/science.1208542

### Coupled, Circumferential Motions of the Cell Wall Synthesis Machinery and MreB Filaments in *B. subtilis*

E. C. Garner et al.

10.1126/science.1203285

### Processive Movement of MreB-Associated Cell Wall Biosynthetic Complexes in Bacteria

J. Domínguez-Escobar et al.

Bacteria elongation involves moving synthetic complexes around the cell wall.

10.1126/science.1203466

### Adult Neural Function Requires MeCP2

C. M. McGraw et al.

An epigenetic program regulated by MeCP2 needs to be maintained throughout life for normal neurological function.

10.1126/science.1206593

## SCIENCENOW

[www.sciencenow.org](http://www.sciencenow.org)

Highlights From Our Daily News Coverage

### On the Fly, German Doctors Find Treatment for Deadly *E. coli* Infections

But more question the evidence for efficacy.

<http://scim.ag/ecoli-infections>

### Satellite Imagery Uncovers Up to 17 Lost Egyptian Pyramids

Eyes in the sky spy buried archaeological treasures.

<http://scim.ag/lost-pyramids>

### Who Needs a Moon?

Earth-like extrasolar planets could be suitable for life even if their rotation is not stabilized by a large moon.

<http://scim.ag/no-moon>

## SCIENCE SIGNALING

[www.sciencesignaling.org](http://www.sciencesignaling.org)

The Signal Transduction Knowledge Environment

31 May issue: <http://scim.ag/ss053111>

### RESEARCH ARTICLE: Reduction of Complex Signaling Networks to a Representative Kernel

J.-R. Kim et al.

An algorithmic approach enables the simplification of complex signaling networks and identifies potential therapeutic targets.

### RESEARCH ARTICLE: Integration of Activating and Inhibitory Receptor Signaling by Regulated Phosphorylation of Vav1 in Immune Cells

S. Mesecke et al.

The extent of phosphorylation of a guanine nucleotide exchange factor determines the cytotoxicity of natural killer cells.

### PERSPECTIVE: Cancer Cells Exploit the Eph-Ephrin System to Promote Invasion and Metastasis—Tales of Unwitting Partners

B. Wang et al.

Eph receptors and their ephrin ligands regulate contact inhibition of locomotion and its evasion in cancer cells.

## SCIENCE TRANSLATIONAL MEDICINE

[www.sciencetranslationalmedicine.org](http://www.sciencetranslationalmedicine.org)

Integrating Medicine and Science

1 June issue: <http://scim.ag/stm060111>

### RESEARCH ARTICLE: Rituximab Targets Podocytes in Recurrent Focal Segmental Glomerulosclerosis

A. Fornoni et al.

### PERSPECTIVE: Rituximab's New Therapeutic Target—The Podocyte Actin Cytoskeleton

A. C. Chan

A well-characterized monoclonal antibody drug imparts therapeutic benefit in kidney disease through an off-target-mediated mechanism.

### RESEARCH ARTICLE: A HIF-Regulated VHL-PTP1B-Src Signaling Axis Identifies a Therapeutic Target in Renal Cell Carcinoma

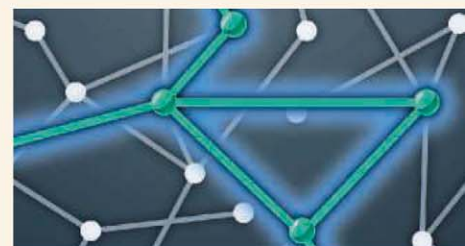
N. Suwaki et al.

Signaling through the VHL-PTP1B-Src pathway in renal cell carcinomas may determine sensitivity to Src inhibitors and provide a basis for treatment planning.

### RESEARCH ARTICLE: MF59 Adjuvant Enhances Diversity and Affinity of Antibody-Mediated Immune Response to Pandemic Influenza Vaccines

S. Khurana et al.

Adjuvant use improves the quality and quantity of the immune response to pandemic influenza vaccines.



SCIENCE SIGNALING  
Reducing network complexity.

## SCIENCE CAREERS

[www.sciencereers.org/career\\_magazine](http://www.sciencereers.org/career_magazine)

Free Career Resources for Scientists

### Reinventing the Standard Model of Science Presentations

S. Reed

A developmental biologist-turned-design expert thinks there are better ways to present scientific information.

<http://scim.ag/presentations1>

### Taken for Granted: Immigrants and Entrepreneurship

B. L. Benderly

Recent research questions some popular estimates of the role of the foreign-born in founding high-tech companies.

[http://scim.ag/tfg\\_entrepreneurs](http://scim.ag/tfg_entrepreneurs)

## SCIENCE PODCAST

[www.sciencemag.org/multimedia/podcast](http://www.sciencemag.org/multimedia/podcast)

Free Weekly Show

On the 3 June Science Podcast: verifying dark matter results, the pace of evolution, highly structured biology courses, and more.

## SCIENCE INSIDER

[news.sciencemag.org/scienceinsider](http://news.sciencemag.org/scienceinsider)

Science Policy News and Analysis

SCIENCE (ISSN 0036-8075) is published weekly on Friday, except the last week in December, by the American Association for the Advancement of Science, 1200 New York Avenue, NW, Washington, DC 20005. Periodicals Mail postage (publication No. 484460) paid at Washington, DC, and additional mailing offices. Copyright © 2011 by the American Association for the Advancement of Science. The title SCIENCE is a registered trademark of the AAAS. Domestic individual membership and subscription (51 issues): \$149 (\$74 allocated to subscription). Domestic institutional subscription (51 issues): \$990; Foreign postage extra: Mexico, Caribbean (surface mail) \$55; other countries (air assist delivery) \$85. First class, airmail, student, and emeritus rates on request. Canadian rates with GST available upon request, GST #1254 88122. Publications Mail Agreement Number 1069624. Printed in the U.S.A.

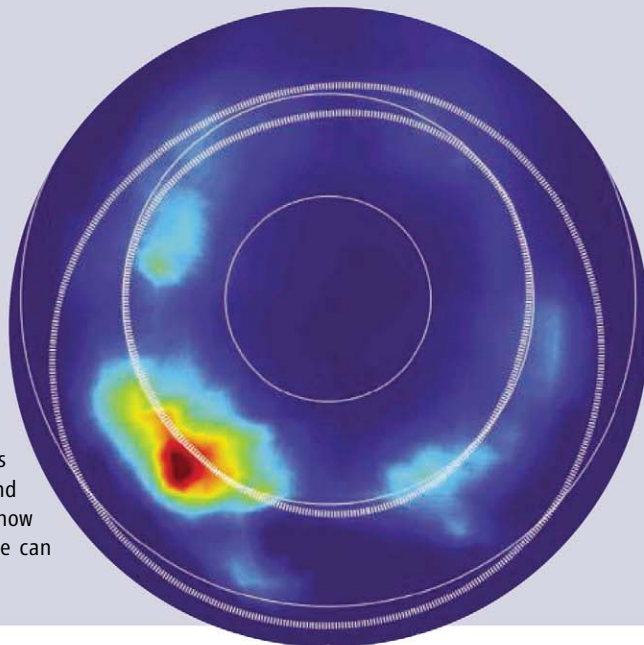
Change of address: Allow 4 weeks, giving old and new addresses and 8-digit account number. Postmaster: Send change of address to AAAS, P.O. Box 96178, Washington, DC 20090-6178. Single-copy sales: \$10.00 current issue, \$15.00 back issue prepaid includes surface postage; bulk rates on request. Authorization to photocopy material for internal or personal use under circumstances not falling within the fair use provisions of the Copyright Act is granted by AAAS to libraries and other users registered with the Copyright Clearance Center (CCC) Transactional Reporting Service, provided that \$25.00 per article is paid directly to CCC, 222 Rosewood Drive, Danvers, MA 01923. The identification code for Science is 0036-8075. Science is indexed in the Reader's Guide to Periodical Literature and in several specialized indexes.



ADVANCING SCIENCE. SERVING SOCIETY

## Generating Sawtooth Oscillations >>

Earth's magnetosphere is subject to sawtooth oscillations as it responds to the constant battering of the solar wind, the stream of charged particles coming from the Sun. Although observations have uncovered many of the properties of this type of disturbance, the mechanism that generates it is unclear. Based on numerical simulations of the interaction of the solar wind with the magnetosphere and the ionosphere, **Brambles *et al.*** (p. 1183) now show that the flow of  $O^+$  ions from the ionosphere to the magnetosphere can produce sawtooth oscillations.

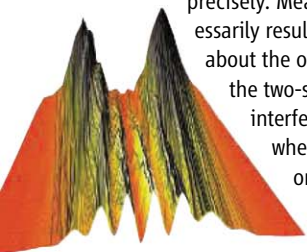


## Toxic Selection

Arsenic is highly toxic to living organisms because it disrupts metabolic pathways, but, chemically, arsenate behaves in a similar way to phosphate, and it is theoretically possible for organisms to substitute one for the other under certain conditions. **Wolfe-Simon *et al.*** (p. 1163, published online 2 December) have found a living example of a bacterium that does not find arsenate poisonous (see related Editor's Note, Technical Comments, and Response p. 1149). Isolates of a halomonad bacterium, originating from the toxic and briny Mono Lake, California, were selected by successive laboratory culture in which phosphate was gradually replaced by arsenate until the bacteria were growing in the absence of the usual salt. Further analysis indicated that arsenate had substituted for phosphate in the bacterium's constituent molecules, even replacing phosphate in its DNA, as well as in its proteins and metabolites.

## Which Path? That Path

A consequence of quantum mechanics and the Heisenberg uncertainty principle is that complementary variables (for example, position and momentum) cannot both be determined precisely. Measuring one variable necessarily results in loss of information about the other. The best example is the two-slit interferometer and the interference pattern that occurs when light or single photons or electrons are transmitted through it. Determining which slit the particle goes through (position) destroys the interference pattern (momentum). **Kocsis *et al.*** (p. 1170; see the News story by **Cho**) implement a recent theoretical proposal in



which an experimental protocol involving weak measurements could answer the "which path did the photon take" question. The results may impact the foundations of quantum and classical physics and potentially find practical application in metrology.

## Going to Ground

In solids with antiferromagnetic interactions, where spins on neighboring lattice sites prefer to align opposite to each other, geometric frustration occurs if the spatial arrangement of the sites is incompatible with the preferred spin orientation. In frustrated systems, some fluctuations remain even at zero temperature, and calculating the true ground state is difficult. The kagome lattice with spin  $1/2$  particles interacting through the Heisenberg Hamiltonian has been one of the most-studied frustrated systems, and recent numerical results indicated that its ground state may be a valence bond crystal. Now, **Yan *et al.*** (p. 1173, published online 28 April; see the cover) use the density matrix renormalization group method to reveal that a lower-energy state, that of a spin liquid, exists where magnetic order is absent even at zero temperature. Excitations of the ground state appear to be gapped, suggesting that the true ground state of this system is a gapped spin liquid.

## Monolayer Generates Reversible Change

The strength and toughness of a metal or alloy can be strongly affected by surface layers that may alter the corrosion resistance, the ability of dislocations to migrate, or the formation of notches that may lead to larger cracks. **Jin and Weissmüller** (p. 1179; see the Perspective by

**Sieradzki**) explore the effect of a monolayer of oxygen species on the surface of nanoporous gold on the plastic yield strength and subsequent flow strength. Nanoporous gold was filled with an electrolyte that only weakly adsorbed onto its surface. Applying a small electrical potential changed the absorption and desorption of oxygen at the gold surface, allowing reversible change of the breaking strength, the stress required to initiate plastic deformation, and the amount of plastic deformation the material will tolerate.

## Io's Magma Revealed

Jupiter's moon, Io, is the most volcanically active body in the solar system, but the presence of a magma ocean in its interior has long been a matter of debate. **Khurana *et al.*** (p. 1186, published online 12 May; see the Perspective by **Coates**) reanalyzed magnetic field measurements acquired by the Galileo spacecraft. Io's inductive response to Jupiter's rotating magnetic field indicates the existence of a globe-encircling, electrically conducting magma layer at depth.

## Benefits Depend on Context

Simple genetic interactions can often result in beneficial phenotypes under selection. However, examples of complex epistatic interactions (in which multiple genes interact, resulting in a nonadditive phenotype) and their selective effects are less well known (see the Perspective by **Kryazhimskiy *et al.***). **Khan *et al.*** (p. 1193) examined the epistatic interactions throughout an entire genome by taking the first five mutations to appear in an experimentally evolving population of bacteria, and constructed strains carrying all combinations of these mutations.



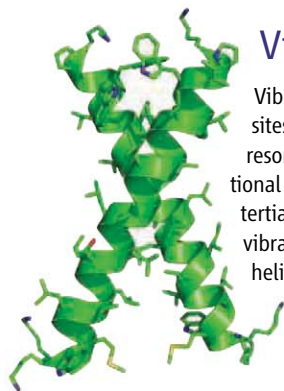
For four out of these five mutations, the benefit conferred by the mutation negatively correlated with the fitness of the progenitor, which suggests that the rate of adaptation slows as fitness increases because of negative epistasis between beneficial mutations. **Chou *et al.*** (p. 1190) addressed how mutations interact with one another by estimating fitness and phenotypic measurements for the ancestor, descendent, and intermediate genotypes and found that epistatic interactions within a genome are primarily antagonistic. Together these studies suggest that adaptation involving the wider context of whole genome networks may behave entirely differently from the adaptation of single loci.

## DNA Computing

One goal of so-called “synthetic biology” is to enable construction of molecular circuitry that can control biological systems or even diagnose and treat living cells from within. **Qian and Winfree** (p. 1196; see the Perspective by **Reif**) describe a system of over 100 distinct DNA strands of 15 to 30 nucleotides whose binding and replication can be controlled to perform AND, OR, NOT, NAND, and NOR logic gates logic operations. The system allowed mathematical computation of square roots in a few hours. In addition a compiler was designed that could translate a logic circuit into its equivalent circuit built of DNA sequences. The strategies used are scalable to build larger circuits, assure reliable digital behavior of the system, and suggest the possibility of embedding designed intelligent systems within biological systems.

## Caught in the Act

Adenosine triphosphate (ATP)–binding cassette (ABC) transporters use the energy from ATP hydrolysis to transport substrates across a membrane against a concentration gradient. The transporters function by alternating between two conformations that expose the substrate-binding site to either side of the membrane. **Oldham and Chen** (p. 1202, published online 12 May) determined the structure of an intermediate pretranslocation state of the maltose transporter bound to the periplasmic maltose binding protein with maltose bound. The substrate binding induces partial closure of the interface between the two cytoplasmic ATP domains, which accelerates ATP hydrolysis and progression of the productive conformational reaction cycle of the transporter.



## Vibrations Beyond the Active Site

Vibrational spectroscopy allows for probing the chemistry of enzymatic active sites with a time resolution roughly a million-fold higher than in nuclear magnetic resonance techniques. However, few studies have succeeded in applying vibrational probes to more global structural elucidation, encompassing secondary and tertiary organizational features. **Remorino *et al.*** (p. 1206) used two-dimensional vibrational echo spectroscopy to uncover the structure of a tertiary contact in the helical dimer of an integrin protein that straddles the cell membrane. The method extracts geometries by measuring distance-dependent rates of vibrational energy transfer between isotopically labeled amino acid residues at specific sites in the peptide sequence.

## Real Life Hif- $\alpha$

Hypoxia-inducible factor- $\alpha$  (Hif- $\alpha$ ) has been linked to Notch in the regulation of stem cell maintenance, tumor cell migration, and melanoma development. However, the Hif- $\alpha$ /Notch interaction in vivo has largely remained uncharacterized. Using genetic tools in *Drosophila*, **Mukherjee *et al.*** (p. 1210) describe an in vivo role for Hif- $\alpha$  in the activation of full-length Notch receptor signaling. A noncanonical, ligand-independent mechanism promoted blood cell survival during both normal hematopoietic development and during a hypoxic stress response.

## Teaching Skills

Students arrive at college with diverse skill sets. Studying the outcomes from large, introductory biology courses, **Haak *et al.*** (p. 1213) found that focusing on problem-solving and data analysis skills, through frequent practice, helped all the students but was particularly helpful to disadvantaged students. The change was enacted by incorporating added structure and active learning techniques to the teaching style and did not require additional funding.

## CELL SYSTEMS // CELL COUNTER

Save time.  
Reduce  
frustration.  
Increase  
productivity.



## That's countelligent.

Bio-Rad's TC10™ automated cell counter is saving researchers one cell at a time. Faster results? Greater accuracy? Less headache? You can count on it. The TC10 is fully automated, just one simple step gives you a reliable count of total and viable mammalian cells.

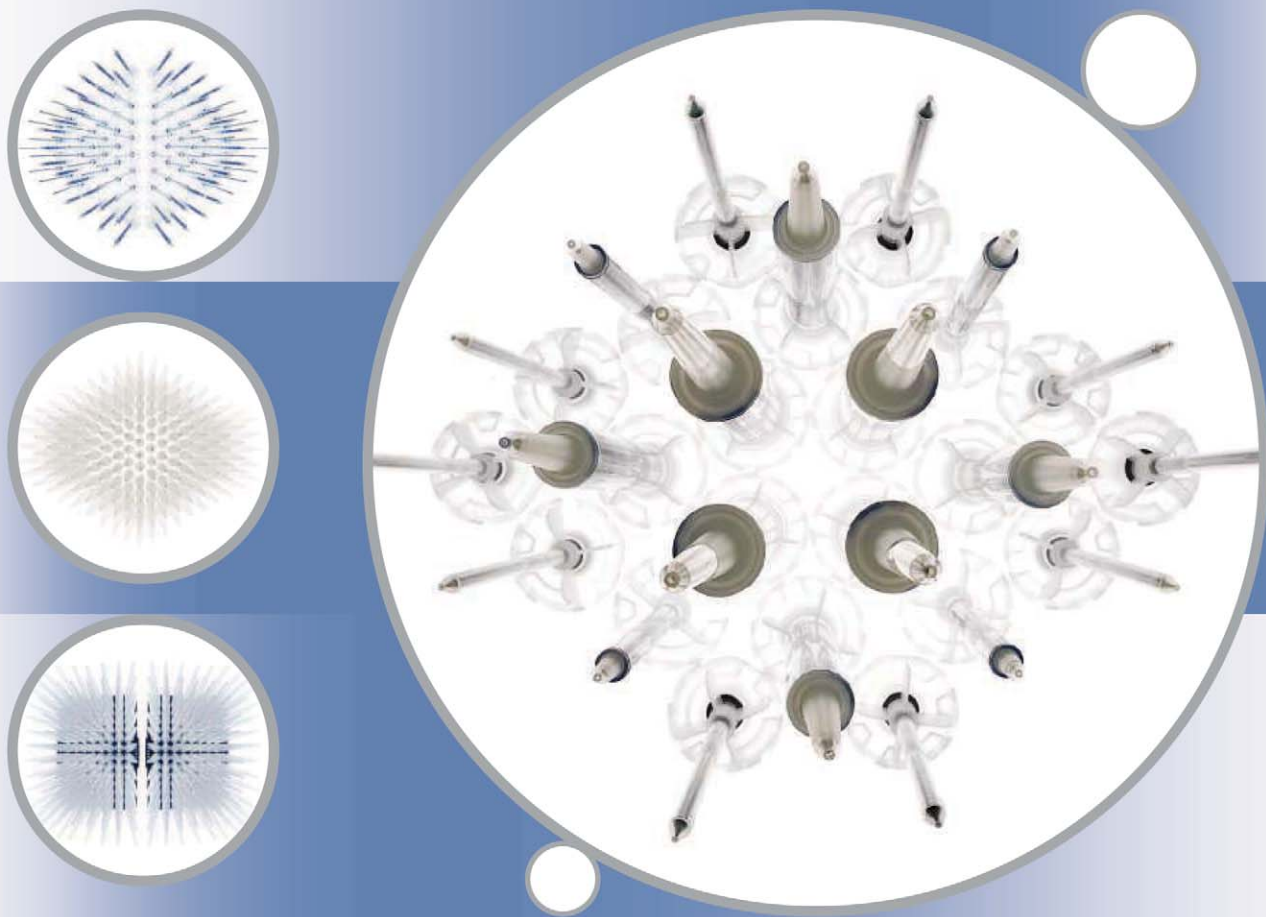
- Fit cell counting into your schedule with an easy-to-use interface and results in less than 30 seconds
- Trust your counts with innovative autofocus technology that removes the subjectivity of manual focusing
- Get faster and more reproducible downstream results using accurate and consistent cell counts

It all adds up to a smarter way of cell counting.

Visit [www.bio-rad.com/ad/countelligent](http://www.bio-rad.com/ad/countelligent) for more information.

**Research. Together.**

**BIO-RAD**



## Go for unaffected assay results!

Choose the right tip for your experiments

### Laboratory consumables can affect bioassays!

Consumables for pipetting and dispensing samples should be selected carefully as they can influence the quality and reproducibility of your entire workflow. Eppendorf epT.I.P.S. pipette tips and Combipips plus are made of carefully selected virgin raw material. All materials do not contain metallic dyes or latex and the automated manufacturing under clean-room conditions eliminates human interaction as source for contamination.

**We develop tips with your research results in mind!**

### epT.I.P.S.:

- Certified trace metal release; no slip agents, plasticizers or biocides used during production
- Batch certified purity levels of Biopur and PCR clean
- Also available as epT.I.P.S. LoRetention and ep Dualfilter T.I.P.S. in certified PCR clean, sterile, pyrogen free

### Combipips plus:

- Certified trace metal release and no plasticizers or biocides used during production
- Batch certified purity levels of Biopur and sterile
- Nine different sizes allow a wide dispensing range

**Experience Eppendorf quality consumables and order your free sample on:**

[www.eppendorf.com/consumables](http://www.eppendorf.com/consumables)

**eppendorf**  
*In touch with life*

Your local distributor [www.eppendorf.com/worldwide](http://www.eppendorf.com/worldwide) · Application Support: [support@eppendorf.com](mailto:support@eppendorf.com)  
Eppendorf AG · Germany · Tel: +49 40 538 01-0 · Eppendorf North America, Inc. · USA · Tel: +1 800 645 3050  
Eppendorf Asia Pacific Headquarters · Malaysia · Tel: +60 3 8023 2769





Ismail Serageldin is the director of the Library of Alexandria, Alexandria, Egypt.

## The Values of Science

IN EGYPT AND TUNISIA, ORDINARY CITIZENS HAVE TOPPLED AUTOCRATS; ELSEWHERE IN THE ARAB World, they still battle dictators, armed with little more than their belief in freedom, human rights, and democracy. What sort of society comes after the revolution? Many fear that the idealism of the revolutionary democrats will only pave the way for theological autocrats who preach an intolerant doctrine. But fighting extremism is best done not by censorship or autocracy but by embracing pluralism and defeating ideas with ideas. And here, science has much to say, particularly about the values that are needed for societies to be truly open and democratic, because these are the values of science.

As the British scientist Jacob Bronowski observed more than half a century ago, the enterprise of science requires the adoption of certain values that are adhered to by its practitioners with exceptional rigor. These values also provide the basis for enhancing human capabilities and human welfare. Truth and honor are of the utmost importance. Any scientist who manufactures data risks being ostracized indefinitely from the scientific community, and he or she jeopardizes the credibility of science for the larger society. A scientist may err in interpreting data, but no one can accept the fabrication of data. What other fields of human activity can rival this level of commitment to absolute truth? Teamwork has become essential in most fields of science, and it requires that all the members of the team receive the recognition they deserve. Contributions are also cumulative, and each should be recognized for his or her contribution. It is a sentiment well captured in Isaac Newton's famous statement that "if I have seen farther than most, it is because I have stood on the shoulders of giants."

Science requires the freedom to enquire, to challenge, to think, to imagine the unimagined. It cannot function within the arbitrary limits of convention, nor can it flourish if it is forced to shy away from challenging the accepted. Science advances by overthrowing an existing paradigm, or at least substantially expanding or modifying it. Thus there is a certain constructive subversiveness built into the scientific enterprise, as a new generation of scientists makes its own contribution. Our respect and admiration for Newton are not diminished by the achievements of Albert Einstein. We can admire both. This constant renewal and advancement of our scientific understanding is a central feature of the scientific enterprise. It requires a tolerant engagement with the contrarian view that is grounded in disputes arbitrated by the rules of evidence and rationality.

Science demands rationality and promotes civility in discourse. Ad hominem attacks are not accepted. Science treats all humans equally. Scientists are concerned with the content of the scientific work, not with the person who produced it. Science is open to all, regardless of nationality, race, religion, or sex. These values of science are universal values worth defending, not just to promote the pursuit of science but to produce a better and more humane society.

The new Arab societies we are building must be open pluralistic societies that are producers of knowledge and new opportunities. Our youth have sparked our revolution, just as other young people have transformed societies, reinvented business enterprise, and redefined our scientific understanding of the world we live in. Today, as they lead the rebuilding of our societies, they must embrace the values of science. Together, all armed with these values, we can think of the unborn, remember the forgotten, give hope to the forlorn, include the excluded, reach out to the unreached, and by our actions from this day onward lay the foundation for better tomorrows.

— Ismail Serageldin



## ASTROPHYSICS

### The Big Bulge

A classical spiral galaxy has three stellar components: a central, roughly spherical bulge; a thin disk around this bulge; and a halo. Typically, the bulge resembles an elliptical galaxy. However, not all bulges follow this classical picture; some, which astronomers call pseudobulges, are disk-like. Fisher and Drory made an inventory of galaxy bulge types within 11 million parsecs from Earth (1 parsec corresponds to ~3.26 light-years). They counted the number of elliptical galaxies (pure bulges) and spiral galaxies with classical bulges, with no bulges, or with pseudobulges by star formation rate and stellar mass. Galaxies without a bulge (pure disk galaxies) or with a pseudobulge are the most common type in the local region analyzed. In this region, two-thirds of new stars are formed in galaxies with pseudobulges and three-quarters of the stellar mass is in disks. It is not clear how pseudobulges form—whether by merging of galaxies or by slow, steady evolution of the disk. The frequency of enhanced star formation in the central regions of galaxies with bulges indicates that long-term, non-episodic processes are at play in bulge growth. If pseudobulges are not the result of mergers, then it is difficult to reconcile the numbers found in this study with those predicted by models of galaxy evolution. — MJC

*Astrophys. J.* **733**, L47 (2011).

## EDUCATION

### One Size Does Not Fit All

Some children, particularly those with a more fearful temperament, are more sensitive than others to the influence of parents, teachers, and environment. Studying preschoolers, Kegel *et al.* attempt to link this with a particular genetic polymorphism. Children played a literacy-gearred computer game that delivered instruction and assignments to all participants, but differed in whether it delivered feedback about the children's choices. A feature that distinguished the groups of children was whether they carried the long variant of the dopamine D4 receptor gene, which is associated with lower dopamine reception efficiency. Children who carried this polymorphism were more susceptible to the effects of feedback from the computer program. They outperformed the control group when



feedback guided their learning, and they did worse than the control group when feedback was absent. In contrast, children with the short variant of the gene seemed to be unruffled by the presence or absence of feedback. For education, just as for shoes, a good fit to the individual produces the best result. — PJH

*Mind Brain Educ.* **5**, 71 (2011).

## CLIMATE SCIENCE

### Wind Winding Down

Increasing concentrations of greenhouse gases in the atmosphere, emitted by human activities, have caused Earth's climate to warm. Climate warming has been linked to a host of other environmental changes, one of the most evident being an increase in the amount of water present as vapor in the atmosphere, a simple change entirely predictable by the Clausius-Clapeyron equation. Other possible changes to the climate system are not so simple or predictable. Gastineau and Soden evaluate the potential impact of warming on windiness, combining daily satellite observations and climate model simulations in

order to determine how tropical surface wind extremes may have responded over the past two decades. They report that both observations and models show a reduction in the strongest wind events, in response to higher tropical sea surface temperatures, and that light wind event frequencies have increased over the same period. These findings help to confirm what has up to now only been suggested by models. The authors suggest that the well-documented increase in the frequency and intensity of extreme precipitation events, which at first may seem inconsistent with a weakening of the large-scale circulation, is therefore mainly a result of increasing atmospheric water vapor. — HJS

*Geophys. Res. Lett.* **38**, L09706 (2011).

## MICROBIOLOGY

### Multiple Metabolic Cooperations

The toxic liquids that ooze out of old mine workings have been fruitful hunting grounds for microbial ecologists, primarily because the range of organisms that can tolerate such extreme conditions is limited and makes for tractable wild ecosystems to study. Bertin *et al.* undertook a metagenomic investigation of the microflora in a stream biofilm exiting the former mine of Carnoulès in France. They found a community dominated by seven organisms



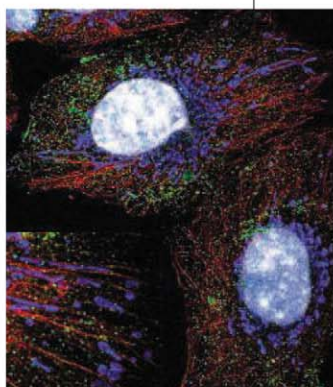
with complementary and apparently intertwined metabolisms. Three strains allied to *Thiomonas*, *Acidithiobacillus*, and *Gallionella* are inorganic nitrogen and carbon dioxide fixers. These primary producers supply other members of the consortium with organic nutrients, in an apparently coordinated way: For example, an *Acidobacteria* clade possesses transporters for simple carbohydrates, whereas a *Thiobacillus*-like organism is equipped to handle complex carbohydrates. A candidate new species of *Fodinabacter* appears to make important contributions to recycling organic compounds released by other organisms, and in turn provides them with essential cofactors, such as cobalamin, which then activates iron oxidation in *Acidithiobacillus*. The seven also seem to be represented by other genotypes, which indicates an ability to shift the metabolic emphasis when conditions change. — CA

*ISME J.* **5**, 10.1038/ismej.2011.51 (2011).

## CELL BIOLOGY

## Not Death-Defying

Caveolae are membrane invaginations found at the surface of mammalian cells that are enriched in cholesterol. Cholesterol-binding proteins known as caveolins play a key role in caveolar formation and are also involved in intracellular cholesterol transport. Mutation or disruption of caveolin genes have been linked to a variety of pathologies, including lipodystrophy, cardiovascular disease, diabetes, and cancer. Bosch *et al.* examined the cellular pathology associated with caveolin disruption in embryonic fibroblast cells from caveolin 1 (CAV1)-deficient mice. The cells exhibited reduced proliferation and survival when subjected to glucose restriction—a phenotype associated with compromised mitochondria. Indeed, mitochondrial membranes from the CAV1-deficient cells contained elevated levels of free cholesterol, which was associated with reduced resistance to antioxidants. The mitochondria thus accumulated reactive oxygen species, which promoted cell death. Thus, mitochondrial dysfunction appears to be the underlying cause of the variety of pathologies observed in CAV1-deficient animals. — SMH



*Curr. Biol.* **21**, 681 (2011).

## POLICY

## Measuring Subsidy Success

After devastating mudslides and floods in 1998 killed thousands of people and displaced millions, the Chinese government undertook a massive effort to fight erosion, called the Sloping Land Conversion Program (SLCP). Under the SLCP, farmers on steep slopes in the Yangtze and Yellow River basins have been given cash subsidies and rice in exchange for allowing their farmland to be restored to forest or grassland and finding jobs other than farming. Part of the goal was to promote a change in the work activities of the people living in these areas to something that would be more sustainable for the ecosystem. Li *et al.* surveyed 20 villages containing participants and nonparticipants in 2008 to determine the effects of this program on the economics of people in a rural area of western China. Participation in the program increased household income, especially for low- and medium-income households. Income inequality was less among households participating in the SLCP than among those that did not; however, it did not change the traditional employment of the participants in the way that had been anticipated—many were still involved in forestry-related activities or animal husbandry. — BJ

*Proc. Natl. Acad. Sci. U.S.A.* **108**, 7721 (2011).

## PHYSICS

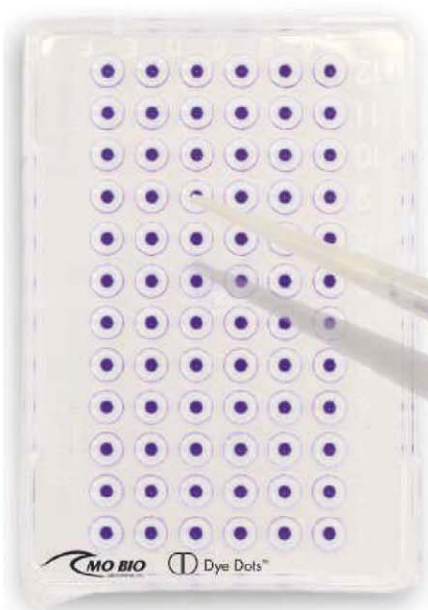
## Scattered Enhancement

One route to enhance the operation of solar cells is to mop up as much of the incident light as possible for subsequent conversion into useful electric current. However, there tends to be a tradeoff between the cost associated with fabricating a complex structure, as well as the amount of material used, and the overall payoff in terms of improved performance. A simple approach is to use a randomly textured back surface reflector to increase the chance of absorption. The optical properties of metal nanoparticles, particularly their ability to strongly scatter light, have made them targets for exploration. Moreover, nanoparticles can couple the scattered light into a nearby dielectric. Spinelli *et al.* use simulations to systematically study how the shape and size of silver nanoparticles influence the scattering of light into a dielectric substrate. Their results provide a method to better understand the scattering and incoupling processes involved and the possibility of optimizing optoelectronic sensors and photovoltaics at the design stage. — ISO

*Opt. Express* **19**, 303 (2011).

# MO BIO Dye Dots™

## Dry Gel Loading Dye



patents pending

*Speed up your  
gel loading process  
today!*

Try a FREE  
Sample Plate at  
[www.mobio.com/dyedots](http://www.mobio.com/dyedots)

Save Tips  
Save Time  
Try Dye Dots™

cat # 15020

**MO BIO**  
Laboratories, Inc.

1200 New York Avenue, NW  
Washington, DC 20005

Editorial: 202-326-6550, FAX 202-289-7562  
News: 202-326-6581, FAX 202-371-9227

Bateman House, 82-88 Hills Road  
Cambridge, UK CB2 1LQ

+44 (0) 1223 326500, FAX +44 (0) 1223 326501

**SUBSCRIPTION SERVICES** For change of address, missing issues, new orders and renewals, and payment questions: 866-434-AAAS (2227) or 202-326-6417, FAX 202-842-1065. Mailing addresses: AAAS, P.O. Box 96178, Washington, DC 20090-6178 or AAAS Member Services, 1200 New York Avenue, NW, Washington, DC 20005

**INSTITUTIONAL SITE LICENSES** please call 202-326-6755 for any questions or information

**REPRINTS:** Author Inquiries 800-635-7181

Commercial Inquiries 803-359-4578

**PERMISSIONS** 202-326-7074, FAX 202-682-0816

**MEMBER BENEFITS** AAAS/Barnes&Noble.com bookstore [www.aaas.org/bn](http://www.aaas.org/bn); AAAS Online Store [www.apisource.com/aaas/](http://www.apisource.com/aaas/) code MK86; AAAS Travels: Betchart Expeditions 800-252-4910; Apple Store [www.apple.com/epstore/aaas](http://www.apple.com/epstore/aaas); Bank of America MasterCard 1-800-833-6262 priority code FAA3YU; Cold Spring Harbor Laboratory Press Publications [www.cshlpress.com/affiliates/aaas.htm](http://www.cshlpress.com/affiliates/aaas.htm); GEICO Auto Insurance [www.geico.com/landingpage/go51.htm?logo=17624](http://www.geico.com/landingpage/go51.htm?logo=17624); Hertz 800-654-2200 CDP#43457; Office Depot <https://bsd.officedepot.com/portalLogin.do>; Seabury & Smith Life Insurance 800-424-9883; Subaru VIP Program 202-326-6417; VIP Moving Services [www.vipmayflower.com/domestic/index.html](http://www.vipmayflower.com/domestic/index.html); Other Benefits: AAAS Member Services 202-326-6417 or [www.aaasmember.org](http://www.aaasmember.org)

science\_editors@aaas.org (for general editorial queries)  
science\_letters@aaas.org (for queries about letters)  
science\_reviews@aaas.org (for returning manuscript reviews)  
science\_bookrevs@aaas.org (for book review queries)

Published by the American Association for the Advancement of Science (AAAS), *Science* serves its readers as a forum for the presentation and discussion of important issues related to the advancement of science, including the presentation of minority or conflicting points of view, rather than by publishing only material on which a consensus has been reached. Accordingly, all articles published in *Science*—including editorials, news and comment, and book reviews—are signed and reflect the individual views of the authors and not official points of view adopted by AAAS or the institutions with which the authors are affiliated.

AAAS was founded in 1848 and incorporated in 1874. Its mission is to advance science, engineering, and innovation throughout the world for the benefit of all people. The goals of the association are to: enhance communication among scientists, engineers, and the public; promote and defend the integrity of science and its use; strengthen support for the science and technology enterprise; provide a voice for science on societal issues; promote the responsible use of science in public policy; strengthen and diversify the science and technology workforce; foster education in science and technology for everyone; increase public engagement with science and technology; and advance international cooperation in science.

## INFORMATION FOR AUTHORS

See pages 784 and 785 of the 11 February 2011 issue or [access www.sciencemag.org/about/authors](http://access.www.sciencemag.org/about/authors)

EDITOR-IN-CHIEF **Bruce Alberts**

EXECUTIVE EDITOR

**Monica M. Bradford**

NEWS EDITOR

**Colin Norman**

MANAGING EDITOR, RESEARCH JOURNALS **Katrina L. Kelner**

DEPUTY EDITORS **R. Brooks Hanson, Barbara R. Jasny, Andrew M. Sugden**

**EDITORIAL SENIOR EDITORS/COMMENTARY** Lisa D. Chong, Brad Wible; **SENIOR EDITORS** Gilbert J. Chin, Pamela J. Hines, Paula A. Kiberstis (Boston), Marc S. Lavine (Toronto), Beverly A. Purnell, L. Bryan Ray, Guy Riddihough, H. Jesse Smith, Phillip D. Szuroim (Tennessee), Valda Vinson, Jake S. Yeston, Laura M. Zahn (San Diego); **ASSOCIATE EDITORS** Kristen L. Mueller, Jelena Stajic, Sacha Vignieri, Nicholas S. Wigginton; **BOOK REVIEW EDITOR** Sherman J. Suter; **ASSOCIATE LETTERS EDITOR** Jennifer Sills; **EDITORIAL MANAGER** Cara Tate; **SENIOR COPY EDITORS** Jeffrey E. Cook, Cynthia Howe, Harry Jach, Lauren Kmeck, Barbara P. Ordway, Trista Wagoner; **COPY EDITOR** Chris Filiatreau; **SENIOR EDITORIAL COORDINATORS** Carolyn Kyle, Beverly Shields; **EDITORIAL COORDINATORS** Joi S. Granger, Anita Wynn; **PUBLICATIONS ASSISTANTS** Ramatoulaye Diop, Emily Guise, Jeffrey Hearn, Michael Hicks, Lisa Johnson, Scott Miller, Jerry Richardson, Brian White; **EDITORIAL ASSISTANT** Patricia M. Moore; **EXECUTIVE EDITORIAL ASSISTANT** Yolanda O'Bannon (San Francisco); **EXECUTIVE ASSISTANT** Alison Crawford; **ADMINISTRATIVE SUPPORT** Maryrose Madrid; **EDITORIAL FELLOW** Melissa R. McCartney

**EDITORIAL DIRECTOR, WEB AND NEW MEDIA** Stewart Wills; **SENIOR WEB EDITOR** Tara S. Marathe; **WEB EDITOR** Robert Frederick; **RESEARCH ASSOCIATE** Corinna Cohn; **WEB DEVELOPMENT MANAGER** Martyn Green; **WEB DEVELOPER** Andrew Whitesell

**NEWS DEPUTY NEWS EDITORS** Robert Coontz, David Grimm (Online), Eliot Marshall, Jeffrey Mervis, Leslie Roberts, John Travis; **CONTRIBUTING EDITORS** Elizabeth Culotta, Polly Shulman; **NEWS WRITERS** Yudhijit Bhattacharjee, Adrian Cho, Jennifer Couzin-Frankel, Jocelyn Kaiser, Richard A. Kerr, Eli Kintisch, Greg Miller, Elizabeth Pennisi, Lauren Schenkman, Robert F. Service (Pacific NW), Erik Stokstad; **WEB DEVELOPER** Daniel Berger; **INTERNS** Sara Reardon; **CONTRIBUTING CORRESPONDENTS** Jon Cohen (San Diego, CA), Daniel Ferber, Ann Gibbons, Sam Kean, Andrew Lawler, Mitchell Leslie, Charles C. Mann, Virginia Morell, Gary Taubes; **COPY EDITORS** Linda B. Felaco, Melvin Gattling, Melissa Raimondi; **ADMINISTRATIVE SUPPORT** Scherraine Mack; **BUREAU** San Diego, CA: 760-942-3252, FAX 760-942-4979; Pacific Northwest: 503-963-1940

**PRODUCTION DIRECTOR** Wendy K. Shank; **ASSISTANT MANAGER** Rebecca Doshi; **SENIOR SPECIALISTS** Steve Forrester, Chris Redwood, Anthony Rosen; **PREFLIGHT DIRECTOR** David M. Tompkins; **MANAGER** Marcus Spiegel; **SPECIALISTS** Jason Hillman, Tara Kelly  
**ART DIRECTOR** Yael Fitzpatrick; **ASSOCIATE ART DIRECTOR** Laura Creveling; **SENIOR ILLUSTRATORS** Chris Bickel, Katharine Sutliff; **ILLUSTRATOR** Yana Hammond; **SENIOR ART ASSOCIATES** Holly Bishop, Preston Huey, Nayomi Kevitiyagala, Matthew Twombly; **ART ASSOCIATE** Kay Engman; **PHOTO EDITOR** Leslie Blizard

## SCIENCE INTERNATIONAL

**EUROPE** ([science-int.co.uk](mailto:science-int.co.uk)) **EDITORIAL:** INTERNATIONAL MANAGING EDITOR Andrew M. Sugden; **SENIOR EDITOR/COMMENTARY** Julia Fahrenkamp-Uppenbrink; **SENIOR EDITORS** Caroline Ash, Stella M. Hurlley, Ian S. Osborne, Peter Stern; **ASSOCIATE EDITOR** Maria Cruz; **LOCOM EDITOR** Helen Pickersgill; **EDITORIAL SUPPORT** Samantha Hogg, Alice Whaley; **ADMINISTRATIVE SUPPORT** John Cannell, Janet Clements, Louise Hartwell; **NEWS:** DEPUTY NEWS EDITOR, U.K. Daniel Clerly; **CONTRIBUTING EDITOR, EUROPE** Martin Enserink; **CONTRIBUTING CORRESPONDENTS** Michael Balter (Paris), John Bohannon (Vienna), Gretchen Vogel (Berlin)

**LATIN AMERICA CONTRIBUTING CORRESPONDENT** Antonio Regalado

**ASIA** Japan Office: Asca Corporation, Tomoko Furusawa, Rustic Bldg. 7F, 77 Tenjin-cho, Shinjuku-ku, Tokyo 162-0808, Japan; +81 3 6802 4616, FAX +81 3 6802 4615, [inquiry@sciencemag.jp](mailto:inquiry@sciencemag.jp); **ASIA NEWS EDITOR** Richard Stone (Beijing): [rstone@aaas.org](mailto:rstone@aaas.org); **CONTRIBUTING CORRESPONDENTS** Dennis Normile [Japan: +81 (0) 3 3391 0630, FAX +81 (0) 3 5936 3531; [dnormile@gol.com](mailto:dnormile@gol.com)]; Hao Xin [China: [cindyhao@gmail.com](mailto:cindyhao@gmail.com)]; Mara Hvistendahl [China: [marahvistendahl.com](mailto:marahvistendahl.com)]; Pallava Bagla [South Asia: +91 (0) 11 2271 2896; [pbagla@vsnl.com](mailto:pbagla@vsnl.com)]

EXECUTIVE PUBLISHER **Alan I. Leshner**  
PUBLISHER **Beth Rosner**

**FULFILLMENT SYSTEMS AND OPERATIONS** ([membership@aaas.org](mailto:membership@aaas.org)); **CUSTOMER SERVICE SUPERVISOR** Pat Butler; **SPECIALISTS** Latoya Casteel, LaVonda Crawford, Vicki Linton, April Marshall; **DATA ENTRY SUPERVISOR** Cynthia Johnson; **SPECIALISTS** Shirlene Hall, Tarrika Hill, William Jones

**BUSINESS OPERATIONS AND ADMINISTRATION DIRECTOR** Deborah Rivera-Wienhold; **BUSINESS SYSTEMS AND FINANCIAL ANALYSIS DIRECTOR** Randy Yi; **MANAGER, FULFILLMENT SYSTEMS** Frits Buningh; **MANAGER, BUSINESS ANALYSIS** Eric Knott; **MANAGER, BUSINESS OPERATIONS** Jessica Tierney; **BUSINESS ANALYSTS** Priti Pamnani, Celeste Troxler; **Christine Wehrli**; **RIGHTS AND PERMISSIONS:** ADMINISTRATOR Emilie David; **ASSOCIATE** Elizabeth Sandler; **MARKETING DIRECTOR** Ian King; **MARKETING MANAGERS** Allison Pritchard, Alison Chandler, Julieanne Wielga, Samantha Smith; **MARKETING ASSOCIATES** Aimee Aponte, Mary Ellen Crowley; **SENIOR MARKETING EXECUTIVE** Jennifer Reeves; **DIRECTOR, SITE LICENSING** Tom Ryan; **DIRECTOR, CORPORATE RELATIONS** Eileen Bernadette Moran; **SENIOR PUBLISHER RELATIONS SPECIALIST** Kiki Forsythe; **PUBLISHER RELATIONS MANAGER** Catherine Holland; **PUBLISHER RELATIONS, EASTERN REGION** Phillip Smith; **PUBLISHER RELATIONS, WESTERN REGION** Ryan Rexroth; **CUSTOMER RELATIONS MANAGER** Iqoo Edim; **CUSTOMER RELATIONS COORDINATOR** David Lee; **MARKETING MANAGER** Christina Schlecht; **MARKETING ASSOCIATES** Laura Tutino, Chad Johnson; **ELECTRONIC MEDIA:** DIRECTOR Elizabeth Harman; **ASSISTANT MANAGER** Lisa Stanford; **SENIOR PRODUCTION SPECIALIST** Ryan Atkins; **PRODUCTION SPECIALISTS** Antoinette Hodal, Michele Johnston, Kimberly Oster; **DIRECTOR, WEB AND NEW MEDIA** Will Collins; **PROJECT MANAGER** Trista Snyder; **SENIOR PRODUCTION SPECIALIST** Christopher Coleman; **COMPUTER SPECIALISTS** Walter Jones, Kai Zhang

**ADVERTISING DIRECTOR, WORLDWIDE AD SALES** Bill Moran

**COMMERCIAL EDITOR** Sean Sanders: 202-326-6430

**ASSISTANT COMMERCIAL EDITOR** Tina Hicklin 202-326-6463

**PRODUCT** ([science\\_advertising@aaas.org](mailto:science_advertising@aaas.org)); **MIDWEST** Rick Bongiovanni: 330-405-7080, FAX 330-405-7081; **EAST COAST/ E. CANADA** Laurie Faraday: 508-747-9395, FAX 617-507-8189; **WEST COAST/W. CANADA** Lynne Stickrod: 415-931-9782, FAX 415-920-6940; **UK/EUROPE/ASIA** Roger Gonçalves: TEL/FAX +41 423 1258; **JAPAN** ASCA Corporation, Makiko Hara: +81 (0) 3 6802 4616, FAX +81 (0) 3 6802 4615; [ads@sciencemag.jp](mailto:ads@sciencemag.jp); **CHINA/TAIWAN** Ruolei Wu: +86 1367 1015 294 [rwu@aaas.org](mailto:rwu@aaas.org)

**WORLDWIDE ASSOCIATE DIRECTOR OF SCIENCE CAREERS** Tracy Holmes: +44 (0) 1223 326525, FAX +44 (0) 1223 326532

**CLASSIFIED** ([advertise@sciencecareers.org](mailto:advertise@sciencecareers.org)); **U.S.: MIDWEST/WEST COAST/ SOUTH CENTRAL/CANADA** Tina Burks: 202-326-6577; **EAST COAST/INDUSTRY** Elizabeth Early: 202-326-6578; **SALES ADMINISTRATOR:** Marci Gallun; **EUROPE/ROW SALES:** Susanne Kharraz, Dan Pennington, Alex Palmer; **SALES ASSISTANT** Lisa Patterson; **JAPAN** ASCA Corporation, Jie Chin +81 (0) 3 6802 4616, FAX +81 (0) 3 6802 4615; [careers@sciencemag.jp](mailto:careers@sciencemag.jp); **CHINA/TAIWAN** Ruolei Wu: +86 1367 1015 294 [rwu@aaas.org](mailto:rwu@aaas.org); **ADVERTISING SUPPORT MANAGER** Karen Foote: 202-326-6740; **ADVERTISING PRODUCTION OPERATIONS MANAGER** Deborah Tompkins; **SENIOR PRODUCTION SPECIALIST/GRAPHIC DESIGNER** Amy Hardcastle; **PRODUCTION SPECIALIST** Yuse Lajiminshup; **SENIOR TRAFFIC ASSOCIATE** Christine Hall; **SALES COORDINATOR** Shirley Young

**AAAS BOARD OF DIRECTORS** RETIRING PRESIDENT, CHAIR Alice Huang; PRESIDENT Nina Fedoroff; PRESIDENT-ELECT William Press; TREASURER David E. Shaw; CHIEF EXECUTIVE OFFICER Alan I. Leshner; BOARD Nancy Knowlton, Stephen Mayo, Raymond Orbach, Julia M. Phillips, Sue V. Rosser, David D. Sabatini, Inder Verma, Thomas A. Woolsey



ADVANCING SCIENCE, SERVING SOCIETY

## SENIOR EDITORIAL BOARD

Cori Bargmann, *The Rockefeller Univ.*  
John I. Brauman, *Chair, Stanford Univ.*  
Richard Losick, *Harvard Univ.*  
Michael S. Turner, *University of Chicago*

## BOARD OF REVIEWING EDITORS

Adriano Aguzzi, *Univ. Hospital Zürich*  
Takuzo Aida, *Univ. of Tokyo*  
Sonia Altizer, *Univ. of Georgia*  
Sebastian Amigorena, *Institut Curie*  
Angelika Amon, *MIT*  
Kathryn Anderson, *Memorial Sloan-Kettering Cancer Center*  
Siv G. E. Andersson, *Uppsala Univ.*  
Peter Andolfatto, *Princeton Univ.*  
Meinrat O. Andreae, *Max Planck Inst., Mainz*  
John A. Bargh, *Yale Univ.*  
Ben Barres, *Stanford Medical School*  
Marisa Bartolomei, *Univ. of Penn. School of Med.*  
Jordi Bascompte, *Estación Biológica de Doñana, CSIC*  
Facundo Batista, *London Research Inst.*  
Ray H. Baughman, *Univ. of Texas, Dallas*  
David Baum, *Univ. of Wisconsin*  
Yasmine Belkaid, *NIAD, NIH*  
Philip Bentley, *Duke Univ.*  
Stephen J. Benke, *Mass. State Univ.*  
Gregory C. Beroza, *Stanford Univ.*  
Peer Bork, *EMBL*  
Bernard Bourdon, *Ecole Normale Supérieure de Lyon*  
Ian Boyd, *Univ. of St. Andrews*  
Robert W. Boyd, *Univ. of Rochester*  
Paul M. Brakefield, *Univ. of Cambridge*  
Christian Büchel, *Universitätsklinikum Hamburg-Eppendorf*  
Joseph A. Burns, *Cornell Univ.*  
William P. Butz, *Population Reference Bureau*  
Georgy Buzsáki, *Rutgers Univ.*  
Mats Carlsson, *Univ. of Oslo*  
Mildred Cho, *Stanford Univ.*  
David Clapham, *Children's Hospital, Boston*  
David Clary, *Univ. of Oxford*  
J. M. Claverie, *CNRS, Marseille*  
Jonathan D. Cohen, *Princeton Univ.*  
Alan Cowman, *Walter & Eliza Hall Inst.*  
Robert H. Crabtree, *Yale Univ.*  
Wolfgang Cramer, *Potsdam Inst. for Climate Impact Research*

F. Fleming Crim, *Univ. of Wisconsin*  
Jeff L. Dangl, *Univ. of North Carolina*  
Tom Daniel, *Univ. of Washington*  
Stanislas Dehaene, *Collège de France*  
Emmanouil T. Dermizakis, *Univ. of Geneva Medical School*  
Robert Desimone, *MIT*  
Claude Despland, *New York Univ.*  
Ap Dijksterhuis, *Radboud Univ. of Nijmegen*  
Dennis Discher, *Univ. of Pennsylvania*  
Scott C. Doney, *Woods Hole Oceanographic Inst.*  
Jennifer A. Doudna, *Univ. of California, Berkeley*  
Julian Downward, *Cancer Research UK*  
Bruce Dunn, *Univ. of California, Los Angeles*  
Christopher Dye, *WHO*  
Michael B. Elowitz, *Calif. Inst. of Technology*  
Tim Elston, *Univ. of North Carolina at Chapel Hill*  
Gerhard Ertl, *Fritz-Haber-Institut, Berlin*  
Barry Everaert, *Cambridge*  
Paul G. Falkowski, *Rutgers Univ.*  
Ernst Fehr, *Univ. of Zurich*  
Tom Fenchel, *Univ. of Copenhagen*  
Alain Fischer, *INSERM*  
Wulfraim Gerstner, *EPFL Lausanne*  
Karl-Heinz Glassmeier, *Inst. for Geophysics & Extraterrestrial Physics*  
Diane Griffin, *Johns Hopkins Bloomberg School of Public Health*  
Elizabeth Grove, *Univ. of Chicago*  
Tackjip Ha, *Univ. of Illinois at Urbana-Champaign*  
Christian Haass, *Ludwig Maximilians Univ.*  
Steven Haehn, *Fred Hutchinson Cancer Research Center*  
Gregory J. Hannon, *Cold Spring Harbor Lab.*  
Dennis L. Hartmann, *Univ. of Washington*  
Martin Heimann, *Max Planck Inst., Jena*  
Isaac Held, *NOAA*  
James A. Hendler, *Rensselaer Polytechnic Inst.*  
Janet G. Hering, *Swiss Fed. Inst. of Aquatic Science & Technology*  
Ray Hilborn, *Univ. of Washington*  
Michael E. Himmel, *National Renewable Energy Lab.*  
Kei Hirose, *Tokyo Inst. of Technology*  
David Hodell, *Univ. of Cambridge*  
Ove Hoegh-Guldberg, *Univ. of Queensland*  
David Holden, *Imperial College*  
Lora Hooper, *UT Southwestern Medical Ctr at Dallas*  
Jeffrey A. Hubbell, *EPFL Lausanne*  
Steven Jacobson, *Univ. of California, Los Angeles*

Kai Johnsson, *EPFL Lausanne*  
Peter Jonas, *Universität Freiburg*  
William Kaelin, *Dana-Farber Cancer Inst.*  
Barbara K. Karger, *Harvard Medical School*  
Daniel Kahne, *Harvard Univ.*  
Bernhard Keimer, *Max Planck Inst., Stuttgart*  
Robert Kingston, *Harvard Medical School*  
Alberto R. Kornblith, *Univ. of Buenos Aires*  
Leonid Kruglyak, *Princeton Univ.*  
Mitchell A. Lazar, *Univ. of Pennsylvania*  
David Lazer, *Harvard Univ.*  
Virginia Lee, *Univ. of Pennsylvania*  
Ottoline Leyser, *Cambridge Univ.*  
Olle Lindvall, *Univ. Hospital, Lund*  
Marcia C. Linn, *Univ. of California, Berkeley*  
John Lis, *Cornell Univ.*  
Richard Losick, *Harvard Univ.*  
Jonathan Loxic, *Harvard Univ.*  
Ke Lu, *Chinese Acad. of Sciences*  
Laura Machesky, *CRUK Beatson Inst. for Cancer Research*  
Andrew P. MacKenzie, *Univ. of St. Andrews*  
Anne Magurran, *Univ. of St. Andrews*  
Oscar Marin, *CSIC & Univ. Miguel Hernández*  
Charles Marshall, *Univ. of California, Berkeley*  
Martin M. Matzuk, *Baylor College of Medicine*  
Graham Medley, *Univ. of Warwick*  
Yasushi Miyashita, *Univ. of Tokyo*  
Richard Morris, *Univ. of Edinburgh*  
Edward Moses, *Norwegian Univ. of Science and Technology*  
Sean Mowbray, *MRC Lab. of Molecular Biology*  
Naoto Nagaosa, *Univ. of Tokyo*  
James Nelson, *Stanford Univ. School of Med.*  
Timothy W. Nilsen, *Case Western Reserve Univ.*  
Pär Nordlund, *Karolinska Inst.*  
Helga Nowotny, *European Research Advisory Board*  
Stuart H. Orkin, *Dana-Farber Cancer Inst.*  
Christine Ortiz, *MIT*  
Elinor Ostrom, *Indiana Univ.*  
Andrew Oswald, *Univ. of Warwick*  
Jane Parker, *Max-Planck Inst. of Plant Breeding Research*  
P. David Pearson, *Univ. of California, Berkeley*  
Reginald M. Penner, *Univ. of California, Irvine*  
John H. J. Petrini, *Memorial Sloan-Kettering Cancer Center*  
Simon Phillips, *Univ. of Florida*  
Philippe Poulin, *CNRS*  
Colin Renfrew, *Univ. of Cambridge*  
Trevor Robbins, *Univ. of Cambridge*

Barbara A. Romanowicz, *Univ. of California, Berkeley*  
Jens Rostrup-Nielsen, *Haldor Topsøe*  
Edmund M. Rubin, *Lawrence Berkeley National Lab*  
Mike Ryan, *Univ. of Texas, Austin*  
Shimon Sakaguchi, *Kyoto Univ.*  
Miquel Salmeron, *Lawrence Berkeley National Lab*  
Jürgen Saatküher, *Medical Univ. of Vienna*  
Randy Seelke, *Univ. of Cincinnati*  
Christine Seidman, *Harvard Medical School*  
Vladimir Shalae, *Purdue Univ.*  
Joseph Silk, *Univ. of Oxford*  
Denis Simion, *Univ. of Oregon*  
Alison Smith, *John Innes Centre*  
Davor Solter, *Inst. of Medical Biology, Singapore*  
John Speakman, *Univ. of Aberdeen*  
Allan C. Spradling, *Carnegie Institution of Washington*  
Jonathan Sprunt, *Garvan Inst. of Medical Research*  
Elsbeth Stern, *ETH Zürich*  
Ira Tabas, *Columbia Univ.*  
Yoshiko Takahashi, *Nara Inst. of Science and Technology*  
John Thomas, *Duke Univ.*  
Herbert Virgin, *Washington Univ.*  
Ber Vogelstein, *Johns Hopkins Univ.*  
Cynthia Volkert, *Univ. of Göttingen*  
Bruce D. Walker, *Harvard Medical School*  
Douglas Wallace, *Leibniz Inst. of Marine Sciences*  
Ian Walmisley, *Univ. of Oxford*  
David A. Wardle, *Swedish Univ. of Agric Sciences*  
Detlef Weigel, *Max Planck Inst., Tübingen*  
Jonathan Weissman, *Univ. of California, San Francisco*  
Sue Wessler, *Univ. of California, Riverside*  
Ian A. Wilson, *The Scripps Res. Inst.*  
Timothy D. Wilson, *Univ. of Virginia*  
Ian Zanen, *Leiden Univ.*  
Mayana Zatz, *University of Sao Paulo*  
Jonathan Zehr, *Ocean Sciences*  
Huda Zoghbi, *Baylor College of Medicine*  
Marta Zuber, *MIT*

## BOOK REVIEW BOARD

John Aldrich, *Duke Univ.*  
David Bloom, *Harvard Univ.*  
Angela Creager, *Princeton Univ.*  
Richard Sweder, *Univ. of Chicago*  
Ed Wasserman, *DuPont*  
Lewis Wolpert, *Univ. College London*



# Science Mobile App Now Available for Android Phones



They say you never know when inspiration will strike. Download the *Science* mobile app for Android devices and be ready the next time you're inspired to read the latest news, research, and career advice from *Science* on your mobile phone.

To download the *Science* mobile app for Android visit [content.aaas.org/mobile](http://content.aaas.org/mobile), visit the Android Market on your phone, or just scan this barcode.

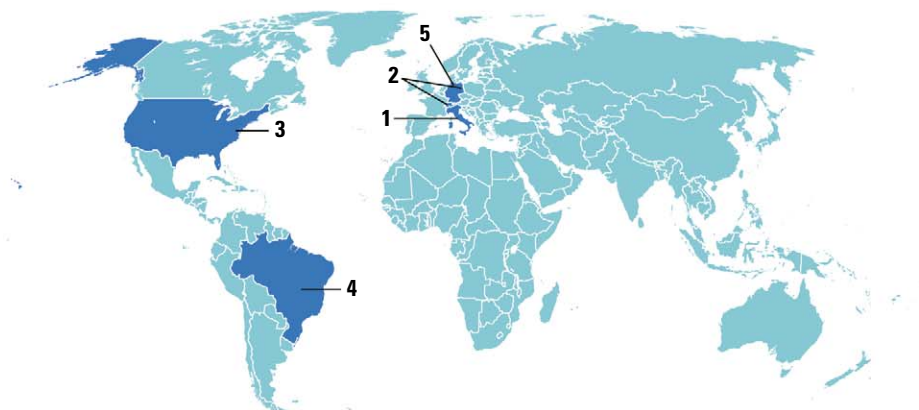


## Features include:

- Summaries and abstracts from *Science*, *Science Translational Medicine*, and *Science Signaling*.
- Ability to e-mail full-text links.
- The latest news from *ScienceNOW*.
- Career advice articles from *Science Careers*.
- Access to the *Science* weekly podcast and other multimedia.
- Content caching for reading without wi-fi access.



## AROUND THE WORLD



## Rome 1

**Manslaughter Trial Approved for Quake Scientists**

Bogus predictions of earthquakes can cause a public panic. But seven scientists and technicians who analyzed seismic activity ahead of the devastating earthquake that struck the Italian town of L'Aquila on 6 April 2009 are about to find out whether the flip side of the coin—erroneously assuring citizens that they are not in imminent danger—could actually be a crime.

On 20 September, the seven will go on trial in an Italian court for manslaughter, a judge decided last week. Last year, it appeared that the charges would be based on a failure to provide residents with adequate warning of the magnitude-6.3 earthquake that killed 308 people. But the case, which the judge ruled had sufficient grounds to go ahead, may instead center on accusations that the defendants gave undue reassurances to residents about their safety in comments that prompted many to remain home despite a series of prequake tremors leading up to the main event. For more, see page 1135.



## Berlin and Bern 2

**Germany and Switzerland Nix Nuclear Energy**

In the wake of the Fukushima disaster, the governments of Germany and Switzerland have announced plans to end the use of nuclear energy. On 30 May, German Chancellor Angela Merkel announced that the country would shut down all of its 17 plants by 2022. Switching to renewable sources without relying on nuclear power is “a great challenge, but above all it is a huge opportunity for future generations,” Merkel said. Meanwhile, following the largest antinuclear protests ever held in Switzerland, the Swiss government announced on 25 May that it plans to close the last of its five reactors by 2034. Parliament will discuss the plan next month, and there could be a referendum. Nuclear plants generate about 23% of Germany's and 40% of Switzerland's electricity.

Also last week, European Union countries agreed on the criteria for so-called stress tests to determine the safety of the E.U.'s 143 nuclear reactors. The tests were slated to begin on 1 June. [http://scim.ag/\\_nix](http://scim.ag/_nix), [http://scim.ag/swiss\\_nuclear](http://scim.ag/swiss_nuclear)

## Washington, D.C. 3

**NASA Aims to Grab Asteroid Dirt**

NASA has announced the next medium-class science mission to explore the solar system. The winner of a three-way competition is a mouthful: Origins Spectral Interpretation Resource Identification Security Regolith Explorer (OSIRIS-REx). It is a spacecraft that would scoop as much as 2 kilograms of rocky soil off a 600-meter-diameter asteroid in 2020 and return the sample to the Utah desert in 2023 for laboratory analysis. While strictly speaking a sci-



ence mission to better understand the nature and origins of a primitive solar system building block, OSIRIS-REx dovetails nicely with President Barack Obama's plans to send astronauts to an asteroid by 2025.

Costing roughly \$1 billion, OSIRIS-REx would launch in 2016 and spend 6 months mapping asteroid 1999 RQ36. Living up to all the ambitions packed into its acronym, the mission would explore the origins of asteroids and thus the solar system itself; connect spectral colors observable from Earth to specific minerals on the asteroid; identify potential resources, such as water for rocket fuel; help evaluate the threat of asteroids to Earth; and return some regolith (asteroid soil) for detailed analysis.

## Brasília 4

**Proposed Brazilian Forest Law Causes Furor**

The passage on 24 May by Brazil's Chamber of Deputies of an amended forest law favorable to ranchers and loggers has brought an outpouring of concern from environmentalists. The bill offers amnesty from penalties for illegal cuts made prior to July 2008 and suspends a rule requiring small landholders in the Amazon (up to 400 hectares) to maintain a minimum of 80% forest cover, among other changes. Brazilian President Dilma Rousseff has threatened to veto parts of the bill, which is still subject to change by Brazil's Senate.

Rural lawmakers say the legislation is a much-needed update to Brazil's forest code, which dates to 1965, and argue that it would help enforce regulations by allowing more plots to become legally recognized. But on 25 May, the Brazilian Academy of Sciences called for another 2 years of scientific review, saying the legislation had no “scientific and technical foundation.”

Marina Silva, Brazil's outspoken former environment minister, called the legislation “one of the biggest steps backwards I've ever seen in Brazil. ... We have returned to the worst possible world.” Indeed, the bill's advance comes amid a recent surge in deforestation, which in March and April reached a pace almost five times that of 2010.

<http://scim.ag/forest-law>



## Germany 5

**E. coli Outbreak Rages On**

Public health experts in Germany are scrambling to bring the world's deadliest outbreak ever of enterohemorrhagic *Escherichia coli* (EHEC) under control. As *Science* went to press, 16 people had died, more than 1400 had fallen ill, and the outbreak—caused by a very rare serotype called O104:H4—showed no signs of abating. Epidemiological studies have fingered raw vegetables as the likely source, but have failed to pinpoint exactly which ones.

In an attempt to save lives, some German nephrologists are turning to a monoclonal antibody called eculizumab, a drug developed to treat a rare blood disorder. Last year, German doctors saw promising results with eculizumab in three children suffering from hemolytic uremic syndrome, EHEC's most severe complication, which is characterized by the destruction of red blood cells and kidney failure. Their findings were published online in *The New England Journal of Medicine* last week. Researchers say the drug appears to be helping some of the current patients as well.

[http://scim.ag/\\_outbreak](http://scim.ag/_outbreak),

[http://scim.ag/\\_eculizumab](http://scim.ag/_eculizumab)

## FINDINGS

**Honey, I Shrunk the Test Subjects**

When Lemuel Gulliver landed on Lilliput, the protagonist in Jonathan Swift's satirical novel didn't think of himself as a giant. Everyone around him, he believed, was tiny. Now researchers have shown we're all a bit like Gulliver.

Researchers at the Karolinska Institute in Stockholm had 198 volunteers wear virtual-reality headsets and lie on their backs, looking at their outstretched legs. Cognitive neuroscientist Björn van der Hoort touched each volunteer's leg while simultaneously touching the leg of a mannequin next to the subject; video of the mannequin was piped to each volunteer's headset. This combination of touch and sight duped the subjects into thinking the mannequin legs were their own.

Then Van der Hoort replaced the mannequin legs with legs many times longer or shorter than the subjects' own, dangled a block in front of the camera, and asked subjects to estimate its size. If their new



## THEY SAID IT

**"I have identical twins. There were times when they would argue and disagree on something. ... Each was absolutely positive truth and justice was on her side. My job was to try to help each of them see the perspective of the other. ... [Now] I've got a whole agency full of identical twins that basically all have truth and justice on their side. All they need to do is get a broader perspective."**

—Marcia McNutt, director of the U.S. Geological Survey, when *The Washington Post* asked her how she learned to be a leader.

legs were tiny, they tended to overestimate; if they were large, they underestimated, the researchers reported 25 May in the journal *PLoS ONE*. The subjects, it seemed, used their bodies as fixed meter sticks and assumed that their environment had either grown or shrunk. <http://scim.ag/i-shrunk>

**Mars Spirit Rover, 2004–2011**

Last year, NASA's Spirit rover watched helplessly as the sun sank lower and lower in the martian sky, the solar power available to warm its innards slowly waning. Inextricably mired in quicksand-like dry powder, the feisty rover beamed a last transmission on 22 March 2010 before the savagely cold martian winter came on. With no word from Spirit since summer's return, NASA officially announced on 24 May that it would cease its efforts to re-establish contact.

Spirit landed in the martian crater Gusev on 3 January 2004 on a minimum 3-month-long mission to explore the crater's dry lakebed. That "lakebed" turned out to be a lava field, but the vehicle rolled on to find ancient water-altered rock in the nearby Columbia Hills, shown in this image composed from a computer model of the rover and a photo Spirit took in March 2005. While exploring the remains of volcanic hot springs, Spirit fell into the powdery trap, where it became easy prey for winter temperatures. Its official lifetime: 2625 martian days. Odometer reading: 7730.50 meters. Spirit is survived by its sister rover, Opportunity, which is in its 30th kilometer and nearing Endeavour crater.

**More Good Cholesterol Doesn't Help**

The effects of good cholesterol are more nuanced than once thought. A clinical trial testing whether people do better when drugs increase their HDL, the cholesterol believed to help prevent heart disease, flopped last week.

The U.S. National Institutes of Health study had enrolled more than 3400 people who had a history of heart disease and paltry levels of HDL. Everyone got a statin, which lowers LDL, or "bad," cholesterol. But some participants also got a form of niacin, a drug that raises HDL. The study was supposed to run for 6 years, finishing in 2012, but it was halted after researchers discovered that people taking niacin were no less likely to suffer heart attacks and strokes.

It's not yet clear why this is. Animal work has found that raising HDL can help, but genetics studies looking at people prone to high or low HDL have turned up mixed results. The drug company Pfizer



## BY THE NUMBERS

**60%** Percentage of the 40 student finalists in the 2011 Intel Science Talent Search whose parents entered the country on temporary H-1B visas. In comparison, less than 1% of the U.S. population are former H-1B visa holders.

**\$757 million** Amount spent by UNICEF on vaccines in 2010. The U.N. agency announced last week that it will publish the prices it pays for vaccines in an effort to boost competition and drive down prices.

## &gt;&gt;FINDINGS

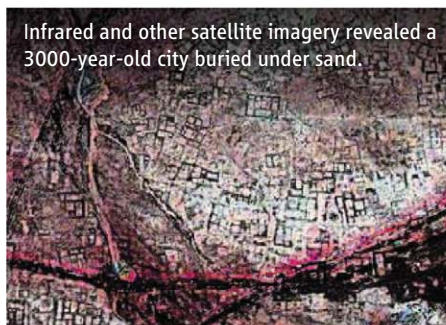
abandoned an HDL-raising drug in 2006 after finding that people on it were 60% more likely to die than those on statins.

## Lost in Time, Found by Satellites

Satellite data have revealed what may be buried pyramids and thousands of ancient settlements beneath Egypt's sands and farmlands.

An American research team led by archaeologist Sarah Parcak of the University of Alabama, Birmingham, discovered the sites by analyzing data from visible as well as infrared satellite imagery. Parcak realized that winter rains soaking into buried mud-brick walls produced a subtle chemical signature in the overlying soil that showed up in high-resolution, infrared satellite images. Based on this clue and others, the team found traces of nearly 3000 ancient settlements and 1000 tombs. They also spotted 17 buried, pyramid-shaped structures; one at Saqqara, famed as a necropolis, was found to be an actual pyramid during a follow-up excavation.

At a 3000-year-old site known as Tanis, the satellite data revealed a warren of mud-



Infrared and other satellite imagery revealed a 3000-year-old city buried under sand.

## Random Sample

## Songs From the Sea

An underwater opera now playing in Berlin gives audiences a chance to hear from one of the most extreme environments on Earth. *AquaAria\_PALAOA* is being staged in the city's striking art deco Neukölln public swimming pool and incorporates scientists' recordings of the soundscape underneath Antarctica's Eckström ice shelf.

The stars of those recordings are Weddell seals. "They are some of the world's most accomplished underwater singers," with more than 50 songs in their repertoire, says Lars Kindermann, a biophysicist at the Alfred Wegener Institute for Polar and Marine Research in Bremerhaven, Germany, which runs the Antarctic recording project.

Kindermann advised the opera's artistic director, Claudia Herr, on both the music and the story, which tells of a woman's search for immortality. He gave Herr, a swimmer-turned-opera singer, a spectrogram of seal vocalizations, which she and the composer were able to use "sort of like sheet music," he says. "[They] were fascinated. She could almost sing from the spectrograms." The vocalists even sing some songs underwater, wearing oxygen tanks and special microphones.

Weddell seals use their voices for survival, echolocating breathing holes in the ice and alerting other seals to the fresh air, Kindermann suspects. The libretto, too, tells "a story of survival in an extreme environment. It is about time, youth and age, love, finding community and loneliness," he says. The 1 May premiere impressed audiences and critics; four more performances of the opera will run in mid-June and mid-September.



brick walls, mazelike streets, and large residences that may have housed the wealthy. A French team already digging there successfully used the American team's images to excavate a specific structure. "They found an almost 100% correlation between what we see on the imagery and what we see on the ground," Parcak says.

The satellite data are a major new contribution to Egyptian archaeology, says Egyptologist Peter Lacovara of the Michael C. Carlos Museum in Atlanta. They also provide a powerful new way for Egypt's government to monitor ancient sites.

## Final Farewell for Mouse Virus and Chronic Fatigue?

The controversial hypothesis that links mouse retroviruses to chronic fatigue syndrome (CFS) suffered yet another devastating blow this week. Two papers published online in *Science* make a strong case for contamination causing earlier studies—one published in *Science*—to find retroviruses, alternately known as XMRV or MLV-related, in CFS patients.

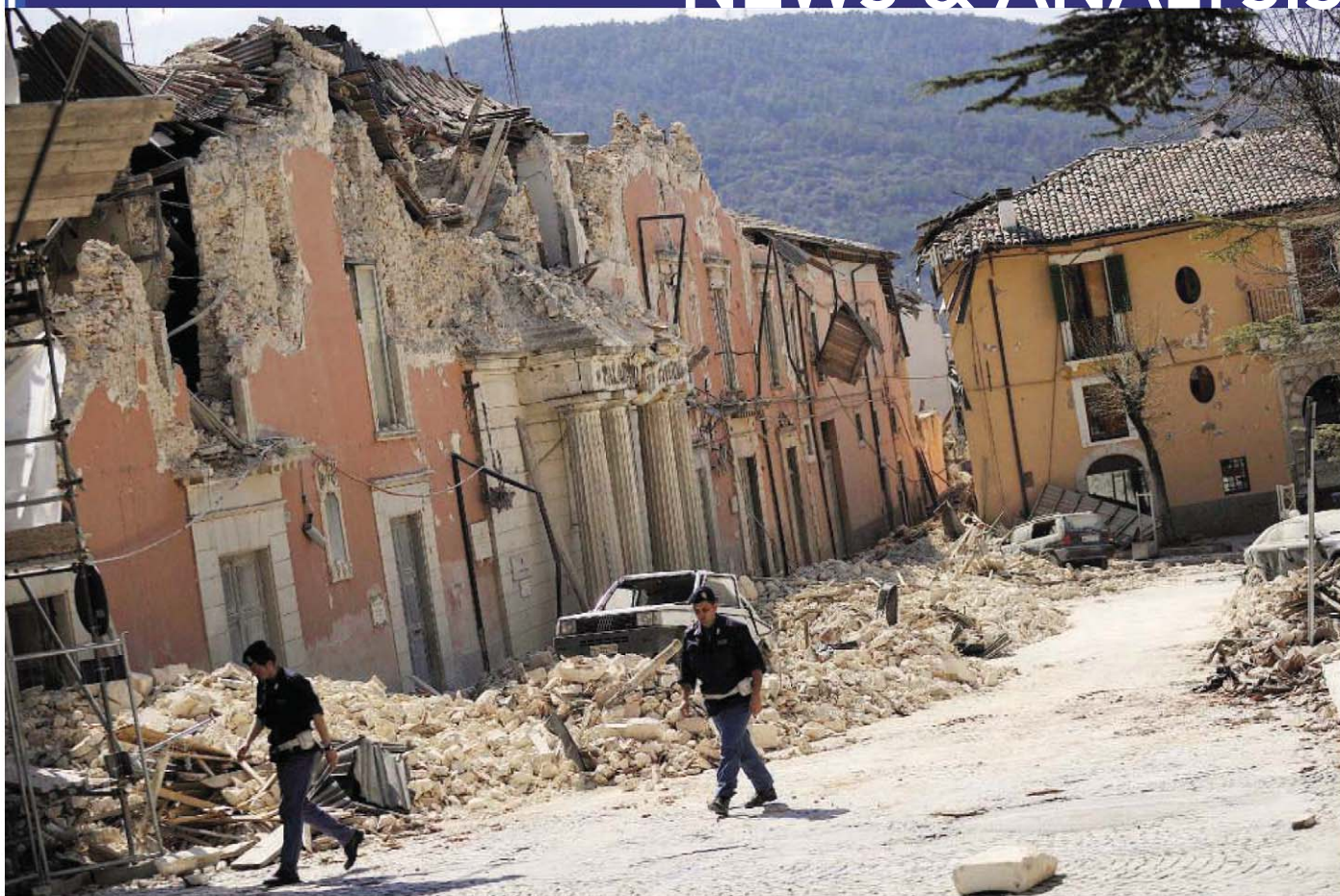
One study examined blood from 61 CFS patients using sensitive polymerase chain reaction and antibody tests and found no evidence of mouse retroviruses. Others have

reported similar negative results, but this study, led by retrovirologist Jay Levy of the University of California, San Francisco, stands out because 43 of the CFS patients had previously tested positive in labs that showed a connection between XMRV and the baffling disease. "They tried very carefully to find the virus and haven't got anything," says Jonathan Stoye, a retrovirologist at the MRC National Institute for Medical Research in London. "That's because there is no virus there." The researchers further showed how the mouse viruses frequently contaminate commonly used lab reagents.

The second report contends that XMRV was born in the 1990s via an experiment that mixed mouse and human cells to create an immortalized line to study prostate cancer. The XMRV-contaminated cell line became widely used. "It's the end, isn't it?" asks Stoye.

Not quite. Judy Mikovits, the corresponding author of the 2009 *Science* paper that found XMRV in CSF patients, refused a request from journal editors to retract the paper. *Science* in turn issued an Expression of Concern, noting that the paper's findings are "seriously in question" and that the journal "eagerly awaits the outcome" of multi-lab studies organized by the U.S. National Institutes of Health to address the question.





ITALY

## Quake Experts to Be Tried For Manslaughter

Seven scientists and technicians who analyzed seismic activity ahead of the devastating earthquake that struck the Italian town of L'Aquila on 6 April 2009 will indeed face trial for manslaughter, a judge announced last week. The defendants are members of Italy's great risks committee, whose job is to assess risks of potential natural disasters. A year ago, they were accused by L'Aquila prosecutors of having failed to provide adequate warning of the magnitude-6.3 earthquake that killed 308 people.

Given the uncertainties in predicting earthquakes, the accusation surprised and angered many. Thousands of seismologists signed a letter of protest, and international scientific groups, including AAAS (publisher of *Science*), condemned the prosecutor's plan to bring manslaughter charges. Nevertheless, Judge Giuseppe Gargarella ruled last week that the case should go to trial.

"The prosecution is without merit,"

says Thomas Jordan, an earth scientist at the University of Southern California in Los Angeles, who chaired an international commission to review earthquake predictions in Italy in the light of the L'Aquila quake. The case may, however, revolve more around what exactly the public was told than whether earthquakes can be predicted.

The seven facing trial, which is due to start on 20 September, are Enzo Boschi, president of Italy's National Institute of Geophysics and Volcanology (INGV); Franco Barberi, great risks committee vice president; Bernardo De Bernardinis, at the time vice president of Italy's Civil Protection Department and now president of the country's Institute for Environmental Protection and Research; Giulio Selvaggi, director of INGV's National Earthquake Centre; Gian Michele Calvi, director of the European Centre for Training and Research in Earthquake Engineering; Claudio Eva, an earth scien-

tist at the University of Genoa; and Mauro Dolce, director of the office of seismic risk at the Civil Protection Department.

Central to the prosecutors' case is a meeting held 6 days before the quake in which the risks committee, as well as local politicians and representatives of the Civil Protection Department, discussed a series of recent tremors that had occurred in the province of L'Aquila, including a quake of magnitude 4.0 the previous day. According to the official minutes of the meeting, the seven accused committee members explained that these tremors did not constitute evidence that a major earthquake was on the way, although, they said, such a possibility could not be ruled out. They agreed that no one can currently predict precisely when, where, and with what strength an earthquake will strike, dismissing claims by Gioacchino Giuliani, a technician at the National Institute of Nuclear Physics near L'Aquila, that he could make such predictions by monitoring levels of radon gas emissions (*Science*, 17 April 2009, p. 322).

Prosecutors claim that the committee gave undue reassurance to the townspeople and that had they not done so, many residents would have evacuated after a smaller tremor that came before the massive quake.

In particular, they take aim at comments made by De Bernardinis in a television interview following the 31 March meeting. “There is no danger,” he said about the ongoing tremors, explaining that “the scientific community continues to confirm to me that in fact it is a favorable situation, that is to say a continuous discharge of energy.”

Committee member Calvi told *Science* that “with the benefit of hindsight, the words of De Bernardinis might

not have been very wise.” He adds that it was perhaps a mistake that it was De Bernardinis who gave the interview, given that his expertise is in floods, not earthquakes. But Calvi dismisses conspiracy theories swirling around the fact that the minutes of the meeting were not finalized until after the earthquake had struck, saying it’s common not to approve minutes until a following meeting, and few changes were made from the draft minutes he had seen.



**Accused.** Enzo Boschi denies misleading the Italian public about earthquake risks and argues he and other scientists shouldn’t face manslaughter charges.

Since the judge’s decision, Boschi has not replied to a request for comment, but his lawyer, Marcello Melandri, says that Boschi has taken the judge’s decision very badly and that his client had not expected that the case would actually go to court. And in October of last year, Boschi told *Science* that he never sought to reassure the local population that there was no risk of a major earthquake. He maintained that he and his scientific colleagues had a responsibility to

provide the “best scientific findings” and that it is “up to politicians” to translate the scientific findings into decisions. In any case, Boschi said, the prosecutors have picked the wrong target, arguing that the “victims of the earthquake are exclusively the result of badly built buildings.”

Jordan has reviewed the minutes of the committee meeting and argues that the statements recorded “were scientifically correct.” He is also convinced that

it was right not to advise people to evacuate the area, pointing out that even though low-level seismic activity does increase the probability of a major earthquake, the absolute probability of a large, local quake occurring in the near future remained very low at the time the committee held its meeting—about 1% according to the best estimates, he says. “You can’t base high-cost actions like evacuation on those kind of probabilities,” he says.

Yet Jordan acknowledges the trickiness of such situations. “There is a fine line between giving information that is scientifically accurate and information that can be actionable by the public,” he notes. Jordan points out that his commission has recommended that Italy, as well as other countries, needs to improve the way it communicates the risks of earthquakes to decision-makers and the public. He also says that the action taken in response to changing forecasts needs to be put on a more systematic basis. “If there is an 80% or 90% chance of a quake, then you have to consider evacuation,” Jordan says. “But what should you do when the probability rises from one chance in 10,000 to one chance in 100? Those kind of questions remain unanswered.”

—EDWIN CARTLIDGE

Edwin Cartlidge is a writer based in Rome.

## MICROBIOLOGY

# Concerns About Arsenic-Laden Bacterium Aired

The debate that erupted 5 months ago over whether a bacterium could thrive on arsenic, even incorporating the element in its DNA, is finally being aired in the scientific literature rather than on blogs. Originally published online by *Science* on 2 December 2010, the paper describing this potentially unprecedented microbe is on page 1163. Eight Technical Comments, released online last week, formally raise many of the criticisms that were quickly hurled when the study was published online and publicized in a NASA briefing. The scientific exchange is unlikely to be the final word on the contentious issue, all agree, especially because there have yet been no independent studies of the microbe at the center of this spat. “The discussion published ... is only a step in a much longer process,” Bruce Alberts, *Science*’s editor-in-chief, remarks in a note introducing the Technical Comments—the most *Science* has published for any one paper—and a response by NASA astrobiology fellow Felisa Wolfe-Simon and the other

authors of the original paper.

The work that set off this furor offered an exception to one of the apparently fundamental rules of life on Earth. To survive, microbes, plants, and animals were all thought to require six essential elements: oxygen, carbon, nitrogen, hydrogen, sulfur, and phosphorus. But Wolfe-Simon and colleagues reported isolating a bacterium that, when grown in high arsenic concentrations and with no added phosphorus, appears to replace some of the latter with the former in key biomolecules, despite arsenic generally being considered toxic and unstable in cells.

The claim startled scientists, many of

*“I think you still won’t find any scientist to say this result has any significant probability of being correct.”*

—ROSIE REDFIELD,  
UNIVERSITY OF BRITISH COLUMBIA

whom quickly complained about the quality of the evidence as well as suggestions by NASA and Wolfe-Simon’s team that the work was relevant to possible extraterrestrial life. “Their hypothesis that this microorganism contains DNA and other standard biomolecules in which arsenate atoms replace phosphorus atoms would, if true, set aside nearly a century of chemical data concerning arsenate and phosphate molecules,” Steven Benner, an astrobiologist at the Foundation for Applied Molecular Evolution in Gainesville, Florida, concludes in one comment.

Several Technical Comments question whether contamination or background levels of phosphorus in the bacterial cultures could have fueled the growth of the controversial microbe, known as GFAJ-1. And microbiologist Rosie Redfield of the University of British Columbia in Vancouver, Canada, airs her concern that the DNA that tested positive for likely having arsenic incorporated in its structure might have been contaminated. She first raised that worry and others in a series

CREDIT: ANSA/SIPA PRESS



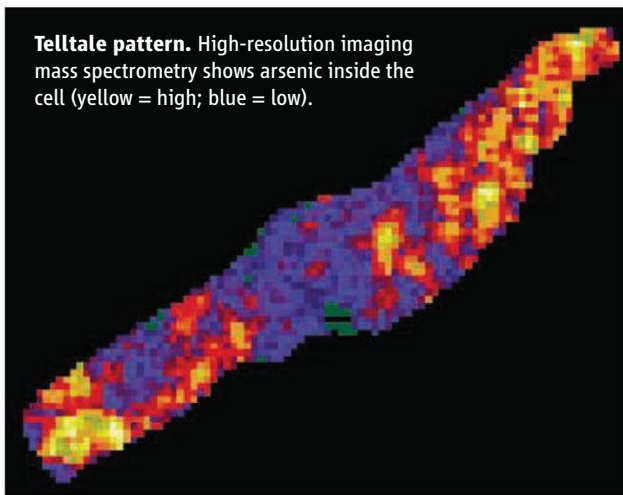
of widely read blog posts that drew hundreds of comments noting additional scientific issues with the work.

Wolfe-Simon's team mentions in their paper that the media used to culture GFAJ-1 contained trace amounts of phosphorus, contributed by mineral salts, but they argue it wasn't enough to drive the microbe's growth or even to sustain its life—a position Redfield challenges with calculations in her comment.

In another critique, James Cotner of the University of Minnesota, Twin Cities, and Edward Hall of the University of Vienna claim that Wolfe-Simon's team misinterpreted their work when the paper cited it as support for the findings. The researchers referenced Cotner and Hall's work as showing that bacteria typically require about 2% phosphorus in their cells—much higher than the 0.02% documented in GFAJ-1. However, the pair point out that the 2% figure comes from studies of *Escherichia coli* under special experimental conditions; they have found a few bacteria that get by with as little phosphorus as GFAJ-1 does.

Three of the comments express skepticism that arsenate compounds would be stable enough in the cell. In the cytoplasm, arsenate would be reduced to arsenite, which would not be able to substitute for phosphate, Barbara Schoepp-Cothenet of the Bioénergétique et Ingénierie des Protéines in Marseilles, France, and colleagues contend. Moreover, phosphorus is incorporated into DNA early in a multistep

**Telltale pattern.** High-resolution imaging mass spectrometry shows arsenic inside the cell (yellow = high; blue = low).



process, and an arsenic substitute would be unlikely to survive that process intact, Benner says. It's also unclear whether the arsenate would change the shape of the DNA, the critics note. Wolfe-Simon points to new research by others, published since her group's announcement, that indicates DNA with arsenic would have the same structure. Also, she says her original studies detected no arsenite in these cells.

Following *Science*'s policy, neither the Technical Comments nor the authors' response offer any new data on GFAJ-1. And indeed, there is little more to report, Wolfe-Simon admits. She says much of her team's last 5 months were spent addressing the community's questions and criticism. Initially, *Science* sent them about 25 letters and comments. Reviewers examined the team's responses to each, and *Science*'s editors eventually culled the redundant critiques down to eight.

Ronald Oremland of the U.S. Geological Survey (USGS) in Menlo Park, California, Wolfe-Simon's group leader, says he and colleagues have done physiological studies to learn how to grow GFAJ-1 better. They have nailed down the source of the background phosphorus in their culture media. "We think we can get it down by an order of magnitude," he says, in part by using ultra-pure ingredients for their media. Growing the bacterium in a phosphorus-free environment would eliminate one of the major sources of skepticism. "But we don't have a lot of people, and they have a lot of other obligations," Oremland says. "We've taken it as far as we can go," given that the lab is not a high-powered molecular, genetics, or chemistry operation.

And Oremland's lab is shrinking, as three of the authors of the original paper, including Wolfe-Simon, are moving on. Wolfe-Simon

continues to be in the spotlight; *Glamour* magazine profiled her, and *Time* named her one of its 100 most influential people. Yet her future is uncertain. Wolfe-Simon says she still has 2 years' support on her NASA fellowship, but last month she left USGS to find a lab better suited for the types of experiments she wants to do and still hasn't found a new home yet.

Wolfe-Simon has found new collaborators though. In 2007, Lianrong Wang and Shi Chen of Wuhan University in China discovered bacteria that incorporated sulfur in the DNA backbone, and earlier this year they described the widespread existence of this type of modification in microbes.

When Wang heard about GFAJ-1's arsenic-laden DNA, he says, "I wanted to grab my glasses and take a serious look at it immediately." Wolfe-Simon has provided them with DNA samples, some of which contain arsenic, and with GFAJ-1 itself, so that they can use mass spectrometry to study how arsenic substitutes for phosphorus. "We are culturing the strain to get a larger amount of DNA for the next step," Wang says.

Wolfe-Simon has provided three other research teams with the strain. One will conduct genomics studies, another may do nuclear magnetic resonance spectroscopy, and a third will check out the incorporation of arsenic by biomolecules other than DNA, in particular, proteins.

Others have asked for the strain, but it's taking time to distribute, Wolfe-Simon says. To resolve that problem, in March she deposited GFAJ-1 in the U.S. ATCC and German DSMZ bacterial repositories. Each has to establish the cultures, freeze-dry the samples, and have those samples verified, so it will be several months before they can be distributed, Oremland says.

Benner isn't sure how many researchers will bother requesting the strain. "I think you still won't find any scientist to say this result has any significant probability of being correct," Redfield says, who has inquired about getting a sample of GFAJ-1. Wolfe-Simon and her colleagues remain confident in their conclusions about the microbe. "With anything this intriguing or controversial, there will always be multiple sides," says Wolfe-Simon's co-author Samuel Webb, a biogeochemist at the Stanford Synchrotron Radiation Lightsource in Menlo Park. "And even if we are proven wrong [about arsenic in the DNA], it's definitely doing something that's crazy and cool." —ELIZABETH PENNISI



**On the hunt.** Felisa Wolfe-Simon is looking for a new lab and new ways to prove arsenic gets into one microbe's DNA.

CREDITS (TOP TO BOTTOM): JENNIFER PETT-RIDGE AND PETER K. WEBER; ZUMAPRESS.COM/NEWS.COM

## BIOMEDICINE

# Wellcome Puts Its Money on Elite Researchers

The Wellcome Trust, the world's largest research charity, this week announced the first winners of a program of large single-investigator awards to prominent biomedical researchers. While this is great news for the 27 new Wellcome Investigators who will share £57 million, hundreds of university-based researchers stand to lose Wellcome funds as the trust phases out some existing programs to pay for the new category of investigators.

"It's a very good mixture of names," says Wellcome chief Mark Walport, who has championed the new awards as the best means of supporting exceptionally talented researchers in Britain and elsewhere with globally competitive and reliable funding. But Paul Marshall, director of the 1994 Group of universities, warned that other funders following the same path could lead to "over-reliance on a small number of research 'stars,' and fears for maintaining a broad base."

The Wellcome Trust, whose endowment stood at £13.9 billion last year, will spend £750 million this year on its full range of fellowships, grant programs, and research laboratories. Its annual budget matches that of the publicly funded Medical Research Council (MRC) and slightly exceeds that of its closest U.S. equivalent, the Howard Hughes Medical Institute (HHMI). The trust announced in 2009 that it was going to phase out several long-running funding streams that support hundreds

of scientists, including its regular program, project, and equipment grants, to free up about £110 million annually for a new program that handsomely rewarded a smaller cadre of scientists judged to have the potential to do groundbreaking research (*Science*, 21 May 2010, p. 964). The plan has been likened to the approach employed by HHMI, which concentrates most of its effort on supporting 300 investigators in the United States.



**Favored few.** Recipients of Wellcome Investigator awards: Liverpool's Alister Craig, Pedro Hallal from Brazil, and Oxford's Peter Rothwell.

Wellcome vetted the resumés of 750 applicants and chose 173 to complete an application form that asked a handful of simple questions about what the applicant was seeking to investigate, how they'd do it, and why it mattered. Nine review panels then picked 55 candidates to attend a "star chamber" of prominent researchers; each was given 10 minutes and three slides to make his or her case, before a brief interrogation.

The result, announced on 2 June, was 25 individual awards and one shared award, over periods of up to 7 years, worth a total of £57 million. Wellcome expects to issue three or four smaller rounds of such awards each year, and if these reflect the first round, it will end up supporting more than 300 awardees at a rate of about £350,000 a year each.

The 26 awards are heavily concentrated among a handful of institutions: 21 of them are going to the so-called golden triangle cities of London, Cambridge, and Oxford, with 15 going to just four universities. Four awards go to scientists elsewhere in the United Kingdom. Pedro Hallal of Federal University of Pelotas in Brazil is the only recipient working outside the United Kingdom.

Awardees say the selection process made a refreshing change from conventional grant applications. The written application process "was much shorter than usual but much harder to do," recalls Laurence Pearl, a structural biologist at the University of Sussex who won about £2.5 million over 7 years to study the role of the Hsp90 molecular carrier in acti-

vating and regulating proteins. "It didn't let you hide behind the detail of what you're planning in the laboratory."

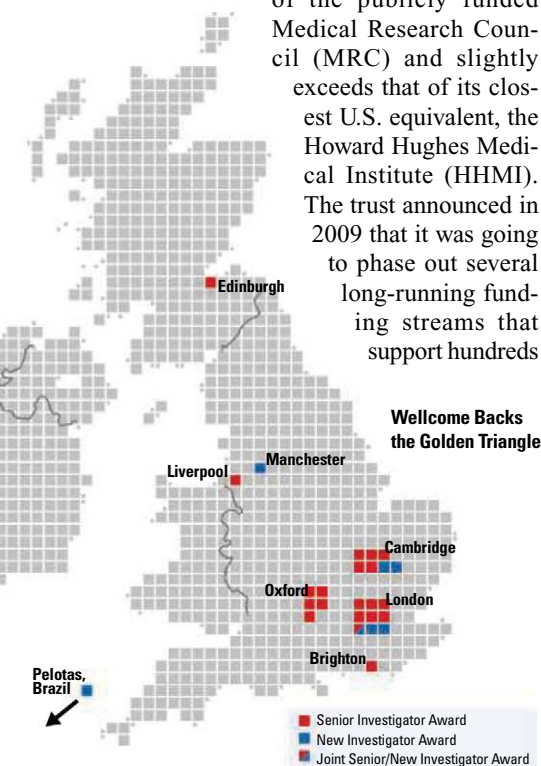
The star chamber "was completely nerve-racking" for molecular parasitologist Alister Craig of the Liverpool School of Tropical Medicine, who won £1.4 million over 5 years to study the accumulation of infected blood cells in the brains of patients with cerebral malaria. Six of the awards are for "New Investigators," people with less than 5 years of postdoctoral experience. Craig, like some other winners, says he's "worried about people who are too old for the 'new' investigator awards and not quite ready for the 'senior' ones." He says he hopes that the trust will work out a way to restore project-specific grants in some shape or form.

Clinician Peter Rothwell of the University of Oxford thinks that he was helped by having a project straddling two fields—in his case, neuroscience and public health. His team will use a £2.5 million award to study practical steps to avert strokes, how variable blood pressure contributes to them, and the nonvascular effects of aspirin. "They were willing to let me draw together these three strands," he says.

Hallal, 31, will study how physical exercise by mothers and children affects lifelong health. "Funding for research in Brazil is almost always short term," says Hallal, who came across the program while visiting the United Kingdom on a Royal Society fellowship. "Seven years of support is extraordinarily important for my career."

Researchers are now eager to see what effect this concentration of funds will have on U.K. biomedical research. Wellcome's project grants "were the first step on the ladder for many of us," says Jonathan Weber, director of medical research at Imperial College London. Applications for MRC grants have gone up "markedly" since the Wellcome ones closed, he says: "We still see that as unresolved." Leszek Borysiewicz, vice-chancellor of the University of Cambridge, which won four awards, believes the impact will be positive: "Universities will adapt to this way of funding research." MRC Chief Executive John Savill points out that the United Kingdom spends £3 billion a year on biomedical research, leaving "a lot of alternatives" to the discontinued Wellcome programs. —COLIN MACILWAIN

Colin Macilwain is a writer based in Edinburgh, U.K.



**Familiar territory.** Wellcome focuses its awards on U.K. powerhouses Oxford, Cambridge, and London.



## ECOLOGY

# Appraising U.K. Ecosystems, Report Envisions Greener Horizon

A group of 500 scientists has just released the first-ever assessment\* of the status of ecosystems in the United Kingdom, evaluating their ability to provide food, sustain biodiversity, and perform many other services. The overall conclusion: Some 30% of these ecosystem functions are currently declining. The report suggests that the government could do a better job managing these ecosystems—and reap more benefits for society—if it took into account the economic value of a broader array of natural benefits, such as recreation and carbon sequestration.

In the most comprehensive attempt yet, the report calculates the economic values of several benefits across an entire nation. The analysis “is the best of its kind” and “a step toward ecosystem accounting,” says Robert Scholes, a systems ecologist with the Council for Scientific and Industrial Research in Pretoria, South Africa, who was not involved in the study.

The new report is modeled on the global Millennium Ecosystem Assessment, which highlighted the parlous state of ecosystems worldwide and emphasized the importance of the benefits they provide (*Science*, 1 April 2005, p. 41). During a 2007 review of the U.K.’s environmental policy, a House of Commons environmental committee called for a similar national assessment. About half the £1.3 million funding came from the Department for the Environment, Food and Rural Affairs (DEFRA), with the remainder coming from other environmental agencies. The effort was co-led by Robert Watson, DEFRA’s science adviser and one of the architects of the Millennium Assessment.

For 2 years, a team of more than 500 experts evaluated the status of 25 ecosystem services within eight broad habitat types, such as cities, farms, and woodlands. The results were mixed. “On important indicators we continue to move down an unsustainable path, despite some improvements,” Scholes says. A third of services are declining, such as soil quality. Many others, like water quality in streams and wetlands, are stable but remain degraded. On the other hand, farm yields have increased dramatically since 1945. The capacity of ecosystems to pro-

vide several services has recovered in recent decades, including air quality, due in part to environmental regulations. Some improvements in ecosystem function, however, come at the expense of other nations: The United Kingdom imports 30% of its food and 80% of its timber, which means the associated ecosystem degradation is happening outside U.K. borders.

To better inform policymakers, the authors went a step further than did the Millennium Assessment and gauged the economic value of several ecosystem services.



**Another path.** Including more values of nature, such as recreation, can better inform land-use policy.

This is easy for crops and timber, which fetch a market price, but can be more difficult and time-consuming for so-called nonmarket values of nature, such as aesthetic pleasure or biodiversity. “It’s superhard to do so that you would believe the numbers at a national level,” says economist Stephen Polasky of the University of Minnesota, Twin Cities, who advised the project.

The team combed through the scientific literature and also conducted original analyses. Charles Perring of Arizona State University in Tempe describes the effort as “a nice, rather conservative, traditional

approach to ecosystem service accounting.” They found, for example, that inland wetlands improve water quality to the tune of £1.5 billion per year. Access to rivers, coasts, and wetlands is worth up to £1.3 billion annually. The calculations, some done to a square-kilometer resolution, show that location matters a lot; woodlands near cities offer a larger sum of recreational benefits than those more distant. “We should have forests around British cities,” says Ian Bateman of the University of East Anglia, who led the economic analysis.

The core of the economic analysis centered on six scenarios of what U.K. ecosystems might look like in 2060, given various policy decisions. For example, in the “World Markets” scenario, the government boosts agricultural production and eases regulations. By contrast, in the “Nature@work” scenario, officials encourage the cultivation of landscapes that balance a variety of needs from timber to hiking.

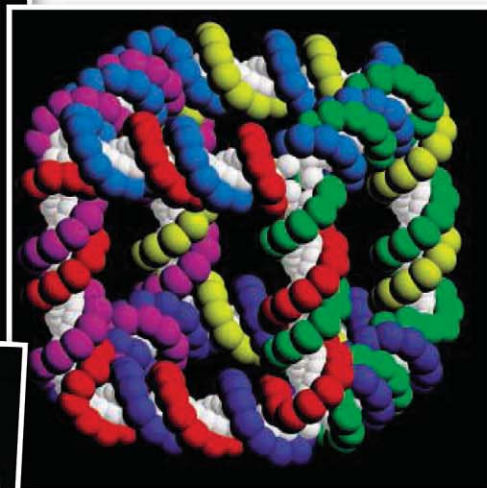
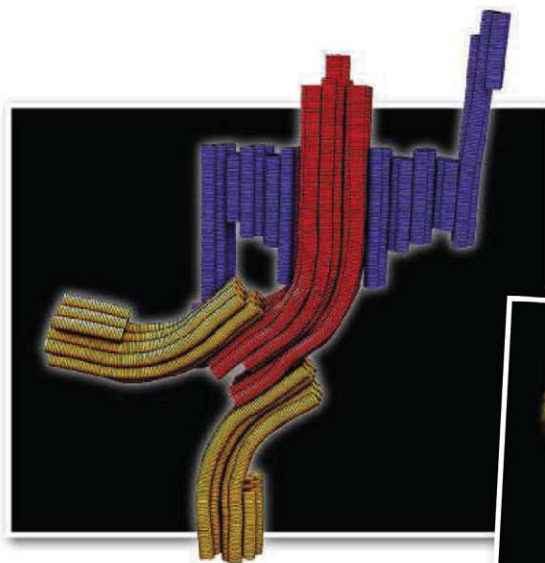
A key point that emerged was the importance of including nonmarket values in policy decisions. When only agricultural output was considered, the World Markets scenario offered the second greatest economic benefits among the six scenarios, and Nature@work was dead last (because it lessens the amount and intensity of agriculture). However, the tables were turned when the economic value of countryside recreation, urban greenspace, and greenhouse gas emissions were monetized. Nature@work offered the largest benefits and World Markets the smallest. “It’s a radical change in the prioritization of the best way forward,” Bateman says.

Co-chair Steve Albon of the James Hutton Institute in Aberdeen, United Kingdom, notes that the team deliberately avoided policy prescriptions: “Our view is that this needs to be a more participatory approach not only with government but the wider stakeholder community, too.” As for the report’s impact, many observers are encouraged by the fact that the government itself commissioned the report—rather than, say, a nonprofit with limited clout—which increases the odds that its messages will be heard and data sets used.

Despite progress on monetizing the value of outdoor recreation and urban greenspace, much research is needed to estimate the economic value of other nonmarket ecosystem benefits such as added value of wild pollinators for crops. “Leaving them out will lead to bad decisions,” Polasky says. “But routinely including them in decision-making will require a lot more work.”

—ERIK STOKSTAD

\*UK National Ecosystem Assessment (2011), Synthesis of the Key Findings, UNEP-WCMC, Cambridge.



# DNA Nanotechnology Grows Up

**Once dismissed as molecular parlor tricks, techniques for piecing ultrasmall structures together with DNA are starting to prove their worth in serious research**

**SNOWBIRD, UTAH**—All scientists face rejection when their proposals are dissected and their papers picked apart. Ned Seeman's worst slapdown came after what he considered at the time his greatest success. Seeman, an x-ray crystallographer at New York University (NYU) in New York City, had spent more than a decade working out the details of how to use DNA not as the master genetic control, but as a construction material for making molecular beams, joints, and girders that could be programmed to weld themselves together in molecular triangles, squares, and other simple shapes. Finally, in 1991, Seeman and colleagues at NYU managed to forge a DNA cube, the first three-dimensional (3D) nanoscale object in which the position of each atom was programmed, defined, and known.

Seeman submitted his manuscript to (ahem) *Science*. But it was promptly returned with a comment from a reviewer who, as Seeman recalls, asked, "Where is the biology?" Today, Seeman is regarded as the founder of the burgeoning field of DNA nanotechnology, in which researchers arrange DNA's four building blocks—molecules of adenine (A), guanine (G), cytosine (C), and thymine (T)—so that they assemble themselves into what-

ever structures the scientists want to build. After cubes, researchers in the field went on to build octahedra, rafts, smiley faces, and even a collection of strands that look like a Rock 'Em Sock 'Em Robot. Many critics are still unconvinced. "People always say, 'Yeah, that's cute. So what? What are you going to do with it?'" Seeman says. Or as Hendrik Dietz, a biophysicist at the Technical University of Munich in Germany, says he often hears it, "It's an amusing but pointless exercise."

"Pointless" may seem harsh for an endeavor that represents nanotechnology's closest thing to building materials atom by atom from the ground up. But until now, the critics had a point: The field has searched for relevance.

No longer. DNA nanotechnology has left its childhood behind and entered adolescence. Like a teenager who clings to parts of childhood, some DNA nanotech continues to be playful and impractical. (The molecular robot boxer can't actually throw a punch.) But the field is also growing in strength and power. It's now churning out applications that are helping researchers map the atomic structure of proteins and compute inside cells (see sidebar, p. 1142), and soon may even start tracking and

**Build up.** DNA folding has constructed ever-more-complex objects, including a simple cube, two-dimensional faces and figures, and a 3D vase.

curing diseases. "We're still playing around," says Andrew Turberfield, a physicist at the University of Oxford in the United Kingdom. "But we've gotten good enough that we can do some interesting things."

## Flying fish

Getting to this stage has been a slog. Thirty years ago, Seeman, then a young assistant professor, was struggling to make a mark in his field of protein crystallography, in which researchers interpret the way beams of x-rays bounce off copies of a protein aligned in a crystal to work out the molecule's structure. Many proteins rebuff efforts to force this order. And Seeman was struggling. "I was confronting this fatal progression of no crystals, no crystallography, no crystallographer," he recalls.

Seeman wondered whether DNA might help. DNA is most commonly thought of as a linear chain of A's, T's, G's, and C's. That's true, of course. But thanks to the propensity of individual nucleotide bases of DNA to pair with one another (T's with A's and G's with C's), DNA in cells forms a double helix, in which two strands of complementary nucleotides zip together. Seeman and others knew that under special circumstances, such as when DNA is copied during cell division, double-stranded DNA can unzip and begin binding to other strands, forming DNAs with branch points, not perfectly linear molecules. By tweaking the DNA's base pair sequence, researchers quickly realized that they could make artificial DNA branches with four arms, six arms, or more.

It was these branched DNAs that gave Seeman his eureka moment. In a tale that has risen to legend in the field, Seeman was drinking a beer in a bar in Albany when an

CREDITS (LEFT TO RIGHT): HENDRIK DIETZ, TU MUNICH, GERMANY; PAUL ROTHMUND AND NICK PAPADAKIS, DONGRAN HAN AND HAO YAN, THE BIODESIGN INST. AND DEPT. OF CHEMISTRY AND BIOCHEM., ARIZONA STATE UNIV.; PERMISSION OF NADRIAN C. SEEMAN



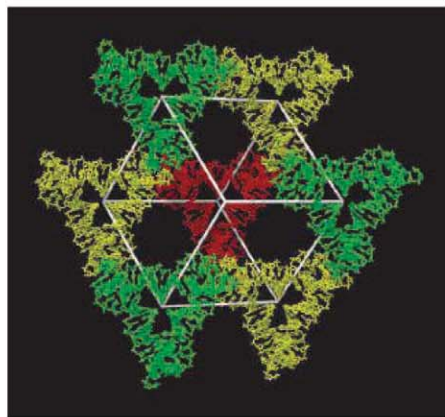
image of the M. C. Escher woodcut *Depth* popped into his head. The woodcut depicts dozens of flying fish soaring in formation, with head and tail, left and right fins, and top and bottom fins all oriented the same way. Seeman realized that artificial DNAs with six arms (front, back, up, down, left, and right) could be tailored to link up into a regular 3D cubic lattice with a large empty space at the center of each cube. And as a crystallographer, Seeman immediately envisioned that such an array could be used to trap copies of a single protein in the voids and get them to line up with the same orientation. In other words, he imagined a tool for determining the structure of virtually any protein at will.

In 1982, Seeman and colleagues laid out their ideas for creating such a lattice and other complex nanostructures in the *Journal of Theoretical Biology*. Actually making the structures was a lot harder. "It took a long time to figure out how to get these experiments to work," Seeman says. Among the challenges were learning how to outfit double-stranded DNAs with single-stranded tails that would link up with a complementary tail on another DNA fragment and how to make normally floppy DNAs rigid enough to form stable structures.

A series of advances cleared these and other hurdles. Over the next few years, Seeman's lab turned out triangles, squares, and other shapes. Then came the 1991 cube, and by 1998 Seeman's team had figured out how to assemble such parts into an extended two-dimensional array. Even then the field remained small, as building new structures required painstaking effort to design and synthesize all the component DNA strands. And synthesizers could churn out DNAs only hundreds of base pairs in length, a constraint that limited the complexity of the final structures.

That changed 4 years ago when Paul Rothemund, a chemist at the California Institute of Technology in Pasadena, and colleagues developed a technique called DNA origami. He and colleagues started with a 7000-base-pair viral genome for which the entire sequence was known.

Next, using a computer, they modeled how they would need to fold this single strand over and back upon itself to create a desired shape. Then they synthesized 250 short "staple" DNA strands designed to bind to sections of the DNA that ended up next to each other when folded, holding the structure in shape. Finally, the researchers added the staples to the viral genome, heated the brew, and cooled it down. Presto, the now iconic image of the DNA smiley face. "Seeing the



**Molecular vise?** A void in this DNA may hold proteins inside to map their atomic structure.

pictures, my jaw dropped," says William Shih, a DNA nanotech expert at Harvard Medical School (HMS) in Boston. "This was a game changer for the field." Adds Dietz: "With origami, it's gone 'whoosh!' to a completely different scale. Now we can make structures in the megadalton range with 16,000 base pairs where the position of every base pair is at a precisely registered position." And since Rothemund's achievement other groups have added versions of the technique to fold DNA origami in 3D, as well as computer-aided design programs able to automate the task.

### Construction boom

These advances haven't quieted all of the critics. At a Foundations of Nanoscience meeting held here in April,\* a prominent U.S. chemist who asked not to be named said that he still thought the field lacks widespread utility. But Shih and other proponents argue

that is beginning to change. "Some people see a DNA robot and say, 'You can build a robot,'" Shih says. "Some people see a robot and say, 'You can build anything.'"

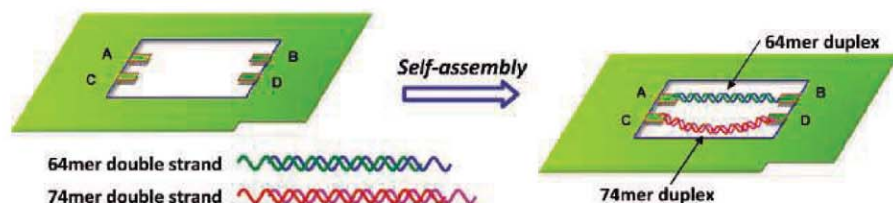
Maybe not anything yet. But Seeman, for one, is now aiming to complete his original dream of using DNA nanostructures to help solve protein structures. In 2009, Seeman and a host of collaborators reported in *Nature* that they had stitched together a series of triangles into a rigid crystalline 3D lattice with rhombohedral voids. Then, using x-ray crystallography, they mapped out the structure of their crystal with a resolution of 4 angstroms. When he showed an image of the crystal at the meeting, Seeman exclaimed: "This is the most exciting slide I've ever shown. I know where every atom is."

More or less, that is. Getting a picture of a molecule with a 4-angstrom resolution suggests that the arms are still wiggling around too much to determine the structure of copies of a protein held within. So Seeman's team is still working on getting its lattices to diffract at a higher resolution and on anchoring copies of a protein to be imaged inside each cell. If they succeed, they will be able to work out the shape of the protein by carrying out x-ray diffraction on the combination and then subtracting out the scaffolding holding the protein in place.

While Seeman's group tinkers with its protein scaffolds, researchers in other groups have been making progress with alternatives. At the meeting, for example, Shih reported that he and colleagues had for the first time used DNA nanotech tools to map the structure of a previously unsolved protein, using nuclear magnetic resonance (NMR) spectroscopy. The technique works by identifying the magnetic signature of atoms in proteins relative to their neighbors. By knowing each atom's neighbors, researchers can piece together the structure of an overall protein, in a process much like solving a complex jigsaw puzzle. But the technique works only for modest-sized proteins, for which sorting out the interactions between neighbors is manageable.

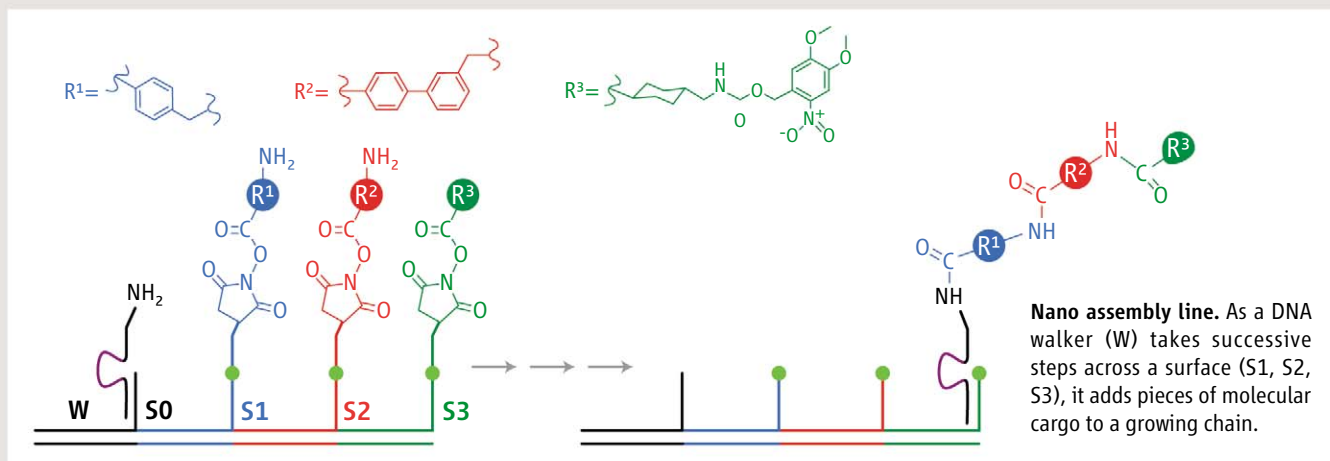
Tweaks to standard NMR have provided researchers with additional bits of information for helping solve their molecular jigsaws. In 1997, for example, researchers at the National Institute of Diabetes and Digestive and Kidney Diseases spiked a protein-containing NMR solution with a compound that spontaneously forms liquid crystals, mate-

*Continued on page 1143*



**Freeze frame.** A tiny reaction chamber built from DNA (green) enables chemists to watch how DNA-binding proteins interact with DNA strands of different length.

\*8th Annual Conference on Foundations of Nanoscience, 11–15 April, Snowbird, Utah.



## Next Step: DNA Robots?

DNA nanotechnology isn't only about using DNA as a set of tiny Tinkertoys. Researchers in the field have long sought to use DNA's ability to store and manipulate information to build a DNA computer. But after years of trying—and failing—to outdo conventional computer technology, the field is finally advancing by going back to DNA's biochemical roots.

The appeal of a molecular computer is easy to see. A single gram of dried DNA contains roughly as much information as 1 trillion compact discs. And the fact that life exists and evolves shows that this information can be stored, read out, manipulated, and copied. In short, it can be used for computation. In principle, the selective binding and unbinding of complementary DNA strands can even be used to process vast amounts of information in parallel.

In 1994, Leonard Adleman, a computer scientist at the University of Southern California in Los Angeles, harnessed that power to solve a so-called Hamiltonian path problem, a version of the well-known "traveling salesman problem" that computer scientists use as a benchmark for tough computations (*Science*, 11 November 1994, p. 1021). Later, Adleman and other researchers moved on to far more complex problems. The idea of using DNA to perform conventional computations, however, quickly fizzled out.

"We gave up on that back around 1998," says Erik Winfree, a DNA computation expert at the California Institute of Technology (Caltech) in Pasadena. DNA computers, Winfree notes, are slow, error-prone, and difficult to scale up to perform millions of operations. That makes them impractical for tasks that microelectronics does well.

Instead, Winfree and others argue, DNA computers should play to their strength: processing information inside organisms or other

wet environments where conventional computer chips can't go. "The real application is making slow, crappy computers that can talk to cells," enabling them to do things such as diagnose and treat diseases, says William Shih, a biological chemist at Harvard Medical School in Boston. "You don't need [Intel's] Core 2 Duo processor to do that."

A striking example of this approach came last year from the laboratory of Niles Pierce, one of Winfree's colleagues at Caltech. In an article published online 7 September 2010 in the *Proceedings of the National Academy of Sciences*, Pierce and Caltech colleagues described how they had used pairs of small synthetic molecules of DNA's short-lived cousin RNA to diagnose and kill tumor cells in vitro. The first RNA strand was designed to recognize and bind to an RNA unique to cancer cells. Latching on to the cellular RNA caused the strand to expose a binding site to which the second RNA could attach itself. That second binding, in turn, unleashed a chemical cascade that made the cancer cell think it had been infected with a virus and triggered the cell to kill itself. Non-cancer cells, meanwhile, were spared.

Pierce and his colleagues also reported online 31 October in *Nature Biotechnology* that a related strategy could be used to image RNA expression inside cells. To researchers in the field, such sensor-triggered step-by-step processes represent biological computer programs.

Chemists are also getting in on the act, using tiny DNA "walkers" to help them build molecules. DNA walkers are rudimentary DNA robots designed to move step by step down a linear track. The robots' legs are DNA strands that bind to specific complementary DNAs on a predesigned surface. Although there are many types of walkers, most take a step each time researchers add a specific DNA snippet,

known as a "fuel" strand, to their brew. Each fuel strand acts like a computer command telling the walker what to do next. The first fuel strand binds the site on the track holding the back "leg" of a two-legged walker, causing it to unbind from its DNA partner on the surface, and then bind to another DNA sequence past the front leg. Another snippet is then added to move the second leg forward, and so on.

In 2010, three groups took the idea a big step forward by putting DNA walkers to work as construction crews. In the 13 May 2010 issue of *Nature*, Nadrian "Ned" Seeman, a DNA nanotech expert at New York University, and his colleagues described creating a fleet of DNA walkers, each with four legs and three DNA arms designed to pick up and move various pieces of molecular cargo. Seeman's DNA walkers linked their successive loads into a growing molecule, creating perhaps the world's smallest assembly line.

Groups led by Andrew Turberfield, a physicist at the University of Oxford in the United Kingdom, and David Liu, a chemist at Harvard University, built related construction robots a short while later. And earlier this year, Turberfield and his team reported in *Nano Letters* that they had programmed their cargo-carrying walkers to move in desired directions down a track with multiple branches that are preprogrammed to display synthesized DNA with binding sites specific to DNA stretches on the legs of the walkers. In the future, Turberfield says, researchers might be able to program multiple robots to construct a wide variety of different molecules simultaneously.

For now, these and other DNA machines are slow and simple. But they've already proved that they can manipulate information in ways that microelectronics may never be able to match.

—R.F.S.



Continued from page 1141

rials that flow but have a regular molecular orientation like a crystal. They found that as the protein molecules tumbled around in solution and repeatedly banged into the walls of this soft crystalline material, they wound up spending ever-so-slightly-more time in one particular orientation than in others. The subtle preference biased the NMR results enough for the researchers to spot clues such as the angle between two atoms bonded in a protein. That information made it possible to solve structures for several proteins that reside in cell membranes and are nearly impossible to crystallize. A big drawback to the technique and later variations of it is that many cell-membrane proteins can stay in solution only with the help of detergents, which often tear apart the liquid crystals.

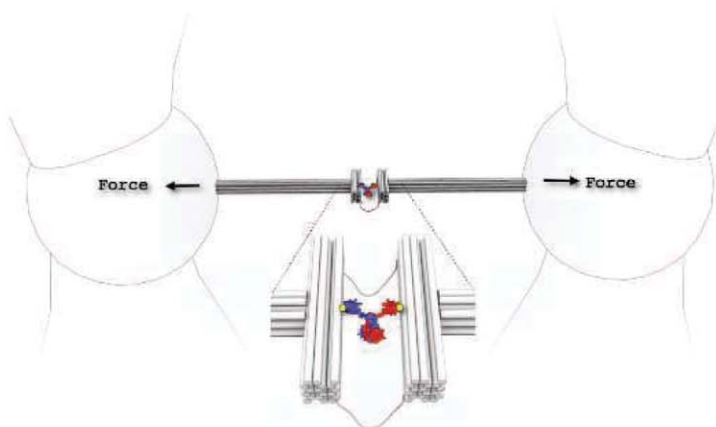
In 2007, Shih and colleagues replaced liquid crystals with origami-based DNA nanotubes that weren't affected by detergents. They showed they could solve the structure of a transmembrane protein domain of a T cell receptor. The structure had previously been determined by other methods, so it wasn't clear whether the technique could be used to solve unknown proteins. At the April meeting, Shih reported that he and his colleagues had used the origami nanotubes to solve the structure of a previously unsolved membrane protein known as UCP2, which helps govern insulin secretion in pancreatic cells.

That's not all. Turberfield's lab at Oxford reported online 10 January in *Nano Letters* that it had used related DNA nanotech tools to improve another protein structure determination technique called cryo-electron microscopy. In this case, Turberfield's team obtained high-resolution images of a hard-to-crystallize protein known as a G protein, the receptor that binds it, and the two paired together.

DNA nanotech's growth isn't limited to mapping proteins. At Kyoto University in Japan, chemical biologist Hiroshi Sugiyama has turned to DNA nanotechnology to help him watch protein catalysts carry out reactions in real time. Sugiyama and colleagues at Kyoto and the Japan Science and Technology Corp. in Tokyo reported online 15 January 2010 in the *Journal of the American Chemical Society* using DNA origami to stitch together what looks like a minuscule picture frame.

They then spanned the frame with two nearly identical double-stranded DNAs tailored to interact with a protein called M.EcoRI, which adds methyl groups to specific sites in DNA as a key part of cellular development.

M.EcoRI works by bending its target DNA by as much 59° in order to insert its methyl group. To see this feat in operation, Sugiyama and his colleagues engineered two DNA strands and stretched them across the frame. The first, 64 bases long, was taut; the other, with 74 nucleic acid bases, was floppier. They then watched the protein with a fast rastering atomic force microscope. M.EcoRI had a far easier time stuffing its methyl group into the longer, relaxed strand, suggesting that DNA's structure plays a big part in how it is modified. Seeman, for one,



**Soft touch.** Rigid DNA linkers (gray bars) gently pull apart plastic beads held by laser tweezers (left and right sides) to reveal how proteins stretched between them fold.

says he's impressed by the results: "It's a chemist's dream to watch individual reactions happen."

Biophysicists are also looking to DNA constructions to help them investigate molecules one at a time. At the meeting, Dietz reported that he and his colleagues are using DNA origami to improve a now-standard set of biophysics tools to see what happens to proteins and DNA as they are pulled apart. In the standard approach, researchers use lasers as molecular tweezers to trap plastic beads in a particular location in solution. Then they attach linkers to these beads and anchor a protein or other target molecule between the two linkers. By making slight adjustments to the lasers, researchers can pull the beads apart and bring them back together to see how the changes in tension affect a protein's ability to fold, among other properties.

But the technique has limitations. For starters, current linkers are floppy. This blurs the resolution of techniques used to track the captured protein. What's more, once the protein is pulled apart, the linkers drift away

from one another, so the experiment cannot be run in reverse or repeated. And in many cases, the floppy linkers must be yanked so hard to get the proteins to move that they pull the protein apart.

So Dietz and his colleagues replaced the usual floppy linkers with stiff rods made from DNA origami containing as many as 18 helical tubes each. They haven't tried them on a working protein yet. But initial tests have shown that the rigid DNA bundles are better at transferring force to their targets, making it possible to move the pinned molecules with less than half the applied force. That should make tracking the effect on proteins easier. The rigid linkers should also stay in place once an experiment is run, allowing it to be reversed. "We're excited," Dietz says. "If you can build on the scale of biological macromolecules, it opens up new areas of scientific exploration."

Someday, DNA nanotechnology may also push past basic science to find real-world applications. Shawn Douglas, a postdoc in the genetics technology lab of George Church at HMS, is working on what he calls a DNA origami nanorobot designed to seek out and destroy cancer cells. Douglas's "robot" looks more like a hollow cylinder some 60 nanometers long and 25 nanometers across. He built it from DNA origami and stapled it closed using DNA strands called aptamers, which in this case were designed to bind specifically to molecules specific to cancer cells. He then loaded the cylinders with fluorescent immune-system proteins that bind to cancer cells and induce apoptosis and added them to cancer cells in an in vitro assay. The loaded cylinders bound to their targets, released their cargo, and killed up to 40% of the cells. The work has a way to go before it will be ready for patients. Nevertheless, "it's beautiful data," says Tim Liedl, a condensed matter physicist at Ludwig Maximilian University in Munich, Germany. "It's getting us closer to the vision of something patrolling our own bloodstreams."

Certainly DNA nanotech has not reached that level of maturity. But Shih and others say it's growing up fast. "In the next 5 years, this is where we're going to make a real contribution, getting control over small collections of individual molecules," Shih says. By then the teenager may find itself a young adult.

—ROBERT F. SERVICE

## PHYSICS

# Possible Sighting of Dark Matter Fires Up Search and Tempers

**A second experiment may have spotted hypothetical dark matter particles called WIMPs, but its leader's take-no-prisoners attitude has competitors steaming**

It's not hard to imagine Juan Collar as a matorador. He *is* Spanish, for one thing, and he certainly seems to relish waving a red flag in front of his rivals. Collar's arena doesn't involve charging bulls or flashing swords, however. The University of Chicago cosmologist is a contender in the intensely competitive race to find dark matter: the mysterious, invisible stuff that is thought to constitute 80% of the universe's mass. And in recent weeks, the 47-year-old researcher has emerged as the bad boy of dark matter detection.

Collar made waves in May at the American Physical Society meeting in Anaheim, California, when he announced preliminary results from an experiment that he has been running inside an abandoned mine in Soudan, Minnesota. The results suggest that Collar's group may have spotted a dark matter signal in their detector, which goes

some theorists have proposed as the main building block of dark matter.

But that's not the only reason Collar is drawing attention. In talks over the past month, he has taken his sword to a rival experiment called XENON, led by Elena Aprile of Columbia University, which has long challenged DAMA's assertion of having detected dark matter. Although Collar has himself expressed skepticism about DAMA's results in the past, he says Aprile and her colleagues are relying on shoddy science and flawed analysis to debunk DAMA's claim.

"I have not seen a sloppier job than what XENON is pushing," says Collar, who seems to straddle a youthful rebelliousness and middle-aged curmudgeonliness.

mine, which has not seen a dark matter signal even though its detector uses the same target material as CoGeNT's: germanium.

Controversy is nothing new to the field of dark matter research. In fact, it is only to be expected in the search for anything that has been hypothesized but not yet detected convincingly. But Collar's taunting of XENON appears to have heated up the debate over DAMA's claim to unprecedented red-hot temperatures. "There's a little bit of Nobelitis going around," says Daniel McKinsey, a particle physicist at Yale University who was once a XENON collaborator. "The stakes are high, and there are strong personalities involved."

He's referring not just to Collar and Aprile, both of whom have a reputation for being pug-nacious, but also to Rita Bernabei, leader of the DAMA project, who is known for her no-nonsense air and impatience with critics. The three scientists may be looking for WIMPs, but their interactions with one another have been anything but weak, and it's safe to say that none of them is a wimp.

## Complicated quest

The existence of dark matter was proposed decades ago when astronomers realized that the mass of stars, dust, gas, and other ordinary matter could not provide sufficient gravitational glue to hold a galaxy together as it spun around. There had to be invisible matter that endowed galaxies

with most of their mass. Theorists hypothesized that this mysterious stuff was made of particles that were massive and barely interacted with the ordinary matter of the universe: WIMPs. Since then, rival hypotheses about what constitutes dark matter have faded in popularity (*Science*, 21 July 2006, p. 287), leaving WIMPs as the leading candidate.

Astronomers and particle physicists have launched a variety of attempts to detect dark matter through astrophysical observations in space and underground particle detectors. The search is complicated not just because WIMPs, if they exist, can barrel through a lot of ordinary matter without leaving a trace, but also because researchers don't know how light or heavy a WIMP might be.

In December 1998, the DAMA collaboration, led by Bernabei, a physicist at the University of Rome, reported that it had seen a dark matter signal. The collaboration's detector was an instrument equipped with nine 10-kg crystals of sodium iodide, a material that scintillates, or produces a tiny flash of light, when its nuclei or electrons recoil after being hit by an incoming particle. The detec-



**A true sighting?** The CoGeNT experiment, led by Juan Collar (*left*), uses a disk of germanium crystals (*inset*) for dark matter detection. It may have seen a dark matter signal.

by the name Coherent Germanium Neutrino Technology (CoGeNT). If the results hold up to scrutiny and are confirmed by more observations from Collar's experiment, it will be the first corroboration of a similar signal that an Italian underground observatory called DAMA has been seeing for 10 years. That would considerably strengthen the case that researchers have indeed detected the weakly interacting massive particles (WIMPs) that

"They cannot fool all of the people all of the time." Collar's stinging remarks—one of his slides describes a particular XENON result as "pure, weapons-grade balonium"—have been countered by scalding rebukes from Aprile, who calls Collar's attack on XENON a "Spanish Inquisition." She says Collar should be more concerned with the fact that CoGeNT's result contradicts yet another, longer-running dark matter experiment located in the same



tor, running inside the Gran Sasso mountain in central Italy, had witnessed a pattern of flashes that Bernabei's group claimed could have been produced only by WIMPs colliding with nuclei in the crystals.

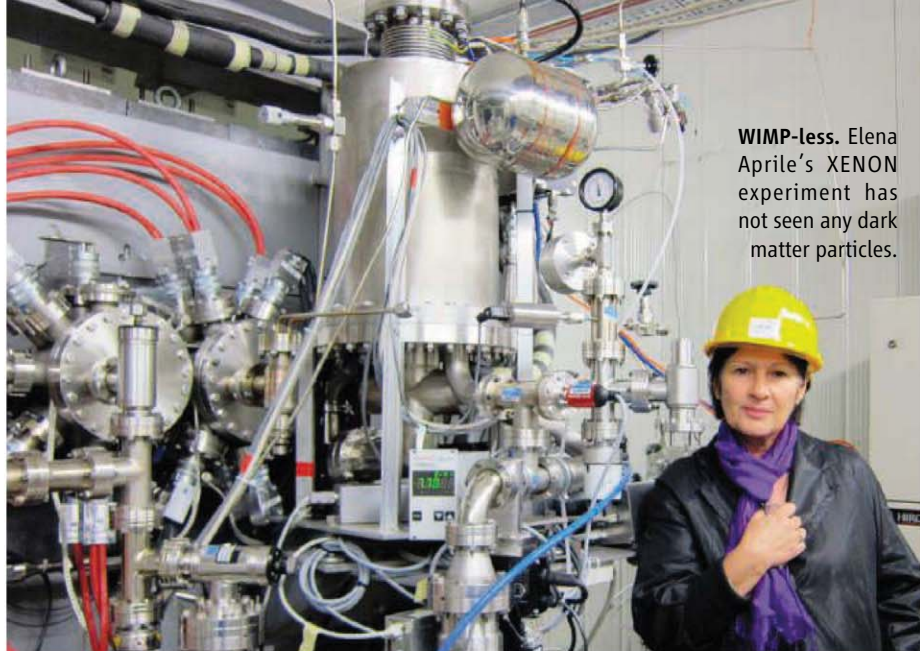
The clinching evidence, the researchers said, was a seasonal fluctuation in the scintillation that was in line with a widely accepted picture of WIMPs. As the sun orbits the galactic center, the solar system swoops through our galaxy's "dark matter halo" like a car driving through rain. Meanwhile, Earth is also circling the sun, moving sometimes into the "rain" of dark matter particles—WIMPs—and sometimes away from it (see figure, p.1147). As a result, the number of WIMPs striking a detector on Earth should peak during the summer and dip in winter. That's exactly the pattern that Bernabei's group reported seeing in its signal.

Many researchers were skeptical about DAMA's claim, in part because the group would not make all of its data available for scrutiny. An independent examination of both published and unpublished data was required, critics said, because of the complicated analysis involved in extracting a WIMP signal from the background noise of mundane events that produce similar flashes of light, such as incoming gamma rays.

Although DAMA reported seeing the annual modulation year after year, skeptics remained unconvinced, much to the frustration of Bernabei and her colleagues. At the top of its home page on the Web, DAMA posted part of Rudyard Kipling's poem *If* to convey the group's feeling of having been treated unfairly. It reads: "If you can bear to hear the truth you've spoken/twisted by knaves to make a trap for fools,... you'll be a Man my son!"

### Hope for the WIMPs

The problem was that other detectors did not see a dark matter signal. One effort was led by Aprile, head of the XENON collaboration, which built a detector by hooking up electronics to a 15-kg vat of liquid xenon. The technology is able to measure both light flashes and electrical charge resulting from nuclear and electronic recoil in xenon atoms when they are struck by external particles. Aprile, like Bernabei an Italian, ran the experiment inside Gran Sasso National Laboratory between March 2006 and October 2007 and failed to see a WIMP signal, which was seen as a strike against DAMA's claim. A second version of the experiment, using 62 kg of xenon to provide much higher sensitivity, did not see any



**WIMP-less.** Elena Aprile's XENON experiment has not seen any dark matter particles.

WIMPs either, Aprile reported in May in a talk at the Space Science Telescope Institute in Baltimore, Maryland.

Another blow to DAMA came from results of a U.S.-based experiment called the Cryogenic Dark Matter Search (CDMS), whose detector consists of germanium and silicon crystals cooled to near absolute zero. The experiment is run by a collaboration of

14 universities, including Stanford; the University of California, Berkeley; the California Institute of Technology, and others. The instrument offers the advantage of being able to distinguish between nuclear recoil events—likely to be caused by a WIMP striking the

target material—and electron recoils, which are caused by non-WIMP events. Deployed in the Soudan mine since 2003, the detector has not seen WIMPs.

In December 2009, Collar and his colleagues began running the CoGeNT experiment in the Soudan mine, right next to CDMS's detector. Although CoGeNT cannot distinguish between electron and nuclear recoils the way CDMS can, it can measure the tiniest of charges produced in the germanium crystals. That allows it to detect very low energy events, which would be the case if WIMPs are light. "It makes CoGeNT the most sensitive instrument available to detect light WIMPs," Collar says.

In 2010, Collar's group reported that the detector had seen some events suggesting evidence for light WIMPs. In April 2011, after a fire in the Soudan mine caused a temporary shutdown of both CoGeNT and CDMS, Collar and his colleagues analyzed the 15 months of data they had collected. They discovered an annual modulation in the signal that was consistent with DAMA's find-

ings, although the statistical significance of  $2.8\sigma$  was too low to support any chest-thumping assertions. And so, in talks describing that result, Collar has been careful to mute his excitement, noting that the modulation needs to be seen consistently over the coming years.

Collar says CoGeNT does not claim to have detected WIMPs, as DAMA has done. "We want to make 100% sure that nobody accuses us of making a claim based on these very limited statistics," he says. "We just want to present the facts, share the data, and take two steps back. Even if we had a stronger statistical case, it would be one for the presence of a modulation, not the presence of WIMPs."


CoGeNT's findings, which Collar was preparing to post on the preprint server arXiv this week, have given DAMA researchers a glimmer of hope that the tide of scientific opinion may at last be turning in their favor. "The results of CoGeNT are very intriguing, and we wait with great interest to read the scientific paper," Bernabei told *Science* in an e-mail interview.

Rafael Lang, a postdoc at Columbia and a member of XENON, says the obvious question Collar needs to answer is why CDMS has not seen the events that CoGeNT has, especially as both detectors use germanium and are located in the same mine. And in Lang's view, the ability to distinguish between electron and nuclear recoils makes CDMS the detector to beat.

Collar says part of the difference arises because of CoGeNT's ability to detect low-energy events, and part of it lies in statistical methods used to analyze the data. He argues that CDMS researchers could have tossed out the dark matter signal from their data. Blas Cabrera, a physicist at Stanford University in Palo Alto, California, who is a spokesperson for the CDMS collabora-

## Online

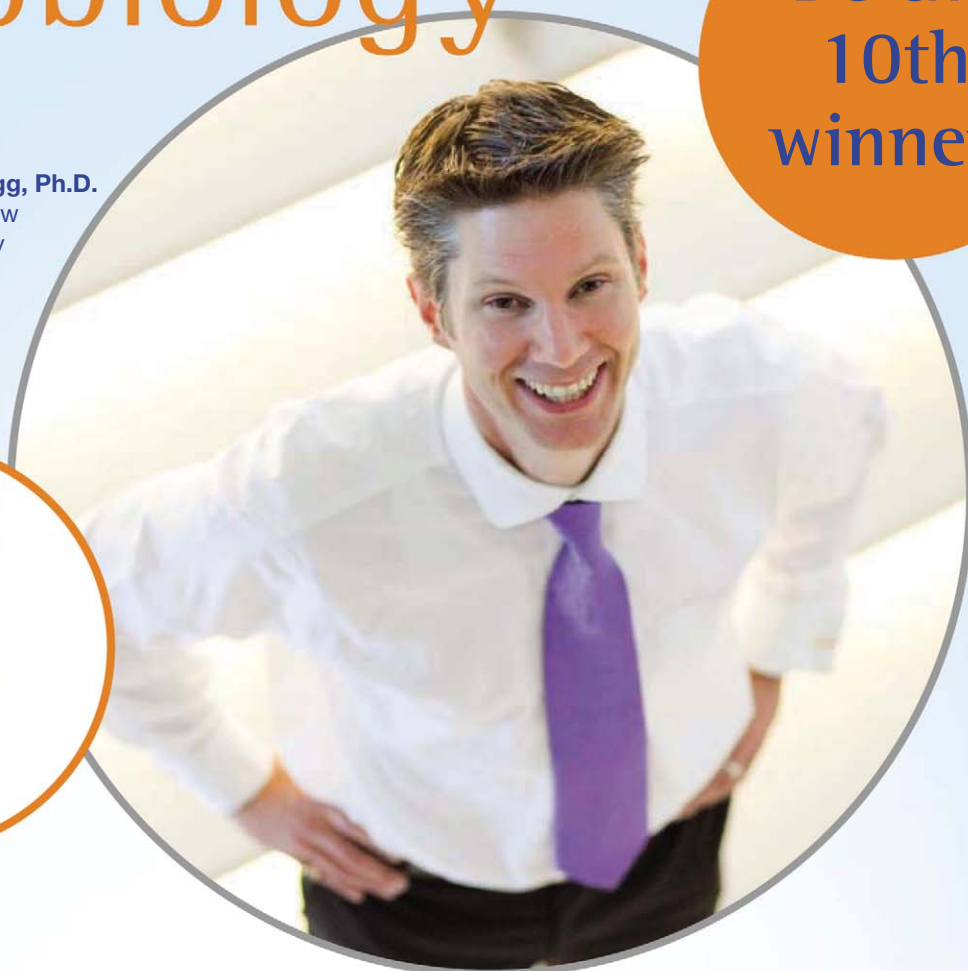
sciencemag.org

 Podcast interview with author Yudhijit Bhattacharjee.

# Eppendorf & Science Prize for Neurobiology

Be the  
10th  
winner!

2010 Winner  
**Christopher Gregg, Ph.D.**  
Postdoctoral Fellow  
Harvard University



Kurstin Roe Photography

Get recognized!  
**US\$ 25,000 Prize**

Deadline for entries  
**June 15, 2011**

It's easy to apply! Learn more at  
**[www.eppendorf.com/prize](http://www.eppendorf.com/prize)**

Congratulations to Dr. Christopher Gregg on winning the 2010 Eppendorf & Science Prize for his studies on genes that alter their expression in the brains of offspring according to whether they were inherited from the father versus the mother. His findings suggest new pathways that may help to understand brain diseases such as autism, schizophrenia and eating disorders.

The annual international US\$ 25,000 Eppendorf & Science Prize for Neurobiology honors young scientists for their outstanding contributions to neurobiological research based on methods of molecular and cell biology. The winner and finalists are selected by a committee of independent scientists, chaired by *Science's* Senior Editor, Dr. Peter Stern.

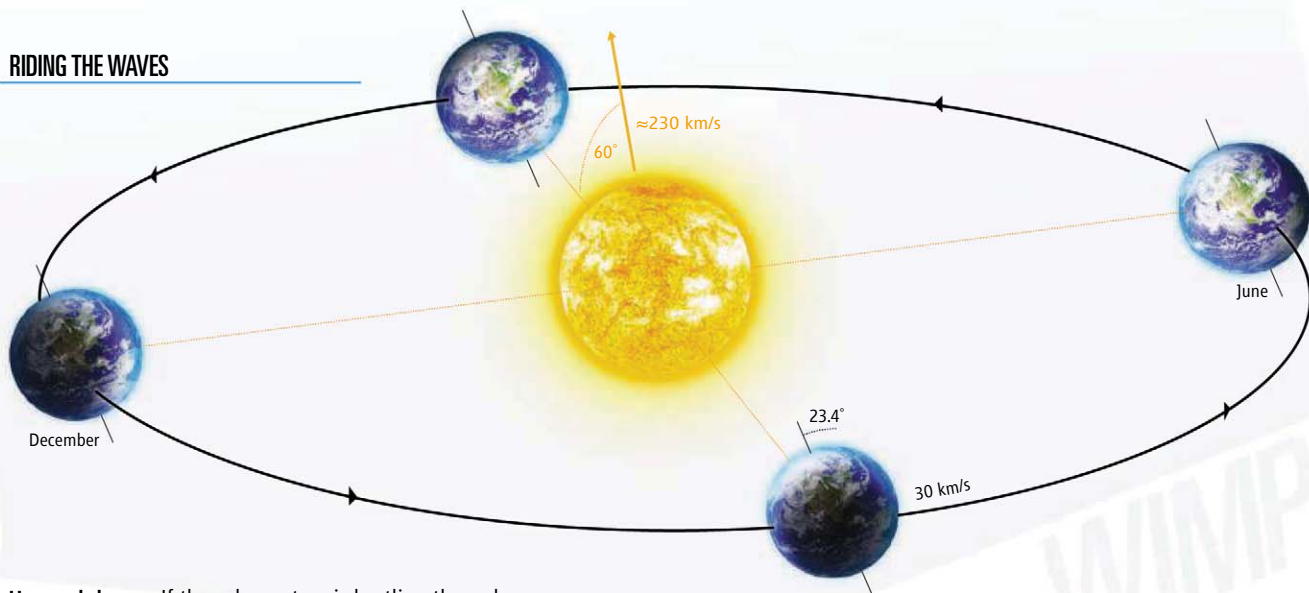
To be eligible, you must be 35 years of age or younger. If you're selected as this year's winner, you will receive US\$ 25,000, have your work published in *Science* and be invited to visit Eppendorf in Hamburg, Germany. Past winners and finalists have come from as far a field as China, Chile, India and New Zealand. Yes, it *can* happen to you!

**eppendorf**  
*In touch with life*





## RIDING THE WAVES



**Ups and downs.** If the solar system is hurtling through a sea of WIMPs, changes in Earth's orientation should make detections rise in June and fall in December.

tion, says CDMS stands by its results. "We believe our paper is pretty solid," Cabrera says, adding that CDMS's findings largely rule out a light WIMP of the kind that CoGeNT is entertaining.

Although Cabrera acknowledges that CoGeNT has the "world's best charge measurement capability," he does not believe it gives CoGeNT an advantage over CDMS when it comes to detecting light WIMPs. He is reluctant to poke holes in CoGeNT's analysis, however, and prefers to stay out of the squabble. Collar's "approach has been like a ton of bricks that doesn't encourage proper scientific discourse," he says.

### Above the noise

In Collar's view, DAMA's assertive claim combined with the refusal to show all of its data has made some in the field overly eager to prove the group wrong. He singles out XENON's researchers for special criticism.

Collar says XENON's Aprile and others should acknowledge that liquid xenon is not such a great target for detecting light WIMPs. Because xenon is a lot heavier than germanium or sodium iodide, he says, a xenon nucleus will recoil much less if a WIMP strikes it. As a result, it might produce a signal too small to be detected reliably over background noise.

In a critique of XENON published last year, Collar and Yale's McKinsey pointed out that XENON's analysis had relied on a flawed and incomplete understanding of how a xenon nucleus behaves when it has a small amount of energy deposited on it, as would be the case in an encounter with a light WIMP. XENON researchers have since redone some

of the analysis, but Collar says Aprile and her colleagues are still a long way from drawing unbiased conclusions. "Whenever they face an uncertainty," Collar says, "they choose the route that helps them obtain the best limits." In other words, they choose an interpretation that rules out WIMPs. And Collar says XENON's researchers are not being transparent about all of their uncertainties and assumptions.

"Juan is losing his mind," says Aprile, scoffing at the notion that XENON might be biasing its results deliberately or otherwise. She says Collar doesn't dare to bring up these criticisms in front of her—the two had a friendly exchange at a recent symposium at Princeton University, she says—because "I'd shut him up pretty quickly." And she says there is a perfectly good reason she and other researchers have gone after DAMA's results in recent years. Their claim is so strong that it "calls for a response," Aprile says.

Aprile laments the growing rivalries within the field and acknowledges that some of the friction goes beyond scientific disagreement to the clashing of egos. When she and Bernabei first met more than a decade ago, "Rita was very charming, extremely kind, praising me," Aprile says. "Then, I got this proposal approved [to start the XENON experiment in Gran Sasso]. All of a sudden, she didn't even care to say hi anymore."

Bernabei agrees that dark matter research is showing its dark side. "In my opinion over the past 10 years, some activities in the field [have] become more aggressive than competitive," she said in an e-mail to *Science*. She will not comment on her rift with Aprile. All that matters in science, Bernabei says, is "serious, reliable and dedicated work with good

detectors and methodological approach." And in that regard, she says, "XENON has many questionable aspects both on experimental and interpretative parts."

Some researchers are more conciliatory. XENON's Lang says the data from the different groups "may not be so irreconcilable" after all. "There's only one truth in science," he says. "The conflict we are having could be the result of uncertainties in the astrophysics or uncertainties in the detectors. Maybe our understanding of dark matter has to be different. We could find ways to say that dark matter does not interact with xenon at all but interacts with germanium." But Lang says he does not understand why the discussion has to be so heated.

Collar says he is taking stabs at XENON not for sport but for the sake of the science. "I certainly like for people to do a proper job, including myself," he says. He is eager to resume the CoGeNT experiment after officials complete safety inspections of the mine this month.

Collar's criticisms of XENON—no matter how sharply worded—will help the field in the long run, says Dan Hooper, a theorist at Fermi National Accelerator Laboratory in Batavia, Illinois. "On one hand, Juan can come across as abrasive to some people, and I don't know if this style does him many favors," Hooper says. "On the other hand, I am very glad to have people like Juan aggressively challenging claims being made by other scientists. He is an exceptional scientist, and the kind of scrutiny he brings to the table ultimately helps the scientific community to better understand the problems at hand."

—YUDHIJIT BHATTACHARJEE

**NEW**

# Women in Science Booklet

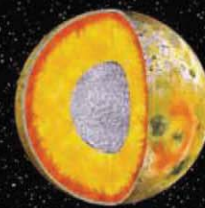
*Science and the L'Oréal Foundation present*



Read inspiring profiles of women  
making a difference in biology.

**Free download at**  
**[ScienceCareers.org/LorealWIS](http://ScienceCareers.org/LorealWIS)**





## LETTERS

edited by Jennifer Sills

## Editor's Note

THE RESEARCH ARTICLE "A BACTERIUM THAT CAN GROW BY USING arsenic instead of phosphorus" by F. Wolfe-Simon *et al.* [p. 1163, (1)] was the subject of extensive discussion and criticism following its online publication. *Science* received a wide range of correspondence that raised specific concerns about the Research Article's methods and interpretations. Eight Technical Comments that represent the main concerns, as well as a Technical Response by Wolfe-Simon *et al.*, are published online with this issue at the addresses listed below (all were previously published in *Science Express* on 27 May). They have been peer-reviewed and revised according to *Science*'s standard procedure.

The print version of the Wolfe-Simon *et al.* paper reflects minor clarifications and copyediting of the *Science Express* version. We hope that publication of this collection will allow readers to better assess the Research Article's original claims and the criticisms of them. Our

procedures for Technical Comments and Responses are such that the original authors are given the last word, and we recognize that some issues remain unresolved. However, the discussion published today is only a step in a much longer process. Wolfe-Simon *et al.* are making bacterial strain GFAJ-1 available for others (2) to test their hypotheses in the usual way that science progresses.

**BRUCE ALBERTS**  
Editor-in-Chief

## References and Notes

1. F. Wolfe-Simon, J. S. Blum, T. R. Kulp, G. W. Gordon, S. E. Hoefft, J. Pett-Ridge, J. F. Stolz, S. M. Webb, P. K. Weber, P. C. W. Davies, A. D. Anbar, R. S. Oremland, *Science* **332**, 1163 (2011); published online 2 December 2010 (10.1126/science.1197258).
2. Cultures of GFAJ-1 were submitted to the American Type Culture Collection and Deutsche Sammlung von Mikroorganismen und Zellkulturen on 21 March 2011 and will be available from these sources within several months. Until then, samples of GFAJ-1 are available to the community from the Oremland lab upon completion of a materials transfer agreement, which is required by the U.S. Geological Survey for the transfer of bacterial cultures.

## TECHNICAL COMMENTS

## Comment on "A Bacterium That Can Grow by Using Arsenic Instead of Phosphorus"

István Csabai and Eörs Szathmáry

[www.sciencemag.org/cgi/content/full/332/6034/1149-b](http://www.sciencemag.org/cgi/content/full/332/6034/1149-b)

## Comment on "A Bacterium That Can Grow by Using Arsenic Instead of Phosphorus"

Steven A. Benner

[www.sciencemag.org/cgi/content/full/332/6034/1149-c](http://www.sciencemag.org/cgi/content/full/332/6034/1149-c)

## Comment on "A Bacterium That Can Grow by Using Arsenic Instead of Phosphorus"

B. Schoepp-Cothenet, W. Nitschke, L. M. Barge, A. Ponce, M. J. Russell, A. I. Tsapin

[www.sciencemag.org/cgi/content/full/332/6034/1149-d](http://www.sciencemag.org/cgi/content/full/332/6034/1149-d)

## Comment on "A Bacterium That Can Grow by Using Arsenic Instead of Phosphorus"

David W. Borhani

[www.sciencemag.org/cgi/content/full/332/6034/1149-e](http://www.sciencemag.org/cgi/content/full/332/6034/1149-e)

## Comment on "A Bacterium That Can Grow by Using Arsenic Instead of Phosphorus"

James B. Cotner and Edward K. Hall

[www.sciencemag.org/cgi/content/full/332/6034/1149-f](http://www.sciencemag.org/cgi/content/full/332/6034/1149-f)

## Comment on "A Bacterium That Can Grow by Using Arsenic Instead of Phosphorus"

Stefan Oehler

[www.sciencemag.org/cgi/content/full/332/6034/1149-g](http://www.sciencemag.org/cgi/content/full/332/6034/1149-g)

## Comment on "A Bacterium That Can Grow by Using Arsenic Instead of Phosphorus"

Rosemary J. Redfield

[www.sciencemag.org/cgi/content/full/332/6034/1149-h](http://www.sciencemag.org/cgi/content/full/332/6034/1149-h)

## Comment on "A Bacterium That Can Grow by Using Arsenic Instead of Phosphorus"

Patricia L. Foster

[www.sciencemag.org/cgi/content/full/332/6034/1149-i](http://www.sciencemag.org/cgi/content/full/332/6034/1149-i)

## Response to Comments on "A Bacterium That Can Grow by Using Arsenic Instead of Phosphorus"

Felisa Wolfe-Simon, Jodi Switzer Blum, Thomas R. Kulp, Gwyneth W. Gordon, Shelley E. Hoefft, Jennifer Pett-Ridge, John F. Stolz, Samuel M. Webb, Peter K. Weber, Paul C. W. Davies, Ariel D. Anbar, Ronald S. Oremland

[www.sciencemag.org/cgi/content/full/332/6034/1149-j](http://www.sciencemag.org/cgi/content/full/332/6034/1149-j)

## Zoos and Captive Breeding

D. A. CONDE AND COLLEAGUES' POLICY FORUM "An emerging role of zoos to conserve biodiversity" (18 March, p. 1390) presents an inspiring view of zoos' potential contributions to conservation through captive breeding and reintroduction. However, their analysis overlooks two key issues.

First, zoos currently devote only a small proportion of their capacity to conserving the most threatened species. Although zoos house ~15% of threatened tetrapods, Conde *et al.*'s histograms reveal that this includes

proportionally fewer species in more-threatened categories, and hardly any amphibians—the group that is most threatened and probably best suited to captive breeding (1). More important, most (185 of 344; 54%) of the most highly threatened tetrapod species in zoos are held in populations that are too small to be viable (2) because they comprise 50 or fewer individuals, and those are often spread across separately managed subpopulations (3). These small population sizes have not improved in the past two decades, at least for mammals (4). Furthermore, many species perform more poorly in captivity than when protected in the wild, with lower reproductive rates and higher offspring losses (5); this exacerbates the problem of small populations in zoos by reducing these species' effective population sizes even further.

Second, Conde *et al.*'s analysis pays little attention to other effects of captivity, such as abnormal behavior, insufficient fear of humans, and exposure to novel diseases, which often limit the success of subsequent reintroduction attempts (6). This may be why releasing zoo-bred animals has had only limited impact on the status of wild populations. Conde *et al.* state that captive-breeding has played a major role in reducing the threat level of 17 tetrapod species [26% of the 64 whose status has been improved by conservation action (7)], but this total involves a miscount and erroneously includes the Seychelles magpie-robin (*Copsychus sechellarum*), the Marquesan Imperial-pigeon (*Ducula galeata*), and the Polynesian megapode (*Megapodius pritchardii*), which were never held in captive breeding programs (8). In reality, zoos have directly provided most of the stock for reintroduction in a much smaller number of cases.

Given the scale of the biodiversity crisis, we therefore recommend that zoos increase the contribution that their captive breeding efforts make to conservation in the wild by focusing efforts more closely on those species with good captive health, welfare, and population viability (5, 9, 10).

ANDREW BALMFORD,<sup>1</sup> JEANETTE KROSHKO,<sup>2</sup>  
NIGEL LEADER-WILLIAMS,<sup>3</sup> GEORGIA MASON<sup>2\*</sup>

<sup>1</sup>Department of Zoology, University of Cambridge, Cambridge, CB2 3EJ, UK. <sup>2</sup>Department of Animal and Poultry Sciences, University of Guelph, Guelph, Ontario, N1G 2W1, Canada. <sup>3</sup>Department of Geography, University of Cambridge, Cambridge, CB2 3EN, UK.

\*To whom correspondence should be addressed. E-mail: gmason@uoguelph.ca

#### References

1. E. Marris, *Nature* **452**, 394 (2008).
2. I. R. Franklin, in *Conservation Biology, An Evolutionary-Ecological Perspective*, M. E. Soulé, B. A. Wilcox, Eds. (Sinauer, Sunderland, MA, 1980), pp. 135–149.
3. M. R. Stanley, J. Price, E. Fa, in *Zoos in the 21st Century: Catalysts for Conservation?* A. Zimmermann, M. Hatchwell, L. Dickie, C. West, Eds. (Cambridge Univ. Press, Cambridge, 2007), pp. 155–177.

4. C. D. Magin *et al.*, in *Creative Conservation: Interactive Management of Wild and Captive Animals*, P. S. Olney, G. M. Mace, A. T. C. Feistner, Eds. (Chapman & Hall, London, 1993), pp. 3–31.
5. G. J. Mason, *Trends Ecol. Evol.* **25**, 713 (2010).
6. K. R. Jule, L. A. Leaver, S. E. G. Lea, *Biol. Conserv.* **141**, 355 (2008).
7. M. Hoffmann *et al.*, *Science* **330**, 1503 (2010).
8. IUCN 2010: IUCN Red List of Threatened Species, Version 2010.4. ([www.iucnredlist.org](http://www.iucnredlist.org)).
9. A. Balmford, G. M. Mace, N. Leader-Williams, *Conserv. Biol.* **10**, 719 (1996).
10. N. Leader-Williams *et al.*, in *Zoos in the 21st Century: Catalysts for Conservation?* A. Zimmermann, M. Hatchwell, L. Dickie, C. West, Eds. (Cambridge Univ. Press, Cambridge, 2007), pp. 236–254.

## Response

BALMFORD *ET AL.* SUGGEST THAT OUR ANALYSIS has embellished the potential of zoos to conserve endangered species, and they state that zoos devote only a small proportion of their capacity to threatened species. Although zoos devote only 8% of their capacity to threatened bird species, 23% of amphibians, 27% of mammals, and 40% of reptiles within zoo collections are threatened (see table 1 in the Policy Forum supporting online material). A comparison of our data and the data by Magin *et al.* that Balmford *et al.* cite (1) shows that the number of threatened species in ISIS zoos has markedly increased over the past 20 years. The most substantial increase has been for threatened amphibians, from just 5 species in 1990 to 56 species in 2009 (an increase of 1020%), followed by birds (509% increase) and reptiles (424% increase). These absolute gains are obscured because, although the number of threatened species in zoos has increased substantially, the number of species classified as threatened has increased relatively more. For example, in 1990 the IUCN listed just 57 threatened amphibians (1), but by 2009 this figure had jumped to 1895 (2). Thus, the number of species of threatened amphibians held in zoos increased by 1020%, while the number listed as threatened increased by 3300%, outpacing the zoos' response to the amphibian crisis. The percentage of all then-threatened species kept in captivity, comparing the 1990 and 2009 figures,

Captive breeding.



declined for amphibians and mammals, and increased for birds and reptiles.

Balmford *et al.* mention that the number of individuals of highly threatened species in zoos is low and has not increased in the past two decades. Magin *et al.* only provide this information for mammals, but they show that, although many zoo populations do remain small, there is an encouraging trend: From 1990 to 2009, there has been a 21.2% increase in the number of threatened mammal species with a zoo metapopulation size exceeding 50 individuals, and a 48.6% increase in the number of species with a metapopulation size exceeding 250 individuals. We argue that, although the zoo community is not keeping up with the rapidly accelerating scale of the species conservation challenge, it is doing much better than Balmford *et al.* suggest. Moreover, despite small population sizes, zoos' intervention has prevented the extinction of a number of species, such as the California condor (*Gymnogyps californianus*) (3), the European bison (*Bison bonasus*) (4), and the Przewalski's horse (*Equus ferus przewalskii*) (5). It is true that 53% of zoos' highly threatened species are represented by fewer than 50 individuals and that many are managed across separate subpopulations, but some zoos are aware of this problem and are linking several species in cooperative breeding programs (6).

Balmford *et al.* also reiterated that the effects of captivity can affect further reintroductions. Although we agree that this could be a serious issue, given the biodiversity crisis it is important to recognize that these effects can often be overcome, as exemplified by reintroduction programs for species such as the whooping crane (7). Balmford *et al.* rightly point out errors in Hoffmann *et al.*'s (8) calculation for the number of species for which captive breeding played an important con-

## Letters to the Editor

Letters (~300 words) discuss material published in *Science* in the past 3 months or matters of general interest. Letters are not acknowledged upon receipt. Whether published in full or in part, Letters are subject to editing for clarity and space. Letters submitted, published, or posted elsewhere, in print or online, will be disqualified. To submit a Letter, go to [www.submit2science.org](http://www.submit2science.org).



servation role. The correct figure is 13 species [Hoffman *et al.* omitted the Californian condor, in addition to the erroneous inclusion of the three species Balmford *et al.* mention together with *Dendrobates azureus* (2)].

Balmford *et al.* further claim that zoos have only contributed stock from captive breeding in a small number of these reintroductions. However, it is important to stress that zoos provided substantial logistical, technical, and/or financial support for at least 9 of these 13 species (9).

These points notwithstanding, we agree with Balmford *et al.*'s closing argument that zoos should continue to increase their captive conservation efforts in a scientifically informed manner. **D. A. CONDE,<sup>1</sup>\* N. FLESNESS,<sup>2</sup>**

**F. COLCHERO,<sup>1</sup> O. R. JONES,<sup>2</sup> A. SCHEUERLEIN<sup>1</sup>**

<sup>1</sup>Max Planck Institute for Demographic Research, 18057 Rostock, Germany. <sup>2</sup>International Species Information System, Eagan, MN 55121, USA.

#### References and Notes

1. C. D. Magin *et al.*, in *Creative Conservation: Interactive Management of Wild and Captive Animals*, P. S. Olney, G. M. Mace, A. T. C. Feistner, Eds. (Chapman & Hall, London, 1993), pp. 3–31.
2. IUCN, IUCN Red List of Threatened Species ([www.iucnredlist.org](http://www.iucnredlist.org)).
3. IUCN, *Gymnogyps californianus* in "IUCN 2010: IUCN Red List of Threatened Species, Version 2010.4" (2008).
4. Z. Pucek *et al.*, "Status survey and conservation action plan: European bison" (IUCN Bison Specialist Group, Gland, Switzerland, 2004).
5. L. Boyd *et al.*, in "IUCN 2010: IUCN Red List of Threatened Species, Version 2010.4" (2008).
6. W. G. Conway, *Zoo Biol.* **30**, 1 (2011).
7. U.S. Fish and Wildlife Service, Reintroduction of a Migratory Flock of Whooping Cranes in the Eastern United States ([www.fws.gov/midwest/whoopingcrane](http://www.fws.gov/midwest/whoopingcrane)).
8. M. Hoffmann *et al.*, *Science* **330**, 1503 (2010).
9. Species that reduced their threat status by captive breeding actions with substantial logistical, technical and/or financial support from zoos include *Gymnogyps californianus* (3), *Bison bonasus* (4), *Equus ferus przewalskii* (5), *Leontopithecus rosalia* (10), *Nesoenas mayeri* (11), *Falco punctatus* (12), *Mustela nigripes* (13), *Leporillus conditor* (14), and *Alytes muletensis* (15).
10. M. C. M. Kierulff *et al.*, in "IUCN 2010: IUCN Red List of Threatened Species, Version 2010.4" (2008).
11. K. J. Swinnerton, J. J. Groombridge, C. G. Jones, R. W. Burn, Y. Mungroo, *Animal Conserv.* **7**, 353 (2004).
12. T. J. Cade, C. G. Jones, *Conserv. Biol.* **7**, 169 (1993).
13. J. Belant, P. Gober, D. Biggins, in "IUCN 2010: IUCN Red List of Threatened Species, Version 2010.4" (2008).
14. B. Breed, F. Ford, *Native Mice and Rats* (CSIRO, Collingwood, Australia, 2007).
15. Durrel Wildlife Conservation Trust, "Mallorcan Midwife Toad Factsheet" (2001).

#### CORRECTIONS AND CLARIFICATIONS

**News & Analysis:** "Spate of suicides roils university, jeopardizing academic reforms" by D. Normile (22 April, p. 410). The article stated that "local media reported that the education ministry found evidence of administrative and financial irregularities, including improperly vetted bonus payments to [KAIST President Suh Nam Pyo]." KAIST contests the ministry's finding; it says that the total amount of the yearly compensation for the president is specified in the employment contract with KAIST and that Suh did not receive any additional compensation other than the specified amount.



## Learn how current events are impacting your work.

**ScienceInsider**, the new policy blog from the journal **Science**, is your source for breaking news and instant analysis from the nexus of politics and science.

Produced by an international team of science journalists, **ScienceInsider** offers hard-hitting coverage on a range of issues including climate change, bioterrorism, research funding, and more.

Before research happens at the bench, science policy is formulated in the halls of government. Make sure you understand how current events are impacting your work. Read **ScienceInsider** today.

[www.ScienceInsider.org](http://www.ScienceInsider.org)

**ScienceInsider**

Breaking news and analysis from the world of science policy



## HISTORY OF SCIENCE

# The Worst Science in the World

Vassiliki Betty Smocovitis

There's a very dark humor that permeates the culture of field science. Tales of hardship, suffering, and endurance are often told with a peculiar form of irony, filled with braggadocio, and sprinkled with in-house jokes. Nowhere is this strange mixture of hardship, suffering, and dark humor more evident than in Apsley Cherry-Garrard's celebrated memoir of Antarctic exploration dramatically titled *The Worst Journey in the World* (1). Its memorable opening line sets its tone: "Polar exploration is at once the cleanest and most isolated way of having a bad time which has been devised." Billed as the *War and Peace* of travel writing, the nearly 600-page epic recounts a disastrous 1911 journey to locate and collect the eggs of the emperor penguin from the rookery on Cape Crozier in the Antarctic. Then thought to be primitive because they were flightless, penguins had drawn the attention

wording of his book's title. Subjected to total darkness, freezing cold (the temperatures Cherry-Garrard, Edward Wilson, and Birdie Bowers experienced on their five-week winter journey averaged  $-40^{\circ}\text{C}$  or below), and some of the worst blizzard conditions recorded in the history of polar exploration, Cherry-Garrard began to question the wisdom of it all. His doubts later grew when the results of the study of the three intact eggs, the entire scientific booty his party managed to bring back, proved inconclusive. (The "scientific report" he offers is actually the most humorous part of his account.) Ruefully, he asked whether the pursuit of scientific knowledge was really worthwhile if it involved such "super-human endurance" or if one took such "appalling risks."

The question remained famously unanswered by Cherry-Garrard. That is perhaps why the irony and the dark humor seem so stark, set against the horrific experience he took such pains to describe. The question recurs—at least implicitly in my mind—on reading Edward Larson's *An Empire of Ice: Scott, Shackleton, and the Heroic Age of Antarctic Science*. Larson (a historian at Pepperdine University) offers yet another compelling account of suffering, heroism, and even martyrdom in retelling the story of Antarctic exploration during the early years of the 20th century (of which, it should be said, the journey to find the penguin rookery is but part). His book appears in time for the 100th anniversary of the

celebrated race to the South Pole between the successful Norwegian Roald Amundsen (who triumphantly got there first and came back) and the ill-fated Englishman Robert Falcon Scott (who arrived a month later and with his companions tragically froze to death en route back to the Ross Sea). It also coincides with the 150th anniversary of the birth of the famed Norwegian explorer Fridtjof Nansen, often praised by aficionados as the greatest of all polar explorer-travelers.

On the surface, Larson's book offers a well-written, broad sweep of a mostly familiar story appropriate to the commemorative tone of the centenary. From previous histories of polar exploration, we all know, for example,

who lives, who dies, and who suffers the most. What takes the book beyond the standard narrative is Larson's presentation of the British expeditions against the backdrop of the imperial geopolitics of the age,

which made science an integral part of Antarctic exploration. Drawing on new sources, and at other times simply rereading familiar ones more closely, he retells the story of Antarctic exploration from the vantage point of science. Larson pays careful attention to

scientific research that has often been downplayed and at times been completely left out of historical understanding. What emerges is a far more interesting and richer account than we have had thus far. Through his considerations of work on magnetism, geology, paleobotany, paleontology, zoology (of course), and even ice itself, Larson argues that Antarctic exploration was not just filled with but in fact driven by science. This was especially true in the case of Scott and his *Terra Nova* expedition, whose primary motives Larson claims were not to get to the South Pole first but to instead garner scientific knowledge.

In what emerges as Larson's recharacterization, Scott's "adversary" Amundsen was hardly a worthy rival because the Norwegian's motives did not include science—he only wanted to be the first to reach the South Pole. Polar biographers and writers such as the influential Roland Huntford—whose *Last Place on Earth* (2) was the basis for a popular television series—have portrayed Amundsen as a brilliant strategist and planner. In Larson's telling, he comes off as an arriviste, someone more keen on status and prominence than on making a lasting contribution to the world of science. And Scott, who has frequently been portrayed (again especially in Huntford's work) as a complacent if not sluggish bungler, comes across as the more authentic and honorable figure, someone more concerned with gathering knowledge than gaining fame. Larson's new interpretation, therefore, leads to a very different and more nuanced understanding of the story's protagonists, if not a radical reinterpretation of the Scott-Amundsen race. In redrawing the issues, reinterpreting motives, and recharacterizing the protagonists in such a well-known story, the book is not unlike Larson's earlier *Summer for the Gods* (3). That Pulitzer Prize-winning history gave us a newly complex portrait of the protagonists, their motives, and the sociopolitical backdrop to what became known as the Scopes "Monkey Trial."

**An Empire of Ice**  
Scott, Shackleton, and  
the Heroic Age of  
Antarctic Science

by Edward J. Larson

Yale University Press, New  
Haven, CT, 2011. 358 pp. \$28,  
£18.99. ISBN 9780300154085.



**Heading off for some eggs.** Birdie Bowers, Edward Wilson, and Apsley Cherry-Garrard (left to right) before departing on their winter journey.

of the many post-Darwinian evolutionists at the turn of the 20th century who believed that anatomical study of their embryos might shed light on the evolutionary relationship of birds and reptiles. Unfortunately for the evolutionists, the birds nest in the Antarctic winter, when travel is most difficult. And so, despite the fact that it was the worst time of year to undertake the 110-km journey from Robert Scott's base camp to the rookery, 100 years ago this month Cherry-Garrard found himself on what became immortalized in the

The reviewer is at the Department of Biology and the Department of History, University of Florida, Gainesville, FL 32611, USA. E-mail: bsmocovi@ufl.edu



In short, Larson has written a fascinating book, one sure to force a rethinking of the Scott-Amundsen race as well as reconsiderations that will include science as a driving force in Antarctic and indeed polar exploration. *An Empire of Ice* nonetheless still leaves open in my mind Cherry-Garrard's unanswerable question while drawing attention to the misery, suffering, and even death that have accompanied polar science. I'm not sure that there is much that is funny in that.

#### References and Notes

1. A. Cherry-Garrard, *The Worst Journey in the World: Antarctic, 1910–1913* (Constable, London, 1922).
2. Originally published as R. Huntford, *Scott and Amundsen* (Hodder and Stoughton, London, 1979).
3. E. J. Larson, *Summer for the Gods: The Scopes Trial and America's Continuing Debate over Science and Religion* (Basic Books, New York, 1997).
4. R. F. Scott, *Scott's Last Expedition...* (Dodd, Mead, New York, 1913).

10.1126/science.1205505

## THEATER: SPACE EXPLORATION

# The Soviet's Chief Designer

On 12 April 1961, cosmonaut Yuri Gagarin became the first human to orbit our planet. His eyes were the first to look down at Earth from the darkness of space; his body the first to break free of our planet's gravitational field. This Soviet achievement was as much a product of the Cold War as of a dream to explore outer space, and it filled people with both wonder and fear.

As a child, playwright Rona Munro shared the world's excitement and romance with space exploration (*1*). In *Little Eagles*, performed by the Royal Shakespeare Company at London's Hampstead Theatre from mid-April into early May, she tells the relatively unknown story of one man behind the dream of space flight, Sergei Pavlovich Korolyov (*2*). Right up until his death in 1966, Korolyov was known only as the "Chief Designer"—his name and role withheld by the Soviet Union as a secret of state. He had been responsible not only for Gagarin's flight but also for Sputnik, Earth's first

artificial satellite, and many other pioneering successes of the Soviet space program, including orbiting the first animal (the dog Laika) and the first spacewalk (Alexei Leonov's 20-minute excursion from Voskhod 2). Set against the backdrop of the space race and recent political and military history, Korolyov's story is as fascinating as it is complex. Munro chose to depict it through a sequence of scenes that provide only glimpses of his life.

The playwright sets the opening scene in 1938, in the Kolyma Gulag in Siberia. The conditions are bleak. Stalin speaks to the prisoners: "Comrades. Our country is attacked from within. Only the most naïve among you can doubt that our enemies are right in the heart of our great nation, like rats in a barrel of wheat." Korolyov is one of those "enemies," robbed of his health but not of his will to live or of his dreams of rockets and space. As a young rocket engineer, he fell victim to one of Stalin's purges and was sentenced to ten years of hard labor. Luckily, his skills were recognized as being too precious to be wasted. Amid the war effort, he was soon reassigned to a rocket-building team in Moscow.

The trip out of the Kolyma Gulag was far from easy. Korolyov, who was still a prisoner, had to get to Moscow on his own. At the end of the play, we learn that he had hitched a ride to the nearest port, only to see that the last boat had already sailed, leaving him to face the Siberian winter, without food or a place to sleep. The secret to surviving, we hear, was to keep walking, to never stop. That is also true of the play: it keeps moving, tirelessly and relentlessly, as if inspired by Korolyov's own drive.

In the space of about three hours, the cast takes the audience from the Kolyma Gulag to Sputnik's design room, from the launch pad at Baikonur to the Red Square, and from the Cuban missile crisis to Korolyov's untimely death. Along the way, we meet an array of historical characters (including Gagarin and Soviet leaders Nikita Khrushchev and Leonid Brezhnev) as well as Korolyov's wife, daughter, and fictional doctor.

Inevitably, a lot of detail has been left out, and at times I was left wondering about the broader context of some of the scenes



**Designer and his craft.** Korolyov (Darrell D'Silva), holding model satellite, and Ivanovsky (James Howard).

and what happened in between them. But the play does succeed in portraying Korolyov's conflicts among his own needs (family- and healthwise), the military and political demands of his country, and his desire to fulfill his dream to pave a road to the cosmos. If, like me, you didn't live through this period of history, you will want to find out more after the show. Fortunately, though, there is no shortage of good references [e.g. (*3*, *4*)] available to fill in the details.

The production, directed by Roxana Silbert, was not particularly daring, but it was engaging and full of emotion. There were some particularly beautiful moments, such as the launch of Vostok 1: the bright orange light of lift-off followed by Gagarin aerially suspended, floating in the air, and telling us "how beautiful the world is."

Alas, that was Gagarin's only trip above Earth's atmosphere, and Korolyov's death in 1966 meant that he did not live to see American astronauts set foot on the Moon. But the dreams of both do live on. Nowadays the road to the cosmos is mostly traveled by robotic explorers and unmanned satellites. However, the images that those bring us, both of Earth and other worlds, are still a source of inspiration.

—Maria Cruz

#### References and Notes

1. From "Eyes on the stars—Space as inspiration," a conversation among Munro, space scientist John Zarnecki (Open University), and NASA astronaut Piers Sellers at the Royal Society, London, 30 March 2011. A webcast of the event, organized in partnership with the Royal Shakespeare Company, is archived at <http://royalsociety.org/All-our-Web-casts/>.
2. Transliterated following the playwright, although the name is more frequently rendered as Korolev.
3. D. Cadbury, *The Space Race: The Untold Story of Two Rivals and Their Struggle for the Moon* (Fourth Estate, London, 2005).
4. V. Hardesty, G. Eisman, *Epic Rivalry: The Inside Story of the Soviet and American Space Race* (National Geographic, Washington, DC, 2007); reviewed in (*5*).
5. J. Baker, *Science* **318**, 48 (2007).

10.1126/science.1208249

## AGRICULTURE

# Research Principles for Developing Country Food Value Chains

M. I. Gómez,<sup>1\*</sup> C. B. Barrett,<sup>1</sup> L. E. Buck,<sup>1</sup> H. De Groot,<sup>2</sup> S. Ferris,<sup>3</sup> H. O. Gao,<sup>1</sup> E. McCullough,<sup>4</sup> D. D. Miller,<sup>1</sup> H. Outhred,<sup>5</sup> A. N. Pell,<sup>1</sup> T. Reardon,<sup>6</sup> M. Retnanestri,<sup>5</sup> R. Ruben,<sup>7</sup> P. Struobi,<sup>8</sup> J. Swinnen,<sup>9</sup> M. A. Touesnard,<sup>1</sup> K. Weinberger,<sup>10</sup> J. D. H. Keatinge,<sup>11</sup> M. B. Milstein,<sup>1</sup> R. Y. Yang<sup>11</sup>

Food value chains (FVCs) comprise all activities required to bring farm products to consumers, including agricultural production, processing, storage, marketing, distribution, and consumption. FVCs are changing rapidly in developing countries (DCs), because of population and income growth; urbanization; and the expansion, globally and domestically, of modern food retailing, distribution, and wholesaling firms (1, 2). One such change is that consumers and regulators increasingly demand product-specific characteristics beyond price—including nutrient content; food safety certification; and indicators of impacts on natural resources, greenhouse gas emissions, and farmworkers. To accommodate these multidimensional demands, regulators and firms are developing new multiattribute product labeling and production standards. We outline below ways in which scientists must integrate existing disciplinary evidence into rigorous models and must develop measures and methods to evaluate the multidimensional performance of FVCs.

## Principles for Advancing FVC Research

These labeling and production initiatives affect those who participate in DC FVCs as growers, workers, or consumers. Under which conditions do poor people benefit from these trends? Which consumer behaviors, public policies, and decisions by private-firm and civil society organizations are likely to promote the emergence of poverty-reducing, environmentally sustainable FVCs? By addressing these challenges, scientists can help identify good FVC practices that can help poor people and protect the environ-

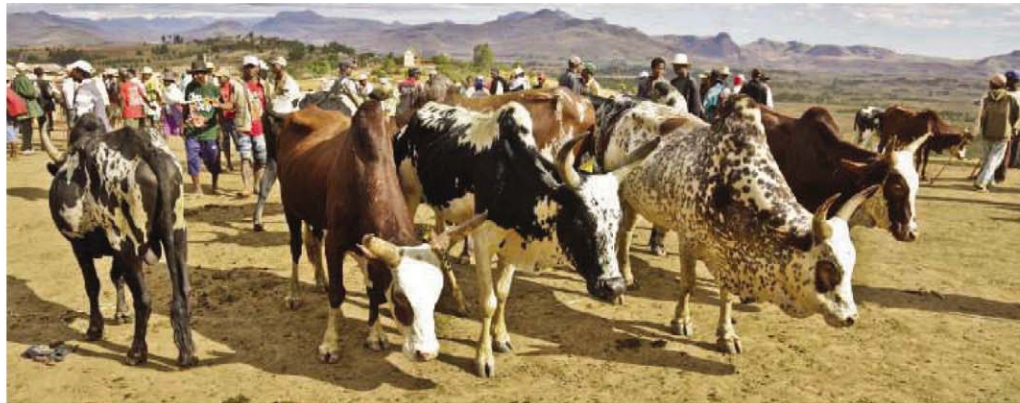
ment. Toward that end, we offer six principles to guide scholars in advancing that research agenda in this rapidly changing landscape.

1. *Focus on opportunities available in domestic markets.* FVCs in DCs are primarily oriented toward domestic markets. DC food exports account for only 1.9% and 8.4% of domestic production in raw tonnage and value, respectively (3). Global supermarket chains are expanding into DCs where in-country retail sales of domestically produced food are three to four times the sales of their food exports (4). Global retailers are setting food quality and safety standards for domestic products in DCs that are similar to standards in developed countries (5). This trend

From farm to table, multidisciplinary research is needed to improve the economic benefit of food production in the developing world.

linking them to domestic markets may generate greater economic gains through follow-on multiplier effects that help reduce poverty (e.g., employment created by local spending by supermarket employees). Research should focus more on identifying what public policies, private-firm decisions, and FVC innovations can improve the functioning of domestic FVCs, not just on export channels.

2. *Pay attention to indirect effects, not only to increased sales from smallholders.* Although opportunities exist in domestic markets, it is often difficult to influence production decisions and to induce increased FVC participation among poor farmers (as sellers) and traders (as intermediaries). These individuals are often harder to reach and lack the assets and skills of their better-off counterparts (9). But because smallholder farm households derive a large share of income



Bulls for sale at the zebu market, Antemoro, Madagascar.

toward increasing supermarket sales is primarily driven by higher incomes and changing diets among urbanizing populations (e.g., increased consumption of meats and processed foods). International markets exhibit higher producer price risk because of fluctuating exchange rates, trade barriers, and more stringent food safety standards. For example, stricter standards for aflatoxin (a liver toxin produced by the fungus *Aspergillus*) in Europe further restrict food imports from Africa (6). Moreover, developed countries' higher import tariffs for processed foods than for raw commodities (7) impede value-addition in export FVCs. Although export-oriented FVCs also offer opportunities for smallholder farmers (8) and farmworkers,

from off-farm employment and are commonly net food buyers, the greatest poverty implications of FVCs likely do not arise directly through purchases from poor farmers. Instead, these effects often occur indirectly through lower cost, more nutritious and safer foods for poor consumers, and increased employment of and safer working conditions for unskilled workers in commercial agriculture and post-harvest processing (10). Researchers too often focus just on the profitability of direct FVC participation. We must not overlook the crucial indirect effects FVCs have on rural and urban poverty.

3. *Enhance marketing channel efficiency.* Poor people in rural and urban areas participate in FVCs not only as farmers but also

<sup>1</sup>Cornell University, Ithaca, NY 14853, USA. <sup>2</sup>International Maize and Wheat Improvement Centre, Nairobi, Kenya. <sup>3</sup>Catholic Relief Services, Baltimore, MD 21201, USA. <sup>4</sup>Bill and Melinda Gates Foundation, Seattle, WA 98102, USA. <sup>5</sup>University of New South Wales, Sydney, New South Wales 2052, Australia. <sup>6</sup>Michigan State University, East Lansing, MI 48824, USA. <sup>7</sup>Radboud University Nijmegen, 6500 Nijmegen, Netherlands. <sup>8</sup>Fairtrasa, Michoacán, CP 60080, Mexico. <sup>9</sup>Katholieke Universiteit, 3000 Leuven, Belgium. <sup>10</sup>Centre for Alleviation of Poverty through Sustainable Agriculture, Bogor, 16111 Indonesia. <sup>11</sup>World Vegetable Center, Tainan 74199, Taiwan.

\*Author for correspondence. E-mail: mig7@cornell.edu



as consumers (9). Only by reducing the difference between retail price and price when sold by the farm can FVCs simultaneously decrease food costs for poor consumers and increase earnings for poor farmers and farmworkers via increased demand and employment. This requires cost-efficient market intermediation, including product aggregation, storage, processing, and distribution. It is otherwise difficult to avoid the “food price dilemma” that higher prices help and incentivize net-seller farmers but also hurt consumers, especially poor people (11). For example, investments in infrastructure that reduce the significant marketing costs Kenyan smallholder farmers incur delivering crop to buyers—estimated at equivalent to a 15% sales tax—can increase earnings without driving up food prices (12). Research is needed on how to reduce market intermediation costs in an equitable and environmentally sustainable manner.

4. *Pay attention to post-harvest losses, both in volume and quality.* Post-harvest losses, estimated at 15 to 50% in DCs (13), disproportionately burden poor people who often lack capacity for food preservation and safe storage. Such losses cause market inefficiencies and have negative environmental effects because of inefficient land and water use. Associated food quality problems, in turn, impede poor growers’ participation in FVCs and pose food safety risks for consumers. For example, mycotoxins and microbial hazards contaminate significant proportions of food supplies in tropical, low-income communities (14). Successful remedies include improved preharvest management and small-scale post-harvest storage and energy-saving technologies, as well as increased food-processing opportunities to prevent spoilage (15). Micronutrient fortification of staple foods and preservation of fruits and vegetables can improve the quality of diets (16). Increased research on post-harvest technologies can help reduce unnecessary losses and thereby reduce pressure on land and water and improve food safety and dietary quality.

5. *On-farm natural resources conservation can enable, and benefit from, smallholder FVC participation.* The increased output required to meet growing food demand can be sustained only with increased labor, energy, land, and water productivity. Historically, agricultural productivity growth reduces poverty through higher profits for net producers, increased employment and/or real wages for workers, and lower prices for consumers (17). Productivity growth has also slowed conversion into cropland or pasture of more environmentally sensitive lands on the agricultural

frontier (18). FVCs can induce participating farmers to invest in water, soil, and energy conservation measures, and such investments enable new farmers to participate in FVCs. For example, solar-powered drip irrigation systems in the West African Sahel improved productivity, increased smallholder farmer income and nutrient intake, and cost less than traditional production systems (19). Farm practices that enable soil carbon sequestration can improve soil quality, eco-efficiency, and profitability (20). Too little is known about how to scale resource-conserving, productivity-boosting innovations and about how to capture consumer valuation of “green” farming innovations.

6. *Certification appears necessary, but not sufficient.* Certification (i.e., attestation of compliance with product standards) assures consumers about key product qualities, often eliciting a price premium for desired attributes such as fair trade, organic, or sustainable practices. In other cases, certification is necessary to show FVC compliance with standards set by regulators. But certification is costly because of the infrastructure required to sustain the scheme and may inadvertently exclude smallholder farmers from high-value markets (21). For example, the costs of Fair Trade certification—a system that identifies products with specific labor, environmental, and developmental standards—may prevent participation of small groups of farmers. In coffee, the certification cost for ~10,000 farmers is 2.4% of retail price; for ~1000 farmers it is 6.2% of retail price; and it is higher for smaller groups (table S1). It is clear that certification and credible product labeling can tap consumer demand for desirable attributes and is thus necessary to elicit the premium prices needed to pay for those attributes. However, it remains unclear whether certification facilitates smallholder entry into higher-return markets, promotes adoption of sustainable farming practices, or fosters farm-level innovation.

#### Agenda for the Future

The preceding six principles carry two important implications for scientists, donors, policy-makers, and private decision-makers. First, we need to be humble about how little we know about complex FVCs and their effects on poverty and the environment and cautious in our policy prescriptions on FVCs.

Second, scientists must begin developing a transdisciplinary, multidimensional conceptual framework to study DC FVCs in order to establish good FVC practices to benefit the poor, protect the environment, and help smallholder farmers meet growing consumer

demand for sustainability attributes. This conceptual framework should include indicators to explicitly identify links among the multiple dimensions of FVC performance—such as economic costs, distributional equity, environmental impacts, energy use, and consumer and farmworker health and safety. Within such a conceptual framework, scientists can then construct rigorous models and conduct empirical research to test their validity. Appropriate foci include measurement of the tradeoffs and complementarities between specific FVC attributes (e.g., under what conditions are economic efficiency and environmental conservation practices complementary?) and comparative studies of FVC performance to establish what attributes are most strongly associated with desirable outcomes in multiple dimensions (e.g., under what conditions and in what dimensions do local FVCs outperform transnational ones?). Finally, we must use existing methods (e.g., models of consumer behavior and political decision-making) to communicate multidimensional food attributes to consumers and policy-makers so as to promote informed decisions by all parties. This can increase the demand for and supply of foods with economically, socially, and environmentally desirable attributes.

#### References and Notes

1. Food and Agriculture Organization of the United Nations (FAO), *Occas. Pap.* (13) (2010).
2. T. Reardon *et al.*, *Am. J. Agric. Econ.* **85**, 1140 (2003).
3. FAO, FAOSTAT; fao.FAOSTAT.org (accessed 19 November 2010).
4. T. Reardon, J. A. Berdegue, *Dev. Policy Rev.* **20**, 371 (2002).
5. T. Reardon *et al.*, *World Dev.* **37**, 1717 (2009).
6. T. Otsuki *et al.*, *Food Policy* **26**, 495 (2001).
7. A. Regmi, M. Gehlhar, *Amber Waves* **3**, 12 (2005).
8. No universal definition of “smallholder” exists, but the typical farm size is <5 ha.
9. C. B. Barrett, *Food Policy* **33**, 299 (2008).
10. M. Maertens, J. F. M. Swinnen, *World Dev.* **37**, 161 (2009).
11. C. P. Timmer *et al.*, *Food Policy Analysis* (Johns Hopkins Univ. Press, Baltimore, MD, 1983).
12. M. Renkow *et al.*, *J. Dev. Econ.* **73**, 349 (2004).
13. A. Kader, *Acta Hort.* **682**, 2169 (2005).
14. L. J. Unnevehr, *Agric. Econ.* **37**, 149 (2007).
15. I. Silva-Barbeau, S. G. Hull, M. S. Prehm, W. E. Barbeau, *Food Nutr. Bull.* **26**, 297 (2005).
16. M. A. Lawrence, *Asia Pac. J. Clin. Nutr.* **17** (suppl. 3), S29 (2008).
17. B. Minten, C. B. Barrett, *World Dev.* **36**, 797 (2008).
18. R. E. Evenson, D. Gollin, *Science* **300**, 758 (2003).
19. J. Burney, L. Woltering, M. Burke, R. Naylor, D. Pasternak, *Proc. Natl. Acad. Sci. U.S.A.* **107**, 1848 (2010).
20. R. Lal, *Crop Sci.* **50** (suppl. 1), S120 (2010).
21. R. Ruben *et al.*, *Dev. Pract.* **19**, 777 (2009).
22. The authors arrived at this consensus statement after discussions in Ithaca, NY, in March 2010. Work supported by the David R. Atkinson Center for a Sustainable Future and the Cornell International Institute for Food, Agriculture, and Development.

#### Supporting Online Material

[www.sciencemag.org/cgi/content/full/332/6034/1154/DC1](http://www.sciencemag.org/cgi/content/full/332/6034/1154/DC1)

10.1126/science.1202543

# Scaling Up DNA Computation

John H. Reif

Computation is increasingly pervasive. Silicon-based computing devices are embedded in a wide variety of manufactured goods and appliances, increasing functionality, communication, and control. An analogous development of molecular-scale computing devices could allow similar advantages at vastly smaller scale. For example, embedding molecular-scale computing devices in biological materials such as serum, cells, or tissues could be used to detect, and possibly treat, disease. On page 1196 of this issue, Qian and Winfree (1) show how such molecular-scale computing devices might be engineered.

One increasingly promising approach, known as DNA-based computation, makes use of DNA in conjunction with biochemical reactions to do molecular computation. The advantage of this approach is that DNA is very stable, and biochemical reactions involving DNA have been very well developed for over a decade. The DNA hybridization reaction occurs when single strands of complementary DNA form double-stranded DNA in a double-helix conformation. DNA can self-assemble via hybridizations into secondary structures known as DNA nanostructures (2). DNA computations can be performed by self-assembly of DNA strands (3) and self-assembly of static DNA nanostructures (tiles) (4). Thus, DNA is used as an engineering material; the interactions that hold a DNA structure together are encoded in the base sequences of the strands. Computation can be incorporated into the assembly of the strands into DNA arrays and nanostructures. Alternatively, DNA-based computations often use dynamic DNA nanostructures to encode computational state, and computational steps are executed using biochemical reactions that manipulate these DNA nanostructures, changing the encoded state.

The approach adopted by Qian and Winfree marks an important advance in DNA-



based computations. The authors make use of dynamic DNA nanostructures called seesaw gates (5) and thresholding gates, within which DNA strands can hybridize in certain positions to encode Boolean values (“True” and “False”). There are multiple advantages to this approach. One is its simplicity. Their method uses only DNA hybridization reactions. Logical operations (AND and OR) are executed by seesaw gates, and restoration to the digital values is through thresholding gates followed by catalytic amplification of any leftover signal. Another advantage of the approach used by Qian and Winfree is that logical operations are executed autonomously—that is, without external control. The DNA hybridization reactions form chain reactions, whereby DNA hybridizations executed by seesaw gates cause further DNA hybridizations in other seesaw gates. The authors use toehold-mediated strand displacement (6) to initiate DNA hybridizations that displace previously hybridized DNA strands, and they drive the operations through transitions of “fuel” strands (7, 8) to lower energy states.

A further advantage of the method is its universality. The ability to evaluate a Boolean circuit with multiple Boolean gates pro-

A technique uses DNA strands to perform calculations that can be scaled up in complexity.

vides universal computation power, because any digital computation can be executed by Boolean circuit evaluation. Moderate scalability provides yet another advantage of this approach. The modularity of seesaw gates allows composition of multiple gates independently to a much larger scale than permitted by most previous DNA-based computations. The scalability is indicated by the authors’ demonstration of error-free computation of square roots of four-bit numbers.

A multidisciplinary approach including computer science and biochemistry was key to the project’s success. In addition to biochemistry laboratory techniques, computer science techniques were essential. Dual rail logic converted arbitrary Boolean logic (NOT, AND, and OR) into seesaw gates executing only AND and OR operations. Computer simulations of seesaw gate circuitry optimized

the design and correlated experimental data. Design compilers for DNA sequences of seesaw gates were developed.

Two limitations of the work by Qian and Winfree present further challenges. The speed of execution of seesaw gates is a major obstacle to scalability and usability of seesaw circuits for biological applications. Each seesaw gate takes 30 to 60 min. Their computation of four-bit square roots has a circuit depth (the maximum number of Boolean operations that need to be sequentially executed) of 7 and takes 6 to 10 hours. By contrast, biological regulatory circuits can respond much faster, often in less than a second. Another limitation is the number of molecules used in computations. Qian and Winfree executed a seesaw circuit computation simultaneously on a vast number (trillions) of DNA molecules within a test tube, whereas biological regulatory circuits make use of relatively small numbers of molecules for a given task.

Why these limitations? A molecular computation is defined as global if its state is spatially distributed (i.e., determined by averaging concentration and configuration of spatially distributed molecules defining the state), and transitions of state are executed



through multiple distributed interactions. Seesaw circuits are global, and their logical operations require long durations for diffusion of DNA signals between gates. One approach to solving such challenges is to exploit locality, a technique extensively used in modern conventional computing devices. A molecular computation is considered to be local if its state is encoded by a spatially contiguous set of molecules (i.e., the state of each computing element is explicitly determined by the configuration of these molecules), and transitions of state are executed through interactions between local computing elements. By avoiding delays due to diffusion, local molecular computations may execute more rapidly. Also, due to locality, the number of molecules involved in a single computation is

vastly reduced. Biological regulatory circuits are usually local, operating within a confined region such as a cell wall or cell organelle, and this may contribute to their generally more rapid rates. Whiplash polymerase chain reaction (9) is a local DNA computation in which polymerization reactions execute state transitions on a single DNA molecule. It remains a challenge to develop DNA-based computational methods that are local and only make use of DNA hybridization operations (and do not require enzymes). A promising approach is to tether together strands and gates used in a hybridization reaction to ensure locality.

A further challenge is to execute molecular computations within biological materials (e.g., serum, cells, or tissues) where the use of DNA-based computational methods is

limited by the presence of DNA-binding and DNA-cutting proteins. Possible approaches include using DNA with nonstandard bases or short RNA, both of which may be less susceptible to these proteins.

#### References

1. L. Qian, E. Winfree, *Science* **332**, 1196 (2011).
2. J. Reif *et al.*, in *Nanofabrication Handbook*, S. Cabrini, S. Kawata, Eds. (Taylor and Francis, New York, 2011).
3. L. M. Adleman, *Science* **266**, 1021 (1994).
4. C. Mao *et al.*, *Nature* **407**, 493 (2000); erratum, **408**, 750 (2000).
5. L. Qian, E. Winfree, in *DNA Computing*, A. Goel, F. C. Simmel, P. Sosik, Eds. (Springer, Berlin, 2009), vol. 5347, pp. 70–89.
6. B. Yurke *et al.*, *Nature* **406**, 605 (2000).
7. A. J. Turberfield *et al.*, *Phys. Rev. Lett.* **90**, 118102 (2003).
8. D. Y. Zhang *et al.*, *Science* **318**, 1121 (2007).
9. K. Sakamoto *et al.*, *Biosystems* **52**, 81 (1999).

10.1126/science.1208068

## PLANETARY SCIENCE

# Io's Tortured Interior

Andrew J. Coates<sup>1,2</sup>

Jupiter's moon Io is the most volcanic object in the solar system, injecting about a metric ton per second of sulfurous material into Jupiter's magnetic environment. Images and movies from spacecraft have caught Io's volcanoes in the act of erupting since their discovery by Voyager in 1979. This prolific activity hints at a tortured inner structure. On page 1186 of this issue, Khurana *et al.* (1) report magnetometer data obtained by the Galileo spacecraft and use it to infer the presence of a global magma ocean at least 50 km thick under Io's icy, pock-marked, and colorful surface. This result makes Io stand out as unique among its icy satellite siblings at Jupiter, Saturn, and beyond, where the other subsurface oceans are water-rich. It also confirms the importance of magnetic field and plasma instruments in probing the internal structure of solar system bodies.

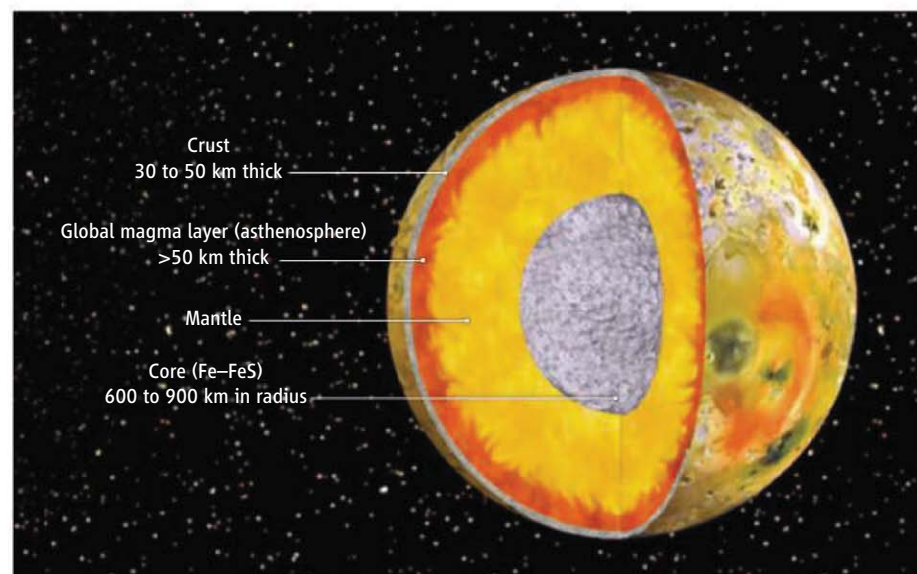
Techniques such as gravity measurements, ground-penetrating radar, radar to provide body shape, and seismometers on the surface can probe the internal structure of icy satellites from relatively brief spacecraft flybys and detect oceans of magma or of water. However, these capabilities were either unavailable or not precise enough to be definitive on Galileo. The Galileo team used magnetic field measurements from close fly-

bys of Europa and other moons, combined with modeling of the interior conductivity (2, 3). The idea is to use Jupiter's rapidly rotating (9-hour 55-min period) magnetic field as it overtakes the slower-orbiting moon. If the moon in question is conducting, a magnetic field is induced, the effects of which can be measured by the onboard magnetometer as the spacecraft flies past. Detailed modeling of subsurface conducting regions and the plasma environment, using concepts from

Magnetic measurements made by the Galileo spacecraft reveal an ocean of magma under Io's frozen surface.

geology and external plasma interactions, is then used to understand the measured magnetic field and its time variation (2, 3). The technique emphasizes the coupled nature of icy satellite interactions, from the interior structure through the surface and exosphere to the surrounding plasma environment, and requires exchanges of material and momentum at all the interfaces.

A technique similar to that used at Europa (2, 3) was used to discover subsurface water



**Probing inside.** Khurana *et al.* modeled magnetometer data to unveil the inner structure of Io with a thick magma ocean beneath the frozen surface.

<sup>1</sup>Mullard Space Science Laboratory, University College London (UCL), Holmbury St. Mary, Dorking RH5 6NT, UK.

<sup>2</sup>Centre for Planetary Sciences at UCL/Birkbeck, Gower Street, London WC1E 6BT, UK. E-mail: ajc@mssl.ucl.ac.uk

oceans under the icy crusts of Ganymede (4) and Callisto (3), although in the case of Ganymede the intrinsic magnetic field complicates matters (4). These salty oceans are likely in contact with silicate (at Europa) or ice (at Ganymede and Europa) (5), but their depth and detailed properties remain unknown. Because of their variety, the Galilean satellites are a fascinating target for future exploration: Europa has the ingredients for life, and Ganymede has its own magnetic field; Io's high activity and Callisto's ancient surface complete the picture.

In Saturn's system, an ocean including ammonia as an antifreeze was expected at Titan [e.g., (6)]. Observations of the rotation rate are consistent with this (7). At Enceladus, the evidence for a subsurface ocean found by the Cassini spacecraft includes the huge plumes of water and ice emanating from the southern polar region there (8), hinting at a large energy source and the reservoir below (9). Measurements of sodium in dust grains (10) are additional evidence for a subsurface ocean. In the case of Enceladus, the magnetic field signature, showing the field draping around the southern polar region, was the first evidence (11) for mass loading of the plasma nearby and led to changes in the mission profile for a closer look. Plasma (12) and imaging instruments (8, 9) confirmed the finding, and estimates of the mass loading show that Enceladus can produce up to a third of the activity of Io. It has been found that, like Io, Europa, and Ganymede at Jupiter, Enceladus has a related auroral spot at the magnetic footprint of this active moon in Saturn's ionosphere that can be used to detect fluctuations in the activity (13).

Saturn's second-largest satellite, Rhea, has a simpler structure; it may have a rocky core and certainly has an icy mantle (14). Dione and Tethys may also have deep oceans under icy crusts, but this remains uncertain, based on data from Cassini. It has also been suggested that subsurface water-rich oceans are possible for Rhea, Titania, Oberon, Triton, and Pluto, and on the largest transneptunian objects (2003 UB313, Sedna, and 2004 DW), if even small amounts of ammonia are present (15).

In the case of Io, however, the results reported by Khurana *et al.* give a well-constrained picture of the interior. The ocean is not water; rather, there is a global magma ocean ("asthenosphere") at least 50 km deep, under a low-density outer crust (30 to 50 km) and surrounding a 600- to 900-km iron-rich core. An asthenosphere had been suggested earlier but was the subject of debate. This latest modeling appears to provide the

answer: It exists, and it's hot; a melt fraction >20% and a temperature >1400 K provide the best fit of the modeling to the data. A magma ocean was needed to fit the multilayer modeling of the interior's conductivity, assuming reasonable conductivity values and a range of melt fractions. Modeling of the exterior plasma environment was done by means of a conducting fluid approach. Although this does not include all the individual particle kinetic effects, and plasma effects may be important, this technique is suitable for large-scale features of the interaction. The result of the coupled model gives a three-dimensional map of the magnetic field around Io and the magnetic field perturbation, including Alfvén wings, that it may produce. A simulated spacecraft fly-through at the distances of two key Galileo flybys provided a detailed comparison of the time variation of the magnetic field.

What makes Io stand out among the outer planet satellites is the global magma ocean, the source of the huge activity of this moon. Whereas the other moons have liquid water oceans, Io's contains sulfurous magma (see the figure).

The Galileo mission ended in 2003 and left many unanswered questions, especially

about the Galilean satellites. The depths of the watery oceans at Europa, Ganymede, and Callisto are unknown, as are the ice shell thicknesses. Similarly, there are still many questions arising from Cassini's exploration at Saturn. Outer planet moons are tempting targets for future exploration, and recent mission studies are aimed at studying Ganymede and Europa in detail, and also Titan and Enceladus. Many questions remain about these fascinating moons. We hope the resources will be available to answer them soon.

#### References

1. K. K. Khurana *et al.*, *Science* **332**, 1186 (2011).
2. M. G. Kivelson *et al.*, *Science* **289**, 1340 (2000).
3. K. K. Khurana *et al.*, *Nature* **395**, 777 (1998).
4. M. G. Kivelson *et al.*, *Icarus* **157**, 507 (2002).
5. C. Sotin, G. Tobie, C. R. Phys. **5**, 769 (2004).
6. O. Grasset, C. Sotin, F. Deschamps, *Planet. Space Sci.* **48**, 617 (2000).
7. R. D. Lorenz *et al.*, *Science* **319**, 1649 (2008).
8. C. C. Porco *et al.*, *Science* **311**, 1393 (2006).
9. J. R. Spencer *et al.*, *Science* **311**, 1401 (2006).
10. F. Postberg *et al.*, *Nature* **459**, 1098 (2009).
11. M. K. Dougherty *et al.*, *Science* **311**, 1406 (2006).
12. R. L. Tokar *et al.*, *Science* **311**, 1409 (2006).
13. W. R. Pryor *et al.*, *Nature* **472**, 331 (2011).
14. J. Castillo-Rogez, *J. Geophys. Res.* **111**, E11005 (2006).
15. H. Hussmann, F. Sohl, T. Spohn, *Icarus* **185**, 258 (2006).

10.1126/science.1206534

#### MATERIALS SCIENCE

## Potential Solutions for Creating Responsive Materials

Karl Sieradzki

Plastic deformation of a nanoporous material can be altered by changing its surface via an electrochemical potential.

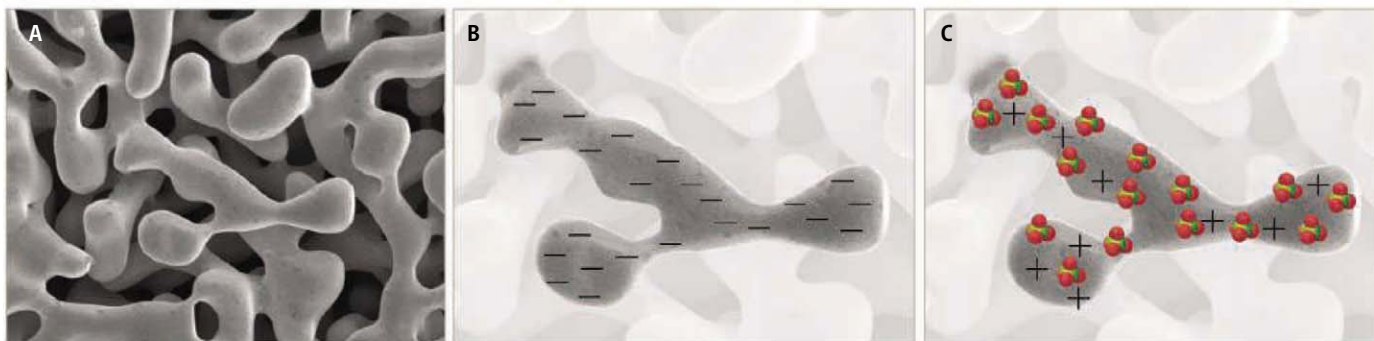
Structural materials are often engineered for toughness—an ability to withstand sudden impact and avoid brittle failure. If these materials could sense their surroundings and if their properties could be "tuned" with an external stimulus, then it might be possible to engineer materials that can self-repair the damage they may incur. Some composite polymeric materials have been developed with such capabilities (1). However, for many applications, we are still years away from knowing how to create and tune the properties of other useful materials. On page 1179 of this issue, Jin and Weissmüller (2) describe

in situ tuning of a two-phase composite structure formed from nanoporous gold infiltrated with a perchloric acid (HClO<sub>4</sub>) electrolyte solution. They demonstrated "reversible" tuning of the flow stress—the pressure needed to maintain plastic deformation—by changing the composition of absorbed molecules on the gold surface with an applied electrochemical potential (3).

The solid phase was made by selective leaching of silver from a silver-gold alloy. A connected network of gold ligaments formed, roughly 10 to 20 nm in diameter, that contained pores of similar dimensions (see the figure, panel A). The network was bicontinuous; that is, both the solid phase and the void space were continuous, and there were no isolated porous regions. The changes that

School for Engineering of Matter, Transport and Energy, Arizona State University, Tempe, AZ 85287, USA. E-mail: karl.sieradzki@asu.edu





**Tuning mechanical properties.** Jin and Weissmüller examined changes in flow stress of a nanoporous gold structure (A) filled with a 1 M  $\text{HClO}_4$  electrolyte. Application of electrochemical potential changes the nature of the surface and

its mechanical response. (B) Between 0 and 0.5 V, the surface builds up a negative charge like a capacitor. (C) Between 0.5 and 1.2 V, the positive charge in the surface is compensated by an adsorbed layer of anions from the electrolyte.

occurred on a gold surface when an electrochemical potential was applied with  $\text{HClO}_4$  as the electrolyte fell into three regimes (4). Between 0 and 0.50 V (5), the surface charged like a capacitor (see the figure, panel B). Between 0.50 and 1.20 V, anions were attracted to the positive charge and adsorbed (see the figure, panel C). Between 1.20 and 1.50 V, a monolayer of oxidized gold formed. The monolayer oxidation process began with hydroxide ( $\text{OH}^-$ ) adsorption into surface sites unoccupied by adsorbed  $\text{ClO}_4^-$ ; as the potential became more positive, more  $\text{OH}^-$  was incorporated and correspondingly  $\text{ClO}_4^-$  desorbed. Finally, the surface underwent a reconstruction in which the oxygen atoms were incorporated into the gold surface atoms to create a layer of gold oxide.

Jin and Weissmüller determined the mechanical properties of this composite material by applying pressure and measuring deformation while an electrochemical potential was applied. The largest changes in material properties occurred when the applied potential was jumped from the region of  $\text{ClO}_4^-$  adsorption (about 1 V) to the monolayer oxidation region (about 1.5 V). In this case, the flow stress increased by as much as a factor of 2. They also observed smaller increases in flow stress when the potential was pulsed from the region of  $\text{ClO}_4^-$  adsorption (about 1 V) into the capacitive charging region (about 0.1 V). The flow stress was smallest in the vicinity of the potential of zero charge (about 0.5 V).

One can conceive of several possible mechanisms by which a two-dimensional gold oxide layer could increase the flow stress of nanoscale structures. The movement of atoms that allows a crystalline material to deform actually occurs via the movement of dislocations—line defects that run through the material. The rate of this process depends on how easily dislocations move and their density. A surface oxide could reduce the surface mobility of a dislocation by pinning it at the point

where it emerges on the surface (6), making it immobile. The oxide could also create an elastically stiff barrier that impedes a dislocation from escaping through the surface.

The mechanical properties reported by Jin and Weissmüller are connected to various observations of surface effects on crystal plasticity often generically termed Rehbinder effects (7). This effect originally referred to the adsorption-induced reduction in hardness or flow stress of a material caused by a concomitant lowering of the surface energy (8). These quantities are related because a portion of the work of plastic flow is associated with the creation of new surfaces as the material stretches. However, Jin and Weissmüller observed a minimum in the flow stress in the range of potentials such that the surface is free of adsorbates.

Their results are also connected to more recent reports of sample size effects on the yield and flow strength of solids (9). Because the surface-to-volume ratio in a nanostructure is relatively large and the bulk dislocation content is likely small, the importance of surface effects is magnified. For potentials that oxidized the surface, the amplitude of the variation in flow stress increased with decreasing gold ligament size. Similar results have been reported for flow stress of nanoscale gold pillars (10), although the cause of this behavior is unclear.

One intriguing aspect of the results reported by Jin and Weissmüller relates to the brittle behavior of the composite structure in the oxidative region and the connection of this behavior to stress-corrosion cracking of metal alloys. In some cases involving noble metal alloys and stainless steels, stress corrosion has been linked to the selective dissolution of an alloy component and the consequent formation of a nanoporous structure (11). In the case of silver-gold alloys, the nanoporous structure initially forms at length scales on the order of 2 to 3 nm (12). The magnitude of the behaviors reported by Jin

and Weissmüller increased with decreasing gold ligament size, so it seems quite plausible that at yet smaller length scales, these effects will be larger and therefore possibly relevant to certain forms of stress-corrosion cracking.

A timely application of the concepts presented in the report by Jin and Weissmüller may be connected to mitigating damage evolution that occurs in rechargeable batteries when metal ions intercalate in and out of electrode materials. The associated volume change can crack the material and electrically isolate parts of it. Such mechanical failure of intercalation materials is believed to be a possible mechanism of capacity loss in lithium-ion batteries (13). It may be possible to design intercalation electrodes with nanoscale morphologies that, under suitable voltage conditions, make use of electric charge or surface-active agents that modify the plastic properties of the electrode structure. Such approaches may relieve, at least to some extent, fatigue damage created by cycles of intercalation and de-intercalation.

## References and Notes

1. R. P. Wool, *Soft Matter* **4**, 400 (2008).
2. H.-J. Jin, J. Weissmüller, *Science* **332**, 1179 (2011).
3. Reversibility is used here not in the thermodynamic sense, but to indicate that the flow stress behavior is recoverable during potential cycling.
4. H. Angerstein-Kozłowska, B. E. Conway, A. Hamelin, L. Stoicoviciu, *Electrochim. Acta* **31**, 1051 (1986).
5. Voltages are measured relative to a standard hydrogen electrode.
6. A. R. C. Westwood, *Philos. Mag.* **7**, 633 (1962).
7. F. R. N. Nabarro, *Theory of Crystal Dislocations* (Oxford Univ. Press, London, 1967), p. 294.
8. P. A. Rehbinder, E. D. Shchukin, *Prog. Surf. Sci.* **3**, 97 (1972).
9. M. D. Uchic, D. M. Dimiduk, J. N. Florando, W. D. Nix, *Science* **305**, 986 (2004).
10. J. R. Greer, W. C. Oliver, W. D. Nix, *Acta Mater.* **53**, 1821 (2005).
11. K. Sieradzki, R. C. Newman, *J. Phys. Chem. Solids* **48**, 1101 (1987).
12. S. G. Corcoran, D. G. Wiesler, K. Sieradzki, *Mater. Res. Soc. Symp. Proc.* **451**, 93 (1997).
13. W. H. Woodford, Y.-M. Chang, W. C. Carter, *J. Electrochem. Soc.* **157**, A1052 (2010).

10.1126/science.1206856

## EVOLUTION

# In Evolution, the Sum Is Less than Its Parts

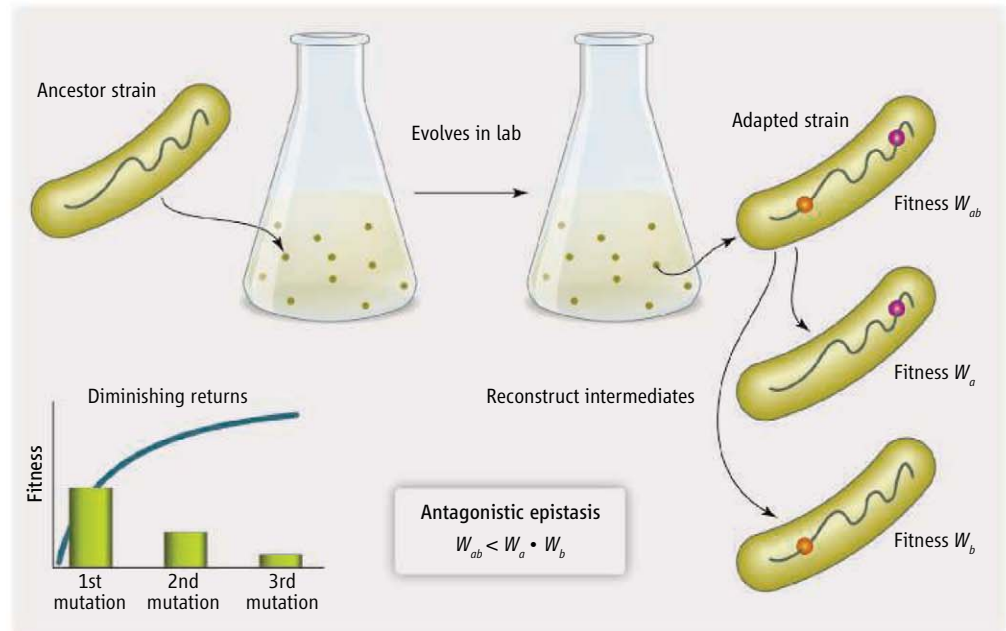
Sergey Kryazhimskiy,<sup>1,2</sup> Jeremy A. Draghi,<sup>1</sup> Joshua B. Plotkin<sup>1</sup>

Laboratory experiments with bacteria shed light on how epistatic interactions influence the pace of evolution.

Propagating bacteria in a lab for thousands of generations may seem tedious, or even irrelevant, to most evolutionary biologists. Nonetheless, such experiments provide an opportunity to deduce quantitative principles of evolution and directly test them in controlled environments. Combined with modern sequencing technologies, as well as theory, recent microbial experiments have suggested a critical role for genetic interactions among mutations, called epistasis, in determining the pace of evolution. Two papers in this issue, by Khan *et al.* on page 1193 (1) and Chou *et al.* (2) on page 1190, present precise experimental measurements of these epistatic interactions.

Microbial evolution experiments in a simple, constant environment reveal a characteristic pattern: At first, a population rapidly acquires beneficial mutations, but then adaptation progressively slows so that thousands of generations pass between subsequent beneficial substitutions (3). Unexpected outcomes, however, can and do occur even in these simple experimental conditions. Populations evolve a dramatically elevated mutation rate (4), discover rare phenotypic innovations (5), or diverge into distinct lineages that either coexist (6) or compete vigorously as each strain races to acquire more adaptive mutations (7). Recent theory suggests that a common cause underlies all these phenomena: the structure of epistatic interactions among mutations.

Epistasis describes how the fitness consequence of a mutation depends on the status of the rest of the genome. In one extreme example, called sign epistasis, a mutation may be beneficial if it arises on one genetic background, but detrimental on another. Although interactions among genes may seem an obvious fact of biology, the myriad possible forms of epistasis have made it difficult to formu-



**Antagonistic epistasis.** Bacteria adapt to a laboratory environment by acquiring beneficial mutations. Khan *et al.* and Chou *et al.* identified the mutations that accrued in an adapted strain, and measured their fitness benefits (growth advantage relative to the ancestor). The mutations conferred smaller marginal benefits in combination than they did individually. This antagonistic epistasis causes progressively slower rates of adaptation over time.

late predictive evolutionary models or to infer such interactions from empirical data. Nevertheless, epistasis is at the heart of classical theories, such as the evolution of sex (8), and also of modern concepts such as robustness and evolvability (a population's ability to evolve) (9). Moreover, recent theoretical work (10) suggests that the overall dynamical pattern of adaptation observed in long-term microbial experiments can be explained by a prevalence of what is called antagonistic epistasis, in which beneficial mutations confer less benefit in combination than they do individually.

To quantify epistasis among beneficial mutations and to test these theoretical predictions, both Khan *et al.* and Chou *et al.* examined the initial substitutions that occurred in populations of bacteria adapting in the laboratory. The researchers identified the handful of mutations across the genome that had substituted in an evolved strain, and then constructed intermediate strains containing combinations of these mutations. By measuring the fitness benefits conferred by these muta-

tions, individually and in combination, the researchers were able to directly quantify the extent and form of epistasis (see the figure).

Both studies found a predominance of antagonistic epistasis, which impeded the rate of ongoing adaptation relative to a null model of independent mutational effects. Chou *et al.* further interpreted the prevalence of antagonistic epistasis in terms of metabolic costs and benefits. The concordance of results from the two studies is noteworthy, especially because Khan *et al.* analyzed *Escherichia coli* populations [from the long-term experiments of Lenski (3)], whereas Chou *et al.* studied an engineered strain of *Methylobacterium extorquens*. The remarkable precision with which both studies quantified epistasis among beneficial mutations was made possible only by leveraging whole-genome sequencing combined with the ability to reconstruct mutational combinations and assay them in the same environment in which the mutations first arose.

The view of epistasis across a genome that emerges from this work contrasts sharply

<sup>1</sup>Department of Biology, University of Pennsylvania, Philadelphia, PA 19103, USA. <sup>2</sup>Department of Organismic and Evolutionary Biology, Harvard University, Cambridge, MA 02138, USA. E-mail: jplotkin@sas.upenn.edu



with the type of epistasis found among adaptive mutations within a single protein (11). Notably, Weinreich *et al.* studied mutations in an antibiotic resistance gene,  $\beta$ -lactamase, and found a prevalence of sign epistasis, which limits the number of genetic paths that evolution can follow (11). In contrast, the epistasis documented by Khan *et al.* and Chou *et al.* exerts less constraint on the order of substitutions that increase fitness, so that the specific path that evolution will take is less predictable. At the same time, the prevalence of antagonistic epistasis measured by the two groups ensures a predictable tempo of adaptation characterized by diminishing marginal returns (10).

Although these new experiments suggest a consistent principle of how epistasis shapes the pattern of adaptation, many questions must be answered before their results can be extended to evolution outside the laboratory. It remains unclear, for instance, whether these results would be altered by changing fundamental evolutionary parameters, such as population size, rate of mutation, and rate of recombination. Likewise, it is unclear

whether experiments in simple environments, with only one or a few niches for coexisting strains, will reflect the pattern of adaptation in more complex ecologies, such as *Pseudomonas fluorescens* in structured environments (6). Nonetheless, the compelling consistency between these two studies should inspire efforts to test the generality of their findings, by measuring epistasis in a wide range of experimental and even natural systems.

These studies, and the long-term laboratory evolution experiments from which they derive, represent a resounding achievement for the reductionist approach to studying biology. The mechanistic picture they paint of evolution is complex but not incomprehensible; although epistatic interactions lead to surprising phenomena, the advantages of a frozen “fossil record” of laboratory-raised isolates, and the ease of manipulating—and, now, fully sequencing—evolved strains enables researchers to tease apart and examine the underlying causes of these phenomena. Moreover, the theory and concepts developed to explain these simple experiments may have broad payoffs. Already,

epistasis has been implicated in the evolution of drug resistance in influenza viruses (12) and in bacterial pathogens (13). Ultimately, populations of bacteria tediously propagated in the lab may be key to predicting the next moves of the most mutable and dangerous human pathogens.

## References

1. A. I. Khan, D. M. Dinh, D. Schneider, R. E. Lenski, T. F. Cooper, *Science* **332**, 1193 (2011).
2. H.-H. Chou, H.-C. Chiu, N. F. Delaney, D. Segrè, C. J. Marx, *Science* **332**, 1190 (2011).
3. S. F. Elena, R. E. Lenski, *Nat. Rev. Genet.* **4**, 457 (2003).
4. P. D. Sniegowski, P. J. Gerrish, R. E. Lenski, *Nature* **387**, 703 (1997).
5. Z. D. Blount, C. Z. Borland, R. E. Lenski, *Proc. Natl. Acad. Sci. U.S.A.* **105**, 7899 (2008).
6. P. B. Rainey, M. Travisano, *Nature* **394**, 69 (1998).
7. R. J. Woods *et al.*, *Science* **331**, 1433 (2011).
8. A. S. Kondrashov, *Nature* **336**, 435 (1988).
9. G. P. Wagner, L. Altenberg, *Evolution* **50**, 967 (1996).
10. S. Kryazhimskiy, G. Tkačik, J. B. Plotkin, *Proc. Natl. Acad. Sci. U.S.A.* **106**, 18638 (2009).
11. D. M. Weinreich, N. F. Delaney, M. A. Depristo, D. L. Hartl, *Science* **312**, 111 (2006).
12. J. D. Bloom, L. I. Gong, D. Baltimore, *Science* **328**, 1272 (2010).
13. S. Trindade *et al.*, *PLoS Genet.* **5**, e1000578 (2009).

10.1126/science.1208072

## GENOMICS

# Behavior and the Dynamic Genome

Alison M. Bell<sup>1,3</sup> and Gene E. Robinson<sup>2,3</sup>

When circumstances change, an organism's first response is often behavioral. But how does adaptive behavior evolve, given that it requires constant and often instantaneous interactions between an individual and its environment? The dominant view emphasizes new random DNA mutation as the starting point. This may lead to behavioral variation. If the resulting variants have different fitness values, then natural selection could result in behavioral evolution through changes in allele frequencies across generations. An alternative theory proposes environmentally induced change in an organism's behavior as the starting point (1), and “phenotypic plasticity” that is inherited across generations through an unspecified process of “genetic assimilation” (2). Despite numerous exam-

ples (3), the latter as a driver of behavioral evolution has never been widely accepted, perhaps as a reaction against Lamarckianism—the idea that characteristics acquired by habit, use, or disuse can be passed on across generations. However, behavioral genetics and genomics, especially for animals in natural populations, lend some plausibility to the phenotypic plasticity view.

The ability to analyze genome-wide gene expression through “transcriptomics” has shown that the genome responds dynamically to stimuli (4). One illustrative example is the honey bee. The African honey bee (*Apis mellifera scutellata*) responds much more fiercely when its hive is attacked than do other subspecies of honey bee. Evolutionary changes in brain gene expression may have resulted in an increase in responsiveness to alarm pheromone (the chemical bees use to alert each other to danger) for African honey bees (5). About 10% of the same genes regulated in the brain by alarm pheromone are also differentially expressed between African and the less aggressive European honey bees. These genes, acting

Does behavior evolve through gene expression changes in the brain in response to the environment?

over both physiological and evolutionary time scales, provide a possible mechanism for how behavioral plasticity might drive rapid behavioral evolution through changes in gene regulation. In an environment with more predators, colonies producing more bees with lower thresholds for responding to alarm pheromone would have fared better, which would then result in a population with patterns of gene expression whose output was an “aroused” behavior, even in the absence of alarm pheromone. Although this view does not rule out the possibility that these differences in aggression arose through new mutation, the transcriptomics agrees with the idea of “genetic accommodation” (3), the modern, more inclusive version of genetic assimilation, which could involve either evolutionary increases or decreases in plasticity. In certain environments, plastic genotypes might be favored, but in other environments, nonplastic genotypes might be preferred instead. Future studies will determine whether differences in honey bee aggression can be explained by selection on regulatory regions of the

<sup>1</sup>Department of Animal Biology, University of Illinois, Urbana-Champaign, IL 61801, USA. <sup>2</sup>Department of Entomology, University of Illinois, Urbana-Champaign, IL 61801, USA. <sup>3</sup>Neuroscience Program, Program in Ecology, Evolutionary Biology and Conservation, Institute for Genomic Biology, University of Illinois, Urbana-Champaign, IL 61801, USA. E-mail: generobi@life.uiuc.edu



**Behavioral evolution.** Male dung beetles with horns (left) fight for mates, whereas hornless males (right) sneak copulations. The morphs show different patterns of gene expression in developing brain tissue. Genes that are differentially expressed between these two morphs have diverged among species.

genome, epigenetic (chemical) modifications to the genome, or both.

Genes that are responsive over different time scales also may be involved in the evolution of animal personality (6). For example, after the retreat of the glaciers during the early Holocene ~12,000 years ago, marine stickleback fish (*Gasterosteus aculeatus*) invaded new freshwater environments filled with predators they had never encountered before. Some sticklebacks must have changed their behavior in response to this threat, and over generations, those behaviors that enhanced survival were favored. As with the African honey bees, their survival might be attributed to behavioral changes that resulted from genetic accommodation of a plastic response to predation risk through selection on gene regulation. Presently, there are genetically distinct populations of “bold” and “shy” stickleback fish adapted to different predation regimes that exhibit different baseline levels of antipredator behavior, even when predators are not immediately present.

These examples suggest that genes with expression differences along the temporal continuum are candidates for driving evolutionary divergence through phenotypic plasticity. The mating behavior in dung beetles (*Onthophagus taurus*) reflects this possibility. Male beetles with prominent horns fight for access to females, whereas hornless males attempt instead to mate surreptitiously, without challenging other males (see the figure). The genes that are differentially expressed between these two male morphs are also evolutionarily divergent (7). Given the ever-increasing cases of genetic accommodation in natural populations, including feeding-induced changes in head shape in snakes (8) and sticklebacks (9), behavioral innovation in Darwin’s finches (10), and range expansion in house finches (11), genomic analyses could clarify whether phenotypic plasticity is often a driver of behavioral evolution.

Transcriptomics and analysis of genetic variation may reveal whether genes linked to phenotypic plasticity and behavior are common or rare; epigenomics can explain how they might go from inducible to constitutively expressed; and molecular systems biology can identify their positions in regulatory networks (12). These kinds of genes might be used repeatedly in evolution to build the circuits and systems underlying certain types of behaviors, even though they do not directly encode behavior.

The dynamic genome also generates testable evolutionary hypotheses about which genes might be most important for human health. Genes that are important over different time scales might be expected to be held in check by stabilizing selection, and to be buffered from developmental perturbations over a lifetime. But from the perspective of “Darwinian medicine,” the genes that facilitate plasticity over multiple time scales might also cause maladaptation when the environment changes. If so, then genes acting over the temporal continuum, or the networks they operate in, may be disproportionately involved in disease conditions such as mental illness. A case in point is *CNTNAP2*, which encodes a neuronal cell adhesion protein. *CNTNAP2* functions in a network that includes the transcription factor Forkhead box protein P2 (*FOXP2*). Mutations in *CNTNAP2* are linked to language delay in children with autism spectrum disorder (13, 14), and *FOXP2* is involved in auditory communication in a variety of vertebrates, including humans (4). Disrupting the expression of *FOXP2* in the basal ganglia in mice (15) and song birds (16) causes communication deficits, and there is evidence for a selective sweep for a *FOXP2* allele in primates that is associated with the evolution of human speech (17).

The relationship between behavioral plasticity and the dynamic genome should become clearer as brain transcriptomics spreads to more species. Similar advances

can be expected for the relationship between gene expression and genetic variation, including cryptic genetic variation, which does not influence the phenotype unless there is a change in the environment (18). With the imminent sequencing of genomes of thousands of species, as well as thousands of individuals of the same species, there will be ample new evidence to test these ideas, but with a twist. Given that genes that are more plastic in their expression can also be more sensitive to mutation (19), there likely will be examples where phenotypic plasticity “lit the match” for adaptive behavioral evolution (3) but cryptic genetic variation provided the fuel.

#### References and Notes

1. J. M. Baldwin, *Development and Evolution* (Macmillan, New York, 1902).
2. C. H. Waddington, *Evolution* **7**, 118 (1953).
3. M. J. West-Eberhard, *Developmental Plasticity and Evolution* (Oxford Univ. Press, Oxford, 2003).
4. G. E. Robinson, R. D. Fernald, D. F. Clayton, *Science* **322**, 896 (2008).
5. C. Alaux et al., *Proc. Natl. Acad. Sci. U.S.A.* **106**, 15400 (2009).
6. A. M. Bell, N. Aubin-Horth, *Philos. Trans. R. Soc. B* **365**, 4001 (2010).
7. E. C. Snell-Rood et al., *Evolution* **65**, 231 (2011).
8. F. Aubret, R. Shine, *Curr. Biol.* **19**, 1932 (2009).
9. M. A. Wund, J. A. Baker, B. Clancy, J. L. Golub, S. A. Foster, *Am. Nat.* **172**, 449 (2008).
10. S. Tebbich, K. Sterelny, I. Teschke, *Philos. Trans. R. Soc. B* **365**, 1099 (2010).
11. A. Badyaev, *Philos. Trans. R. Soc. B* **364**, 1125 (2009).
12. G. Konopka, D. H. Geschwind, *Neuron* **68**, 231 (2010).
13. D. E. Arking et al., *Am. J. Hum. Genet.* **82**, 160 (2008).
14. B. Bakaloglu et al., *Am. J. Hum. Genet.* **82**, 165 (2008).
15. W. Shu et al., *Proc. Natl. Acad. Sci. U.S.A.* **102**, 9643 (2005).
16. S. Haesler et al., *PLoS Biol.* **5**, e321 (2007).
17. W. Enard et al., *Nature* **418**, 869 (2002).
18. K. McGuigan, C. M. Sgro, *Trends Ecol. Evol.* **24**, 305 (2009).
19. C. R. Landry, B. Lemos, S. A. Rifkin, W. J. Dickinson, D. L. Hartl, *Science* **317**, 118 (2007).
20. We thank M. McNeill, K. Nowick, D. C. Queller, E. C. Snell-Rood, M. B. Sokolowski, J. E. Strassmann, A. L. Toth, M. J. West-Eberhard, and S. W. Woodard for comments that improved this manuscript.

10.1126/science.1203295

CREDIT: DOUGLAS EMLEN



# A Bacterium That Can Grow by Using Arsenic Instead of Phosphorus

Felisa Wolfe-Simon,<sup>1,2\*</sup> Jodi Switzer Blum,<sup>2</sup> Thomas R. Kulp,<sup>2</sup> Gwyneth W. Gordon,<sup>3</sup> Shelley E. Hoefft,<sup>2</sup> Jennifer Pett-Ridge,<sup>4</sup> John F. Stolz,<sup>5</sup> Samuel M. Webb,<sup>6</sup> Peter K. Weber,<sup>4</sup> Paul C. W. Davies,<sup>1,7</sup> Ariel D. Anbar,<sup>1,3,8</sup> Ronald S. Oremland<sup>2</sup>

Life is mostly composed of the elements carbon, hydrogen, nitrogen, oxygen, sulfur, and phosphorus. Although these six elements make up nucleic acids, proteins, and lipids and thus the bulk of living matter, it is theoretically possible that some other elements in the periodic table could serve the same functions. Here, we describe a bacterium, strain GFAJ-1 of the Halomonadaceae, isolated from Mono Lake, California, that is able to substitute arsenic for phosphorus to sustain its growth. Our data show evidence for arsenate in macromolecules that normally contain phosphate, most notably nucleic acids and proteins. Exchange of one of the major bio-elements may have profound evolutionary and geochemical importance.

**B**iological dependence on the six major nutrient elements carbon, hydrogen, nitrogen, oxygen, sulfur, and phosphorus (P) is complemented by a selected array of other elements, usually metals or metalloids present in trace quantities that serve critical cellular functions, such as enzyme co-factors (1). There are many cases of these trace elements substituting for one another. A few examples include the substitution of tungsten for molybdenum and cadmium for zinc in some enzyme families (2, 3) and copper for iron as an oxygen-carrier in some arthropods and mollusks (4). In these examples and others, the trace elements that interchange share chemical similarities that facilitate the swap. However, there are no prior reports of substitutions for any of the six major elements essential for life. Here, we present evidence that arsenic can substitute for phosphorus in the biomolecules of a naturally occurring bacterium.

Arsenic (As) is a chemical analog of P, which lies directly below P on the periodic table. Arsenic possesses a similar atomic radius, as well as near identical electronegativity to P (5). The most common form of P in biology is phosphate ( $\text{PO}_4^{3-}$ ), which behaves similarly to arsenate ( $\text{AsO}_4^{3-}$ ) over the range of biologically relevant pH and redox gradients (6). The physicochemical similarity between  $\text{AsO}_4^{3-}$  and  $\text{PO}_4^{3-}$  contributes to the biological toxicity of  $\text{AsO}_4^{3-}$  because metabolic pathways intended for  $\text{PO}_4^{3-}$  cannot distinguish between the two molecules (7) and  $\text{AsO}_4^{3-}$  may

be incorporated into some early steps in the pathways [(6) and references therein]. However, it is thought that downstream metabolic processes are generally not compatible with As-incorporating molecules because of differences in the reactivities of P and As compounds (8). These down-

stream biochemical pathways may require the more chemically stable P-based metabolites; the lifetimes of more easily hydrolyzed As-bearing analogs are thought to be too short. However, given the similarities of As and P—and by analogy with trace element substitutions—we hypothesized that  $\text{AsO}_4^{3-}$  could specifically substitute for  $\text{PO}_4^{3-}$  in an organism possessing mechanisms to cope with the inherent instability of  $\text{AsO}_4^{3-}$  compounds (6). Here, we experimentally tested this hypothesis by using  $\text{AsO}_4^{3-}$ , combined with no added  $\text{PO}_4^{3-}$ , to select for and isolate a microbe capable of accomplishing this substitution.

**Geomicrobiology of GFAJ-1.** Mono Lake, located in eastern California, is a hypersaline and alkaline water body with high dissolved arsenic concentrations [200  $\mu\text{M}$  on average (9)]. We used lake sediments as inocula into an aerobic defined artificial medium at pH 9.8 (10, 11) containing 10 mM glucose, vitamins, and trace metals but no added  $\text{PO}_4^{3-}$  or any additional complex organic supplements (such as yeast extract or peptone), with a regimen of increasing  $\text{AsO}_4^{3-}$  additions initially spanning the range from 100  $\mu\text{M}$  to 5 mM. These enrichments were taken through many decimal-dilution transfers, greatly reducing any potential carryover of autochthonous phosphorus

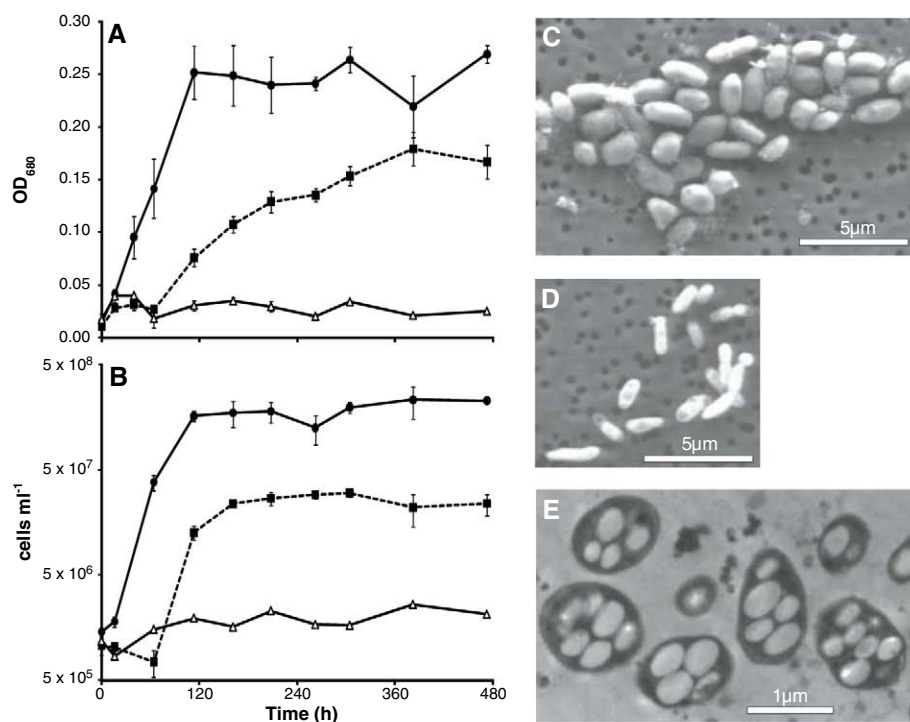


**Fig. 1.** Growth and electron microscopy of strain GFAJ-1. (A and B) Growth curves of GFAJ-1 grown on the defined synthetic medium amended with either 1.5 mM  $\text{PO}_4^{3-}$  (solid circles), 40 mM  $\text{AsO}_4^{3-}$  (solid squares), or neither  $\text{PO}_4^{3-}$  nor  $\text{AsO}_4^{3-}$  (open triangles). Cell growth was monitored both by an increase in (A) optical density and (B) cell numbers of the cultures. Symbols represent the mean  $\pm$  SD of (A)  $n = 6$  experimental and  $n = 2$  controls and (B)  $n = 3$  experimental and  $n = 1$  control. This was a single experiment with six replicates; however, material was conserved to extend the duration of the experiment to allow material for cell-counting samples. (C and D) Scanning electron micrographs of strain GFAJ-1 under two conditions, (C) +As/-P and (D) -As/+P. (E) Transmission electron micrograph of +As/-P GFAJ-1 showed internal vacuole-like structures. Scale bars are as indicated in the figure (11).

<sup>1</sup>NASA Astrobiology Institute, USA. <sup>2</sup>U.S. Geological Survey, Menlo Park, CA 94025, USA. <sup>3</sup>School of Earth and Space Exploration, Arizona State University, Tempe, AZ 85287, USA. <sup>4</sup>Lawrence Livermore National Laboratory, Livermore, CA 94551, USA. <sup>5</sup>Department of Biological Sciences, Duquesne University, Pittsburgh, PA 15282, USA. <sup>6</sup>Stanford Synchrotron Radiation Lightsource, Menlo Park, CA 94025, USA. <sup>7</sup>BEYOND: Center for Fundamental Concepts in Science, Arizona State University, Tempe, AZ 85287, USA. <sup>8</sup>Department of Chemistry and Biochemistry, Arizona State University, Tempe, AZ 85287, USA.

\*To whom correspondence should be addressed. E-mail: felisawolfesimon@gmail.com

(11). The background  $\text{PO}_4^{3-}$  in the medium was  $3.1 (\pm 0.3) \mu\text{M}$  on average, with or without added  $\text{AsO}_4^{3-}$ , coming from trace impurities in the major salts (table S1) (11). The sixth transfer of the 5 mM  $\text{AsO}_4^{3-}$  (no added  $\text{PO}_4^{3-}$ ) condition was closely monitored and demonstrated an approximate growth rate ( $\mu$ ) of  $0.1 \text{ day}^{-1}$ . After  $10^{-7}$  dilutions, we used the 5 mM  $\text{AsO}_4^{3-}$  enrichment to inoculate an agar plate that contained the same chemical composition as the artificial medium. An isolated colony was picked from the agar plates and reintroduced into an artificial liquid medium with no added  $\text{PO}_4^{3-}$ , where we then progressively increased the  $\text{AsO}_4^{3-}$  concentration to determine the optimal level for growth. Currently, this isolate—strain GFAJ-1 identified by 16S ribosomal RNA sequence phylogeny as a member of the Halomonadaceae family of Gammaproteobacteria (fig. S1) (11)—is maintained aerobically with 40 mM  $\text{AsO}_4^{3-}$ , 10 mM glucose, and no added  $\text{PO}_4^{3-}$  (+As/−P condition). Members of this family have been previously shown to accumulate intracellular As (12).

GFAJ-1 grew at an average  $\mu_{\text{max}}$  of  $0.53 \text{ day}^{-1}$  under +As/−P, increasing by over 20-fold in cell numbers after 6 days. It also grew faster and

more extensively with the addition of 1.5 mM  $\text{PO}_4^{3-}$  (−As/+P,  $\mu_{\text{max}}$  of  $0.86 \text{ day}^{-1}$ ) (Fig. 1, A and B). However, when neither  $\text{AsO}_4^{3-}$  nor  $\text{PO}_4^{3-}$  was added no growth was observed (Fig. 1, A and B). We include both optical density and direct cell counts to unambiguously demonstrate growth using two independent methods. Cells grown under +As/−P were oblong and approximately 2 by 1  $\mu\text{m}$  when imaged by means of scanning electron microscopy (Fig. 1C) (11). When grown under +As/−P conditions, GFAJ-1 cells had more than 1.5-fold greater intracellular volume ( $\approx 2.5 \pm 0.4 \mu\text{m}^3$ ) as compared with that of −As/+P ( $\approx 1.5 \pm 0.5 \mu\text{m}^3$ ) (Fig. 1D) (11). Transmission electron microscopy revealed large vacuole-like regions in +As/−P-grown cells that may account for this increase in size (Fig. 1E). These experiments demonstrated  $\text{AsO}_4^{3-}$ -dependent growth, morphological differences in GFAJ-1 driven by  $\text{AsO}_4^{3-}$  in the growth medium, and that the level of  $\text{PO}_4^{3-}$  impurities in the medium was insufficient to elicit growth in the control (−As/−P).

**Cellular stoichiometry and elemental distribution.** To determine whether GFAJ-1 was taking up  $\text{AsO}_4^{3-}$  from the medium, we measured the

intracellular As content by means of inductively coupled plasma mass spectrometry (ICP-MS) (11). In +As/−P-grown cells, the mean intracellular As was  $0.19 \pm 0.25\%$  by dry weight (Table 1), whereas the cells contained only  $0.019 \pm 0.009\%$  P by dry weight. This P was presumably scavenged from trace  $\text{PO}_4^{3-}$  impurities in the reagents and not likely due to carryover, given our enrichment and isolation strategy (11). Moreover, when grown +As/−P this intracellular P is 96.5% less than our measured P values for this microbe when grown −As/+P and far below the 1 to 3% P by dry weight required to support growth in a typical heterotrophic bacterium (13). In contrast, GFAJ-1 cells grown under −As/+P conditions had a mean P content of  $0.54 \pm 0.21\%$  by dry weight. There was variation in the total As content of the +As/−P cells, which is possibly a result of collection during stationary phase and losses during the repeated centrifugations and washing cycles because of the potential instability of the cellular structures given their swollen state (Fig. 2, C and E). In contrast, the integrity of the −As/+P cells appeared robust (Fig. 2D), and thus intracellular P measured for these cells probably reflects their content. However, the low total intracellular P in +As/−P cells was consistently far below the quantity needed to support growth, suggesting that these low values are correct despite variation in data from the +As/−P cells. Low intracellular P in concert with high intracellular As was further confirmed through high-resolution secondary ion mass spectrometry and x-ray analyses, as discussed below.

We used radiolabeled  $^{73}\text{AsO}_4^{3-}$  to obtain more specific information about the intracellular distribution of arsenic (11). We observed intracellular arsenic in protein, metabolite, lipid, and nucleic acid cellular fractions (Table 2). Stationary phase cells incorporated approximately  $1/10$  of the total intracellular  $^{73}\text{AsO}_4^{3-}$  label into nucleic acids but more than three quarters of the  $^{73}\text{AsO}_4^{3-}$  into the phenol extracted “protein” fraction, with a small fraction going into lipids. We caution that the large “protein” fraction is probably an overestimate because this extraction step likely contains numerous small, non-proteinaceous metabolites as well. To determine whether this distribution pattern reflected a use of  $\text{AsO}_4^{3-}$  in place of  $\text{PO}_4^{3-}$  in DNA, we estimated the average sequenced bacterial genome to be 3.8 megabase pairs (Mbp), which would contain approximately  $7.5 \times 10^6$  atoms or  $12.5 \times 10^{-18}$  moles of P. Assuming one complete genome per cell, this would equal 0.39 fg of P in the genome. Using ICP-MS, we measured about 9.0 fg P per cell in the −As/+P condition, which implies that only ~4% of total intracellular P is associated with the genome. Because these cells were harvested in stationary phase (11), the fraction of P associated with RNA is likely small (14). Hence, roughly 96% of P is presumably distributed between the “lipid” and “protein” fractions. If  $\text{AsO}_4^{3-}$  is substituting for  $\text{PO}_4^{3-}$  in DNA, then we can assume that roughly the same fraction of the total intracellular

**Table 1.** Bulk intracellular elemental profile of strain GFAJ-1. Cells were grown and prepared with trace metal clean techniques (11). Numbers in parentheses indicate replicate samples analyzed. As:P ratios were calculated based on all samples analyzed (11). Units are percent dry weight.

Condition	As	P	As:P
+As/−P (8)	$0.19 \pm 0.25$	$0.019 \pm 0.009$	7.3
−As/+P (4)	$0.001 \pm 0.0005$	$0.54 \pm 0.21$	0.002

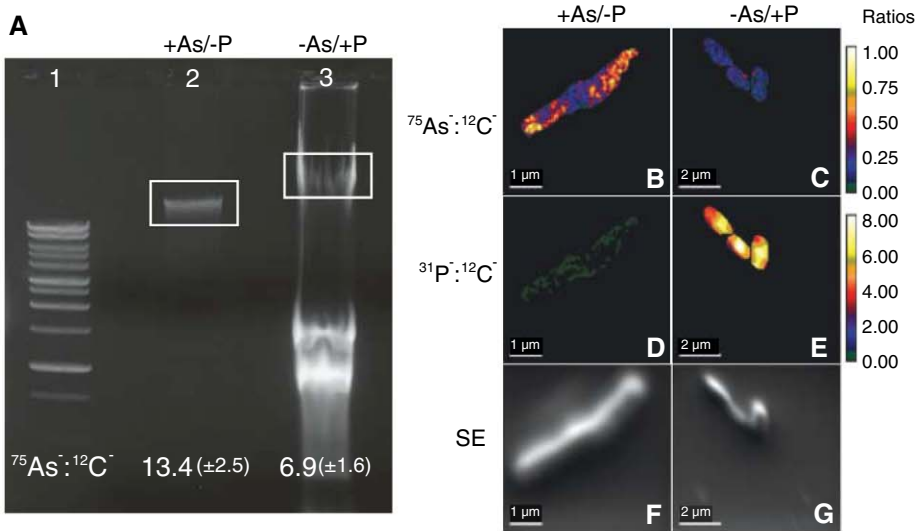


**Fig. 2.** NanoSIMS analyses of GFAJ-1: extracted DNA and whole-cells elemental ratio maps. (A) Agarose gel loaded with DNA/RNA extracted from GFAJ-1 grown (lane 2) +As/−P and (lane 3) −As/+P as compared with (lane 1) a DNA standard. Genomic bands were excised as indicated and analyzed with NanoSIMS. Ion ratios of  $^{75}\text{As}:^{12}\text{C}$  of excised gel bands are indicated below with  $2\sigma$  error shown (all values multiplied by  $10^{-6}$ ). (B to G) NanoSIMS images of whole GFAJ-1 cells grown either [(B), (D), and (F)] +As/−P or [(C), (E), and (G)] −As/+P. Shown are the ion ratios of [(B) and (C)]  $^{75}\text{As}:^{12}\text{C}$ , [(D) and (E)]  $^{31}\text{P}:^{12}\text{C}$ , and [(F) and (G)] secondary electron (SE). Ratios in (B) and (C) are multiplied by  $10^{-4}$  and in (D) and (E) are multiplied by  $10^{-3}$ . The color bars indicate measured elemental ratios on a log scale as indicated. Length scale is as indicated on images; images contain equivalent pixel density (11).



$\text{AsO}_4^{3-}$  would reflect a similar distribution to our estimated  $\text{PO}_4^{3-}$  distribution. The distribution of intracellular  $^{73}\text{AsO}_4^{3-}$  in our experiments was consistent with these estimates. If  $\text{AsO}_4^{3-}$  is fulfilling the biological role of  $\text{PO}_4^{3-}$ , then  $\text{AsO}_4^{3-}$  should act in many analogous biochemical roles, including DNA, protein phosphorylation, small molecular weight metabolites [such as arsenylated analogs of the reduced form of nicotinamide adenine dinucleotide (NADH), adenosine triphosphate (ATP), and intermediates like glucose and acetyl-coenzyme A (acetyl-CoA)], and phospholipids.

Our data suggested that As was present in a number of biomolecules, and in particular we sought to confirm the presence of As in the DNA fraction. Initially, we measured traces of As with ICP-MS analysis of extracted nucleic acid and

protein/metabolite fractions from +As/-P-grown cells (table S1) (11). We then used high-resolution secondary ion mass spectrometry (NanoSIMS) to identify As in extracted, gel-isolated genomic DNA (Fig. 2A). These data showed that DNA from +As/-P cells had elevated As and low P relative to DNA from the -As/+P cells. NanoSIMS analysis of the DNA showed that the As:P ratio on an atom-per-atom basis was significantly higher in the +As/-P versus -As/+P grown cells ( $P = 0.02$ ) (Fig. 2A and table S2) (11). Whether expressed as an ion ratio relative to C ( $^{75}\text{As}^-:^{12}\text{C}^-$ ), (Fig. 2A) or  $^{31}\text{P}^-:^{12}\text{C}^-$  (table S2) (11), or normalized by relative ion yield and expressed as a concentration in parts per billion (table S2) (11), we saw a similarly consistent trend, with significantly higher As in the +As/-P DNA ( $P = 0.03$ ) and higher P in the -As/+P DNA ( $P = 0.0003$ ). In

both cases, the nonamended element concentration was equal or less than background levels. These measurements therefore specifically demonstrated that the purified DNA extracted from +As/-P cells contained As. Our NanoSIMS analyses, combined with the evidence for intracellular arsenic by ICP-MS and our radiolabeled  $^{73}\text{AsO}_4^{3-}$  experiments, indicated that intracellular  $\text{AsO}_4^{3-}$  was incorporated into key biomolecules, specifically DNA.

**Characterization of the intracellular arsenic chemical environment.** We next used synchrotron x-ray studies to determine the speciation and chemical environment of the intracellular arsenic (11). Micro-x-ray absorption near-edge spectroscopy ( $\mu\text{XANES}$ ) of +As/-P-grown cells exhibited an absorption edge characteristic of As(V) coordination with no evidence of As(III) observed. Best fits of the micro-extended x-ray absorption fine structure ( $\mu\text{EXAFS}$ ) spectra are listed in Table 3 and shown in Fig. 3. The first neighbor shell around the arsenic in +As/-P cells consisted of four oxygen ligands (Table 3) but had a second shell that is inconsistent with our As-Fe and As-S models, free  $\text{AsO}_4^{3-}$  ions, or published spectra for organo-arsenicals (Fig. 3A) (15, 16). Although other arsenical compounds such as dimethylarsinate (DMA) also have As-O and As-C bonds, they have edge positions that are shifted to lower energy from the observed As(V) and have much shorter observed As-C bond distances (16). In contrast to the models, these As-O and As-C distances are consistent with that reported from the solved crystal structure of DNA for the analogous structural position of P relative to O and C atoms (Fig. 3A) (16, 17). Therefore, our x-ray data support the position of  $\text{AsO}_4^{3-}$  in a similar configuration to  $\text{PO}_4^{3-}$  in a DNA backbone or potentially other biomolecules as well. These data are also consistent with the presence of  $\text{AsO}_4^{3-}$  in small-molecular-weight metabolites (for example, arsenylated analogs of NADH, ATP, glucose, and acetyl-CoA) as well as arsenylated proteins in which  $\text{AsO}_4^{3-}$  would substitute for  $\text{PO}_4^{3-}$  at serine, tyrosine, and threonine residues (table S3) (1, 11). Micro-x-ray fluorescence data ( $\mu\text{XRF}$ ) further confirmed our ICP-MS measurements and showed low background P, which contrasted with regions of high arsenic correlated with high iron and zinc (Fig. 3B and fig. S2) (11). These latter two elements are routinely used as proxies for the presence of cellular material (such as C, N, and O) in our experiments because these light elements could not be detected with x-ray fluorescence under our non-vacuum conditions. However, to further support the distribution of arsenic with cellular material we used NanoSIMS to map cellular ion ratios of  $^{75}\text{As}^-:^{12}\text{C}^-$  and  $^{31}\text{P}^-:^{12}\text{C}^-$  (Fig. 2, B to G, and fig. S2) (11). These analyses confirmed, at a much finer resolution, that for the +As/-P condition the cells contain As with a low background of P (Fig. 2, B, D, and F). This is in contrast to the low As and higher P in -As/+P-grown cells (Fig. 2, C, E, and G). Because the x-ray absorption data

**Table 2.** Intracellular radiolabeled  $^{73}\text{AsO}_4^{3-}$  arsenate distribution. All major cellular subfractions contained radiolabel after cell-washing procedures. Small molecular weight (s.m.w.) metabolites potentially include arsenylated analogs of ATP, NADH, acetyl-CoA, and others (11). SE is shown.

Solvent (subcellular fraction)	Cellular radiolabel recovered (percent of total)
Phenol (protein + s.m.w. metabolites)	$80.3 \pm 1.7$
Phenol:Chloroform (proteins + lipids)	$5.1 \pm 4.1$
Chloroform (lipids)	$1.5 \pm 0.8$
Final aqueous fraction (DNA/RNA)	$11.0 \pm 0.1$

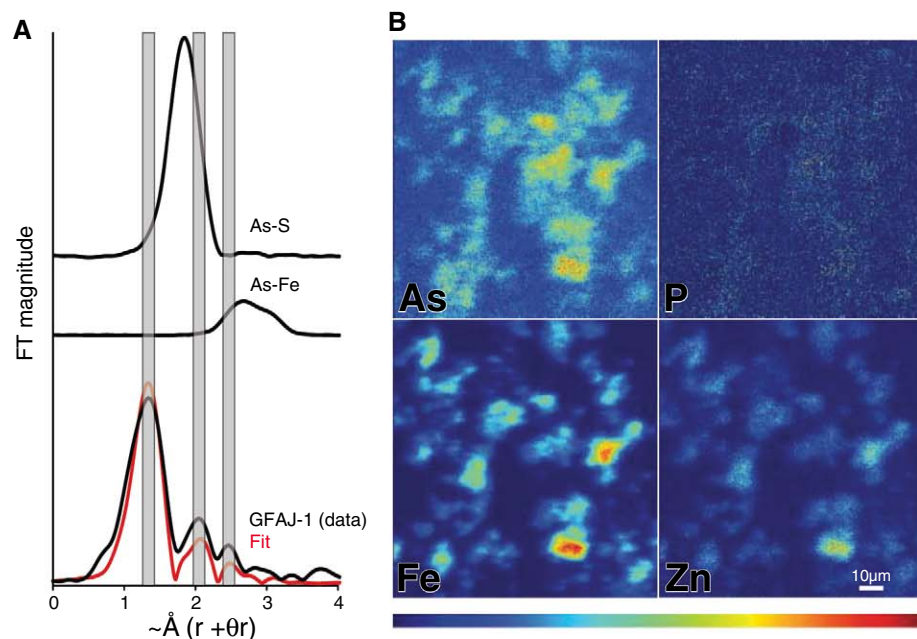


**Fig. 3.** X-ray analysis of GFAJ-1 +As/-P described similarity of As coordinated like P in DNA. (A) EXAFS comparisons of the Fourier transformed data for As in model environments and GFAJ-1 (washed and fixed, collected on whole cells). Identification of each spectrum is indicated on the figure and from top to bottom are As-S, As-Fe, and GFAJ-1 data (collected on whole cells) and fit to the GFAJ-1 data (red line). (B) XRF maps indicated the correlation between As, iron (Fe) and zinc (Zn) and not with P with some variability but consistent with the trend that these elements are often found together (fig. S3, element correlation plots). The scale bar in the Zn quadrant of the maps is as designated and applies to all parts of the figure. Given the spatial resolution of these images, the structures identified as containing high As, Fe, and Zn are aggregates of cells. Ranges as indicated in the color bar run from cold to hot, in units of  $\mu\text{g cm}^{-2}$ , as follows: As, 0 to 1.6; P, 0 to 40; Fe, 0 to 32.1; and Zn, 0 to 2.8. Standards were used to calibrate signal and background (11).

**Table 3.** Results of fitting arsenic K-edge EXAFS of GFAJ-1.  $S_0 = 1$ , global amplitude factor and  $E_0 = 13.97$ , offset for calibration. Type, the coordination type; Number, the coordination number;  $R$ , interatomic distance; and  $\sigma^2$ , the measure of the static disorder of the shell. See table S2 for comparison to P in P-containing biomolecules (11).

Type	Number	$R$	$\sigma^2$
As-O	4.2 (0.6)	1.73 (2)	0.003 (2)
As-C	2.5 (0.5)	2.35 (4)	0.003 (2)
As-C	2.2 (0.5)	2.92 (6)	0.003 (2)

provided information about the average coordination of arsenic, our data identified a mixture of compounds in the cells. These results indicated that these compounds are dominated by arsenic(V)-oxygen-carbon-coordinated structures, and thus the bonding environment we described is consistent with our NanoSIMS data (Fig. 2A) and can be attributed to DNA. These data show that As is in the +5 redox state and bound to O and distal C atoms within acceptable covalent bond lengths, identifying  $\text{AsO}_4^{3-}$  assimilated into biomolecules within the cells in specifically relevant coordination.

Our data show arsenic-dependent growth by GFAJ-1 (Fig. 1). Growth was accompanied by  $\text{AsO}_4^{3-}$  uptake and assimilation into biomolecules including nucleic acids, proteins, and metabolites (Figs. 2 and 3 and Tables 1 and 2). In some organisms, arsenic induces specific resistance genes to cope with its toxicity (7), whereas some dissimilatory arsenic-utilizing microbes can conserve energy for growth from the oxidation of reduced arsenic species, or “breathe”  $\text{AsO}_4^{3-}$ , as a terminal electron acceptor (18). Our study differs because we used As as a selective agent and excluded P, a major requirement in all hitherto known organisms. However, GFAJ-1 is not an obligate arsenophile and grew considerably better when provided with P (Fig. 1, A and B). Although  $\text{AsO}_4^{3-}$  esters are predicted to be orders of magnitude less stable than  $\text{PO}_4^{3-}$  esters, at least for simple molecules (8), GFAJ-1 can cope with this instability. The vacuole-like regions observed in GFAJ-1 cells when growing under +As/-P conditions are potentially poly- $\beta$ -hydroxybutyrate rich [as shown in other *Halomonas* species (19)], which may

stabilize As(V)-O-C type structures because non-aqueous environments appear to promote slower hydrolysis rates for related compounds (8). We propose that intracellular regions or mechanisms that exclude water may also promote this stability.

We report the discovery of an unusual microbe, strain GFAJ-1, that exceptionally can vary the elemental composition of its basic biomolecules by substituting As for P. How As insinuates itself into the structure of biomolecules is unclear, and the mechanisms by which such molecules operate are unknown.

#### References and Notes

1. J. Berg, J. Tymoczko, L. Stryer, *Biochemistry* (W. H. Freeman & Co., New York, ed. 6, 2007).
2. R. Hille, *Trends Biochem. Sci.* **27**, 360 (2002).
3. T. W. Lane, F. M. Morel, *Proc. Natl. Acad. Sci. U.S.A.* **97**, 4627 (2000).
4. G. Jameson, J. Ibers, in *Biological Inorganic Chemistry: Structure and Reactivity*, I. Bertini, H. Gray, I. Stiefel, J. Valentine, Eds. (University Science Books, Sausalito, CA, 2007), pp. 354–386.
5. D. Lide, Ed., *CRC Handbook of Chemistry and Physics, 90th Edition (Internet Version 2010)* (CRC Press/Taylor & Francis, Boca Raton, FL, 2010).
6. F. Wolfe-Simon, P. C. W. Davies, A. D. Anbar, *Int. J. Astrobiol.* **8**, 69 (2009).
7. B. P. Rosen, *FEBS Lett.* **529**, 86 (2002).
8. C. D. Baer, J. O. Edwards, P. H. Rieger, *Inorg. Chem.* **20**, 905 (1981).
9. R. S. Oremland, J. F. Stolz, J. T. Hollibaugh, *FEMS Microbiol. Ecol.* **48**, 15 (2004).
10. J. Switzer Blum, A. Burns Bindi, J. Buzzelli, J. F. Stolz, R. S. Oremland, *Arch. Microbiol.* **171**, 19 (1998).
11. Materials and methods are available as supporting material on Science Online.
12. M. Takeuchi et al., *J. Biotechnol.* **127**, 434 (2007).
13. W. Makino, J. Cotner, R. Sterner, J. Elser, *Funct. Ecol.* **17**, 121 (2003).

14. J. Mandelstam, *Bacteriol. Rev.* **24**, 289 (1960).
15. P. G. Smith et al., *Environ. Sci. Technol.* **39**, 248 (2005).
16. I. J. Pickering et al., *Plant Physiol.* **122**, 1171 (2000).
17. S. Holbrook, R. Dickerson, S. H. Kim, *Acta Crystallogr. B* **41**, 255 (1985).
18. R. S. Oremland, J. F. Stolz, *Science* **300**, 939 (2003).
19. J. Quillaguan, O. Delgado, B. Mattiasson, R. Hatti-Kaul, *Enzyme Microb. Technol.* **38**, 148 (2006).

**Acknowledgments:** The authors thank S. Benner, W. Hastings, I. L. ten Kate, A. Pohorille, B. Rosen, D. Schulze-Makuch, and R. Shapiro for stimulating discussions. We thank G. King, A. Oren, and L. Young for constructive criticisms of earlier drafts of this manuscript and S. Baesman, M. Dudash, and L. Miller for technical assistance. Cultures of GFAJ-1 were submitted to the American Type Culture Collection and Deutsche Sammlung von Mikroorganismen und Zellkulturen (DSMZ) culture collections on 21 March 2011 and will be available from these sources within several months. Until then, samples of GFAJ-1 are available to the community from the Oremland lab upon completion of a materials transfer agreement, which is required by the U.S. Geological Survey for the transfer of bacterial cultures. Sequence data are deposited with GenBank (accession HQ449183). Portions of this research were carried out at the Stanford Synchrotron Radiation Lightsource (SSRL), a division of SLAC National Accelerator Laboratory and an Office of Science User Facility operated for the U.S. Department of Energy (DOE) Office of Science by Stanford University. The SSRL Structural Molecular Biology Program is supported by the DOE Office of Basic Energy Sciences, Office of Biological and Environmental Research, and by the National Institutes of Health, National Center for Research Resources, Biomedical Technology Program. NanoSIMS analyses were performed under the auspices of the DOE at Lawrence Livermore National Laboratory under contract DE-AC52-07NA27344. J.P.R. and P.K.W. were supported in part by the DOE OBER Genomic Sciences program SCW1039. R.S.O. and J.F.S. were supported by NASA Exobiology. F.W.S. acknowledges support from the NASA Postdoctoral Program, NASA Astrobiology/Exobiology, and the NASA Astrobiology Institute while in residence at the U.S. Geological Survey, Menlo Park, CA. The authors declare no conflicts of interest.

#### Supporting Online Material

www.sciencemag.org/cgi/content/full/science.1197258/DC1  
Materials and Methods

Figs. S1 to S3  
Tables S1 to S4  
References

1 September 2010; accepted 8 November 2010  
Published online 2 December 2010;  
10.1126/science.1197258

# Polariton Superfluids Reveal Quantum Hydrodynamic Solitons

A. Amo,<sup>1,2\*</sup> S. Pigeon,<sup>3</sup> D. Sanvitto,<sup>4</sup> V. G. Sala,<sup>1</sup> R. Hivet,<sup>1</sup> I. Carusotto,<sup>5</sup> F. Pisanello,<sup>1,4,6</sup> G. Leménager,<sup>1</sup> R. Houdré,<sup>7</sup> E. Giacobino,<sup>1</sup> C. Ciuti,<sup>3</sup> A. Bramati<sup>1\*</sup>

A quantum fluid passing an obstacle behaves differently from a classical one. When the flow is slow enough, the quantum gas enters a superfluid regime, and neither whirlpools nor waves form around the obstacle. For higher flow velocities, it has been predicted that the perturbation induced by the defect gives rise to the turbulent emission of quantized vortices and to the nucleation of solitons. Using an interacting Bose gas of exciton-polaritons in a semiconductor microcavity, we report the transition from superfluidity to the hydrodynamic formation of oblique dark solitons and vortex streets in the wake of a potential barrier. The direct observation of these topological excitations provides key information on the mechanisms of superflow and shows the potential of polariton condensates for quantum turbulence studies.

Superfluidity is the remarkable property of flow without friction (1). It is characterized by the absence of excitations when the fluid hits a localized static obstacle at flow speeds  $v_{\text{flow}}$  below some critical velocity  $v_c$ . For small potential barriers, the critical velocity is given by the Landau criterion as the minimum of  $\omega(k)/k$ , with  $\omega(k)$  being the dispersion of elementary excitations in the fluid. In the case of dilute Bose-Einstein condensates (BECs),  $v_c$  corresponds to  $c_s$ , the speed of sound of the quantum gas. For supersonic flows ( $v_{\text{flow}} > c_s$ ), small obstacles induce dissipation (drag) via the emission of sound waves (2, 3).

When the barrier is big, larger than the fluid's healing length—the minimum distance induced by particle interactions for changes in the density of the condensate—the density modulations caused by the barrier can generate topological excitations, such as vortices and solitons. These quantum hydrodynamic effects have been predicted to reduce the critical velocity (4, 5).

Despite the amount of theoretical work (4–6), few experimental studies have addressed hydrodynamic features in atomic condensates through the observation of the break-up of superfluidity at fluid velocities lower than the speed of sound (7, 8). Solitons in a quasi-one-dimensional (1D)

geometry (9) and the nucleation of vortex pairs in an oblate BEC have been reported (10, 11). Far from the hydrodynamic regime, formation of vortices and solitons has been shown by engineering the density and phase profile of the atomic condensate (12, 13), or by the collision of two condensates (14).

Polariton superfluids appear promising in view of quantitative studies of quantum hydrodynamics. Polaritons are 2D composite bosons arising from the strong coupling between quantum well excitons and photons confined in a monolithic semiconductor microcavity. They possess an extremely small mass  $m_{\text{pol}}$  on the order of  $10^{-8}$  that of hydrogen, which allows for their Bose-Einstein condensation at temperatures ranging from a few kelvins (15) up to room temperature (16). All parameters of the system, such as the flow velocity, density, and shape and strength of the potential barriers, can be finely tuned with the use of just one (3) or two (17) resonant lasers, and by sample (18) or light-induced engineering (19). A crucial advantage with respect to atomic condensates is the possibility of fully reconstructing both the density and the phase pattern of the polariton condensate from the properties of the emitted light (20). This has been exploited in the recent observations of macroscopic coherence and long-range order (15, 18, 21), quantized vortices (20), superfluid flow past an obstacle (3, 17, 22), and persistent superfluid currents (23).

Here we use a polariton condensate to reveal quantum hydrodynamic features, whereby dark solitons and vortices are generated in the wake of a potential barrier. Following a recent theoretical proposal (24), we investigate different regimes at different flow speeds and densities, ranging from superfluidity to the turbulent emission of trains of vortices, and the formation of pairs of oblique dark solitons of high stability. For spatially large enough barriers, soliton quadruplets are also observed.

Our experiments are performed in an InGaAs-GaAs-AlGaAs microcavity at 10 K (25). We ex-

cite the system with a continuous-wave (cw) single-mode laser quasi-resonant with the lower polariton branch at an angle of incidence  $\theta$ , resulting in the injection of a polariton fluid with a well-defined in-plane wave vector (3) ( $k = k_0 \sin \theta$ , where  $k_0$  is the wave vector of the excitation laser field) and velocity  $v_{\text{flow}} = \hbar k / m_{\text{pol}}$ . The speed of sound of the fluid  $c_s$  is related to the polariton density  $|\psi|^2$  via the relation (22)  $c_s =$

$\sqrt{\hbar g |\psi|^2 / m_{\text{pol}}}$ , where  $g$  is the polariton-polariton interaction constant.

Figure 1A shows the image of a polariton fluid with  $k = 0.73 \mu\text{m}^{-1}$  and  $v_{\text{flow}} = 1.7 \mu\text{m/ps}$ , created with a Gaussian excitation spot  $30 \mu\text{m}$  in diameter. The resonant pump is centered slightly upstream from a photonic defect of  $4.5 \mu\text{m}$  present in the microcavity, in order not to lock the phase of the flowing condensate past the defect. Two oblique dark solitons with a width of  $3$  to  $5 \mu\text{m}$  (Fig. 1B) are spontaneously generated in the wake of the barrier created by the defect and propagate within the polariton fluid in a straight line.

An unambiguous characteristic of solitons in BECs is the phase jump across the soliton (12, 13, 26). To reveal the phase variations in the polariton quantum fluid, we make the emission from the condensate interfere with a reference beam of homogeneous phase, with a given angle between the two beams (20). The result (Fig. 1C) shows a phase jump of up to  $\pi$  (half an interference period) as a discontinuity in the interference maxima along the soliton.

The 1D soliton relationships obtained from the solution of the Gross-Pitaevskii equation (13, 26) can be extended to two dimensions to relate the soliton velocity  $v_s$  in the reference frame of the fluid, the phase jump  $\delta$ , and depth  $n_s$  with respect to the polariton density  $n$  away from the soliton:

$$\cos\left(\frac{\delta}{2}\right) = \left(1 - \frac{n_s}{n}\right)^{1/2} = \frac{v_s}{c_s} \quad (1)$$

In our geometry, a soliton standing in a straight line in the laboratory frame implies a constant  $v_s = v_{\text{flow}} \sin \alpha$ , where  $\alpha$  is defined in Fig. 1A. As the soliton becomes darker ( $n_s$  approaching  $n$ ), the phase jump saturates at  $\delta = \pi$ . Indeed, the solitons remain quite deep up to the first  $40 \mu\text{m}$  of trajectory (Fig. 1, B and D), with a corresponding phase jump close to, but smaller than,  $\pi$ . At longer distances, the depth decreases along with the phase jump. Open triangles in Fig. 1D show the ratio  $n_s/n$  as obtained from the measured phase jump and Eq. 1. This confirms that the soliton relationships, which were derived for condensates without dissipation (26), are applicable locally to the case of polaritons under cw pumping, where the polariton density is stationary in time. The polariton density continuously decreases downstream from the barrier due to the finite polariton

<sup>1</sup>Laboratoire Kastler Brossel, Université Pierre et Marie Curie-Paris 6, École Normale Supérieure et CNRS, UPMC Case 74, 4 place Jussieu, 75005 Paris, France. <sup>2</sup>CNRS-Laboratoire de Photonique et Nanostructures, Route de Nozay, 91460 Marcoussis, France. <sup>3</sup>Laboratoire Matériaux et Phénomènes Quantiques, UMR 7162, Université Paris Diderot-Paris 7 et CNRS, 75013 Paris, France. <sup>4</sup>NNL, Istituto Nanoscienze-CNR, Via Arnesano, 73100 Lecce, Italy. <sup>5</sup>INO-CNR BEC Center and Dipartimento di Fisica, Università di Trento, via Sommarive 14, I-38123 Povo, Italy. <sup>6</sup>Scuola Superiore ISUI, Università del Salento, Via Arnesano, 73100 Lecce, Italy. <sup>7</sup>Institut de Physique de la Matière Condensée, Faculté des Sciences de Base, bâtiment de Physique, Station 3, EPFL, CH-1015 Lausanne, Switzerland.

\*To whom correspondence should be addressed. E-mail: alberto.amo@ipn.cnrs.fr (A.A.); bramati@spectro.jussieu.fr (A.B.)



lifetime. This results in a decrease in the speed of sound (from  $c_s = 3.5 \pm 1 \mu\text{m/ps}$  at  $\Delta y = 14 \mu\text{m}$ , to  $c_s = 1.2 \pm 0.5 \mu\text{m/ps}$  at  $\Delta y = 50 \mu\text{m}$  [see (25) for the estimation of  $c_s$ ], which compensates the expected acceleration of the soliton when it becomes less deep (smaller  $n_s/n$  in Eq. 1). Consequently, the solitons present an almost rectilinear shape.

Simulations based on the Gross-Pitaevskii equation, with pumping and decay (25) according to the model described in (24) for the experimental parameters of Fig. 1, show the nucleation of a pair of solitons (Fig. 2A) with its associated phase jump (Fig. 2B). The model confirms that dark solitons nucleate hydrodynamically due to the gradient of flow speeds occurring around the potential barrier, which result in density variations on the order of the healing length. Once the soliton is formed, the repulsive interparticle interactions stabilize its shape as it propagates (6, 27–29). By contrast, no stable soliton was observed at low excitation density when polariton-polariton interactions are negligible (see fig. S3).

Other hydrodynamic regimes can be explored by varying the mean polariton density (i.e., the speed of sound) for a fixed flow speed (Fig. 3). Here, polaritons move slower than in Fig. 1 ( $v_{\text{flow}} = 0.79 \mu\text{m/ps}$ ,  $k = 0.34 \mu\text{m}^{-1}$ ), and due to their limited lifetime, they cannot propagate far away from the excitation spot. Hence, we have designed an excitation spot with the shape of half a Gaussian, with an abrupt intensity cut-off (fig. S1). Below the red line in Fig. 3, A to C, only polaritons propagating away from the pumped area are present, and their phase is not imposed by the resonant pump beam.

Figure 3A shows the polariton flow at subsonic speeds ( $v_{\text{flow}} = 0.25\bar{c}_s$ , where the bar indicates the mean speed of sound), at high excitation density. The condensate is in the superfluid regime, as evidenced by the absence of density modulations in the fluid hitting the barrier and from the homogeneous phase (Fig. 3D), showing a high value of the zero time first-order coherence (25),  $g^{(1)}$  (Fig. 3G). When the excitation density and, correspondingly, the sound speed is decreased to  $v_{\text{flow}} = 0.4\bar{c}_s$  (Fig. 3B), the fluid enters into a regime of turbulence characterized by the appearance of two low-density channels in the wake created by the barrier, with extended phase dislocations (Fig. 3E). We interpret this regime as corresponding to the continuous emission of pairs of quantized vortices and antivortices moving through those channels (4–6, 24). Although a direct observation of the phase singularity of the emitted vortices is not possible under time-integrated cw experiments, the effects of the vortex flow are clearly seen when looking at  $g^{(1)}$ . Figure 3H shows a trace of low degree of coherence along each channel, due to the continuous passage of individual vortices. Finally, if the density is further decreased, we observe the formation of oblique dark solitons (Fig. 3C;  $v_{\text{flow}} = 0.6\bar{c}_s$ ), with the characteristic phase jump along their trajectory (Fig. 3F), and a constant value of  $g^{(1)}$  close to 1 (Fig. 3I).

The three regimes depicted in Fig. 3 have been anticipated by the nonequilibrium Gross-Pitaevskii model (24). We report a break-up of

the superfluid regime at  $v_{\text{flow}} \sim 0.4\bar{c}_s$ , a value consistent with predictions for the onset of drag in the presence of large circular barriers (4, 5). Our

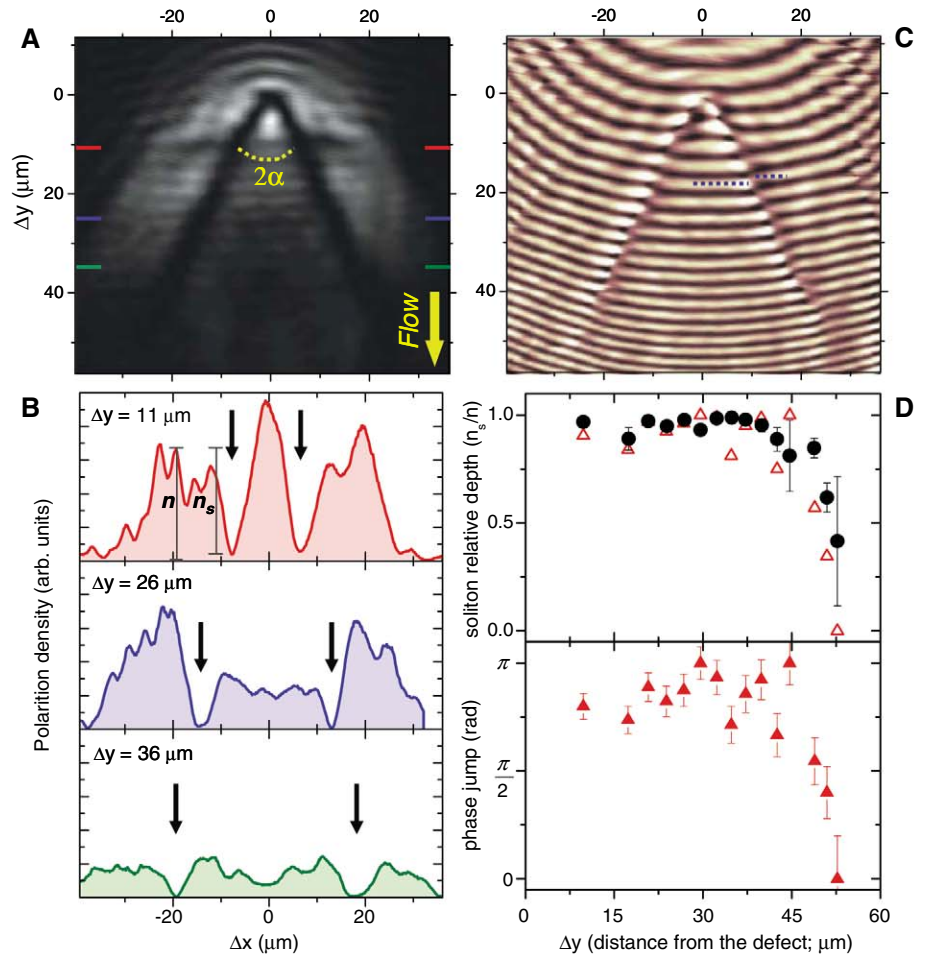


**Fig. 1. (A)** Real-space emission showing a soliton doublet nucleated in the wake of a photonic defect located at the origin. **(B)** Horizontal profiles at different downflow distances from the defect  $\Delta y$ . Arrows indicate the soliton position. **(C)** Interference between the emitted intensity and a constant-phase reference beam, showing phase jumps along the solitons (dashed lines). The curved shaped of the fringes and the decreasing interfringe distance arise from the geometry of the reference beam. **(D)** Soliton depth (black circles) and phase jump obtained from (C) (filled triangles; see fig. S4), showing a strong correlation. Open triangles: soliton depth obtained from the measured phase jump and Eq. 1.

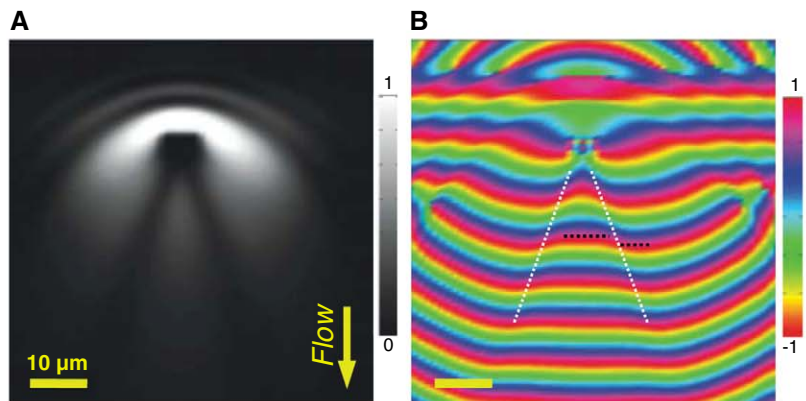


**Fig. 2. (A)** Real-space emission obtained from the solution of the nonequilibrium Gross-Pitaevskii equation for the parameters of the experiment depicted in Fig. 1. **(B)** Normalized real part of the polariton wave function, showing a phase jump (dark dashed lines) along the solitons (white dotted lines).

observations show that solitons in the polariton fluid can be stable down to subsonic speeds. This is in contrast to calculations for atomic condensates, in which oblique dark solitons are predicted

to be stable only at supersonic speeds (6, 27). Because our nonequilibrium simulations (Fig. 2) reproduce the observed nucleation at subsonic speeds, we infer that the additional damping in

the polariton system arising from the finite lifetime is responsible for the stabilization of the soliton at subsonic speeds.

Finally, we have explored the possibility of going beyond the generation of soliton doublets by using a large circular potential barrier (6). Figure 4A shows a polariton flow at low momentum ( $k = 0.2 \mu\text{m}^{-1}$ ) injected in a Gaussian spot slightly above the obstacle, which nucleates a soliton doublet. If the momentum of the flow is increased above a certain value, the strong density mismatch before and after the defect can generate a soliton quadruplet (Fig. 4B,  $k = 1.1 \mu\text{m}^{-1}$ ). In principle, it should be possible to access even higher-order solitons by increasing both the obstacle size and the ratio  $v_{\text{flow}}/c_s$ .

Our results demonstrate the potential of polariton superfluids for experimental studies of quantum hydrodynamics. Both the velocity and the density of the quantum fluid can be finely controlled by optical means, and simultaneous access to the condensate density, phase, and coherence is available from the emitted light. These features have been essential in the reported observation of hydrodynamic generation of oblique solitons in the wake of potential barriers, and offer the opportunity to probe more complex phenomena like Andreev reflections (30), nucleation and trapping of vortex lattices (24), and quantum turbulence (31).

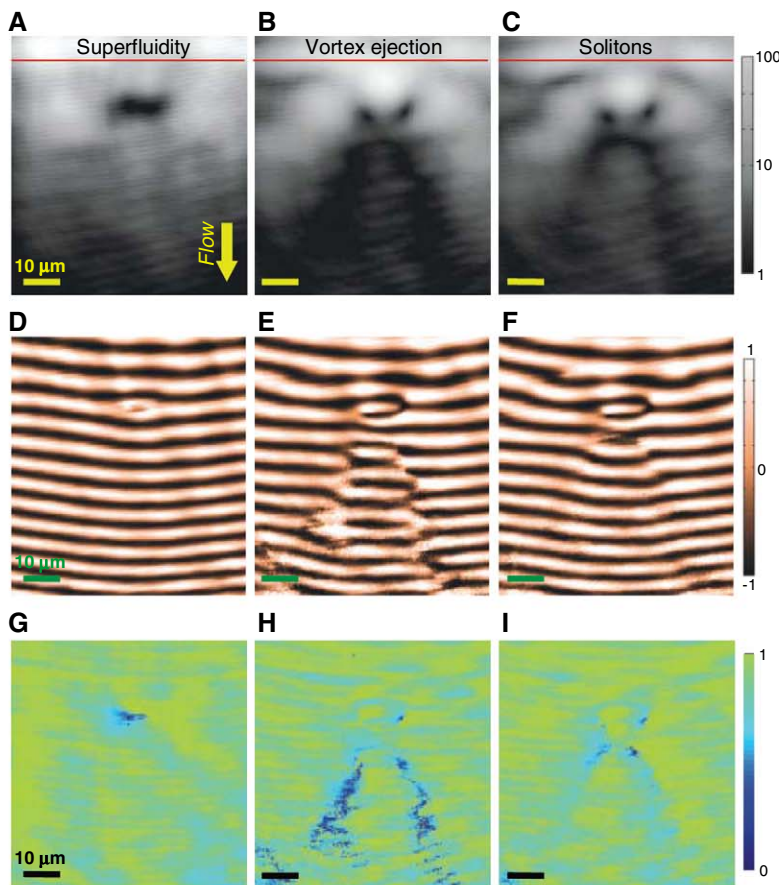


**Fig. 3.** (A to C) Real-space images of the polariton gas flowing downward at different excitation densities in the presence of a double defect (total width:  $15 \mu\text{m}$ ). The gas is injected above the red line (25). At high density (A) (117 mW), the fluid is subsonic ( $v_{\text{flow}} = 0.25c_s$ ) and flows in a superfluid fashion around the defect. At lower densities (B) (36 mW;  $v_{\text{flow}} = 0.4c_s$ ), a turbulent pattern appears in the wake of the defect, eventually giving rise to the formation of two oblique dark solitons (C) ( $v_{\text{flow}} = 0.6c_s$ ; 27 mW). (D to F) Interferograms corresponding to (A) to (C), respectively. (G to I) show the corresponding degree of first-order coherence [ $g^{(1)}$ , see (25)]. Saturated values of  $g^{(1)}$  are due to the uncertainty in the measurements.

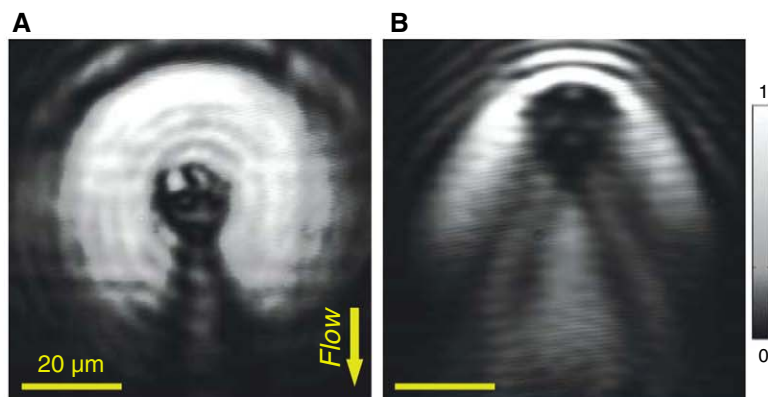


**Fig. 4.** Real-space images of the polariton flow around a large defect ( $17 \mu\text{m}$  in diameter) at low (A) ( $k = 0.2 \mu\text{m}^{-1}$ ) and high (B) ( $k = 1.1 \mu\text{m}^{-1}$ ) injected wave vectors showing, respectively, the formation of a soliton doublet and quadruplet.

## References and Notes

1. A. J. Leggett, *Rev. Mod. Phys.* **71**, 5318 (1999).
2. I. Carusotto, S. X. Hu, L. A. Collins, A. Smerzi, *Phys. Rev. Lett.* **97**, 260403 (2006).
3. A. Amo *et al.*, *Nat. Phys.* **5**, 805 (2009).
4. T. Frisch, Y. Pomeau, S. Rica, *Phys. Rev. Lett.* **69**, 1644 (1992).
5. T. Winiński, B. Jackson, J. F. McCann, C. S. Adams, *J. Phys. At. Mol. Opt. Phys.* **33**, 4069 (2000).
6. G. A. El, A. Gammal, A. M. Kamchatnov, *Phys. Rev. Lett.* **97**, 180405 (2006).
7. C. Raman *et al.*, *Phys. Rev. Lett.* **83**, 2502 (1999).
8. R. Onofrio *et al.*, *Phys. Rev. Lett.* **85**, 2228 (2000).
9. P. Engels, C. Atherton, *Phys. Rev. Lett.* **99**, 160405 (2007).
10. S. Inouye *et al.*, *Phys. Rev. Lett.* **87**, 080402 (2001).
11. T. W. Neely, E. C. Samson, A. S. Bradley, M. J. Davis, B. P. Anderson, *Phys. Rev. Lett.* **104**, 160401 (2010).
12. S. Burger, K. Bongs, S. Dettmer, W. Ertmer, K. Sengstock, *Phys. Rev. Lett.* **83**, 5198 (1999).
13. J. Denschlag *et al.*, *Science* **287**, 97 (2000).
14. J. J. Chang, P. Engels, M. A. Hofer, *Phys. Rev. Lett.* **101**, 170404 (2008).
15. J. Kasprzak *et al.*, *Nature* **443**, 409 (2006).
16. S. Christopoulos *et al.*, *Phys. Rev. Lett.* **98**, 126405 (2007).
17. A. Amo *et al.*, *Nature* **457**, 291 (2009).
18. E. Wertz *et al.*, *Nat. Phys.* **6**, 860 (2010).
19. A. Amo *et al.*, *Phys. Rev. B* **82**, 081301 (2010).
20. K. G. Lagoudakis *et al.*, *Nat. Phys.* **4**, 706 (2008).
21. C. W. Lai *et al.*, *Nature* **450**, 529 (2007).
22. I. Carusotto, C. Ciuti, *Phys. Rev. Lett.* **93**, 166401 (2004).
23. D. Sanvitto *et al.*, *Nat. Phys.* **6**, 527 (2010).
24. S. Pigeon, I. Carusotto, C. Ciuti, *Phys. Rev. B* **83**, 144513 (2011).
25. Materials and methods are available on Science Online.
26. A. D. Jackson, G. M. Kavoulakis, C. J. Pethick, *Phys. Rev. A* **58**, 2417 (1998).
27. A. M. Kamchatnov, L. P. Pitaevskii, *Phys. Rev. Lett.* **100**, 160402 (2008).
28. A. V. Yulin, O. A. Egorov, F. Lederer, D. V. Skryabin, *Phys. Rev. A* **78**, 061801 (2008).



29. Y. Larionova, W. Stolz, C. O. Weiss, *Opt. Lett.* **33**, 321 (2008).
30. A. J. Daley, P. Zoller, B. Trauzettel, *Phys. Rev. Lett.* **100**, 110404 (2008).
31. N. G. Berloff, Turbulence in exciton-polariton condensates. Preprint available at <http://arxiv.org/abs/1010.5225> (2010).

**Acknowledgments:** We thank S. Barbay, J. Bloch, R. Kuszelewicz, W. D. Phillips, L. P. Pitaevskii, and M. Wouters for useful discussions, and L. Martiradonna for the confocal masks. This work was supported by the IFRAF, CLERMONT4, and the Agence Nationale de la Recherche. A.B. and C.C. are members of the Institut Universitaire de France.

**Supporting Online Material**  
[www.sciencemag.org/cgi/content/full/332/6034/1167/DC1](http://www.sciencemag.org/cgi/content/full/332/6034/1167/DC1)  
Materials and Methods  
Figs. S1 to S4

28 December 2010; accepted 11 April 2011  
10.1126/science.1202307

# Observing the Average Trajectories of Single Photons in a Two-Slit Interferometer

Sacha Kocsis,<sup>1,2\*</sup> Boris Braverman,<sup>1\*</sup> Sylvain Ravets,<sup>3\*</sup> Martin J. Stevens,<sup>4</sup> Richard P. Mirin,<sup>4</sup> L. Krister Shalm,<sup>1,5</sup> Aephraim M. Steinberg<sup>1†</sup>

A consequence of the quantum mechanical uncertainty principle is that one may not discuss the path or “trajectory” that a quantum particle takes, because any measurement of position irrevocably disturbs the momentum, and vice versa. Using weak measurements, however, it is possible to operationally define a set of trajectories for an ensemble of quantum particles. We sent single photons emitted by a quantum dot through a double-slit interferometer and reconstructed these trajectories by performing a weak measurement of the photon momentum, postselected according to the result of a strong measurement of photon position in a series of planes. The results provide an observationally grounded description of the propagation of subensembles of quantum particles in a two-slit interferometer.

In classical physics, the dynamics of a particle’s evolution are governed by its position and velocity; to simultaneously know the particle’s position and velocity is to know its past, present, and future. However, the Heisenberg

uncertainty principle in quantum mechanics forbids simultaneous knowledge of the precise position and velocity of a particle. This makes it impossible to determine the trajectory of a single quantum particle in the same way as one would

that of a classical particle: Any information gained about the quantum particle’s position irrevocably alters its momentum (and vice versa) in a way that is fundamentally uncertain. One consequence is that in Young’s double-slit experiment one cannot determine through which slit a particle passes (position) and still observe interference effects on a distant detection screen (equivalent to measuring the momentum). Particle-like trajectories and wavelike interference are “complementary” aspects of the behavior of a quantum system, and an experiment designed to observe one neces-

<sup>1</sup>Centre for Quantum Information and Quantum Control and Institute for Optical Sciences, Department of Physics, University of Toronto, 60 St. George Street, ON M5S 1A7, Canada. <sup>2</sup>Centre for Quantum Dynamics, Griffith University, Brisbane 4111, Australia. <sup>3</sup>Laboratoire Charles Fabry, Institut d’Optique, CNRS, Université Paris-Sud, Campus Polytechnique, 2 avenue Augustin Fresnel, RD 128, 91127 Palaiseau cedex, France. <sup>4</sup>National Institute of Standards and Technology, 325 Broadway, Boulder, CO 80305, USA. <sup>5</sup>Institute for Quantum Computing, University of Waterloo, 200 University Avenue West, Waterloo, ON N2L 3G1, Canada.

\*These authors contributed equally to this work.  
†To whom correspondence should be addressed. E-mail: [steinberg@physics.utoronto.ca](mailto:steinberg@physics.utoronto.ca)

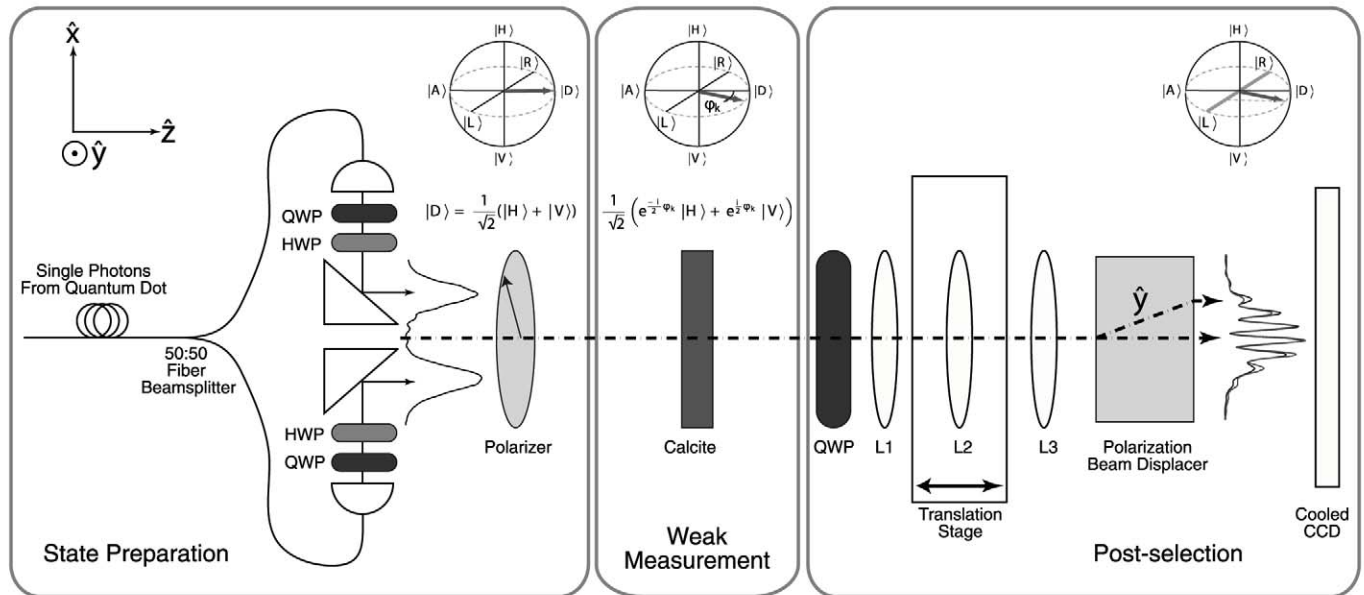


**Fig. 1.** Experimental setup for measuring the average photon trajectories. Single photons from an InGaAs quantum dot are split on a 50:50 beam splitter and then outcoupled from two collimated fiber couplers that act as double slits. A polarizer prepares the photons with a diagonal polarization  $|D\rangle = \frac{1}{\sqrt{2}}(|H\rangle + |V\rangle)$ . Quarter waveplates (QWP) and half waveplates (HWP) before the polarizer allow the number of photons passing through each slit to be varied. The weak measurement is performed by using a 0.7-mm-thick piece of calcite with its optic axis at  $42^\circ$  in the  $x$ - $z$  plane that rotates the

polarization state to  $\frac{1}{\sqrt{2}}(e^{-i\phi_k/2}|H\rangle + e^{i\phi_k/2}|V\rangle)$ . A QWP and a beam displacer are used to measure the polarization of the photons in the circular basis, allowing the weak momentum value  $k_x$  to be extracted. A cooled CCD measures the final  $x$  position of the photons. Lenses L1, L2, and L3 allow different imaging planes to be measured. The polarization states of the photons are represented on the Poincaré sphere, where the six compass points correspond to the polarization states  $|H\rangle, |V\rangle, |D\rangle, |A\rangle = \frac{1}{\sqrt{2}}(|H\rangle - |V\rangle), |L\rangle = \frac{1}{\sqrt{2}}(|H\rangle + i|V\rangle)$ , and  $|R\rangle = \frac{1}{\sqrt{2}}(|H\rangle - i|V\rangle)$ .



sarily gives up the option of observing the other (1–6). However, it is possible to “weakly” measure a system, gaining some information about one property without appreciably disturbing the future evolution (7); although the information obtained from any individual measurement is limited, averaging over many trials determines an accurate mean value for the observable of interest, even for subensembles defined by some subse-

quent selection (perhaps even on a complementary observable). It was recently pointed out (8) that this provides a natural way to operationally define a set of particle trajectories: One can ascertain the mean momentum of the subensemble of particles that arrive at any given position, and, by thus determining the momentum at many positions in a series of planes, one can experimentally reconstruct a set of average trajectories. We use a modified version of this protocol to reconstruct the “weak-valued trajectories” followed by single photons as they undergo two-slit interference. In the case of single-particle quantum mechanics, the trajectories measured in this fashion reproduce those predicted in the Bohm-de Broglie interpretation of quantum mechanics (9, 10).

Weak measurements, first proposed 2 decades ago (7, 11), have recently attracted widespread attention as a powerful tool for investigating fundamental questions in quantum mechanics (12–15) and have generated excitement for their potential applications to enhancing precision measurement (16, 17). In a typical von Neumann measurement, an observable of a system is coupled to a measurement apparatus or “pointer” via its momentum. This coupling leads to an average shift in the pointer position that is proportional to the expectation value of the system observable. In a “strong” measurement, this shift is large relative to the initial uncertainty in pointer position, so that significant information is acquired in a single shot. However, this implies that the pointer momentum must be very uncertain, and it is this uncertainty that creates the uncontrollable, irreversible disturbance associated with measurement. In a “weak” measurement, the pointer shift is small and little information can be gained on a single shot; but, on the other hand, there may be arbitrarily little disturbance imparted to the system. It is possible to subsequently postselect the system on a desired final state. Postselecting on

a final state allows a particular subensemble to be studied, and the mean value obtained from repeating the weak measurement many times is known as the weak value. Unlike the results of strong measurements, weak values are not constrained to lie within the eigenvalue spectrum of the observable being measured (7). This has led to controversy over the meaning and role of weak values, but continuing research has made strides in clarifying their interpretation and demonstrating a variety of situations in which they are clearly useful (16–21).

In our experiment, we sent an ensemble of single photons through a two-slit interferometer and performed a weak measurement on each photon to gain a small amount of information about its momentum, followed by a strong measurement that postselects the subensemble of photons arriving at a particular position [see (22) for more details]. We used the polarization degree of freedom of the photons as a pointer that weakly couples to and measures the momentum of the photons. This weak momentum measurement does not appreciably disturb the system, and interference is still observed. The two measurements must be repeated on a large ensemble of particles in order to extract a useful amount of information about the system. From this set of measurements, we can determine the average momentum of the photons reaching any particular position in the image plane, and, by repeating this procedure in a series of planes, we can reconstruct trajectories over that range. In this sense, weak measurement finally allows us to speak about what happens to an ensemble of particles inside an interferometer.

Our quantum particles are single photons emitted by a liquid helium-cooled InGaAs quantum dot (23, 24) embedded in a GaAs/AlAs micropillar cavity. The dot is optically pumped by a CW laser at 810 nm and emits single photons at

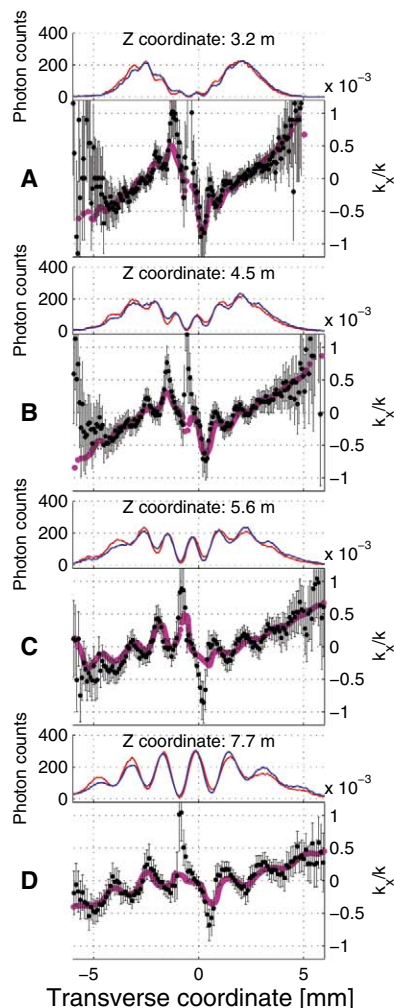
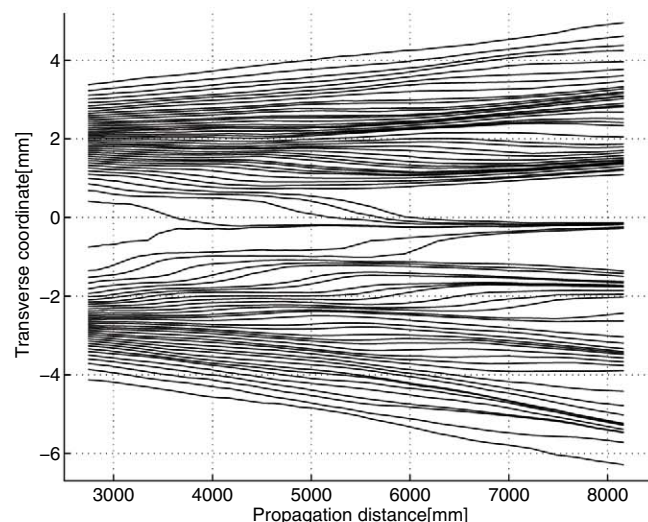


**Fig. 2.** Measured intensities (photon counts) of the two circular polarization components of  $|\psi\rangle$ , measured on the CCD screen (red and blue curves), as well as the weak momentum values calculated from these intensities (black) for imaging planes at (A)  $z = 3.2$  m, (B)  $z = 4.5$  m, (C)  $z = 5.6$  m, and (D)  $z = 7.7$  m. The red and blue data points are the intensity data with constant background subtracted. The errors for the momentum values were calculated by simulating the effect of Poissonian noise in the photon counts. The magenta curve shows momentum values obtained from enforcing probability density conservation between adjacent  $z$  planes. Because of the coarse-grained averaging over three imaging planes, the probability-conserving momentum values are not as sensitive as the measured weak momentum values to highly localized regions in the pattern with steep momentum gradients.

**Fig. 3.** The reconstructed average trajectories of an ensemble of single photons in the double-slit apparatus. The trajectories are reconstructed over the range  $2.75 \pm 0.05$  to  $8.2 \pm 0.1$  m by using the momentum data (black points in Fig. 2) from 41 imaging planes. To reconstruct a set of trajectories, we determined the weak momentum values for the transverse  $x$  positions at the initial plane. On the basis of this initial position and momentum information, the  $x$  position on the subsequent imaging plane that each trajectory lands is calculated, and the measured weak momentum value  $k_x$  at this point found. This process is repeated until the final imaging plane is reached and the trajectories are traced out. If a trajectory lands on a point that is not the center of a pixel, then a cubic spline interpolation between neighboring momentum values is used.



a wavelength  $\lambda$  of 943 nm. A Hanbury Brown-Twiss interferometer is used to measure a second-order correlation function  $g^{(2)}(0)$  of  $0.17 \pm 0.04$  (SD), confirming the single-photon nature of the dot emission (25). The photons are coupled into single-mode fiber and sent through an in-fiber 50:50 beam splitter. The outputs of the beam splitter exit two fiber launchers as Gaussian beams with their waists at the fiber launchers and are redirected to be parallel along the  $z$  axis by mirrored prisms to create the initial “slit function” (Fig. 1). The two Gaussian beams have a waist  $1/e^2$  radius of  $0.608 \pm 0.006$  mm and a peak-to-peak separation of  $4.69 \pm 0.02$  mm. The polarization of the photons, which serves as the ancilla system for the weak measurement, is prepared in the initial state  $|\psi\rangle = (1/\sqrt{2})(|H\rangle + |V\rangle)$ , where  $|H\rangle$  is identified with the  $x$  axis and  $|V\rangle$  with the  $y$  axis.

The weak measurement is accomplished with a thin piece of birefringent calcite that changes the polarization of the photons passing through by introducing a phase shift between the ordinary and extraordinary components of polarization. The photons diffract out from the slits and impinge upon the crystal with an incident angle  $\theta$  that depends on their transverse momentum  $k_x$  (where the momentum of a photon is  $\mathbf{p} = \hbar\mathbf{k}$ ). By orienting the calcite's optic axis to lie in the  $x$ - $z$  plane,  $|H\rangle$  becomes the extraordinary polarization that encounters an angle-dependent index of refraction,  $n_e(\theta)$ , and  $|V\rangle$  becomes the ordinary polarization that encounters a constant index of refraction,  $n_o$ . The calcite piece is 0.7 mm thick with its optic axis in the  $x$ - $z$  plane at  $42^\circ$  to the  $z$  axis and imparts a small  $k_x$ -dependent birefringent phase shift that transforms the incident linear polarization state of the photons to a slightly elliptical polarization state. In this way, we carry out a measurement of the momentum with the polarization serving as a pointer that records the value of this observable. By arranging for the magnitude of the polarization rotation to be small with respect to the uncertainty in the photons' polarization, we ensure that the measurement is weak. No single measurement provides unambiguous information about the exact propagation direction, and hence no significant measurement disturbance is introduced. After averaging the results over many photons, it becomes possible to extract the average value of photon momentum.

The birefringent phase shift  $\varphi(k_x)$  that the photons receive depends on the different paths and indices of refraction for the two polarizations in the calcite (26). The spread of the angles of the diffracting photons passing through calcite is small, allowing us to approximate the induced birefringent phase shift  $\varphi(k_x)$  as a linear function of  $k_x$ :

$$\varphi(k_x) = \zeta \frac{k_x}{|\mathbf{k}|} + \varphi_0 \quad (1)$$

The coefficient  $\zeta$  designates the coupling strength between the phase we are measuring

and the photon momentum, and its value was found to be  $373.5 \pm 3.4$  (22). The calcite is tilted in the  $x$ - $z$  plane to tune  $\varphi_0 = 0$  modulo  $2\pi$ .

A system of three cylindrical lenses, with the middle lens translatable in the  $z$  direction, allows the initial slit function to be imaged over an arbitrary distance. It is important to note that the thin calcite crystal performing the weak measurement remains fixed in place before the lenses. This does not affect the outcome of the final postselection at the various imaging planes along  $z$  as the interaction Hamiltonian between the polarization pointer and the photon's transverse momentum commutes with the free-propagation Hamiltonian of the system. The trajectories were reconstructed over the range  $2.75 \pm 0.05$  to  $8.2 \pm 0.1$  m to show the transition from the near-field to far-field intensity distribution. The polarization state of each photon is projected into the circular basis by using a quarter waveplate with its fast axis set to  $-45^\circ$  to  $x$ , located in front of the lens system, and a polarizing beam displacer located behind the lenses. The beam displacer transmits the right-hand circularly polarized component of  $|\psi\rangle$  undeviated and displaces the left-hand circularly polarized component of  $|\psi\rangle$  vertically by about 2 mm. The photons are then detected on a cooled charge-coupled device (CCD). The exposure time on the CCD was set to 15 s, allowing the two vertically separated interference patterns to accumulate. During each exposure, about 31,000 single photons were detected by the CCD. By projecting into the circular basis, the mo-

mentum information encoded in polarization is transformed into an intensity modulation between the two vertically displaced patterns. The intensity of the top pattern (corresponding to the projection onto the right-hand circular polarization) is  $I_R \propto [1 + \sin\varphi(k_x)]$ , whereas the intensity of the bottom pattern (corresponding to the projection on to the left-hand circular polarization) goes as  $I_L \propto [1 - \sin\varphi(k_x)]$ . In the measured interference patterns at four different imaging planes (Fig. 2), the pixel on the CCD where each photon is detected corresponds to the photon's  $x$  position. The 26- $\mu\text{m}$  pixel width sets the precision with which the photon's  $x$  position can be measured.

By using Eq. 1, we can simultaneously extract the weak value of the transverse component of the photon wave vector  $k_x$  at each pixel position

$$\frac{k_x}{|\mathbf{k}|} = \frac{1}{\zeta} \left[ \sin^{-1} \left( \frac{I_R - I_L}{I_R + I_L} \right) \right] \quad (2)$$

Thus for each value of the photon's position  $x$ , we are able to calculate the weak value of its transverse momentum  $k_x$  by taking the difference in modulated intensity between the two vertically displaced patterns at the same imaging plane along the  $z$  axis. The weak momentum values for four different imaging planes calculated in this way are shown in Fig. 2. By repeating the measurement for many imaging planes closely spaced along  $z$ , a vector field is produced from

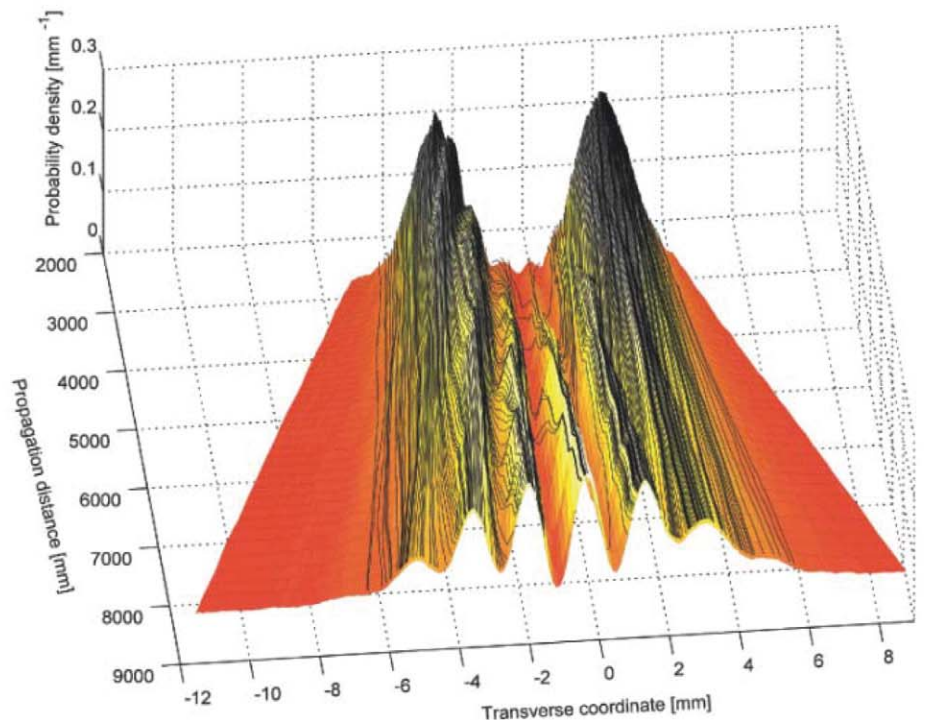


**Fig. 4.** The trajectories from Fig. 3 plotted on top of the measured probability density distribution. Even though the trajectories were reconstructed by using only local knowledge, they reproduce the global propagation behavior of the interference pattern.

which the weak-valued photon trajectories are reconstructed.

For the experimentally reconstructed trajectories for our double slit (Fig. 3), it is worth stressing that photons are not constrained to follow these precise trajectories; the exact trajectory of an individual quantum particle is not a well-defined concept. Rather, these trajectories represent the average behavior of the ensemble of photons when the weakly measured momentum in each plane is recorded contingent upon the final position at which a photon is observed. The trajectories resemble a hydrodynamic flow with a central line of symmetry clearly visible: Trajectories originating from one slit do not cross the central line of symmetry into the opposite side of the interference pattern. Trajectories at the edges of bright fringes tend to cross over to join more central bright fringes, thus generating the observed intensity distribution because of interference. The trajectories cross over dark fringes at relatively steep angles; there is a low probability of finding a photon in these regions that correspond to postselecting on a state nearly orthogonal to the initial state of the system. The separation of the imaging planes sets the scale over which features in the trajectories can be observed. The evolution of the interference in our double-slit apparatus takes place over a scale that is much longer than the separation between imaging planes, and our trajectories can accurately track the evolution of this interference. The one place where the accuracy can suffer is when a trajectory quickly passes through a dark fringe; here the fine scale behavior is smaller than the spacing between imaging planes. By overlaying the trajectories on top of the measured intensity distribution (Fig. 4), we observe that the trajectories reproduce the global interference pattern well. The tendency of the reconstructed trajectories to “bunch” together within each bright interference fringe is an artifact of measurement noise with the position error accumulating as the

trajectory reconstruction is carried out further and further from the initial plane at  $z = 2.75$  m. Single-particle trajectories measured in this fashion reproduce those predicted by the Bohm-de Broglie interpretation of quantum mechanics (8), although the reconstruction is in no way dependent on a choice of interpretation.

Controversy surrounding the role of measurement in quantum mechanics is as old as the quantum theory itself, and nowhere have the paradoxes been thrown into such stark relief as in the context of the double-slit experiment. Our experimentally observed trajectories provide an intuitive picture of the way in which a single particle interferes with itself. It is of course impossible to rigorously discuss the trajectory of an individual particle, but in a well-defined operational sense we gain information about the average momentum of the particle at each position within the interferometer, leading to a set of “average trajectories.” The exact interpretation of these observed trajectories will require continued investigation, but these weak-measurement results can be grounded in experimental measurements that promise to elucidate a broad range of quantum phenomena (7, 11–13, 15–17). By using the power of weak measurements, we are able to provide a new perspective on the double-slit experiment, which Feynman famously considered to have in it “the heart of quantum mechanics” (27).

#### References and Notes

1. N. Bohr, *Collected Works* (North-Holland, Amsterdam, 1972).
2. W. K. Wootters, W. H. Zurek, *Phys. Rev. D* **19**, 473 (1979).
3. N. Bohr, *Naturwissenschaften* **16**, 245 (1928).
4. M. O. Scully, B.-G. Englert, H. Walther, *Nature* **351**, 111 (1991).
5. C. Brukner, A. Zeilinger, *Phys. Rev. Lett.* **83**, 3354 (1999).
6. V. Jacques *et al.*, *Science* **315**, 966 (2007).
7. Y. Aharonov, D. Z. Albert, L. Vaidman, *Phys. Rev. Lett.* **60**, 1351 (1988).
8. H. Wiseman, *N. J. Phys.* **9**, 165 (2007).
9. D. Bohm, *Phys. Rev.* **85**, 166 (1952).

10. D. Bohm, *Phys. Rev.* **85**, 180 (1952).
11. N. W. M. Ritchie, J. G. Story, R. G. Hulet, *Phys. Rev. Lett.* **66**, 1107 (1991).
12. R. Mir *et al.*, *N. J. Phys.* **9**, 287 (2007).
13. J. S. Lundeen, A. M. Steinberg, *Phys. Rev. Lett.* **102**, 020404 (2009).
14. K. Yokota, T. Yamamoto, M. Koashi, N. Imoto, *N. J. Phys.* **11**, 033011 (2009).
15. G. J. Pryde, J. L. O'Brien, A. G. White, T. C. Ralph, H. M. Wiseman, *Phys. Rev. Lett.* **94**, 220405 (2005).
16. O. Hosten, P. Kwiat, *Science* **319**, 787 (2008); 10.1126/science.1152697.
17. P. B. Dixon, D. J. Starling, A. N. Jordan, J. C. Howell, *Phys. Rev. Lett.* **102**, 173601 (2009).
18. A. Peres, *Phys. Rev. Lett.* **62**, 2326 (1989).
19. A. J. Leggett, *Phys. Rev. Lett.* **62**, 2325 (1989).
20. Y. Aharonov, L. Vaidman, *Phys. Rev. Lett.* **62**, 2327 (1989).
21. J. Dressel, S. Agarwal, A. N. Jordan, *Phys. Rev. Lett.* **104**, 240401 (2010).
22. Materials and methods are available as supporting material on Science Online.
23. R. P. Mirin, *Appl. Phys. Lett.* **84**, 1260 (2004).
24. R. H. Hadfield *et al.*, *Opt. Express* **13**, 10846 (2005).
25. R. Loudon, *The Quantum Theory of Light* (Oxford Univ. Press, Oxford, ed. 3, 2000).
26. M. Born, E. Wolf, *Principles of Optics* (Cambridge Univ. Press, Cambridge, 1999).
27. R. Feynman, *The Feynman Lectures on Physics* (Addison-Wesley, Boston, 1989).

**Acknowledgments:** A.M.S. conceived of the experiment and supervised the work; M.J.S. and R.P.M. designed and fabricated the single-photon sources; S.K. constructed the experiment and acquired the data with assistance from B.B. and S.R. and much guidance from L.K.S.; B.B., S.K., and S.R. carried out the data analysis and generated the figures; S.K. and L.K.S. wrote the text with input from all the other co-authors. This work was supported by the Natural Sciences and Engineering Research Council of Canada, the Canadian Institute for Advanced Research, and QuantumWorks. S.K. thanks B. Higgins and L.K.S. thanks K. J. Resch for useful discussions. The data from the experiment has been archived and is available at [www.physics.utoronto.ca/~aephraim/data/PhotonTrajectories](http://www.physics.utoronto.ca/~aephraim/data/PhotonTrajectories).

#### Supporting Online Material

[www.sciencemag.org/cgi/content/full/332/6034/1170/DC1](http://www.sciencemag.org/cgi/content/full/332/6034/1170/DC1)  
Materials and Methods

27 December 2010; accepted 11 April 2011  
10.1126/science.1202218

## Spin-Liquid Ground State of the $S = 1/2$ Kagome Heisenberg Antiferromagnet

Simeng Yan,<sup>1</sup> David A. Huse,<sup>2,3</sup> Steven R. White<sup>1\*</sup>

We use the density matrix renormalization group to perform accurate calculations of the ground state of the nearest-neighbor quantum spin  $S = 1/2$  Heisenberg antiferromagnet on the kagome lattice. We study this model on numerous long cylinders with circumferences up to 12 lattice spacings. Through a combination of very-low-energy and small finite-size effects, our results provide strong evidence that, for the infinite two-dimensional system, the ground state of this model is a fully gapped spin liquid.

We consider the quantum spin  $S = 1/2$  kagome Heisenberg antiferromagnet (KHA) with only nearest-neighbor isotropic exchange interactions (Hamiltonian  $H = \sum \vec{S}_i \cdot \vec{S}_j$ , where  $\vec{S}_i$  and  $\vec{S}_j$  are the spin operators for sites  $i$  and  $j$ , respectively) on a kagome

lattice (Fig. 1A). This frustrated spin system has long been thought to be an ideal candidate for a simple, physically realistic model that shows a spin-liquid ground state (1–3). A spin liquid is a magnetic system that has “melted” in its ground state because of quantum fluctuations, so it has

no spontaneously broken symmetries (4). A key problem in searching for spin liquids in two-dimensional (2D) models is that there are no exact or nearly exact analytical or computational methods to solve infinite 2D quantum lattice systems. For 1D systems, the density matrix renormalization group (DMRG) (5, 6), the method we use here, serves in this capacity. In addition to its interest as an important topic in quantum magnetism, the search for spin liquids thus serves as a test-bed for the development of accurate and widely applicable computational methods for 2D many-body quantum systems.

<sup>1</sup>Department of Physics and Astronomy, University of California, Irvine, CA 92617, USA. <sup>2</sup>Department of Physics, Princeton University, Princeton, NJ 08544, USA. <sup>3</sup>Institute for Advanced Study, Princeton, NJ 08540, USA.

\*To whom correspondence should be addressed. E-mail: srwhite@uci.edu



The KHA has been studied with approximate approaches for decades (1), with proposals for spin-liquid and valence-bond-crystal (VBC) ground states (2, 3). In the past few years, numerical evidence had suggested that the KHA ground state might be a VBC with a 36-site unit cell of bonds with spatially nonuniform spin-spin correlations in the ground state that break the translational symmetry of the kagome lattice. First proposed in (2), and explored in more detail in (7), this honeycomb VBC (HVBC) was also studied with a perturbative series expansion (8, 9). The series for the ground-state energy rapidly converges to a low energy (8, 9). Subsequently, Evenly and Vidal (10) used the multiscale entanglement renormalization ansatz (MERA), obtaining the HVBC and an energy close to the series result. Another approximate numerical approach based on an effective quantum dimer model also yielded the HVBC as the ground state, but noted that a  $Z_2$  spin liquid is close by in a generalized parameter space (11). A recent DMRG study (12), in contrast, found a spin-liquid ground state, but on the largest lattices the energy obtained was substantially above that of the HVBC, suggesting that the method had not found the true ground state. The simple KHA is clearly near a number of different possible ground-state phases upon adding small perturbations to its Hamiltonian [such as a second-neighbor exchange interaction (13)], and it is this proximity of many competing states that has made this such a challenging system. A variational state that may serve as a multicritical state between all these possible ground-state phases is the critical gapless spin liquid of (14).

We performed an extensive DMRG study of the KHA with important differences in technique from the previous study. Most importantly, we studied long cylinders with open ends, thus avoiding fully periodic (toroidal) boundary conditions, which are known to greatly magnify the truncation errors in the DMRG (6). We also show why the series expansions appear to converge well, yet reach the incorrect HVBC state: The path connecting the series expansion starting point and the KHA is interrupted by a first-order phase transition (15). For details on the competition between the spin liquid and HVBC states, see figs. S1 to S3.

DMRG efficiently finds the ground state for long 1D systems, but for 2D systems one must study cylinders or strips of limited width. We studied mostly cylinders with a maximum circumference of 12 lattice spacings, obtaining ground-state energies with uncertainties of less than 0.1%, with much higher accuracy for the narrower cylinders. We labeled the cylinders by their orientation, circumference, and any shift in wrapping the cylinder periodically (Fig. 1A) (15). For example, “YC9-2” denotes a cylinder (C) with some of the bonds oriented in the  $y$  direction (Y), with circumference of nine lattice spacings and a shift of two columns when connected periodically. We estimate the energy per site for each type of infinitely long cylinder by subtracting energies of

cylinders of different length to remove end effects.

Our DMRG results for ground-state energies, along with results from other approaches, are shown in Fig. 1B. The DMRG energies are consistent with the Lanczos results (16, 17) and well below the energies of MERA (10) and the series expansion for the HVBC (8, 9). The previous DMRG result (12) is close to the true ground state (17) for a torus with a circumference of six (circumference-6) lattice spacings. The entanglement across a cut that separates a circumference-six torus into two parts is roughly the same as that across a cut that separates a circumference-12 cylinder—our current limit. Thus, it is not surprising that the DMRG energies for tori (12) are overestimates for circumferences larger than six lattice spacings. We also obtain a new rigorous upper bound on the ground-state energy of the infinite 2D system using the DMRG on strips with open boundary conditions (15); this is well below the previous bound from MERA (10).

The 36-site unit cell of the HVBC does fit on the XC8 cylinder ( $1/c \cong 0.14$ , where  $c$  is the circumference), allowing a direct comparison between the HVBC series and our DMRG: the DMRG energy is lower by 0.004(1). Comparing this cylinder to the corresponding torus, the energy shows strong finite-size effects in the HVBC series (8, 9), but the same comparison between Lanczos (16) and our DMRG shows that the true finite-size effect is much smaller (15). These finite-size effects remain small for even smaller circumferences (17). This is consistent with the small correlation length that we find: less than 1.5 lattice spacings (15). We conclude that the ground-state energies of our widest cylinders

have minimal finite-size effects and thus provide reliable estimates of the 2D energy.

The ground state that we find has only short-range correlations, with a nonzero energy gap for any excitations, including spin-singlet excitations. We have tested the response of this ground state to many sorts of perturbations that would select out ordered states, if they exist, without detecting any signs of any ordering. Thus, we conclude that the ground state is a gapped spin liquid. Such a state can be represented as some sort of short-range resonating-valence-bond (RVB) state (18–24). The shortest resonant loops of singlet dimers in a nearest-neighbor RVB state on a kagome lattice each surround only one hexagon of the lattice (7). If the RVB state had all dimer covers equally weighted, all 32 of these elementary resonant loops would be equally present. Instead, the ground state appears to substantially overemphasize certain eight-site loops of a diamond shape (Fig. 2B). To test the response of the ground state to enhancing each of these 32 elementary resonant loops, we slightly increased the exchange couplings along the bonds of such a loop at the center of a YC8 cylinder and measured how much this enhanced the spin-spin correlations along the loop and elsewhere. It is the eight-site diamond loop that elicits the strongest response (Fig. 2B). The six-site “perfect hexagon” loop (Fig. 2A) (2, 7, 8), shows a much smaller response, suggesting that this resonant loop is actually underweighted in the ground state.

One cannot tile a kagome lattice with just these favored resonant diamonds. However, a particular “diamond-pattern” VBC (Fig. 2C), appears to be closely related to the spin liquid, and it is useful to think of the spin liquid as a melted

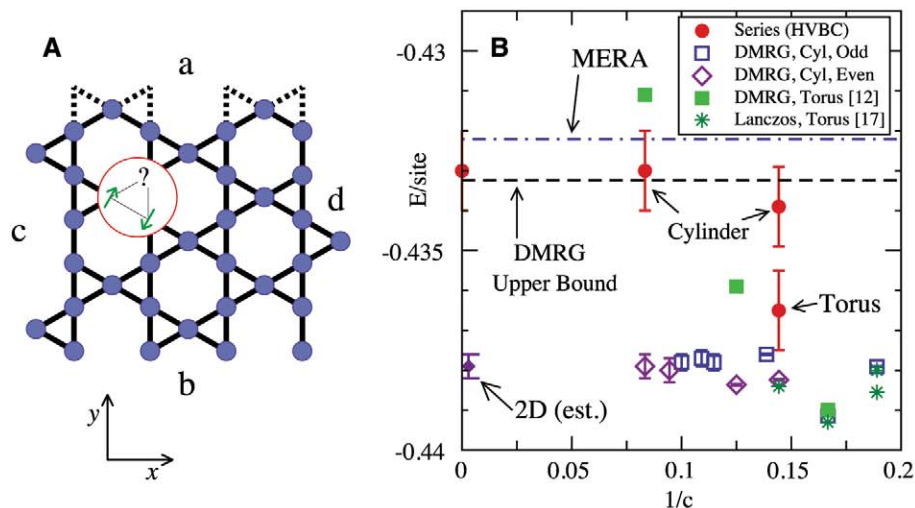


**Fig. 1.** (A) A section of kagome lattice. The frustration is indicated by the spins shown on one triangle. To make a cylinder the top (a) is connected to the bottom (b) by the dotted bonds indicated; this example makes cylinder YC6 (15). To make a torus, similarly connect sides c and d. (B) Comparison of energies per site for various lattices and methods. For cylinders, the horizontal axis is the inverse circumference in units of inverse lattice spacings. For tori (12, 16, 17), the smallest circumference is used. The MERA (10) and our DMRG upper bound (15) results apply directly to an infinite 2D system, as does the series HVBC result (8, 9) on the axis. Error bars indicate estimated uncertainties.

state of this crystal. We have measured the correlation length for VBC energy correlations in this diamond pattern along cylinder YC8 and find that it is less than 1.5 lattice spacings (15). Unlike the HVBC, which shows a first-order phase transition to the spin liquid (15), this diamond VBC evolves smoothly into the spin liquid without any phase transition as one changes the strengths of the exchanges that are altered to favor it (we call this “pinning it,” Fig. 2C). For the even cylinders on which this diamond VBC does fit, this process allows a careful production of the spin liquid by approaching it in a smooth fashion from the diamond VBC (15).

The infinitely long cylinders may be viewed as one-dimensional systems with a unit cell containing  $N_c$  spins. Even- $N_c$  cylinders (e.g.,  $N_c = 12$  for YC8) are compatible with the diamond VBC, and the ground state of the infinite cylinder appears to be nondegenerate. Odd- $N_c$  cylinders are not compatible with the diamond VBC, and the Lieb-Schultz-Mattis theorem implies that the ground state must be degenerate (25). Ground states on these odd cylinders weakly break translational invariance, spontaneously doubling the unit cell, which produces a pair of degenerate ground states, still with a gap to higher excited singlet states. The symmetry breaking is in a “striped” pattern (Fig. 3). For YC6 and YC10, the stripes run around the circumference, whereas for the other odd spiral cylinders the stripes are spirals.

The ends of our cylinders may have low-lying states below the bulk singlet and triplet gaps. The following DMRG procedure avoids these edge states: First target only one state, and sweep enough to obtain a high-accuracy ground state. Then restrict the range of bonds that are updated in the DMRG sweeps to the central half of the sample and target the two lowest-energy states, again sweeping to high accuracy, but keeping the end regions of the samples locally in the ground state. This technique is particularly important for obtaining the singlet gap. For the triplet gap, one can also keep the excitation away from the ends with local magnetic fields. With this approach, we can target both states together—one with total  $S_z = 0$  and the other with  $S_z = 1$ —or run them separately. These different approaches allowed for fairly independent checks on the results. Figure 4 shows the measured bulk gaps. Gaps are more demanding than ground-state energies,

so we do not have gap estimates for our widest cylinder (15). See table S1 for energies and gaps of all the cylinders studied.

The singlet gap is 0.050, within the errors, for the even XC8 and YC8 cylinders, and it remains near this value for the wider even XC12-2 cylinder. The odd cylinders come in at least two families: YC6 and YC10 are not spirals, whereas YC5-2, YC7-2, and YC9-2 are a series of spirals with increasing circumference. In each of these (small) families of odd cylinders, the singlet gap increases as the circumference increases, supporting our conclusion that the singlet gap is  $\sim 0.05$  in the 2D limit. This is quite different from the exact diagonalization results, where there are many lower-lying singlets, and the lowest singlet gap is only  $\sim 0.01$  on the standard 36-site torus (26). The singlet gap is a strong function of a second-neighbor exchange coupling ( $J_2$ ) (13), with an apparent phase transition at a very small ferromagnetic value of  $J_2$ . The location of this nearby transition is quite sensitive to circumferences, and this produces the large differences in the singlet gap between the torus and our cylinders.

The triplet (spin) gap on the 36-site torus is 0.164 from exact diagonalization (26). Although XC8 and YC8 have gaps that are quite close to this, our results on other cylinders suggest that the 2D triplet gap is smaller (Fig. 4). The triplet excitations are composed of two spinons, but we cannot resolve whether or not the two spinons bind, although in some cylinders any binding must be very weak. This composite nature of the excitation seems to make the finite-size effects and variation between the cylinders more pronounced. We do not yet understand the details of these effects. As for the singlet gap, the spiral odd cylinders have the smallest triplet gaps, and the even cylinders the largest. The triplet gap remains above the singlet gap in all the systems we have studied; thus, we believe it remains nonzero in the 2D limit.

A nearest-neighbor RVB wave function is a linear combination of nearest-neighbor singlet dimers covering the kagome lattice (24). For a kagome lattice wrapped on a cylinder, such dimer covers are in two topologically distinct sectors that differ by a  $Z_2$  winding number, and dimer resonances on finite loops do not change this winding number (19, 20, 22–24). We can force our even cylinders to have one or the other of the two

winding numbers by choosing how many spins to leave at each end. For a finite circumference  $c$ , these two sectors have different ground-state energies ( $E$ ) per site; for YC8, their difference is  $\delta E \approx 0.00069(3)$ . For odd cylinders, the two sectors are related by translation along the length of the cylinder and, thus, are degenerate. If an even cylinder is topologically ordered, one expects  $\delta E \sim \exp(-c/\xi)$  (where  $\xi$  is a correlation length) at large  $c$ , but we do not yet have reliable  $\delta E$  results for larger cylinders to test this hypothesis. This is partly because the singlet gap above the ground state in the higher-energy sector is substantially smaller than the singlet gap above the overall ground state, slowing DMRG’s convergence.

A domain wall along the cylinder where the  $Z_2$  winding number changes is a spinon. For the odd cylinders, the degeneracy of the two sectors means the spinons are unconfined. However, two

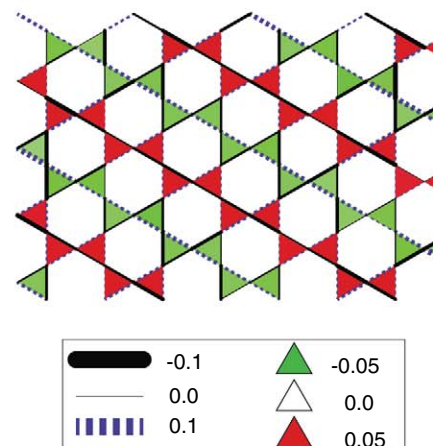


**Fig. 3.** Ground-state energy pattern for a YC9-2 cylinder. The colors of the triangles and their intensities indicate the deviation of the sum of the spin-spin correlations on the three bonds forming the triangle from  $3e_0$ , with  $e_0 = -0.219$ .

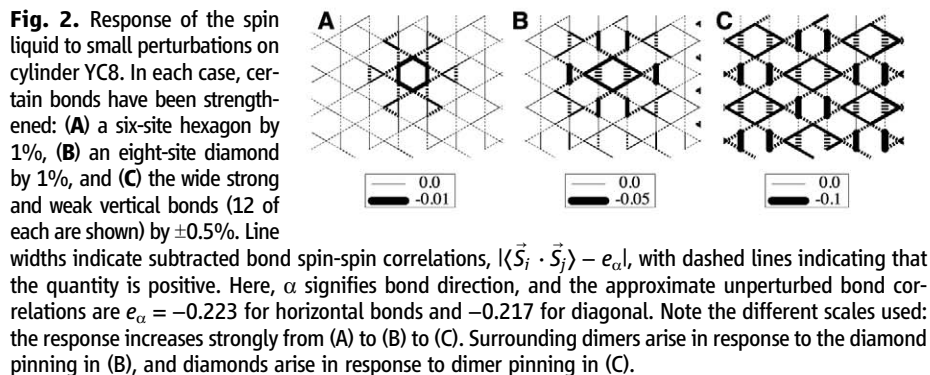


**Fig. 2.** Response of the spin liquid to small perturbations on cylinder YC8. In each case, certain bonds have been strengthened: (A) a six-site hexagon by 1%, (B) an eight-site diamond by 1%, and (C) the wide strong and weak vertical bonds (12 of each are shown) by  $\pm 0.5\%$ . Line widths indicate subtracted bond spin-spin correlations,  $|\langle \vec{S}_i \cdot \vec{S}_j \rangle - e_\alpha|$ , with dashed lines indicating that the quantity is positive. Here,  $\alpha$  signifies bond direction, and the approximate unperturbed bond correlations are  $e_\alpha = -0.223$  for horizontal bonds and  $-0.217$  for diagonal. Note the different scales used: the response increases strongly from (A) to (B) to (C). Surrounding dimers arise in response to the diamond pinning in (B), and diamonds arise in response to dimer pinning in (C).

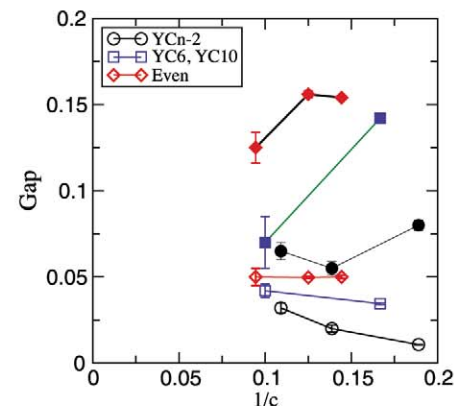


**Fig. 4.** Spin triplet (solid symbols) and singlet (hollow symbols) gaps for various cylinders with circumferences  $c$ . The type of cylinder (15) is indicated in the key (inset).

spinons might bind with a finite binding energy—it appears that this might be happening on cylinder YC10 and, thus, it might also occur in the 2D limit. For the even cylinders, on the other hand, the spinons are confined by an effective potential that grows linearly with the distance, because the domain between them is in the higher-energy sector. As a result, the excitation across the spin gap for the even cylinders is a bound spinon pair. It remains to be determined if they remain bound in the 2D limit.

Much remains to be understood concerning the low-energy behavior of the KHA, particularly the detailed structure, exchange statistics, and dispersion relations of the various excitations. It will be instructive to also explore the phase diagram in the vicinity of this simple nearest-neighbor-only Heisenberg model by changing the Hamiltonian in various ways (*13*) to find what other phases are nearby and perhaps to move “deeper” into this spin liquid where it might be easier to study.

## References and Notes

1. V. Elser, *Phys. Rev. Lett.* **62**, 2405 (1989).
2. J. B. Marston, C. Zeng, *J. Appl. Phys.* **69**, 5962 (1991).
3. S. Sachdev, *Phys. Rev. B* **45**, 12377 (1992).
4. L. Balents, *Nature* **464**, 199 (2010).
5. S. R. White, *Phys. Rev. Lett.* **69**, 2863 (1992).
6. S. R. White, *Phys. Rev. B* **48**, 10345 (1993).
7. P. Nikolic, T. Senthil, *Phys. Rev. B* **68**, 214415 (2003).
8. R. R. P. Singh, D. A. Huse, *Phys. Rev. B* **76**, 180407 (2007).
9. R. R. P. Singh, D. A. Huse, *Phys. Rev. B* **77**, 144415 (2008).
10. G. Evenbly, G. Vidal, *Phys. Rev. Lett.* **104**, 187203 (2010).
11. D. Poilblanc, M. Mambrini, D. Schwandt, *Phys. Rev. B* **81**, 180402(R) (2010).
12. H. C. Jiang, Z. Y. Weng, D. N. Sheng, *Phys. Rev. Lett.* **101**, 117203 (2008).
13. P. Sindzingre, C. Lhuillier, *Europhys. Lett.* **88**, 27009 (2009).
14. Y. Ran, M. Hermele, P. A. Lee, X.-G. Wen, *Phys. Rev. Lett.* **98**, 117205 (2007).
15. Supporting material is available on Science Online.
16. P. W. Leung, V. Elser, *Phys. Rev. B* **47**, 5459 (1993).
17. A. M. Läuchli, J. Sudan, E. S. Sørensen, <http://arxiv.org/abs/1103.1159>.
18. P. W. Anderson, *Mater. Res. Bull.* **8**, 153 (1973).
19. S. A. Kivelson, D. S. Rokhsar, J. P. Sethna, *Phys. Rev. B* **35**, 8865 (1987).

20. N. Read, B. Chakraborty, *Phys. Rev. B* **40**, 7133 (1989).
  21. N. Read, S. Sachdev, *Phys. Rev. Lett.* **66**, 1773 (1991).
  22. X. G. Wen, *Phys. Rev. B* **44**, 2664 (1991).
  23. R. Moessner, S. L. Sondhi, *Phys. Rev. Lett.* **86**, 1881 (2001).
  24. G. Misguich, D. Serban, V. Pasquier, *Phys. Rev. B* **67**, 214413 (2003).
  25. E. Lieb, T. Schultz, D. Mattis, *Ann. Phys.* **16**, 407 (1961).
  26. C. Waldtmann *et al.*, *Eur. Phys. J. B* **2**, 501 (1998).
- Acknowledgments:** We thank A. Läuchli for Lanczos results; R. Singh for series results; and C. Lhuillier, M. P. A. Fisher, T. Senthil, E. Sørensen, S. Sondhi, G. Vidal, X.-G. Wen, O. Tchernyshyov, and M. Stoudenmire for discussions. This work was supported by NSF grants DMR-0907500 and DMR-0819860.

## Supporting Online Material

[www.sciencemag.org/cgi/content/full/science.1201080/DC1](http://www.sciencemag.org/cgi/content/full/science.1201080/DC1)  
Materials and Methods

SOM Text

Figs. S1 to S3

Table S1

References (5, 6, 8–10, 12, 16, 17, 27–29)

30 November 2010; accepted 7 April 2011

Published online 28 April 2011;

10.1126/science.1201080

# Two-Dimensional Mott-Hubbard Electrons in an Artificial Honeycomb Lattice

A. Singha,<sup>1\*</sup> M. Gibertini,<sup>1</sup> B. Karmakar,<sup>1</sup> S. Yuan,<sup>2</sup> M. Polini,<sup>1,3†</sup> G. Vignale,<sup>4,3</sup> M. I. Katsnelson,<sup>2</sup> A. Pinczuk,<sup>5</sup> L. N. Pfeiffer,<sup>6</sup> K. W. West,<sup>6</sup> V. Pellegrini<sup>1†</sup>

Artificial crystal lattices can be used to tune repulsive Coulomb interactions between electrons. We trapped electrons, confined as a two-dimensional gas in a gallium arsenide quantum well, in a nanofabricated lattice with honeycomb geometry. We probed the excitation spectrum in a magnetic field, identifying collective modes that emerged from the Coulomb interaction in the artificial lattice, as predicted by the Mott-Hubbard model. These observations allow us to determine the Hubbard gap and suggest the existence of a Coulomb-driven ground state.

The conduction electrons of a crystal experience the potential created by a periodic arrangement of coupled quantum units (such as ions and atoms). Numerous properties of solids can be explained in terms of Bloch bands (*1*), neglecting Coulomb interactions between electrons. These interactions often lead to qualitative changes that are particularly pronounced in solids with narrow energy bands (2–4). These strongly correlated materials display exotic ordering

phenomena and metal-insulator phase transitions (3, 4). Mott showed (5) that interaction-induced insulators are better described in real space (rather than in momentum space), in which the solid is viewed as a collection of localized electrons bound to atoms with partially filled shells. Electrons hopping through the lattice are absorbed and emitted from the atoms, thus originating two bands, which are split by the energy cost of having two electrons with antiparallel spin on the same atomic site.

Hubbard subsequently introduced a model Hamiltonian with onsite interactions that displays split bands (Hubbard bands, or HBs) in the strongly correlated (or atomic) limit (6). HBs (and their coexistence with quasiparticle bands in the correlated metallic phase) are characteristic features of such strongly correlated systems. Fermions on a honeycomb lattice, in particular, have been predicted to display unusual correlated phases of matter such as topological Mott insulating (7) and quantum spin liquid phases (8).

The creation of artificial systems with a high degree of tunability offers a way to explore Mott-Hubbard (M-H) physics systematically

(9, 10). Here we report the creation of an artificial lattice with honeycomb geometry for trapping electrons, and we demonstrate the formation of HBs through strong correlations. We nanofabricated the artificial lattice on the surface of a gallium arsenide (GaAs) heterostructure that hosts a high-quality two-dimensional electron gas (2DEG) (*11–13*). Similar nanostructures have been studied in the past in the context of the Hofstadter's fractal energy spectrum (*14, 15*). We probed the electron excitation spectrum by inelastic light-scattering and observed signatures stemming from strong Coulomb interactions, which we could tune by applying an external magnetic field. Carriers in the patterned structures supported an unusual collective mode; its energy scales like  $\sqrt{B}$ , where  $B$  is the component of the magnetic field perpendicular to the 2DEG. A theoretical analysis based on a minimal Hubbard model reveals that the mode energy is determined by the onsite Coulomb interaction and represents direct evidence of the existence of HBs in the 2DEG subjected to the artificial lattice. At low temperatures and large  $B$  fields, we found evidence for the opening of an unexpected gap in the spin excitation spectrum. We argue that the observed gap reveals the occurrence of a new correlated phase of electrons in a honeycomb lattice akin to one of those discussed in the context of graphene in high magnetic fields (*16–18*). These findings pave the way for the possibility to explore graphene-like physics in the ultrahigh magnetic field limit, in which the magnetic length is smaller than the lattice constant of the artificial crystal—a regime not accessible in graphene.

The sample used in this study was the host of a 2DEG in a 25-nm-wide, one-side modulation-doped  $\text{Al}_{0.1}\text{Ga}_{0.9}\text{As}/\text{GaAs}$  quantum well. The procedures for nanofabricating the artificial honeycomb lattice extended over a 100- $\mu\text{m}$ -by-100- $\mu\text{m}$

<sup>1</sup>National Enterprise for nanoScience and nanoTechnology, Istituto Nanoscienze-CNR, and Scuola Normale Superiore, I-56126 Pisa, Italy. <sup>2</sup>Radboud University Nijmegen, Institute for Molecules and Materials, NL-6525 AJ Nijmegen, Netherlands. <sup>3</sup>Kavli Institute for Theoretical Physics China, Chinese Academy of Sciences, Beijing 100190, China. <sup>4</sup>Department of Physics and Astronomy, University of Missouri, Columbia, MO 65211, USA. <sup>5</sup>Department of Applied Physics and Applied Mathematics and Department of Physics, Columbia University, New York, NY, USA. <sup>6</sup>Department of Electrical Engineering, Princeton University, Princeton, NJ, USA.

\*Present address: Department of Physics, Bose Institute, 93/1 Acharya Prafulla Chandra Road, Kolkata 700009, India.

†To whom correspondence should be addressed. E-mail: vp@sns.it (V.P.); m.polini@sns.it (M.P.)



square region with a lattice constant  $a \sim 130$  nm (Fig. 1A). We denote by  $V_0$  the amplitude of the artificial lattice potential. Here we focus on a sample with an estimated (12)  $V_0 \sim 4$  meV and electron density after processing  $n_e \sim 3 \times 10^{10}$  to  $4 \times 10^{10}$  cm $^{-2}$  corresponding to an average number of eight electrons per site. The inelastic light-scattering experiments were performed in a backscattering configuration (Fig. 1B) in the temperature range from 50 mK to 4 K. The light-scattering technique gives direct access to the collective modes of the system that manifest as sharp peaks in the intensity of the scattered light

at a given energy shift from the laser energy. Resonant enhancement of the light-scattering cross section occurs as the incident laser energy is scanned across an interband transition of the host GaAs semiconductor (20).

The nanostructured 2DEG displays well-resolved quantum Hall signatures below 3 T, with the honeycomb potential manifesting itself in a modulation of the magnetoresistivity periodic in  $B$  (12). At higher fields, an increase in the longitudinal resistivity signals a crossover to a regime of suppressed intersite hopping in which collective modes emerge.

In addition to the ordinary cyclotron mode (black curve in Fig. 1C and black circles in Fig. 1D) at energy  $\hbar\omega_c = \hbar eB/(m^*c)$ ,  $m^*$  being the GaAs electron effective mass (21), the light-scattering spectra display an additional mode at lower energies (red curve in Fig. 1C), whose collective character is reflected in the sharpness and intensity of the light-scattering peak (22, 23). The surprising sublinear dependence of the energy of this mode on  $B$  is shown in Fig. 1D (red squares).

We identified the sublinear collective mode as a Hubbard mode: an excitation across split HBs. In the simplest scenario, this excitation emerges within the single-band Hubbard model (3, 4, 6) that assumes a maximum concentration of two electrons per site. We proceeded by first evaluating the M-H excitation gap as a function of  $B$  and then showing that it weakly depends on electron concentration, consistent with the experimental data presented below. Similar conclusions can be reached by using multiband generalizations of the Hubbard model (20).

The single-band Hubbard Hamiltonian encodes a competition between two energy scales: the kinetic energy  $t$ , which measures the overlap between electronic wave functions on neighboring lattice sites, and the interaction energy  $U$ , which measures the strength of the onsite Coulomb repulsion between two electrons

$$H = -t \sum_{\langle i,j \rangle} c_i^\dagger c_j + \epsilon_0 \sum_i n_i + U \sum_i n_{i\uparrow} n_{i\downarrow} \quad (1)$$

Here the operator  $c_i^\dagger$  ( $c_i$ ) creates (destroys) an electron at site  $i$  (the sum in the first term is over all pairs of nearest-neighbor sites), and  $n_i = c_i^\dagger c_i$  is the local number operator;  $\epsilon_0$  denotes the energy of the single state that is available at each site  $i$ . This can be either empty, singly, or doubly occupied. In writing Eq. 1, we have neglected first-neighbor (intersite) interactions. In the atomic, strongly correlated limit  $U \gg t$ , two split HBs emerge out of a single narrow band (6). More precisely, this means that for  $U \gg t$ , the spectral function (that is, the tunneling density of states  $A(\omega)$ ) of the model described by Eq. 1 develops two peaks, one at  $\hbar\omega = \epsilon_0$  and one at  $\hbar\omega = \epsilon_0 + U$ . The emergence of HBs when the ratio  $U/t$  increases from the weakly to the strongly correlated regime is accurately described by dynamical mean-field theory (2–4).

In the experiments, the strongly correlated regime  $U \gg t$  is achieved when  $B$  quenches the hopping amplitude  $t$  and increases the interaction energy  $U$ . The Hubbard- $U$  interaction scale can be written in terms of localized Wannier functions  $\Phi(\mathbf{r})$  as

$$U = \int d^2\mathbf{r} \int d^2\mathbf{r}' |\Phi(\mathbf{r})|^2 V_{ee}(|\mathbf{r} - \mathbf{r}'|) |\Phi(\mathbf{r}')|^2 \quad (2)$$

where  $V_{ee}(r) = e^2/(\epsilon r)$  is the long-range Coulomb interaction, with  $\epsilon$  an effective dielectric constant. In the atomic limit, the Wannier functions can be roughly approximated by a zero-angular-

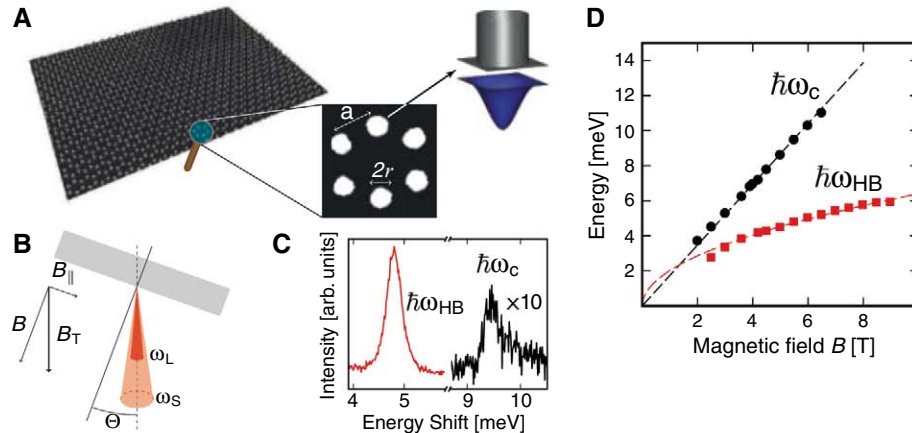


**Fig. 1.** (A) Scanning electron microscopy (SEM) image of the semiconductor artificial lattice. An expanded view of the SEM image showing a single honeycomb cell ( $2r \sim 60$  nm,  $a \sim 130$  nm) is shown at middle right. The 2DEG is positioned 170 nm below the surface with a low-temperature mobility of  $2.7 \times 10^6$  cm $^2$ /(Vs). A cartoon of the two-dimensional potential trap for electrons induced by the nanofabricated pillar at the surface is shown at far right (arrow). (B) Geometry of the light-scattering experiment:  $\omega_L, \omega_S$  labels the incident (scattered) photon energy and  $\Theta = 5^\circ$  is the tilt angle. (C) Resonant inelastic light-scattering spectra showing the cyclotron mode and the new low-lying collective mode at  $B = 5.48$  T and  $T = 1.7$  K. (D) Evolution of the energies of the cyclotron mode (black circles) and of the new collective mode at frequencies  $\omega_{HB}$  (red squares) at  $T = 1.7$  K. The black dashed line is a linear fit to the data using  $\hbar\omega_c = \hbar eB/(m^*c)$ . We find  $m^* = 0.067 m_e$  with  $m_e$  the bare electron mass, in agreement with the bulk GaAs value. The red dashed line is a fit with  $\hbar\omega_{HB} = \alpha\sqrt{B}$  [T] and  $\alpha \sim 2$  meV.

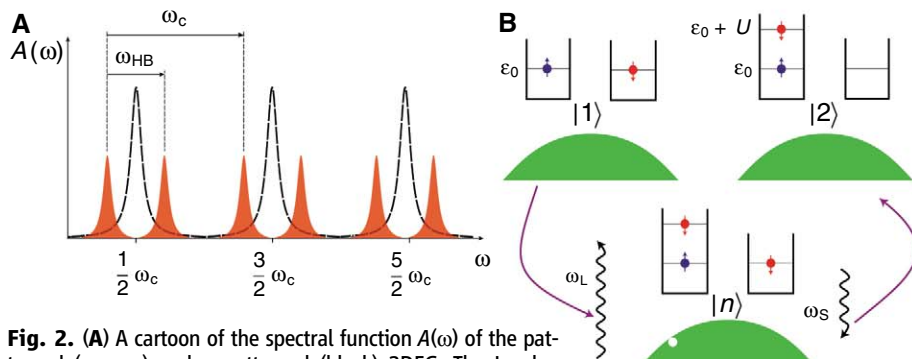


**Fig. 2.** (A) A cartoon of the spectral function  $A(\omega)$  of the patterned (orange) and unpatterned (black) 2DEG. The Landau level peaks at  $\omega_n = \omega_c(n + 1/2)$  are split by onsite Coulomb interactions into Hubbard lower and upper peaks, which are separated by  $U \sim e^2/l_B$ , where  $l_B = \sqrt{\hbar c/eB}$  is the magnetic length. (B) The relevant electronic process that contributes to the Raman scattering cross section. The initial state is labeled by  $|1\rangle$ , the final state by  $|2\rangle$ , and the intermediate state with one hole and an extra electron is labeled by  $|n\rangle$ . The final excited state is separated from the ground state by the Hubbard charge gap  $U$ ; that is, by the energy cost of having two antiparallel spin electrons on the same site. In the intermediate state, we have also depicted the absorbed (at frequency  $\omega_L$ ) and emitted (at frequency  $\omega_S$ ) photons. The square wells denote two neighboring minima of the artificial-lattice potential. The core levels are not shown. The green areas denote valence-band electrons, which are assumed to be unaffected by the periodic modulation.

momentum wavefunction in the symmetric gauge,  $\phi(\mathbf{r}) = (2\pi l_B^2)^{-1/2} \exp[-r^2/(4l_B^2)]$ , where  $l_B = \sqrt{\hbar c/eB}$  is the magnetic length. Simple algebraic manipulations on Eq. 2 yield

$$U = \sqrt{\frac{\pi}{4\epsilon}} \frac{e^2}{\epsilon l_B} \quad (3)$$

implying that, at least asymptotically,  $U$  grows proportionally to  $\sqrt{B}$ . Microscopic details such as the precise shape of the confinement potential or the geometry of the lattice might affect the result in Eq. 3 quantitatively but not qualitatively: The scaling  $\propto \sqrt{B}$  is robust in the asymptotic limit  $l_B \ll 2r$ , where  $2r$  is the width of the potential minima of the artificial lattice (Fig. 1A).

The function  $A(\omega)$  in a  $B$  field is pictorially illustrated in red in Fig. 2A. As a comparison, the black dashed line labels  $A(\omega)$  for an unpatterned 2DEG: We distinguish the usual Landau-level peaks at frequencies  $\omega_n = \omega_c(n + 1/2)$  with integer  $n$ . In the nanopatterned sample, these peaks are split into upper and lower Hubbard peaks by strong interactions. In this cartoon, the measured cyclotron mode at  $\omega_c \propto B$  is an inter-Landau-level excitation. The measured sublinear mode seen in Fig. 1, instead, can be neatly explained as an intra-Landau-level excitation, which lies at a frequency  $\omega_{HB} = U/\hbar \propto \sqrt{B}$ , between interaction-induced Hubbard peaks (24, 25).

After fitting the data labeled by red squares in Fig. 1D with the simple functional form  $\hbar\omega_{HB} = \alpha\sqrt{B[T]}$ , we found that  $\alpha$  was  $\sim 2$  meV, thereby providing a direct measurement of the Hubbard- $U$  onsite energy scale for our nanopatterned 2DEG. The measured  $U$  is by a factor of 2 smaller than the value extracted from Eq. 3 with the high-frequency GaAs dielectric constant  $\epsilon = 13$ . In Fig. 2B, we illustrate a possible two-photon process that contributes to the scattering cross section of the HB collective mode. The calculated scattering cross section decays exponentially for sufficiently large values of  $B$  (20). In Fig. 3 we report the resonant inelastic light-scattering spectra of the Hubbard mode as a function of external parameters. Figure 3A shows that, in contrast to the cyclotron mode, the intensity of the Hubbard mode increased up to  $B \approx 5.5$  T and then collapsed exponentially at higher fields, in agreement with the theoretical prediction.

The Hubbard mode energy exhibited a rather weak dependence on electron concentration (Fig. 3B); we decreased the electron concentration using a photodepletion technique (20). In the atomic limit, the dependence of the M-H gap  $\hbar\omega_{HB}$  on electron concentration is indeed a small effect, of the first order in the parameter  $t/U$ . In the limit of vanishing electron concentration, the strength of the transition between the two HBs also vanishes because there are no available states in the upper HB (20). This finding is in agreement with the large dependence of the intensity of the Hubbard mode on electron density reported in Fig. 3B. Finally, the Hubbard mode displays a large sensitivity to temperature changes (Fig. 3C) and disappears near 5 K.

We now focus on the low-energy portion of the excitation spectra,  $\hbar\omega < 1$  meV, which in ordinary 2DEGs is characterized by the spin-wave (SW) mode—a spin-flip excitation across the spin gap that, at long wavelength, occurs at the bare Zeeman energy  $g\mu_B B_T$ , where  $\mu_B$  is the Bohr magneton,  $g$  is the Landé gyromagnetic factor, and  $B_T = \sqrt{B_{||}^2 + B^2}$  is the total magnetic field (Fig. 1B). The inset to Fig. 4 shows a representative result at  $B_T = 5.5$  T. The SW mode was visible at energies near 0.15 meV. The SW energy versus total field is reported in Fig. 4 as black circles. The spin mode was not visible below  $B_T = 3$  T.

The inset to Fig. 4 displays an additional strong and sharp mode above the SW, which has no counterpart in an unpatterned 2DEG. The energy dependence of this mode is shown in Fig. 4 as red triangles. The splitting  $\Delta$  of this mode from the SW (black squares) occurs above a

threshold  $B$  value and depends on the perpendicular magnetic field only, a fact that underlines the pivotal role of electron-electron interactions. The two modes disappear at temperatures approaching 1 K. The observation of a spin doublet suggests the occurrence of a correlated state with a gap  $\Delta$ . Different types of Coulomb-driven broken-symmetry scenarios have been proposed in the context of graphene at large magnetic fields (26–31) and linked to observations of gap openings in magneto-transport experiments (16–18). One of these scenarios (28) predicts a splitting of the SW mode similar to what we saw in our experiment (32) associated to the occurrence of lattice-scale order in the honeycomb lattice.

In the case of graphene, however, the high-field regime is not experimentally accessible, because the magnetic length is much greater than the interatomic distance. This is not the case in our artificial honeycomb lattice. To support the existence of graphene-like effects in our system,

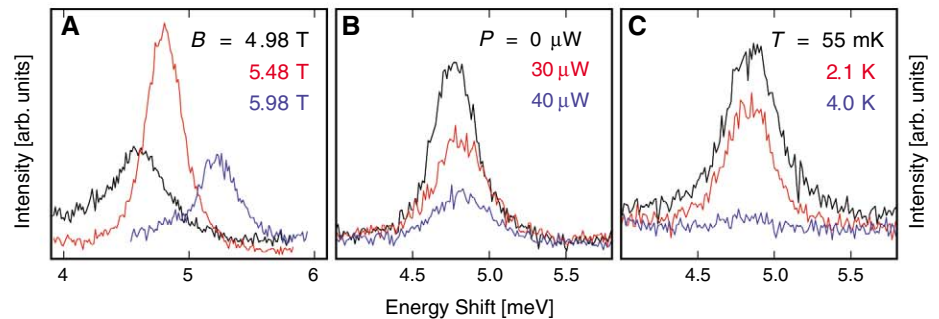
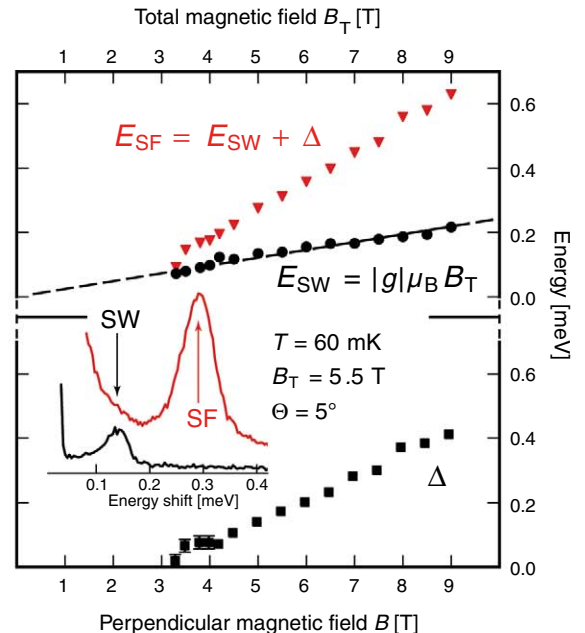


**Fig. 3.** (A) Resonant inelastic light-scattering spectra of the Hubbard mode at three values of the magnetic field and  $T = 1.7$  K. (B) Dependence of the Hubbard mode at  $T = 1.5$  K on the power  $P$  (in microwatts) of the HeNe laser used to photodeplete the 2DEG. From black to blue, the electron concentration per site decreases from  $8 \pm 2$  to  $3 \pm 2$  (21). Data in (A) are at  $P = 0$   $\mu$ W. (C) Temperature dependence of the Hubbard mode at  $B = 5.48$  T and  $P = 0$   $\mu$ W, displaying an activated behavior with an activation energy of 0.2 meV.

**Fig. 4.** Energies of the spin-wave mode (black circles) and the higher-energy spin-flip mode (red triangles). The black dashed line is a linear fit to the data using the standard Zeeman formula:  $E_{SW} = |g|\mu_B B_T$ . We find  $|g| = 0.42$ , in agreement with the value expected for GaAs. Representative examples of the two spin excitation modes at two different laser energies (red line, 1522.6 meV; black line, 1522.4 meV) are shown in the inset. The black squares label the splitting  $\Delta$  between the two spin modes.



we carried out calculations of the density of states based on a tight-binding model (33) in the presence of disorder comparable to the hopping energy and in the ultrahigh-magnetic-field regime ( $l_B < a$ ). These results reveal the persistence of a structure reminiscent of the zero-energy Landau level of graphene (20). Similar to the case in graphene (16–18, 31), electron-electron interactions can lead to a reorganization of this low-energy sector, yielding a broken-symmetry ground state with an energy gap  $\sim \Delta$ . Additionally, the observed opening of the gap above a threshold magnetic field indicates a delicate interplay between hopping, disorder, and many-body effects.

The capability of observing M-H physics in nanostructured semiconductor devices with honeycomb geometry may open new approaches for the investigation of quantum phases of strongly correlated condensed-matter systems. Given that the interaction strengths governing the physics of the 2DEG can be finely tuned by design and by the application of external electric and magnetic fields, such scalable solid-state systems offer great promise to further expand the current realms of study offered by quantum emulators that so far have been realized with cold atom gases in optical lattices (34–36).

#### References and Notes

1. N. W. Ashcroft, N. D. Mermin, *Solid State Physics* (Saunders College, Philadelphia, PA, 1976).
2. G. Kottiar, D. Vollhardt, *Phys. Today* **57**, 53 (2004).
3. G. Kottiar *et al.*, *Rev. Mod. Phys.* **78**, 865 (2006).
4. D. Vollhardt, A. Avella, F. Mancini, *AIP Conf. Proc.* **1297**, 339 (2010).
5. N. F. Mott, *Proc. Phys. Soc. (London) A* **62**, 416 (1949).
6. J. Hubbard, *Proc. Roy. Soc. (London) A* **281**, 401 (1964).

7. S. Raghu, X.-L. Qi, C. Honerkamp, S.-C. Zhang, *Phys. Rev. Lett.* **100**, 156401 (2008).
8. Z. Y. Meng, T. C. Lang, S. Wessel, F. F. Assaad, A. Muramatsu, *Nature* **464**, 847 (2010).
9. I. Buluta, F. Nori, *Science* **326**, 108 (2009).
10. T. Byrnes, N. Y. Kim, K. Kusudo, Y. Yamamoto, *Phys. Rev. B* **78**, 075320 (2008).
11. M. Gibertini, A. Singha, V. Pellegrini, M. Polini, G. Vignale, A. Pinczuk, L. N. Pfeiffer, K. W. West, *Phys. Rev. B* **79**, 241406(R) (2009).
12. G. De Simoni *et al.*, *Appl. Phys. Lett.* **97**, 132113 (2010).
13. C.-H. Park, S. G. Louie, *Nano Lett.* **9**, 1793 (2009).
14. C. Albrecht *et al.*, *Phys. Rev. Lett.* **86**, 147 (2001).
15. S. Melinte *et al.*, *Phys. Rev. Lett.* **92**, 036802 (2004).
16. Y. Zhang *et al.*, *Phys. Rev. Lett.* **96**, 136806 (2006).
17. J. G. Checkelsky, L. Li, N. P. Ong, *Phys. Rev. Lett.* **100**, 206801 (2008).
18. A. J. M. Giesbers *et al.*, *Phys. Rev. B* **80**, 201403 (2009).
19. C. P. García *et al.*, *Phys. Rev. Lett.* **95**, 266806 (2005).
20. See supporting material on Science Online.
21. A. Pinczuk *et al.*, *Phys. Rev. Lett.* **68**, 3623 (1992).
22. For example, intra-dot excitations probed in arrays of isolated quantum dots display broad (several milli-electron volts) and weak transitions (23).
23. S. Kalliakos *et al.*, *Nat. Phys.* **4**, 467 (2008).
24. Inelastic light-scattering does not directly probe  $A(\omega)$  but the density-density dynamical structure factor  $S(\omega)$ . The latter function contains, in general, extra excitations with respect to the former: These are of two-particle nature and stem from vertex corrections (25). In the single-band Hubbard model, though, these effects are of minor relevance. In this model and in the strongly correlated regime, a double-peaked spectral function implies a resonance in  $S(\omega)$  at a frequency  $\omega_{\text{HB}} = U/\hbar$ .
25. M. I. Katsnelson, A. I. Lichtenstein, *J. Phys. Condens. Matter* **22**, 382201 (2010).
26. K. Nomura, A. H. MacDonald, *Phys. Rev. Lett.* **96**, 256602 (2006).
27. D. A. Abanin, P. A. Lee, L. S. Levitov, *Phys. Rev. Lett.* **96**, 176803 (2006).
28. J. Alicea, M. P. A. Fisher, *Phys. Rev. B* **74**, 075422 (2006).
29. V. P. Gusynin, V. A. Miransky, S. G. Sharapov, I. A. Shovkovy, *Phys. Rev. B* **74**, 195429 (2006).

30. For a recent review, see, for example, (36).
31. D. S. L. Abergel, V. Apalkov, J. Berashevich, K. Ziegler, T. Chakraborty, *Adv. Phys.* **59**, 261 (2010).
32. In our experiment, in which the electron density [and not the filling factor (28)] was fixed, the splitting should increase with  $\sqrt{B}$ , as in the case of the mode at  $\hbar\omega_{\text{HB}}$  discussed above. This is, however, not consistent with the experimental data in Fig. 4, probably due to the relevance of disorder at low energies.
33. S. Yuan, H. De Raedt, M. I. Katsnelson, *Phys. Rev. B* **82**, 115448 (2010).
34. M. Greiner, O. Mandel, T. Esslinger, T. W. Hänsch, I. Bloch, *Nature* **415**, 39 (2002).
35. M. Lewenstein *et al.*, *Adv. Phys.* **56**, 243 (2007).
36. I. Bloch, J. Dalibard, W. Zwerger, *Rev. Mod. Phys.* **80**, 885 (2008).

**Acknowledgments:** We acknowledge financial support by the Project “Knowledge Innovation Program” (PKIP) of the Chinese Academy of Sciences, grant no. KJCX2.YW.W10 (M.P. and G.V.); FOM (Foundation for Fundamental Research on Matter), the Netherlands (S.Y. and M.I.K.); NSF grants DMR-0803691 (A.P.), CHE-0641523 (A.P.), and DMR-0705460 (G.V.); and the Italian Ministry of research through the FIRB (Fondo per gli Investimenti della Ricerca di Base) and PRIN (Programmi di ricerca de Relevante Interesse Nazionale) programs (V.P.). S.Y. and M.I.K. acknowledge computer time from NCF (the Netherlands). Work at Princeton University was partially funded by the Gordon and Betty Moore Foundation as well as the NSF Materials Research Science and Engineering Centers Program through the Princeton Center for Complex Materials (grant DMR-0819860). We thank R. Fazio, A. MacDonald, and P. Pingue for useful conversations.

#### Supporting Online Material

www.sciencemag.org/cgi/content/full/332/6034/1176/DC1

SOM Text

Figs. S1 to S6

References

15 February 2011; accepted 1 April 2011

10.1126/science.1204333

# A Material with Electrically Tunable Strength and Flow Stress

Hai-Jun Jin<sup>1,2\*</sup> and Jörg Weissmüller<sup>3,4</sup>

The selection of a structural material requires a compromise between strength and ductility. The material properties will then be set by the choice of alloy composition and microstructure during synthesis and processing, although the requirements may change during service life. Materials design strategies that allow for a recoverable tuning of the mechanical properties would thus be desirable, either in response to external control signals or in the form of a spontaneous adaptation, for instance in self-healing. We have designed a material that has a hybrid nanostructure consisting of a strong metal backbone that is interpenetrated by an electrolyte as the second component. By polarizing the internal interface via an applied electric potential, we accomplish fast and repeatable tuning of yield strength, flow stress, and ductility. The concept allows the user to select, for instance, a soft and ductile state for processing and a high-strength state for service as a structural material.

Environmental exposure and in-service wear influence the mechanical performance of engineering materials. Environmental effects are often adverse, as exemplified by stress corrosion cracking (1). Immersion in corrosive media may also impair strength and flow stress without immediate failure (2–4). More recently, nanoindentation studies have revealed a decisive effect of the surface state on the hardness

(5). Although the microscopic processes that couple the plasticity to the environment have not been conclusively determined, the observations demonstrate that a material’s mechanical performance can vary depending on the environment to which it is exposed during service. Here, we exploit these observations in designing a material with controllable strength and ductility. Our approach rests on two principles. First, we max-

imize the impact of surface processes by working with nanomaterials with an extremely large surface area. Second, we design the material as a hybrid in which an electrolyte becomes an inherent part of the microstructure. Interfacial properties and processes can be controlled via an electric potential, with consequences for the macroscopic behavior of the nanocomposite. In this way, the yield strength and flow stress of our material can be recoverably varied by as much as a factor of 2.

Our samples are made by dealloying, a corrosion process that selectively dissolves the less noble component from an alloy and leaves behind a monolithic body with a uniform, nanometer-scale structure composed of a contiguous skeleton of “ligaments” of the more noble component interpenetrated by an equally contiguous pore

<sup>1</sup>Shenyang National Laboratory for Materials Science, Institute of Metal Research, Chinese Academy of Sciences, 110016 Shenyang, P.R. China. <sup>2</sup>Institute of Nanotechnology, Karlsruhe Institute of Technology, D-76021 Karlsruhe, Germany. <sup>3</sup>Institut für Werkstoffphysik und -Technologie, Technische Universität Hamburg-Harburg, D-21073 Hamburg, Germany. <sup>4</sup>Institut für Werkstoffphysik, Werkstoffmechanik, Helmholtz Zentrum Geesthacht, D-21502 Geesthacht, Germany.

\*To whom correspondence should be addressed. E-mail: hjjin@imr.ac.cn



space (6, 7). Previous work has revealed extremely large local strength of the individual ligaments (8) and excellent compressive ductility of macroscopic nanoporous gold (npg) samples (9). It has also been shown that nanoporous metal wetted by electrolyte may serve as an actuator material with high stroke and high work density (10, 11).

The hybrid material is made by imbibition of the pores of npg with 1 M HClO<sub>4</sub>, an electrolyte exhibiting only weak adsorption on gold in a wide range of the electrode potential  $E$ . Figure 1 displays the microstructure of the porous metal (Fig. 1B), along with a schematic illustration of the compression test and of the in situ electrochemical control setup (Fig. 1A). The electrochemical characteristics are exemplified in the cyclic voltammogram, showing the dominantly capacitive polarization of the internal interfaces at more negative potential and the adsorption and desorption of about one monolayer of oxygen species (12) at the metal surface at more positive potential (Fig. 1C). Bulk gold oxide is not formed under these conditions (13).

We started out by compressing the hybrid material at constant potential. Figure 2A shows the compression stress-strain curves of a sample with ligament diameter  $L = 20$  nm at two values of  $E$ , 1.03 V and 1.48 V, as measured versus the standard hydrogen electrode (SHE). The potentials correspond to “clean” and “oxygen-covered” surfaces of the ligaments, respectively. The two different surface states lead to distinctly different compression performance. At the lower potential, the sample is ductile up to high strain. The inset in Fig. 2A shows photographs of the initial and final sample shapes, testifying to deformation by uniform densification at negligible transverse plastic strain. Compression at the higher potential brings a quite different behavior. Not only does the yield strength increase by 36%, from 22 MPa to 30 MPa, but there is also a noticeable loss of ductility. The differences in mechanical behavior, despite the practically identical microstructure, demonstrate the importance of changes of state at the internal interfaces for yielding and plastic flow.

The recoverability of the mechanical property changes can be verified by implementing cyclic potential jumps during compression tests. Figure 2B shows a typical stress-strain curve for such a test, superimposed on a curve recorded at a constant  $E = 1.03$  V. Both samples have  $L = 20$  nm. The segments of both graphs agree well when  $E = 1.03$  V, exemplifying the excellent sample-to-sample reproducibility of the mechanical behavior. When the potential is increased to 1.48 V, the flow stress is seen to increase rapidly. This change can be reversed, because the flow behavior at the lower voltage is recovered when the potential is switched back to 1.03 V.

Collecting data for different samples, Fig. 2C shows that the flow stress variation increases with increasing strain. At the higher strains, the flow stress can be as much as doubled by varying

the potential. The figure also contains data for samples with larger ligament diameters,  $L = 45$  and 200 nm. The results confirm the trend of larger flow stress at larger potential, while the amplitude of the variation decreases with increasing  $L$ .

The recoverable changes in plastic behavior concur with the formation and removal of the surface oxygen adsorbate layer. However, compression tests with potential jumps within the regime of capacitive charging demonstrate that adsorption is not a requirement. Figure 2D shows the recoverable change of flow stress when  $E$  is varied between 1.03 and 0.08 V, avoiding oxygen adsorption. The flow stress variation is here smaller, 10 to 15% for  $L = 20$  nm, but still appreciable. Remarkably, the sign of the flow stress–potential response is reversed compared to that in the oxygen adsorption/desorption regime. Figure 2D also shows that the flow stress change is considerably more pronounced when varying the potential between 0.08 V and 0.53 V than between 0.53 V and 1.03 V. The observations are consistent with a roughly parabolic variation of flow stress with potential, with a minimum near  $E = 0.53$  V. This is close to the potential of zero charge (pzc), which is in the range 0.24 to 0.55 V for gold in HClO<sub>4</sub> (14).

Dry npg samples were also tested to verify the extent to which the surface states and the corresponding mechanical response are preserved when the electrolyte and the potential control are removed. Samples with  $L = 20$  nm were held at 1.03 V and 1.48 V, respectively, for 30 min, then rinsed in pure water and dried at room temperature in open air for 8 to 9 days. Their stress–

strain curves are shown in Fig. 3. The dry sample with oxygen-covered surface (conditioned at 1.48 V) was less brittle than that measured in situ at 1.48 V in electrolyte, but the yield strengths were almost identical. By contrast, at  $E = 1.03$  V, the yield stress of dry samples with clean surface was lower than that measured in situ in the “wet” state (<10 MPa versus 22 MPa). This finding can be attributed to the structure coarsening to  $L = 40$  nm during drying, as evidenced by scanning electron microscopy (SEM) observation. The dependence of the flow properties on the conditioning, even after drying, implies that the surface oxygen coverage and the corresponding material strengthening can be maintained, for at least a few days, after switching off the potential and even after removing the electrolyte.

The potential-controlled plasticity we present here has parallels to the “Rehbinder effect” (2–4) and to other observations in relation to the impact of the environment on the plasticity of engineering materials (1, 15, 16). However, reports in that context document an effective weakening of metals (lesser flow stress at given strain rate or enhanced deformation rate at given stress) when exposed to electrolyte (2–4, 15, 16), whereas the present material shows the opposite behavior: Our samples are weakest when dry and with clean surfaces or near the pzc, and are strengthened by exposure to the environment. Moreover, the Rehbinder effect is suppressed by even a small addition of impurities, because solid solution hardening in the bulk dominates over surface effects on dislocation movement (17). Yet the present material exhibits a large effect of potential on the mechanical behavior, despite 5 to 10 atomic per-

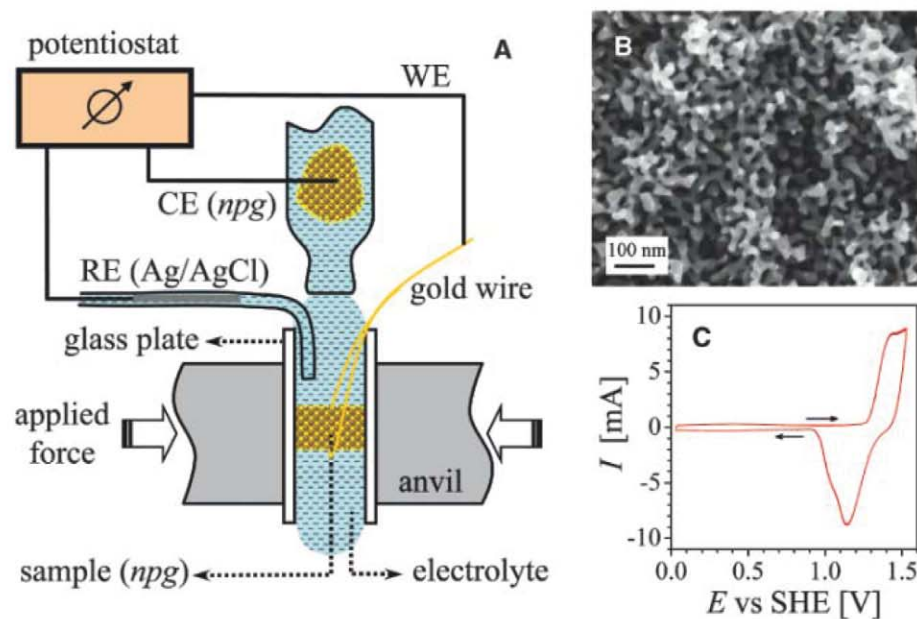


**Fig. 1.** (A) Schematic illustration of compression of bulk npg samples in situ with electrochemical control. WE, working electrode; RE, reference electrode; CE, counterelectrode. (B) SEM image of a npg sample, showing uniform and small structure size ( $L = 20$  nm). (C) Cyclic voltammogram (five successive scans) of current  $I$  versus potential  $E$  for npg in 1 M HClO<sub>4</sub> solution at the potential scan rate of 5 mV/s. Potential is specified versus the standard hydrogen electrode, SHE.

cent Ag impurities. The impact of the potential variation on the mechanical behavior even increases at larger strain, despite dislocation cell structure formation (9) and the concomitant work hardening. Obviously, the correlation between potential and strength in our nanomaterial is distinctly different from the results reported for the Rehbinder effect in bulk metals.

It seems premature to try to conclusively identify a single mechanism responsible for our observations. However, experiments similar to the ones presented here connect to important issues in the general context of nanomaterial deformation and provide new ways of probing the underlying mechanisms. As a context for inspecting some of the related aspects, let us make a rough estimate of the jump in the local flow stress,  $\sigma_L$ , of the ligaments. By means of example, we inspect the first jump in the data of Fig. 2B, where the macroscopic flow stress,  $\sigma_M$ , varies by  $\sim 30\%$ , from  $\sim 29$  MPa to  $>38$  MPa for a material with  $L = 20$  nm and an initial solid volume fraction,  $v_0$ , of 0.25. At this point, the material has undergone  $\sim 15\%$  plastic compression. Because the compression does not entail transverse plastic expansion (9), the solid volume fraction,  $v$ , scales

with the plastic engineering compression strain,  $\epsilon$ , according to  $v = v_0/(1 - \epsilon)$ . Thus,  $v$  in the example has increased to 0.29. The Gibson-Ashby foam scaling equation,  $\sigma_M = 0.3\sigma_L v^{3/2}$ , provides an approximate relation among  $\sigma_M$ ,  $v$ , and  $\sigma_L$  (18). This implies that during the potential jump, the ligament strength increases by 190 MPa, from 620 to 810 MPa. We discuss possible origins of that jump, starting with the impact of two relevant capillary parameters (19): surface stress and surface tension.

The surface stress,  $f$ , imposes a bulk stress in the solid that scales inversely with the size and varies with the electrode potential (10, 11). At extremely small ligament size and  $f > 0$ , the surface-induced bulk stress may be large enough to trigger the spontaneous shear of a nanometer-size solid (20). Previous work has found  $f$  to decrease with increasing potential throughout the potential interval under study here (21). Decreasing  $f$  requires increasing bulk stress and, consequently, elastic expansion of the porous solid. The in situ dilatometry experiments of Fig. 4 verify this effect, with a macroscopic elastic strain  $\Delta l/l_0$  (in the absence of external load) on the order of  $1.0 \times 10^{-4}$  when cycling npg with a ligament size

of 55 nm through the oxygen adsorption-desorption region. With a  $1/L$  scaling, the above finding implies  $2.8 \times 10^{-4}$  strain for the sample with  $L = 20$  nm. Using the value  $Y = 79$  GPa for Young's modulus of gold, we thus find that oxygen adsorption induces an axial stress increase of  $\sim 22$  MPa. This stress may act as a prestress that increases the external load required for yielding. The magnitude of this stress is clearly too small to account for the ligament strength increase of 190 MPa. Furthermore, the changes in flow stress and surface stress are not consistent when attention is turned to the capacitive regime. Here, the surface stress still decreases with increasing potential (see the strain data of Fig. 4), but—contrary to what is found in the OH-adsorption regime—the flow stress now decreases. In summary, our findings suggest that surface stress does not play an important role in potential-dependent strengthening.

We next consider the effect of changes in surface tension. When a ligament is sheared by the motion of a dislocation over a cross-sectional glide plane, the step edge created at the surface increases the total surface area. The condition that the mechanical work done by the Peach-Köhler forces acting on the moving dislocation is at least equal to the increase in total surface energy (extra area  $\times$  surface tension) couples the yield stress with changes in the surface tension. In support of that concept, a minimum in creep rate and a maximum in strength have been reported for macroscopic metal samples near their electrocapillary maximum of  $\gamma$  (3, 15, 16). The mechanism is specifically relevant for npg, because the ligaments are so small that almost all dislocations traveling therein may be expected to have one end or two ends moving on the surface (22, 23). Yet the concept is incompatible with our observations: The electrocapillary maximum agrees

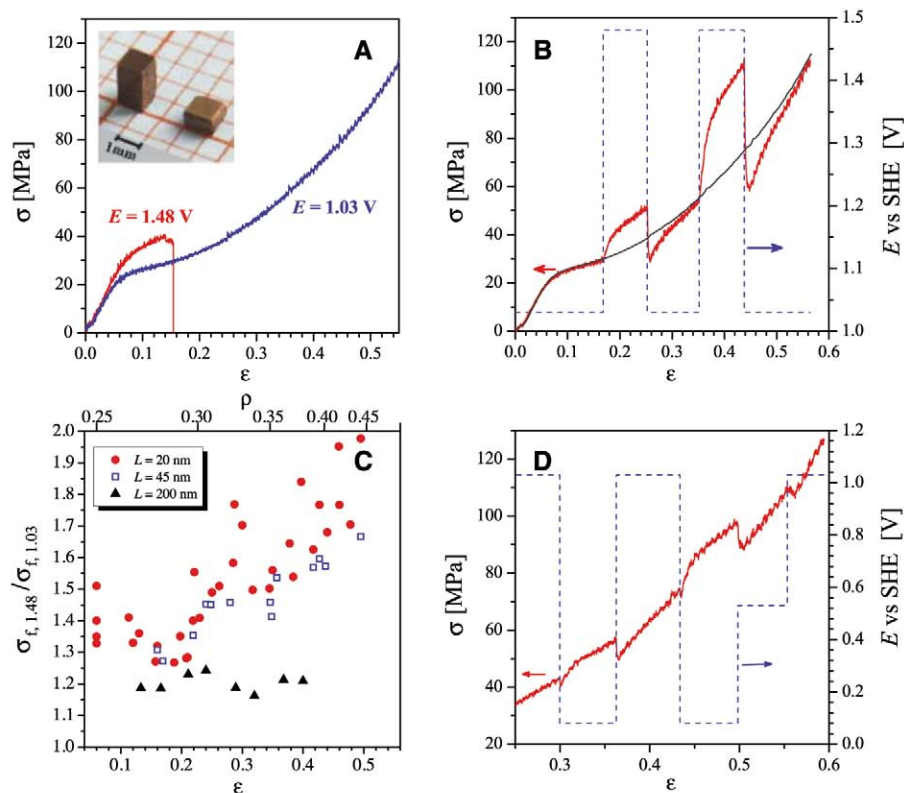


**Fig. 2.** Potential dependence of strength and flow stress of npg. (A) Compressive stress-strain curves of engineering stress,  $\sigma$ , versus engineering strain,  $\epsilon$ , measured in situ at constant potentials. Ligament surface is covered with submonolayer-thick oxygen when  $E = 1.48$  V and is clean when potential is held at 1.03 V. The inset is a photograph of npg samples with clean surface before and after compression [adapted from (9)]. (B) Responses of plastic flow (red) to potential jumps. Data obtained at a constant potential of 1.03 V (gray) were plotted for comparison. (C) Summary of strength and flow stress increase ( $\sigma_{f,1.48}/\sigma_{f,1.03}$ ) induced by surface oxygen adsorption. Note that the relative density,  $\rho$ , increases during compression. (D) Response of flow stress to potential jumps in double-layer region. Ligament diameter is 20 nm for samples in (A), (B), and (D).

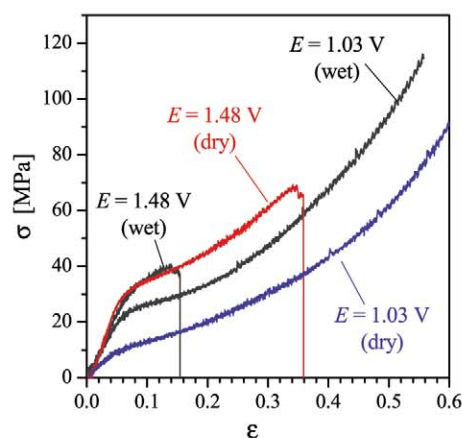
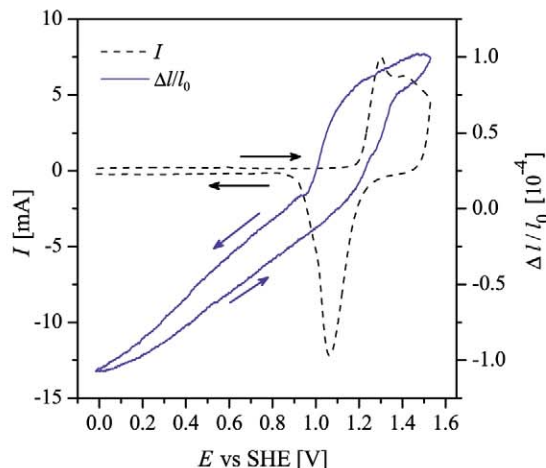


**Fig. 3.** Compression behavior of "dry" npg samples with and without surface oxygen, corresponding to pretreatment potential of 1.48 V and 1.03 V, respectively. Graphs show engineering stress,  $\sigma$ , versus engineering strain,  $\epsilon$ . Data measured in "wet" state with potentiostatic control are shown for comparison. Ligament diameter is  $L = 20$  nm except for the  $E = 1.03$  V (dry) sample, which experienced coarsening to  $L = 40$  nm during drying.

**Fig. 4.** In situ dilatometry trace (solid blue line) of outer dimension change,  $\Delta l/l_0$ , of a npg sample ( $L = 55$  nm) in response to potential sweeping in 1 M  $\text{HClO}_4$  solution at 10 mV/s. Dashed black line shows cyclic voltammogram measured during the same scan.



with the pzc (19), which is near the center of our experimental potential interval, where the flow stress is found to be at minimum. Environmental effects on the plasticity of ionic crystals have been discussed in terms of a different link between surface tension and flow stress, which does predict a flow stress minimum near the pzc: Image forces may induce cross-slip and, consequently, pinning for screw dislocation segments near free surfaces (24). The step line tension counteracts the cross slip. A reduction in surface tension and line tension would thus reduce the barrier to cross-slip, promoting pinning and ultimately strengthening the material.

As an additional interaction mechanism, we consider the possible impact of adsorption on the elastic interaction of dislocations with the surface. The drag exerted by adsorbates on moving dislocation endpoints has been termed “adsorption locking” (17). Similar to Cottrell clouds in the bulk of conventional solid solutions, adsorbed anions decorate stress fields at the surface (25). It is conceivable that the adsorbed species tend to pin the dislocation, enhancing the flow stress. Adsorption may also affect the local surface excess elastic constants and, through them, the interaction of dislocations with the surface. The modified compliance of the surface would result in a size- and potential-dependent macroscopic elastic response. In nanoporous metals, the surface effects on the effective compliance are open to experimental investigation (26).

The relevance of the dislocation endpoint drag picture of electrochemical strengthening—whether related to cross-slip or to adsorption locking—is actually supported by the results in Fig. 2C. We observed the largest flow stress change at the highest strain. In the initial nanoporous structure there are few dislocations, so the very small volumes of the ligaments may be deformed without dislocation interaction (27, 28). Yet electron backscatter diffraction imaging on npg has shown that large deformation does lead to dislocation interaction, as evidenced by the formation of subgrain boundaries by increased strain rate sensitivity (9). The creation of internal pinning points in deformed samples implies that

the free arms of the dislocations that end at the surface will become shorter, so that more stress is required to activate them. The flow stress may then be dominated by operation of many single-arm dislocations with one end locked in the interior of the material and another end traveling—with friction—on the surface. The maximum arm length is here shorter than the ligament diameter, which amplifies the surface effects. This mechanism would be characteristic for nanoscale porous materials, whereas coarser microstructures would favor coarser subgrain structures and hence would have a lesser impact of dislocation storage on the variation in flow stress. This notion agrees with the observation that the flow stress variation becomes less strain-dependent as the ligament size increases, as shown in Fig. 2C.

The action of surface dislocation endpoint drag is also consistent with the transient undershoot of the flow stress during oxygen desorption (Fig. 2B). The stress here initially falls below the constant-potential flow stress at 1.03 V, but it recovers that behavior as the deformation proceeds. The observation cannot be explained by stored elastic energy. Instead, the removal of surface oxygen apparently eases the motion of mobile dislocations or, alternatively, acts to unpin dislocations that were immobilized in the oxygen-covered state. Thus, the minimum flow stress during desorption would correspond to a transient peak in mobile dislocation density. Subsequent egression similar to what is known as “mechanical annealing” (29), or pinning by dislocation interaction, can recover the steady-state flow behavior.

We have demonstrated a hybrid material concept that affords control over mechanical performance. The material’s strength and ductility can thus be matched to altering requirements in service. For instance, the material may be switched to a soft and ductile state for processing, or to a high-strength state for service as a structural material. The recoverable changes in the flow stress approach a factor of 2. On a more speculative level, hybrid materials similar to the one investigated may even adapt their performance spontaneously. The response of the internal stresses to surface charging is analogous to the response

of the local electrode potential to elastic strain (30, 31). In a properly designed electrochemical environment, this change may prompt local adsorption processes at stress concentrations (25, 32). As we have shown, such processes may drastically enhance the strength. This provides a mechanism for selectively removing weak spots from a microstructure, which is an essential part of a self-healing strategy. Essential to this strategy is our demonstration that deposition of submonolayer adsorbate layers is sufficient to largely enhance the strength of nanoscale hybrid materials.

## References and Notes

1. K. Sieradzki, R. C. Newman, *Philos. Mag. A* **51**, 95 (1985).
2. P. Rehner, *Nature* **159**, 866 (1947).
3. A. Pfützenreuter, G. Masing, *Z. Metallk.* **42**, 361 (1951).
4. F. R. N. Nabarro, *Theory of Crystal Dislocations* (Clarendon, Oxford, 1967), pp. 294–297.
5. S. G. Corcoran, S. R. Brankovic, N. Dimitrov, K. Sieradzki, *Mat. Res. Soc. Symp. Proc.* **505**, 77 (1998).
6. J. Erlebacher, M. J. Aziz, A. Karma, N. Dimitrov, K. Sieradzki, *Nature* **410**, 450 (2001).
7. J. Weissmüller, R. C. Newman, H. J. Jin, A. M. Hodge, J. W. Kysar, *MRS Bull.* **34**, 577 (2009).
8. J. Biener et al., *Nano Lett.* **6**, 2379 (2006).
9. H. J. Jin et al., *Acta Mater.* **57**, 2665 (2009).
10. J. Weissmüller et al., *Science* **300**, 312 (2003).
11. H. J. Jin, J. Weissmüller, *Adv. Eng. Mater.* **12**, 714 (2010).
12. B. E. Conway, *Prog. Surf. Sci.* **49**, 331 (1995).
13. H. J. Jin, S. Parida, D. Kramer, J. Weissmüller, *Surf. Sci.* **602**, 3588 (2008).
14. D. M. Kolb, J. Schneider, *Electrochim. Acta* **31**, 929 (1986).
15. A. R. C. Westwood, R. M. Latanision, *Metall. Sci. Eng.* **25**, 225 (1976).
16. C. J. van der Weken, *J. Electrochem. Soc.* **129**, 706 (1982).
17. A. R. C. Westwood, *Philos. Mag.* **7**, 633 (1962).
18. L. J. Gibson, M. F. Ashby, *Cellular Solids: Structure and Properties* (Cambridge Univ. Press, Cambridge, 1997).
19. D. Kramer, J. Weissmüller, *Surf. Sci.* **601**, 3042 (2007).
20. J. K. Diao, K. Gall, M. L. Dunn, *Phys. Rev. B* **70**, 075413 (2004).
21. H. Ibach, C. E. Bach, M. Giesen, A. Grossmann, *Surf. Sci.* **375**, 107 (1997).
22. C. Motz, D. Weygand, J. Senger, P. Gumbsch, *Acta Mater.* **57**, 1744 (2009).
23. C. R. Weinberger, W. Cai, *Scr. Mater.* **64**, 529 (2011).
24. J. J. Gilman, *Philos. Mag.* **6**, 159 (1961).
25. M. Gsell, P. Jakob, D. Menzel, *Science* **280**, 717 (1998).
26. A. Mathur, J. Erlebacher, *Appl. Phys. Lett.* **90**, 061910 (2007).
27. M. D. Uchic, D. M. Dimiduk, J. N. Florando, W. D. Nix, *Science* **305**, 986 (2004).
28. C. A. Volkert, E. T. Lilleodden, *Philos. Mag.* **86**, 5567 (2006).
29. Z. W. Shan, R. K. Mishra, S. A. Syed Asif, O. L. Warren, A. M. Minor, *Nat. Mater.* **7**, 115 (2008).
30. M. Smetanin, D. Kramer, S. Mohanan, U. Herr, J. Weissmüller, *Phys. Chem. Chem. Phys.* **11**, 9008 (2009).
31. J. Weissmüller, R. N. Viswanath, L. A. Kibler, D. M. Kolb, *Phys. Chem. Chem. Phys.* **13**, 2114 (2011).
32. L. A. Kibler, A. M. El-Aziz, R. Hoyer, D. M. Kolb, *Angew. Chem. Int. Ed.* **44**, 2080 (2005).

**Acknowledgments:** Supported by Deutsche Forschungsgemeinschaft grant We1424/14 and by the Hundred Talents Program of the Chinese Academy of Sciences (H.-J.J.). We thank L. Kurmanova and Y. Ivanisenko for assistance with the compression experiments, K. Sieradzki and H. Gleiter for stimulating discussions, and K. Lu for critical reading of the manuscript.

## Supporting Online Material

www.sciencemag.org/cgi/content/full/332/6034/1179/DC1  
Materials and Methods  
Figs. S1 and S2

27 December 2010; accepted 8 April 2011  
10.1126/science.1202190



# Magnetosphere Sawtooth Oscillations Induced by Ionospheric Outflow

O. J. Brambles,<sup>1\*</sup> W. Lotko,<sup>1</sup> B. Zhang,<sup>1</sup> M. Wiltberger,<sup>2</sup> J. Lyon,<sup>3</sup> R. J. Strangeway<sup>4</sup>

The sawtooth mode of convection of Earth's magnetosphere is a 2- to 4-hour planetary-scale oscillation powered by the solar wind–magnetosphere–ionosphere (SW-M-I) interaction. Using global simulations of geospace, we have shown that ionospheric O<sup>+</sup> outflows can generate sawtooth oscillations. As the outflowing ions fill the inner magnetosphere, their pressure distends the nightside magnetic field. When the outflow fluence exceeds a threshold, magnetic field tension cannot confine the accumulating fluid; an O<sup>+</sup>-rich plasmoid is ejected, and the field dipolarizes. Below the threshold, the magnetosphere undergoes quasi-steady convection. Repetition and the sawtooth period are controlled by the strength of the SW-M-I interaction, which regulates the outflow fluence.

Sawtooth oscillations were first observed in the fluxes of energetic charged particles at geosynchronous orbit (1, 2) and are so called because the time series of the particle fluxes resemble the teeth of a saw blade, with a 2- to 4-hour periodic sequence of slow decrease followed by rapid increase. Many other geophysical processes have since been shown to vary in sync with periodic particle injections: magnetic fields measured at geostationary orbit, in the magnetotail, and at ground stations; the auroral electrojet index; auroral precipitation; and the polar cap index (3–7). Although observational studies of sawtooth oscillations have revealed a rich phenomenology of magnetospheric responses to quasi-steady driving by the solar wind, basic understanding of why they occur is lacking. This deficiency affects our ability to model magnetospheric dynamics accurately and to forecast space weather.

Sawtooth oscillations occur during relatively stable solar wind conditions when external triggering by variability in the interplanetary medium is absent. This behavior suggests that the response of the magnetosphere–ionosphere (M-I) system is conditioned by an internal mechanism. However, the mean sawtooth period of 3 hours (8, 9) is much longer than any known electrodynamic cavity oscillation of the M-I system, even when extended to include the bow shock as a boundary (10). The ionospheric and magnetospheric signatures of an individual sawtooth are similar to those of isolated substorms (5); that is, episodic conversions of magnetic energy to plasma energy in Earth's magnetotail, with two noteworthy exceptions: The signatures of sawtooth substorms are more broadly distributed in local time, with particle injections, dipolarizations, and ground signatures spanning from midnight to the

dawn-dusk meridian and even into the dayside; and sawtooth signatures are more intense in the geostationary region than are those of isolated substorms. The sawtooth mode is also distinguished from the steady magnetospheric convection (SMC) mode, which is driven by similar, though somewhat weaker, upstream conditions (11–13). Energy transfer from dayside and nightside magnetic reconnection is in near balance during SMC events (14), which do not exhibit the oscillations in convection characteristic of sawtooth events. It is not known why the solar wind–magnetosphere–ionosphere (SW-M-I) interaction settles into an SMC state versus a sawtooth oscillation under similar driving conditions or why differences in driving conditions should lead to one state or the other.

Global simulations of magnetospheric dynamics based on equations of magnetohydrodynamics (MHD) provide physical insights into system behavior that are difficult to infer from *in situ* satellite measurements alone. Previous global simulations have been able to capture observed features of geomagnetic storms (15, 16), isolated substorms (17, 18), and other events. They produce the SMC mode (19, 20), the stretching of magnetic fields associated with sawtooth oscillations (21), and fast periodic reconnections of the magnetotail when a non-MHD electric field is included (22), but they fail to give ~3-hour global-scale, quasi-periodic substorms that define the sawtooth mode. This shortcoming suggests that sawtooth dynamics are governed by a physical process not included in existing global models. We used global simulations to show that the outflow of heavy ions from Earth's ionosphere can dramatically change the convection cycle of the magnetosphere and promote sawtooth oscillations.

The magnetosphere is a variable admixture of plasmas of ionospheric and solar wind origin (23), with the ionospheric source becoming more prevalent during the strong driving conditions typical of geomagnetic storms and sawtooth events (24). Heavy ion outflows from the ionosphere are most intense in the dayside cusp region (25) and near the polar cap boundary of the nightside auroral zone (26), where shear Alfvén waves (trans-

verse electromagnetic waves that propagate energy along magnetic field lines in an MHD fluid) deposit electromagnetic power (27, 28). Alfvén wave energy can be converted to ion energy either directly when the transverse scale of the wave becomes comparable to the ion gyroradius (29) or indirectly via secondary instabilities that excite ion gyroscale waves driven by the wave field-aligned current and velocity shear (30). Satellite studies estimate that 95% of heavy ion upflows are produced by low-frequency broadband turbulence typical of Alfvén waves and associated instabilities (31).

We used the multifluid Lyon-Fedder-Mobarry (LFM) global model (32, 33) to simulate the SW-M-I system, including the effects of O<sup>+</sup> ionospheric outflows [supporting online material (SOM)]. The outflow boundary condition is specified in terms of an observed statistical correlation between Alfvénic Poynting flux  $S_{||}$  and accelerated O<sup>+</sup> outflow flux  $F_{O^+}$

$$F_{O^+} = 2.97 \times 10^{10} S_{||}^{1.2} \quad (1)$$

with  $F_{O^+}$  given in ions/cm<sup>2</sup>-s and  $S_{||}$  in mW/m<sup>2</sup>. Although this statistical correlation exhibits considerable variance in observations and alone does not establish a direct causal link between  $F_{O^+}$  and  $S_{||}$ , it does provide an empirical means of specifying an average outflow flux at the low-altitude simulation boundary for a given Poynting flux flowing downward through the boundary.

We evaluated the impact of the outflow on global convection from an ensemble of controlled simulations. The first set of investigations explored the dependence of convection on the outflow fluence  $F_{TOT}$  (in ions/s), calculated as the integrated flux in the Northern Hemisphere at a radial geocentric distance of 2.5 Earth radii ( $R_E$ ). To understand the effects of variance in the empirical relationship (Eq. 1), we rescaled the equation with a constant scaling parameter  $\alpha$  so that  $S_{||} \rightarrow \alpha S_{||}$  and considered a range of  $\alpha \geq 0$  (34). The second set of experiments explored the dependence of the convection state on varying solar wind conditions for fixed  $\alpha = 3.8$  (Table 1).

Studies using satellite measurements find that the outflow fluence under strong driving conditions is on the order of  $10^{26}$  ions/s (35). The simulated fluences listed in Table 1 are thus representative of observations when  $\alpha$  is in the range from 1 to 6. The strength of interplanetary driving is measured by the SW-M coupling parameter  $\epsilon \equiv V_{SW} B_{IMF} \sin^2(\theta/2) P_{dyn}^{1/6}$  (36), where  $V_{SW}$  is the solar wind velocity,  $B_{IMF}$  is the magnitude of the interplanetary magnetic field,  $\theta$  is IMF clock angle in the  $y$ - $z$  plane ( $= 180^\circ$  for all simulations in Table 1), and  $P_{dyn} = \rho_{SW} V_{SW}^2$  is the dynamic pressure of the solar wind of mass density  $\rho_{SW}$ . For fixed  $\alpha (= 3.8)$ , Table 1 shows that the outflow fluence increases with increasing  $\epsilon$  in this model. The trend is linear:  $\langle F_{TOT} \rangle = 0.6 \times \epsilon + 0.2$  with  $\langle F_{TOT} \rangle$  in  $10^{26}$  ions/s and  $\epsilon$  in (mV/m) (nPa)<sup>1/6</sup>.

<sup>1</sup>Thayer School of Engineering, Dartmouth College, Hanover, NH, USA. <sup>2</sup>High Altitude Observatory, National Center for Atmospheric Research, Boulder, CO, USA. <sup>3</sup>Department of Physics and Astronomy, Dartmouth College, Hanover, NH, USA. <sup>4</sup>Institute for Geophysics and Planetary Physics, University of California, Los Angeles, CA, USA.

\*To whom correspondence should be addressed. E-mail: ojbrambles@dartmouth.edu

The outflow is located throughout the simulated auroral oval, with a peak in the premidnight sector (Fig. 1). The dawn-dusk asymmetry is a consequence of the asymmetry in the precipitation-induced ionospheric conductance derived from LFM’s electron precipitation model. The nightside morphology resembles statistical maps of both Alfvénic Poynting flux (27) and O<sup>+</sup> outflow flux (28) derived from satellite data; however, these simulations do not produce the persistent O<sup>+</sup> outflow fluxes typically observed in the dayside cusp. This difference is possibly due to the steady solar wind conditions in the simulations, which do not generate significant time-variable perturbations of the dayside magnetic field and accompanying Alfvén wave power flowing into the cusp ionosphere. Other simulations using a heuristic model for cusp outflows show that their interaction with the M-I system is weak because the bulk of the cusp outflow intersects the plasma sheet tailward of the nightside reconnection line (33). Thus, cusp O<sup>+</sup> outflows are not expected to change the qualitative nature of the results reported here.

The magnetosphere in the baseline simulation (no outflow,  $\alpha = 0$ ) settles into an SMC state, with magnetic reconnection occurring in the nightside plasma sheet at a tailward distance of approximately 25  $R_E$ . The inclusion of O<sup>+</sup> outflow inflates the magnetotail and causes reconnection to migrate further tailward. For  $\alpha = 1$  (run A), the tail is more dynamic, with nightside reconnection variably located between 30 and 45  $R_E$ . Despite this increased variability, the system remains in an SMC state. As the outflow fluence increases in runs B to F, the nightside field lines become more stretched, and nightside reconnection migrates even further tailward to 50 to 65  $R_E$ . This stretching originates from the additional pressure of the magnetospheric O<sup>+</sup> population, which enhances both the “ballooning” pressure force and the diamagnetic ring current that shears the ambient magnetic field. Both effects distend and stress the magnetic field lines. It is not clear at this point which is dominant. For sufficiently high outflow fluence, the nightside field lines are stressed to the point of inducing plasmoid ejection. The now unbalanced magnetic field tension forces the fluid and embedded field Earthward to dipolarize in the inner region. This release of stored energy is manifested as a substorm. A large fraction of the O<sup>+</sup> fluid is lost downstream in the plasmoid and to the magnetopause during the convective surge associated with the substorm. The nightside ionospheric outflow then continues to fill the inner magnetosphere, stretching the field lines once again, resulting in another substorm (fig. S2).

We analyzed the simulation magnetic inclination angle near geostationary orbit to estimate the substorm periodicity and to compare the simulation results with sawtooth substorms observed in satellite data (Fig. 2). The baseline run 0 and run J exhibit SMC behavior, whereas the other three cases (C, H, and I) in Fig. 2 exhibit sawtooth oscillations with decreasing period and

**Table 1.** Simulation parameters: Bold numbers indicate simulations with quasi-steady convection; nonbold numbers indicate simulations with quasi-periodic behavior. The solar wind density and temperature are constant at 5/cm<sup>3</sup> and 10 eV, and Earth’s dipole tilt angle is zero. The mean fluence  $\langle F_{\text{TOT}} \rangle$  was derived from a 20-hour average in each simulation.

Run	$V_{\text{sw}}$ (km/s)	$B_z$ (nT)	$\alpha$	$\epsilon$	$\langle F_{\text{TOT}} \rangle$ 10 <sup>26</sup> /s
<b>0</b>	<b>400</b>	<b>−10</b>	<b>0</b>	<b>3.7</b>	<b>0</b>
<b>A</b>	<b>400</b>	<b>−10</b>	<b>1</b>	<b>3.7</b>	<b>0.46</b>
B	400	−10	2.14	3.7	1.18
C	400	−10	3.80	3.7	2.36
D	400	−10	5.32	3.7	3.55
E	400	−10	6.76	3.7	4.80
F	400	−10	12.0	3.7	9.59
<b>G</b>	<b>200</b>	<b>−10</b>	<b>3.80</b>	<b>1.5</b>	<b>1.08</b>
H	600	−10	3.80	6.4	4.02
I	400	−5	3.80	1.9	1.36
<b>J</b>	<b>400</b>	<b>−2.5</b>	<b>3.80</b>	<b>0.9</b>	<b>0.79</b>

**Fig. 1.** Morphology of ion outflow from simulation C, averaged over 1 hour, starting 3 hours after the simulation startup period. The auroral oval, defined by Feldstein (white) (42), is superimposed. For reference, the flux has been mapped along field lines to the ionosphere using  $F_{\text{O}^+}/B_d = \text{constant}$  ( $B_d$  is the magnitude of the dipole magnetic field).

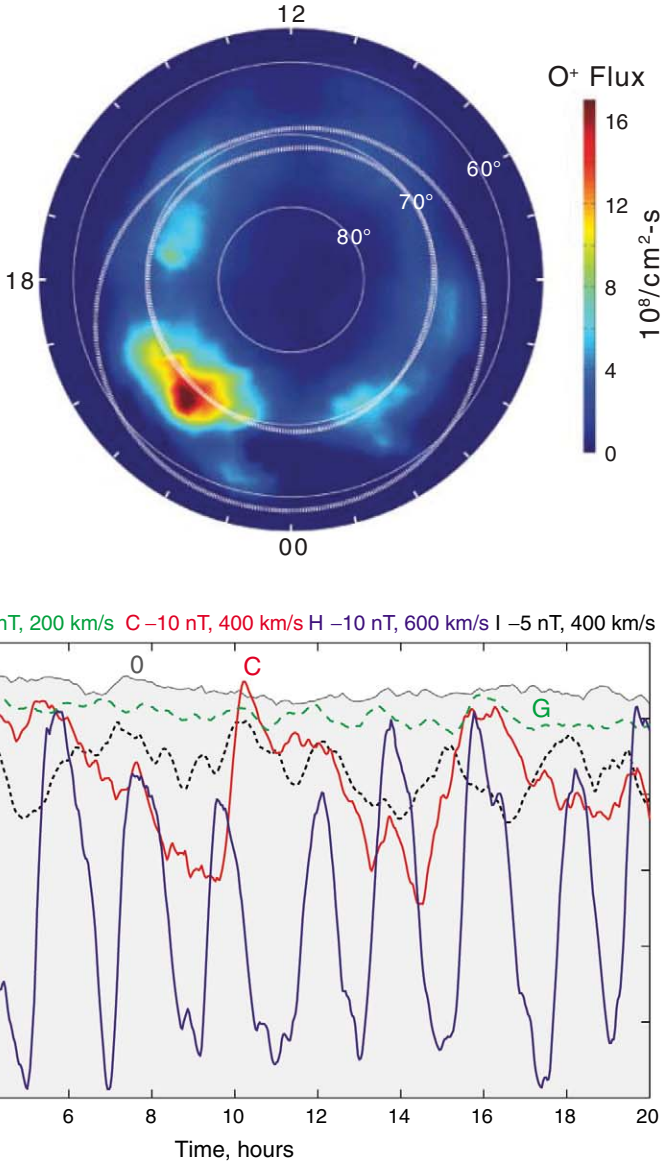


**Fig. 2.** Simulated magnetic inclination angle,  $\theta_i = \sin^{-1}(B_z/B)$ , as a function of simulation time at 2330 MLT,  $(x^2 + y^2)^{1/2} = 6.6 R_E$ , and  $z = 0.5 R_E$ .  $B_z$  and  $B$  are the z-component and total field magnitude at the simulation measurement point. Comparisons are shown for runs 0, C, G, H, and I.

increasing amplitude of the magnetic inclination angle evident as the strength of interplanetary driving ( $\epsilon$ ) is increased. Observed SMC and sawtooth states both require quasi-steady solar wind drivers, but the magnitude of the driver is observed to be stronger for sawtooth oscillations (37), as in the simulations. From Table 1, an outflow fluence exceeding about  $1.1 \times 10^{26}$  ions/s is a necessary condition for the onset of sawtooth oscillations in the simulations. Although the SW-M-I system is more complicated than the simulations, the relationship between  $\epsilon$ , outflow fluence, sawtooth versus SMC state, and sawtooth period can be tested observationally.

We used the power spectral density of the time variation in magnetic inclination angle to determine the sawtooth period, with variance in period defined as the full width at half maximum of the spectral peak defining the period. As the outflow fluence was increased in simulations B through F, the period decreased and tended to a value of approximately 2 hours (Fig. 3). Simu-

lations C to E and H produce outflow fluences in agreement with the observed estimates on the order of  $10^{26}$  ions/s (35). They also yield sawtooth oscillations with periods ranging from 2 to 5 hours, consistent with the 2- to 4-hour range derived from satellite measurements (9).

The dipolarization time in the simulations ranged from 0.5 to 1 hour, compared to an average of 22 min in observed sawtooth oscillations, with standard deviation of 15 min (9). Thus, for simulated events with periods approaching 2 hours or less, the periodic waveforms resemble nonlinear sinusoids rather than sawteeth. The apparent minimum period in Fig. 3 may be a consequence of the artificially long dipolarization time in the simulations. This longer dipolarization may be a feature of numerically induced magnetic reconnection in the simulations, which does not allow for explosive local reconnection enabled by kinetic effects or a current-driven instability (38). Alternatively, if the  $O^+$  abundance of the reconnection inflow is anomalously high,

giving a lower Alfvén speed relative to that of the actual system, then the mass-loaded inflow may also produce slower dipolarization in the simulations.

A distinguishing feature of the sawtooth mode as compared to isolated substorms is the wide extent in magnetic local time (MLT) (39) of signatures such as field line stretching and dipolarization. We examined this feature by comparing a superposed epoch analysis of magnetic inclination angle for all simulated sawtooth events in Fig. 3 with periods of 1.75 to 5 hours to a superposed epoch derived from observed sawtooth events (5) (Fig. 4). The simulated and observed results exhibit a number of striking similarities: The minimum inclination angle of the simulated sawteeth is  $27^\circ$  as compared to  $26^\circ$  of observed sawteeth, with both being lower than the average minimum inclination angle of  $43^\circ$  observed at geostationary orbit for isolated substorms (5). The observed and simulated sawteeth produce more intense signatures at geostationary orbit than do isolated substorms, and both exhibit dawn-dusk asymmetry, with more pronounced features in the premidnight sector. The asymmetry in the simulated onset is caused by the asymmetry in outflow as discussed above. The MLT extent of the simulated sawteeth is not as broad as in observations; for example, the  $44^\circ$  contour at 0.0 UT in the simulated sawteeth spans 10 hours of MLT, as compared to 12 hours of MLT for the observed sawteeth. However, the MLT extent in the simulations is still far wider than the average MLT extent of 2 hours for an isolated substorm (5). This profound difference arises from internal processes, which supplant and overcome the evolution of open field lines in the Dungey convection cycle (40). These processes intensify the ring current through the addition of adiabatically energized  $O^+$  of ionospheric origin, which also

**Fig. 3.** Relationship between outflow fluence and sawtooth period for each simulation exhibiting quasi-periodic behavior. The colors represent solar wind conditions as follows:  $V_{SW} = 400$  km/s,  $B_z = -10$  nT (blue);  $V_{SW} = 600$  km/s,  $B_z = -10$  nT (red);  $V_{SW} = 400$  km/s,  $B_z = -5$  nT (black). Squares indicate simulations with  $\alpha = 3.8$ ; circles indicate simulations with different values of  $\alpha$ .

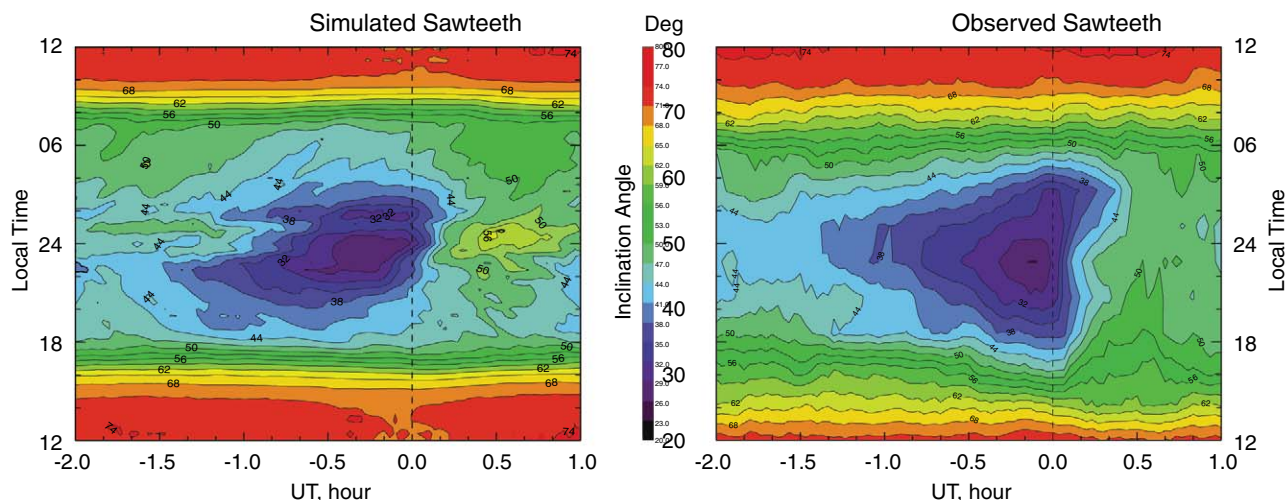
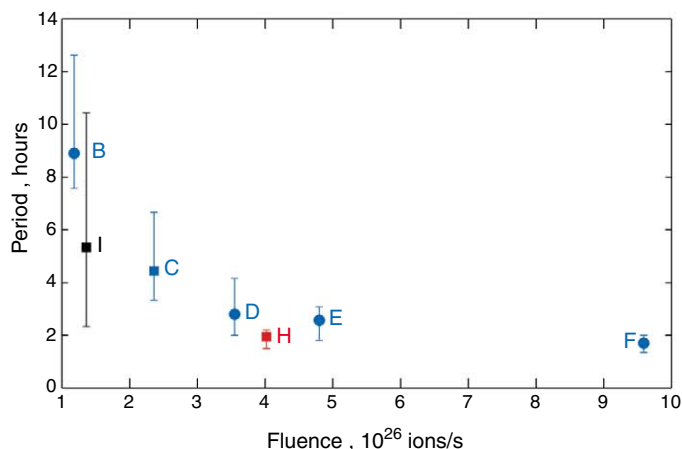


**Fig. 4.** Superposed epoch analysis of magnetic inclination angle near geostationary orbit for simulated (left) and observed (right) sawteeth (5). The magnetic inclination angle is evaluated on the circle  $(x^2 + y^2)^{1/2} = 6.6 R_E$  in the plane  $z = 0.5 R_E$  for simulated sawteeth and at geostationary

satellites for observed sawteeth. For each sawtooth, dipolarization onset (fiducial time 0 UT) is visually inferred as the last minimum before the rapid increase in magnetic inclination angle in the 2330 to 0030 MLT sector (5).



augments the radial pressure force to the point that magnetic tension in the geostationary magnetosphere can no longer contain the fluid, not even in the dawn-dusk meridian. In this sense, the convection cycle of a sawtooth substorm resembles the Vasyliunas cycle (41) at Jupiter, wherein corotating, mass-loaded flux tubes pinch off to form plasmoids in the premidnight sector, then cyclically refill after rotating around the magnetosphere again. The Vasyliunas cycle at Jupiter is periodic in space; its analog at Earth is periodic in time. Jupiter's periodic cycle is powered by planetary rotation; in contrast, Earth's cycle is powered by the SW-M dynamo and its propensity to produce ionospheric outflows.

Although we have shown that ionospheric outflow in MHD simulations can produce the sawtooth convection mode, we do not know if it is the only (or the most important) mechanism.

## References and Notes

- R. D. Belian, T. E. Cayton, *Proc. Res. Inst. Atmos. Nagoya Univ.* **36**, 127 (1989).
- J. E. Borovsky, R. J. Nemzek, R. D. Belian, *J. Geophys. Res.* **98**, 3807 (1993).
- C. Huang *et al.*, *J. Geophys. Res.* **108**, 1255 (2003).
- K. Kitamura, H. Kawano, S. Ohtani, A. Yoshikawa, K. Yumoto, *J. Geophys. Res.* **110**, A07208 (2005).
- X. Cai, M. G. Henderson, C. R. Clauer, *Ann. Geophys.* **24**, 3481 (2006).
- M. G. Henderson *et al.*, *J. Geophys. Res.* **111**, A01590 (2006).
- O. Troshichev, A. Janzhura, *J. Atmos. Sol. Terr. Phys.* **71**, 1340 (2009).
- C. Huang, *Geophys. Res. Lett.* **29**, 2189 (2002).
- X. Cai, C. R. Clauer, *J. Geophys. Res.* **114**, A06201 (2009).
- I. Mann, A. Wright, K. Mills, V. Nakariakov, *J. Geophys. Res.* **104**, 333 (1999).
- V. A. Sergeev, *Phys. Sol. Terr. Potsdam* **5**, 39 (1977).
- T. Pytte, R. L. McPherron, E. W. Hones Jr., H. I. West Jr., *J. Geophys. Res.* **83**, 663 (1978).
- V. A. Sergeev, R. J. Pellinen, T. I. Pulkkinen, *Space Sci. Rev.* **75**, 551 (1996).
- R. L. McPherron, T. P. O'Brien, S. Thompson, in *Multiscale Coupling of Sun-Earth Processes*, A. T. Y. Lui, Y. Kamide, G. Consolini, Eds. (Elsevier, Amsterdam, 2005), pp. 113–124.
- R. M. Winglee, D. Chua, M. Brittner, G. K. Parks, G. Lu, *J. Geophys. Res.* **107**, 1237 (2002).
- A. Gloer, G. Toth, T. Gombosi, D. Welling, *J. Geophys. Res.* **114**, A05216 (2009).
- M. Wiltberger, T. Pulkkinen, J. Lyon, C. Goodrich, *J. Geophys. Res.* **105**, 27649 (2000).
- J. Raeder, D. Larson, W. Li, E. L. Kepko, T. Fuller-Rowell, *Space Sci. Rev.* **141**, 535 (2008).
- C. C. Goodrich, T. I. Pulkkinen, J. G. Lyon, V. G. Merkin, *J. Geophys. Res.* **112**, A08201 (2007).
- T. I. Pulkkinen, C. C. Goodrich, J. G. Lyon, *Geophys. Res. Lett.* **34**, L21101 (2007).
- B. Lavraud, J. E. Borovsky, *J. Geophys. Res.* **113**, A00B08 (2008).
- M. M. Kuznetsova *et al.*, *J. Geophys. Res.* **112**, A10210 (2007).
- E. Shelley, R. Johnson, R. Sharp, *J. Geophys. Res.* **77**, 6104 (1972).
- M. Nosé *et al.*, *J. Geophys. Res.* **110**, A09524 (2005).
- B. Thelin, B. Aparicio, R. Lundin, *J. Geophys. Res.* **95**, 5931 (1990).
- Y.-K. Tung *et al.*, *J. Geophys. Res.* **106**, 3603 (2001).
- A. Keiling, J. R. Wygant, C. A. Cattell, F. S. Mozer, C. T. Russell, *Science* **299**, 383 (2003).
- C. C. Chaston, C. W. Carlson, J. P. McFadden, R. E. Ergun, R. J. Strangeway, *Geophys. Res. Lett.* **34**, L07101 (2007).
- C. C. Chaston *et al.*, *J. Geophys. Res.* **109**, A04205 (2004).
- C. E. Seyler, K. Liu, *J. Geophys. Res.* **112**, A09302 (2007).
- P. Norqvist, M. André, M. Tyrland, *J. Geophys. Res.* **103**, 23459 (1998).
- J. Lyon, J. Fedder, C. Mobarry, *J. Atmos. Sol. Terr. Phys.* **66**, 1333 (2004).
- O. Brambles *et al.*, *J. Geophys. Res.* **115**, A00J04 (2010).
- Variations in outflow flux with electromagnetic power input may be due to seasonal or solar cycle influences on the source population or to variations in preconditioning of the M-I system before the initiation of a sawtooth event. In addition, the simulation model may not accurately replicate the power typically observed in the Alfvénic band (see SOM).
- C. M. Cully, E. F. Donovan, A. W. Yau, G. G. Arkos, *J. Geophys. Res.* **108**, 1093 (2003).
- V. M. Vasyliunas, J. R. Kan, G. L. Siscoe, S.-I. Akasofu, *Planet. Space Sci.* **30**, 359 (1982).
- A. D. DeJong, A. J. Ridley, X. Cai, C. R. Clauer, *J. Geophys. Res.* **114**, A08215 (2009).
- The reconnection in the LFM code is predominantly averaging error; opposing magnetic flux enters a single cell and is averaged (annihilated) out of existence (32). The rate of reconnection is sensitive to the conditions external to the actual reconnection region. In cases where the external flow toward the reconnection site is zero, the reconnection is effectively also zero. When reconnection is driven (that is, forced by convergent flow), the rate can be quite high. The maximum rate is constrained by a Petschek-like inflow condition to be a fraction (~0.1) of the Alfvén speed in the inflow.
- For zero dipole tilt angle in these simulations, MLT is similar to geographic local time, where 1200 MLT always directly faces the sun.
- J. W. Dungey, *Phys. Rev. Lett.* **6**, 47 (1961).
- V. M. Vasyliunas, in *Physics of the Jovian Magnetosphere*, A. J. Dessler, Ed. (Cambridge Univ. Press, New York, 1983), pp. 395–453.
- Y. I. Feldstein, G. V. Starkov, *Planet. Space Sci.* **18**, 501 (1970).
- M. Wiltberger, R. S. Weigel, W. Lotko, J. A. Fedder, *J. Geophys. Res.* **114**, A01204 (2009).
- P. Banks, T. Holzer, *J. Geophys. Res.* **73**, 6846 (1968).
- W. Baumjohann, R. A. Treumann, *Basic Space Plasma Physics* (Imperial College Press, London, 1996), chap. 2.
- A. W. Yau, M. André, *Space. Sci. Rev.* **80**, 1 (1997).
- B. Hultqvist, M. Oieroset, G. Paschmann, R. Treumann, Eds., *Magnetospheric Plasma Sources and Losses* (Springer, New York, 1999).
- R. J. Strangeway, R. E. Ergun, Y. Su, C. W. Carlson, R. C. Elphic, *J. Geophys. Res.* **110**, A03221 (2005).
- G. Paschmann, S. Haaland, R. Treumann, Eds., *Auroral Plasma Physics* (Space Sciences Series of ISSI, Kluwer Academic, Dordrecht, Netherlands, 2003), pp. 70–74.
- M. Bouhram *et al.*, *Ann. Geophys.* **22**, 1787 (2004).
- W. Lotko, *J. Atmos. Sol. Terr. Phys.* **66**, 1443 (2004).

**Acknowledgments:** This research was supported by the NASA Sun-Earth Connection Theory Program (grant NNX08AI36G), the NASA Living With a Star Targeted Research and Technology Program (grants NNX07AQ16G and NNX07AT15G), and the Center for Integrated Space Weather Modeling funded by the NSF Science and Technology Centers program under cooperative agreement ATM-0120950. Computing resources for the research were provided by the National Center for Atmospheric Research under Computational Information Systems Laboratory Project 36761008. The National Center for Atmospheric Research is supported by NSF. Simulation data are available from O. Brambles. FAST satellite data are available online at <http://sprg.ssl.berkeley.edu/fast/>.

## Supporting Online Material

[www.sciencemag.org/cgi/content/full/332/6034/1183/DC1](http://www.sciencemag.org/cgi/content/full/332/6034/1183/DC1)  
SOM Text  
Figs. S1 and S2  
References (43–51)

14 January 2011; accepted 27 April 2011  
10.1126/science.1202869

# Evidence of a Global Magma Ocean in Io's Interior

Krishan K. Khurana,<sup>1\*</sup> Xianzhe Jia,<sup>2</sup> Margaret G. Kivelson,<sup>1,2</sup> Francis Nimmo,<sup>3</sup> Gerald Schubert,<sup>1</sup> Christopher T. Russell<sup>1</sup>

Extensive volcanism and high-temperature lavas hint at a global magma reservoir in Io, but no direct evidence has been available. We exploited Jupiter's rotating magnetic field as a sounding signal and show that the magnetometer data collected by the Galileo spacecraft near Io provide evidence of electromagnetic induction from a global conducting layer. We demonstrate that a completely solid mantle provides insufficient response to explain the magnetometer observations, but a global subsurface magma layer with a thickness of over 50 kilometers and a rock melt fraction of 20% or more is fully consistent with the observations. We also place a stronger upper limit of about 110 nanoteslas (surface equatorial field) on the dynamo dipolar field generated inside Io.

**I**o, the most volcanic planetary body in the solar system, is known for its prodigious thermal output [ $>2$  W/m<sup>2</sup>, roughly 30 times Earth's averaged output, (1, 2)]. Gravity studies suggest (3) that Io's differentiation has resulted in a metallic iron core with a radius of 650 to 950 km,

surrounded by a mantle believed to be peridotitic (4) with a density of 3250 to 3700 kg m<sup>-3</sup> and forsterite (Mg<sub>2</sub>SiO<sub>4</sub>) likely the most abundant mineral (5). Extensive volcanism has probably created a lower-density, cold, rigid outer crust (6). Surface lava temperatures hint at an upper-mantle

temperature of 1250° to 1450°C, suggesting that beneath the crust there lies a fully or partially molten layer [the asthenosphere (7, 8)], but its existence and state are matters of considerable debate (9–12). Here we interpret magnetic field measurements made near Io as strengthening the evidence for such a layer.

Induction caused by Jupiter's rotating magnetic field was previously used to identify electrically conducting subsurface oceans in the icy satellites Europa, Ganymede, and Callisto (13–15). At Io, too, the inductive response can be used to infer the properties of its interior, because the conductivities of subsurface layers depend on the temperatures and the melt states of their constituent rocks (16–19). The conductivities of dry solid ultramafic rocks increase from  $10^{-9}$  S/m at room temperature (20) to  $\sim 10^{-3}$  S/m at 1200°C and  $\sim 10^{-2}$  S/m at 1400°C at pressures prevailing in Io's upper mantle (17, 18). Ultramafic rock melts have conductivities in the range of 1 to 5 S/m at 1200° to 1400°C, and partially molten rocks have conductivities ranging from  $10^{-4}$  to 5 S/m, depending on factors such as temperature, composition, melt fraction, and melt connectivity (17–19).

Magnetic data useful for induction studies were obtained by the Galileo spacecraft from Io on four passes, labeled I24, I27, I31, and I32. The I24 and I27 passes are especially useful because they probed low Io latitudes, where the induction signature maximizes, and occurred when Io was outside of the dense part of the jovian plasma sheet near the time of maximum inducing field ( $>500$  nT). For these near-equatorial flybys, in the Cartesian coordinate system called  $I\phi\Omega$ , with  $x$  parallel to Io's orbital velocity,  $y$  directed toward Jupiter, and  $z$  completing the orthogonal triad, induction contributed minimally to the  $B_z$  component, allowing us to focus on the fit to the observed  $B_z$  profile to validate our plasma interaction model and on the  $B_x$  and  $B_y$  components to establish the magnitude of the inductive response. I31 and I32 are less valuable for induction studies because they probed polar regions where the expected induction field is weak as compared with the field perturbations imposed by interaction with jovian plasma.

Near Io, field perturbations arise from both external and internal sources. Magnetohydrodynamic (MHD) perturbations result from the interaction of Io's atmosphere with Jupiter's corotating plasma (21). There, the jovian plasma is slowed by mass loading, charge exchange, and interaction with Io's conducting ionosphere.

Alfvénic perturbations called Alfvén wings couple Io to Jupiter's ionosphere, exerting forces that drive mass-loaded plasma toward corotation (22). We calculated this interaction field from a three-dimensional MHD simulation model (23) analogous to that used successfully for interpreting data acquired near Ganymede (24). An additional perturbation source is the inductive response of Io to the first three rotational harmonics (12.953, 5.619, and 4.962 hours) in Jupiter's field.

The vector amplitudes (in nanoteslas) of the three harmonics are (309, 734, 118), (70, 106, 11), and (10, 14, 1) in the  $I\phi\Omega$  coordinate system. The second and third harmonics are excited by the quadrupolar and octupolar terms of Jupiter's internal dynamo. To model the inductive response to this multifrequency primary field, we used multiple-shell models of internal conductivity (25). In the models, the cold crust had zero conductivity and a thickness of 50 km (6). To obtain

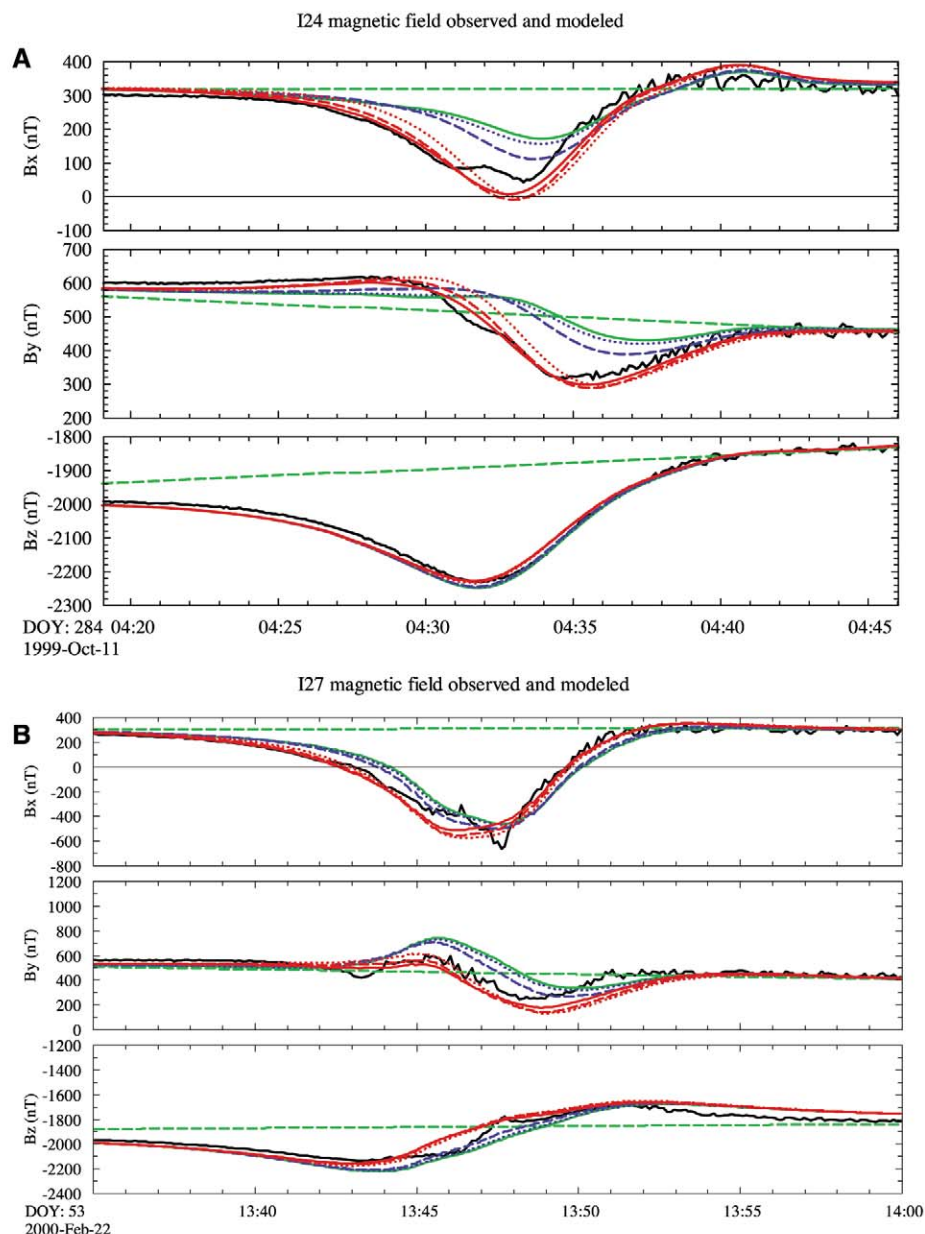


**Fig. 1.** (A) Observations (solid black curves) and model fields (colored lines) for the I24 pass. The dashed green line represents the jovian background field near Io. The MHD model (no induction) is plotted with solid green lines. The MHD models that include the inductive field from the following are shown: a warm solid mantle at 1200°C (conductivity = 0.002 S/m, dotted blue lines), a hot solid mantle at 1400°C (conductivity = 0.007 S/m, dashed blue lines), an asthenosphere with a 5% melt fraction (conductivity = 0.1 S/m) overlying a hot solid mantle (dotted red lines), an asthenosphere with a 20% melt fraction (conductivity = 0.43 S/m) overlying a hot solid mantle (dashed red lines), and a perfectly conducting shell located underneath the crust (solid red lines). (B) Same as (A), except for the I27 pass.

<sup>1</sup>Institute of Geophysics and Planetary Physics, University of California at Los Angeles, Los Angeles, CA 90095, USA. <sup>2</sup>Department of Atmospheric, Oceanic and Space Sciences, University of Michigan, Ann Arbor, MI 48109-2143, USA. <sup>3</sup>Department of Earth and Planetary Sciences, University of California Santa Cruz, Santa Cruz, CA 95064, USA.

\*To whom correspondence should be addressed. E-mail: kkhurana@igpp.ucla.edu

the conductivity of the mantle, we assumed that Io has fully differentiated (3), starting from a chondritic bulk composition (8). After the removal of silicate-rich material for a 30- to 50-km crust and of iron to form a core with a radius of 900 to 1000 km, the three main constituents remaining in the mantle were  $\text{SiO}_2$ ,  $\text{MgO}$ , and  $\text{FeO}$  with weight %'s of 44, 32, and 14% (8). A good Earth analog for this type of rock is a lherzolite (derived from Spitzbergen, Norway), an ultramafic igneous rock believed to be derived from Earth's upper mantle (18). We used the electrical properties of this rock (18) to simulate Io's mantle.

As in earlier work on Europa's subsurface ocean, the solutions to the electromagnetic diffusion equation for the multiple-shell model with a perfectly conducting core were expressed in terms of Bessel functions (14, 25). The amplitude and phase responses were computed from all three jovian rotational harmonics and then summed and used to represent the internal field of Io in an MHD simulation. Even though MHD models with induction from a solid mantle fit the observations better than a model without an inductive layer, the fits were unsatisfactory (Fig. 1).

To refine the modeling further, we explored three-layer models in which a conducting asthenosphere overlies a solid mantle (Fig. 2). Even for a warm solid mantle [with conductivity ( $\sigma_1$ ) = 0.002 S/m], the primary signal does not penetrate to the core, thus no appreciable induction is expected from the core and the conductivity of the core becomes irrelevant. Figure 2 demonstrates that for asthenospheric conductivity,  $\sigma_0 \rightarrow 1$  S/m (expected in rocks with >20% melt fraction), induced fields >600 nT can be generated near Io. Further, asthenospheric thickness ( $h$ ) cannot be established when it exceeds 100 km, because the response saturates. However,  $\sigma_0$  and hence the melt fraction of the asthenosphere can still be inferred.

With little guidance available on asthenospheric thickness and melt fraction from tidal dissipation models (11, 26–28), we treated these as fit parameters of our model. We obtained the conductivity of the partial melt from the melt fraction using an empirical relationship derived from laboratory experiments performed on ultramafic rocks from Earth's upper mantle (17, 19). Responses from all three jovian spin harmonics were included. It is clear that an asthenospheric melt fraction  $\geq 20\%$  is required for a satisfactory model of the measurements from the I24 and I27 flybys (Fig. 1). Thus, our work shows that Io currently hosts a partially or fully molten asthenosphere, with a thickness exceeding 50 km and a melt fraction of at least a few tens of percent. Current observations from Galileo are inadequate to place any stronger limits on  $h$ . Signals at longer than 13-hour periodicity are required to probe more deeply into Io's interior.

We fitted the difference fields (observations minus MHD responses without induction) from the four flybys to equatorial magnetic dipoles

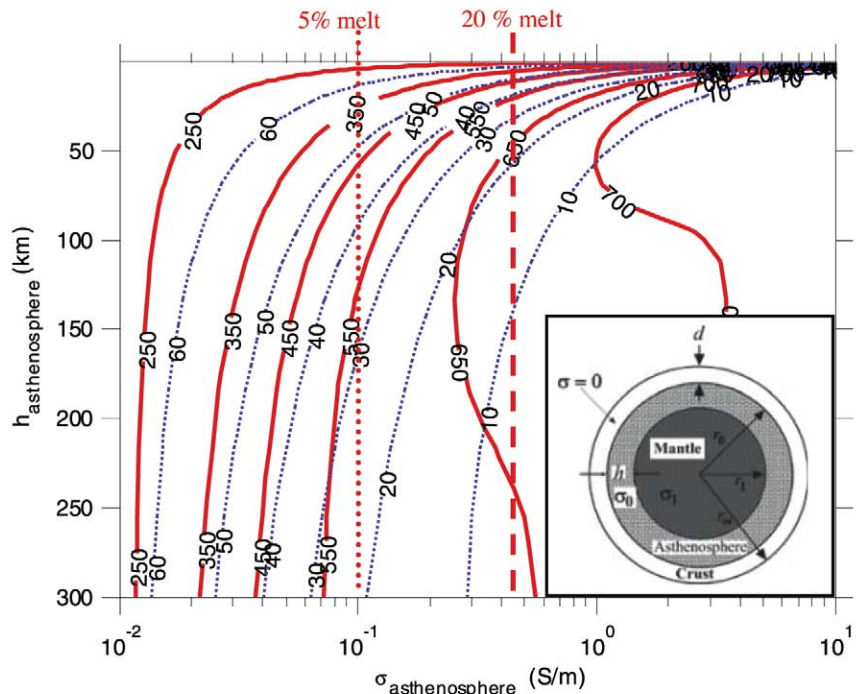


**Fig. 2.** The amplitude in nanoteslas at the pole of the induced dipole on Io's surface (labels on red curves) and the phase delay in degrees (labels on dotted blue curves) of the magnetic field for a three-layer model of Io consisting of a crust, a partially molten asthenosphere, and a hot solid mantle (inset) for a range of asthenospheric conductivities (x axis) and thicknesses (y axis). The period and amplitude of the inducing field were assumed to be 12.953 hours and 800 nT.

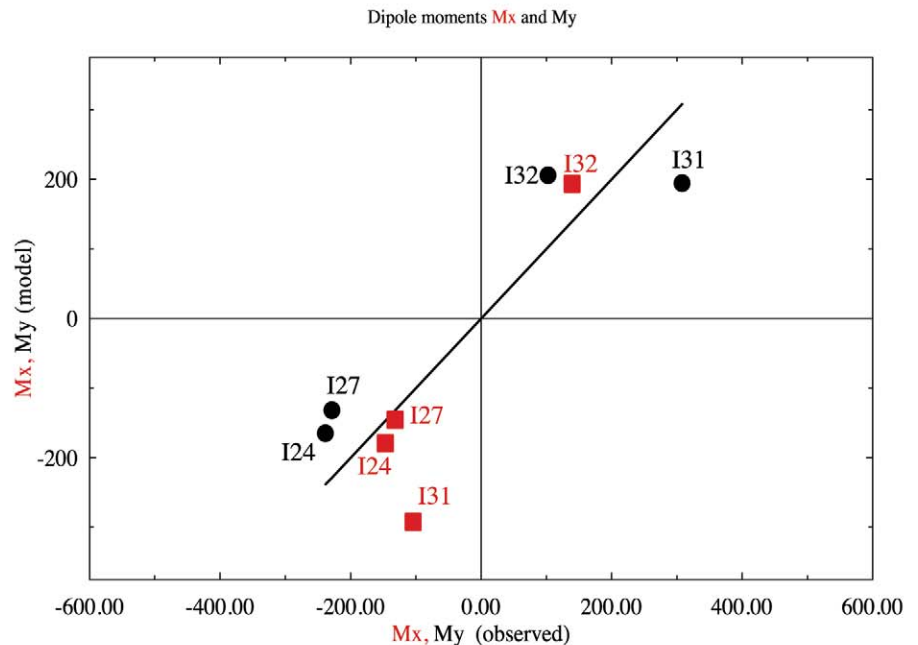


**Fig. 3.** The components of the observed dipole moments [ordinate,  $M_x$  (red squares) and  $M_y$  (black circles)] for the four flybys plotted against those expected from a 100% induction model (abscissa). The black solid line has a slope of unity.

(Fig. 3). Even though there is some scatter, it is clear that the observations require induction from a globally distributed good conductor. The observed dipole moment changes in strength

and direction in response to the changing primary field, ruling out a dynamo-generated field. The form of the observed field (dipolar and global) rules out localized regions of melt as



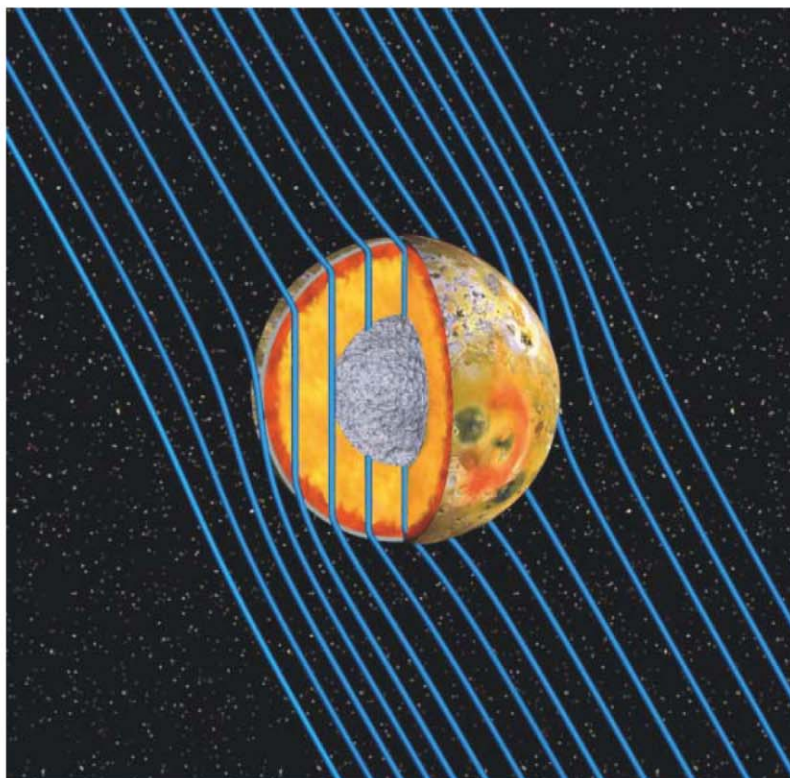


**Fig. 4.** The internal structure of Io as revealed by the present study. Underneath a low-density crust 30 to 50 km thick (gray outline in the cross section) exists a global magma layer (asthenosphere) with a thickness exceeding 50 km and a rock melt fraction of a few tens of percent (red-brown outline). The high electrical conductivity of the asthenosphere prevents the time-varying horizontal component of the jovian field from significantly penetrating into the mantle. The almost constant vertical magnetic field pervades the ultramafic mantle (golden hues in cross section), which must have a temperature exceeding 1200°C to support rock melts in the asthenosphere. The 600- to 900-km-radius core composed of Fe-FeS is rendered in a metallic silver hue.

sources, because such unconnected conductors would induce higher-order spherical harmonics (which we did not observe), with a dipolar moment much weaker than the saturated response that we observed. On the other hand, a global layer of interconnected melts is a valid explanation for our data.

After subtracting the MHD + inductive response (calculated from our 20% melt model) from the observations, we inverted the residual fields from the four flybys for a common dipole moment. The value (−38.2, 73.6, 67.5) nT obtained for the dipole moment in  $I\phi\Omega$  coordinates shows that if Io has a permanent internal magnetic field, it is extremely weak.

The presence of a partially molten asthenosphere (Fig. 4) in Io supports the idea that Io's mantle is too hot to effectively cool its core, thus explaining the apparent absence of a dynamo (29) and making it more likely that Io's core is completely molten. This result marks the asthenosphere as a primary site of tidal heating and allows us to predict that Io's heat flux, if predominantly due to tidal heating in the asthenosphere, will be higher in equatorial regions as compared to the poles (26). Lateral variations of asthenospheric

thickness and/or melt fraction that would arise from non-uniform heating modify the magnetic induction spectrum at frequencies not resolved in our data set.

#### References and Notes

1. G. J. Veeder, D. Matson, T. Johnson, D. Blaney, J. Gougen, *J. Geophys. Res.* **99**, 17095 (1994).
2. J. A. Rathbun *et al.*, *Icarus* **169**, 127 (2004).
3. J. D. Anderson, R. A. Jacobson, E. L. Lau, W. B. Moore, G. S. Schubert, *J. Geophys. Res.* **106**, 32,963 (2001).
4. W. B. Moore, G. Schubert, J. D. Anderson, J. S. Spencer, in *Io After Galileo*, R. M. C. Lopes, J. R. Spencer, Eds. (Springer-Praxis, Chichester, UK, 2007), pp. 89–108.
5. F. Sohl, D. Spohn, D. Breuer, K. Nagel, *Icarus* **157**, 104 (2002).
6. L. Keszthelyi, A. McEwen, *Icarus* **130**, 437 (1997).
7. L. Keszthelyi, A. S. McEwen, G. J. Taylor, *Icarus* **141**, 415 (1999).
8. L. Keszthelyi *et al.*, *Icarus* **192**, 491 (2007).
9. M. N. Ross, G. Schubert, *Icarus* **64**, 391 (1985).
10. J. R. Spencer, N. M. Schneider, *Annu. Rev. Earth Planet. Sci.* **24**, 125 (1996).
11. M. Segatz, T. Spohn, M. N. Ross, G. Schubert, *Icarus* **75**, 187 (1988).
12. L. Keszthelyi, W. L. Jaeger, E. P. Turtle, M. Milazzo, J. Radebaugh, *Icarus* **169**, 271 (2004).
13. K. K. Khurana *et al.*, *Nature* **395**, 777 (1998).
14. C. Zimmer, K. K. Khurana, M. G. Kivelson, *Icarus* **147**, 329 (2000).

15. M. G. Kivelson, K. K. Khurana, M. Volwerk, *Icarus* **157**, 507 (2002).
16. M. C. Sinha *et al.*, *Philos. Trans. R. Soc. London Ser. A* **355**, 233 (1997).
17. G. M. Partzsch, F. R. Schilling, J. Arndt, *Tectonophysics* **317**, 189 (2000).
18. J. Maumus, N. Bagdassarov, H. Schmeling, *Geochim. Cosmochim. Acta* **69**, 4703 (2005).
19. F. R. Schilling, G. M. Partzsch, H. Brasse, G. Schwarz, *Phys. Earth Planet. Inter.* **103**, 17 (1997).
20. G. R. Olhoeft, in *Physical Properties of Rocks and Minerals*, Y. S. Touloukian, W. R. Judd, R. F. Roy, Eds. (Hemisphere Publishing, New York, 1989), pp. 257–329.
21. An earlier simulation of I24 and I27 flybys (30) treated the multifluid nature of the atmosphere and the plasma with sophistication but sacrificed self-consistency of the magnetic field. Furthermore, the large perturbations obtained in that simulation were found in a run using upstream plasma conditions that were markedly different from those measured on the passes we analyzed.
22. F. M. Neubauer, *J. Geophys. Res.* **103**, 19843 (1998).
23. X. Jia, R. J. Walker, M. G. Kivelson, K. K. Khurana, J. A. Linker, *J. Geophys. Res.* **114**, A09209 (2009).
24. Materials and methods are available as supporting material on Science Online.
25. W. D. Parkinson, *Introduction to Geomagnetism* (Scottish Academic Press, Edinburgh, 1983).
26. M. N. Ross, G. Schubert, T. Spohn, R. W. Gaskell, *Icarus* **85**, 309 (1990).
27. H. Fischer, J. T. Spohn, *Icarus* **83**, 39 (1990).
28. W. B. Moore, *Icarus* **154**, 548 (2001).
29. U. Weinbruch, T. Spohn, *Planet. Space Sci.* **43**, 1045 (1995).
30. J. Saur, F. M. Neubauer, D. F. Strobel, M. E. Summers, *J. Geophys. Res.* **107**, 1422 (2002).
31. E. Lellouch, *Space Sci. Rev.* **116**, 211 (2005).
32. J. R. Spencer *et al.*, *Icarus* **176**, 283 (2005).
33. L. M. Feaga, M. McGrath, P. D. Feldman, *Icarus* **201**, 570 (2009).
34. R. E. Johnson, *Astrophys. J.* **609**, L99 (2004).
35. M. C. Wong, W. H. Smyth, *Icarus* **146**, 60 (2000).
36. R. E. Johnson *et al.*, in *Jupiter: The Planets, Satellites and Magnetosphere*, F. Bagenal, T. E. Dowling, W. B. McKinnon, Eds. (Cambridge Univ. Press, Cambridge, 2004), pp. 485–512.
37. J. A. Linker, K. K. Khurana, M. G. Kivelson, R. J. Walker, *J. Geophys. Res.* **103**, 19,867 (1998).
38. X. Jia, R. J. Walker, M. G. Kivelson, K. K. Khurana, J. A. Linker, *J. Geophys. Res.* **113**, A06212 (2008).
39. M. A. McGrath, R. E. Johnson, *J. Geophys. Res.* **94**, (A3), 2677 (1989).
40. L. A. Frank, W. R. Paterson, *J. Geophys. Res.* **105**, 25,363 (2000).
41. L. A. Frank, W. R. Paterson, *J. Geophys. Res.* **106**, 26,209 (2001).
42. L. A. Frank, W. R. Paterson, *J. Geophys. Res.* **107**, 1220 (2002).
43. D. A. Gurnett, A. M. Persoon, W. S. Kurth, A. Roux, S. J. Bolton, *J. Geophys. Res.* **106**, 26,225 (2001).

**Acknowledgments:** The work at the University of California at Los Angeles was supported by NASA grant NNX08AT48G and NSF Planetary Astronomy grant AST-0909206. The field and plasma data used in this work are available online on the Planetary Data System at <http://ppi.pds.nasa.gov/search/?s=GALILEO%20ORBITER>.

#### Supporting Online Material

[www.sciencemag.org/cgi/content/full/science.1201425/DC1](http://www.sciencemag.org/cgi/content/full/science.1201425/DC1)  
SOM Text  
References (31–43)

8 December 2010; accepted 15 April 2011  
Published online 12 May 2011;  
10.1126/science.1201425

# Diminishing Returns Epistasis Among Beneficial Mutations Decelerates Adaptation

Hsin-Hung Chou,<sup>1\*</sup> Hsuan-Chao Chiu,<sup>2</sup> Nigel F. Delaney,<sup>1</sup> Daniel Segrè,<sup>2,3</sup> Christopher J. Marx<sup>1,4†</sup>

Epistasis has substantial impacts on evolution, in particular, the rate of adaptation. We generated combinations of beneficial mutations that arose in a lineage during rapid adaptation of a bacterium whose growth depended on a newly introduced metabolic pathway. The proportional selective benefit for three of the four loci consistently decreased when they were introduced onto more fit backgrounds. These three alleles all reduced morphological defects caused by expression of the foreign pathway. A simple theoretical model segregating the apparent contribution of individual alleles to benefits and costs effectively predicted the interactions between them. These results provide the first evidence that patterns of epistasis may differ for within- and between-gene interactions during adaptation and that diminishing returns epistasis contributes to the consistent observation of decelerating fitness gains during adaptation.

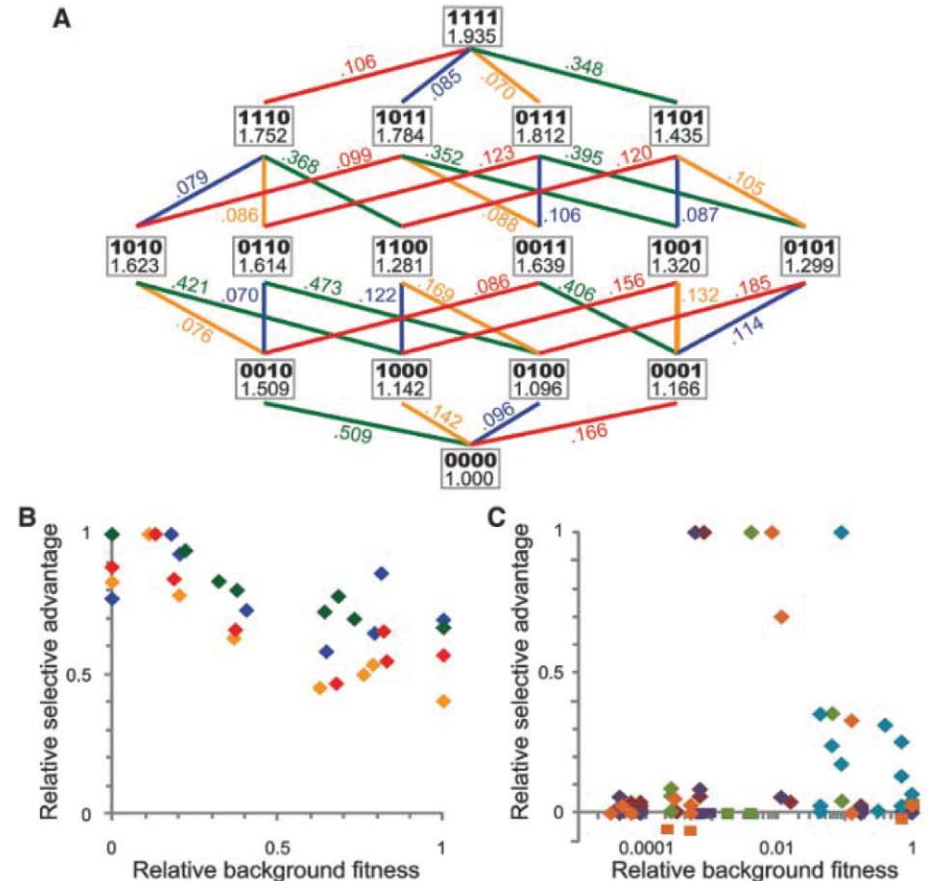
Epistasis describes genetic interactions in terms of how phenotypic effects of a mutation depend on other mutations in the genome. If two mutations act on a given phenotype independently, each would be expected to exert the same proportional effect regardless of whether the other allele was present, although other models can be applied (1–3). Deviations from this null expectation have been used to uncover interacting genes via genetic screens for

second mutations that suppress the effect of the first, to identify the order of enzymes in biochemical pathways, and to unravel systems-level interaction patterns characterized with genome-wide double-knockout libraries. One general trend has been that the detrimental effect of a lesion in a pathway (or module) (4) is greater alone than when there is already another deleterious mutation in that process (i.e., antagonistic epistasis). In contrast, lesions in parallel pathways

producing the same product tend to cause stronger phenotypes (synergistic epistasis) than expected; the extreme case of the latter, termed synthetic lethality, results in a nonviable genotype.

Epistasis between beneficial mutations remains largely unexplored. Previous studies examined epistasis between five amino acid (or promoter) substitutions within an allele of  $\beta$ -lactamase selected for cefotaxime resistance in *Escherichia coli* (5). By constructing all possible mutation combinations within the  $\beta$ -lactamase locus, a single-peaked fitness landscape was revealed with numerous cases where the identical mutation increased resistance on some backgrounds but decreased it on others (i.e., sign epistasis). Similar results have been found for cofactor use by isopropylmalate dehydrogenase (6) and for hormone receptors (7). In contrast, few studies have addressed interactions between beneficial mutations in different genes (8, 9).

**Fig. 1.** Mutational network and distinct patterns of epistasis for mutations between and within genes. **(A)** Each node displays the allelic composition (*fghA*, *pntAB*, *gshA*, *GB*) of a given genotype (bold) and its fitness. Ancestral and evolved alleles are indicated by 0 and 1, respectively, leading from the ancestral EM strain (0000) to the evolved EVO isolate (1111). Each edge indicates an allelic replacement (*fghA*, orange; *pntAB*, blue; *gshA*, green; *GB*, red) and the corresponding selective coefficient. Variation in relative selective effect (normalized to maximum  $s_i$ ) of each allele as a function of the fitness of the background it was introduced into is shown for: **(B)** between-gene epistasis in *Methylobacterium* [background fitness normalized from EM = 0 to maximum = 1; colors as in (A)] or **(C)** within-gene epistasis for *E. coli*  $\beta$ -lactamase [background fitness normalized to minimum inhibitory concentration maximum of 1; log scale for visualization; squares indicate deleterious effects]. [Data from (5)]



<sup>1</sup>Department of Organismic and Evolutionary Biology, Harvard University, Cambridge, MA 02138, USA. <sup>2</sup>Graduate Program in Bioinformatics, Boston University, Boston, MA 02215, USA. <sup>3</sup>Department of Biology and Department of Biomedical Engineering, Boston University, Boston, MA 02215, USA. <sup>4</sup>Faculty of Arts and Sciences Center for Systems Biology, Harvard University, Cambridge, MA 02138, USA.

\*Present address: Institute of Molecular Systems Biology, ETH Zürich, CH-8093 Zürich, Switzerland.

†To whom correspondence should be addressed. E-mail: cmarx@oeb.harvard.edu



The distribution of epistatic interactions between mutations may greatly influence evolutionary outcomes—from the maintenance of sexual reproduction to the fixation rate of beneficial alleles—and hence the speed of adaptation itself. The most consistent finding across studies of laboratory-evolved populations has been a rapid deceleration of the rate of fitness increase (10). Theoretical analysis suggests that the observed dynamics of fitness increase and accumulation of substitutions (11) are best described by a class of fitness landscapes with antagonistic interactions between beneficial mutations (12).

We took both experimental and theoretical approaches to investigate potential epistasis in populations that were initiated with an engineered strain of *Methylobacterium extorquens* AM1 (hereafter, EM) (table S1) and evolved in batch culture with methanol as the sole carbon source (3). In order to grow on methanol, *Methylobacterium* must oxidize formaldehyde into formate. Wild-type *Methylobacterium* (WT) performs this oxidation with a tetrahydromethanopterin-dependent pathway (13). In EM, this native

pathway was eliminated and replaced by a non-orthologous, glutathione (GSH)-dependent pathway from *Paracoccus denitrificans* (fig. S1) (14). As a result, the EM strain could grow on methanol, but at a rate one-third that of WT (fig. S2). Adaptation in eight replicate populations dependent on this engineered metabolic function (analogous to natural horizontal gene transfer) resulted in an average fitness increase after 600 generations of 66.8% (fig. S3), as determined by competition assays (3), and was largely carbon substrate-specific (fig. S4).

The genome of an evolved isolate from generation 600 (“EVO”) (9) with the highest fitness ( $W_{\text{EVO}} = 1.94$ ) (table S2) was sequenced to identify the genetic basis of adaptation in that lineage (3). In total, nine mutations were identified (fig. S5) (3). We found an 11-base pair (bp) deletion between the two genes that encode the GSH-dependent pathway, *flhA* and *fghA* (i.e., *fghA*<sup>EVO</sup>), in a plasmid specifically introduced into EM (pCM410) (fig. S6). This deletion removed the apparent ribosome-binding site for *fghA* and decreased expression of these enzymes by 55%

and 73% (3), respectively. This change, however, increased fitness by 14.2% (Fig. 1A), which suggested that production of these enzymes in the EM ancestor was higher than the optimum. In WT, where the GSH pathway is extraneous, a strain with an empty vector had a 14.1% fitness advantage relative to fitness when both genes were expressed. It therefore appeared that the primary advantage of the *fghA*<sup>EVO</sup> allele was to reduce the costs of protein overexpression (e.g., energy consumption, ribosome sequestering, and protein misfolding). We also identified a single-nucleotide polymorphism (SNP) in the promoter region of pyridine nucleotide transhydrogenase (*pntAB*<sup>EVO</sup>), and a 2-bp deletion in the promoter of the most rate-limiting enzyme of GSH biosynthesis,  $\gamma$ -glutamylcysteine synthetase (*gshA*<sup>EVO</sup>). These gene products have clear linkages to methanol utilization in EM (3). The remaining six genetic changes included a large deletion (fig. S7), a synonymous SNP, the loss of a plasmid, two transposon insertions, and a 6-bp insertion (3). The last-named six are difficult to reconstruct genetically, were individually neutral under our experimental conditions (15), or were deemed unlikely to greatly contribute to fitness. We thus treated them as a single collective locus, the “genetic background” (*GB*<sup>EVO</sup>), for the purpose of examining epistasis between beneficial mutations. All identified alleles, when present individually in the ancestral background conferred fitness benefits ranging from 10 to 51% (Fig. 1A).

In order to investigate epistasis between these beneficial mutations, strains with each allelic combination ( $2^4 = 16$ ) were constructed (3), and their fitness values were measured (Fig. 1A). The adaptive landscape of this genotypic space contained a single peak; each allele was universally beneficial across genetic backgrounds (i.e., showed no sign epistasis, but the degree of benefit conferred varied) (Fig. 1B). Except for *pntAB*<sup>EVO</sup>, the remaining three alleles exhibited a significant trend of diminishing returns: Their selective benefits declined in genetic backgrounds with higher fitness. In contrast, the resistance to cefotaxime conferred by each mutation within the *E. coli*  $\beta$ -lactamase gene (5) was idiosyncratic with regard to the

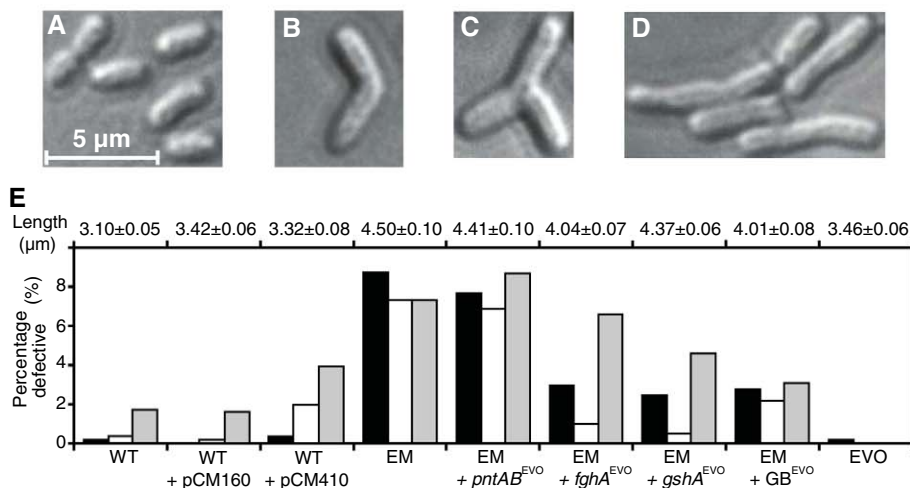


**Fig. 2.** Morphological aberrations caused by expression of the foreign pathway. Distinct cellular morphologies of (A) WT or an EM ancestor showing (B) curved, (C) branched, or (D) elongated cells. (E) Mean cell length and proportion of elongated (black), branched (white), and curved (gray) cells for various strains. Plasmid pCM410 expresses the foreign pathway; pCM160 is an empty control plasmid.

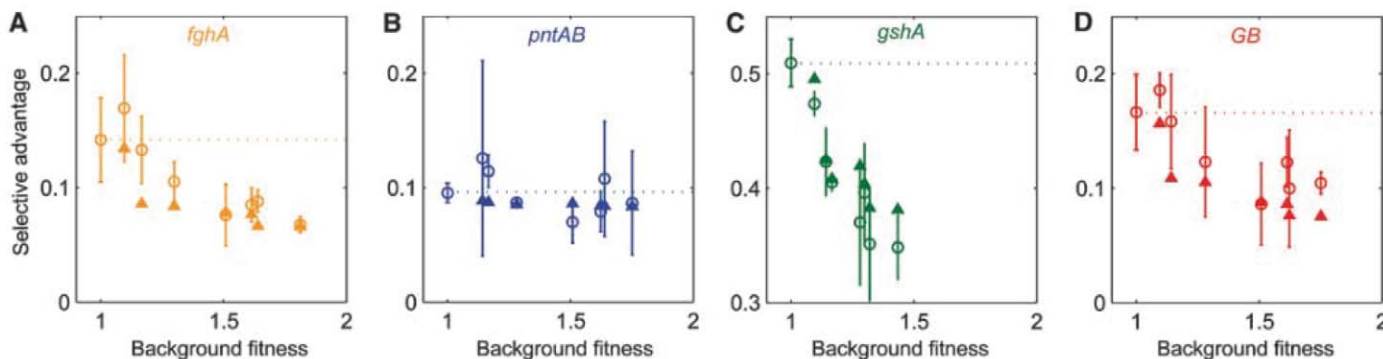


**Fig. 3.** Antagonistic trend of epistasis detected from the data and captured by the benefit-cost model. (A to D) Plots of measured (open circles) and predicted (solid triangles) selective coefficients  $s$  for each of the four evolved alleles,

respectively, versus the fitness of the background onto which the allele was introduced. Dashed lines indicate selective advantages for each allele on the ancestral background (i.e., expectation for no epistasis).



resistance of the background onto which it was introduced (Fig. 1C).

We found a connection between antagonistic epistasis and a physiological problem caused by protein overexpression in EM. Cells of the EM ancestor showed an increased length and aberrant morphologies relative to WT (Fig. 2 and fig. S8), similar to those commonly observed for protein overexpression (16). Reducing expression of the foreign pathway in EM via *fghA<sup>EVO</sup>* suppressed cellular abnormalities, whereas expressing it in WT (where it is redundant) induced similar defects. This confirmed that the morphological defects were caused by overexpression of the foreign pathway. In addition, the *gshA<sup>EVO</sup>* and *GB<sup>EVO</sup>* alleles (but not *pntAB<sup>EVO</sup>*) also individually reduced morphological defects (to about one-third), and when all the evolved alleles are present together (e.g., the EVO strain), abnormal cells were nearly absent (a finding recapitulated across all eight populations) (fig. S2D). These data suggest that part of the benefit conferred by the three alleles whose selective benefit wanes on fitter backgrounds resulted from directly or indirectly decreasing protein overexpression costs.

Epistasis has been often represented as the deviation from a null model in which individual mutations affect the ancestor's fitness ( $W_0 = 1.0$ ) with independent multiplicative factors  $\lambda_i$  (double mutant's fitness,  $W_{ij} = \lambda_i \lambda_j W_0$ ). However, in our system, rather than being captured by a single indivisible phenotype, cell growth seems to depend on at least one separately measurable component, i.e., the growth burden imposed by expressing the foreign pathway. As stated above, three of the four alleles identified in the EVO strain appear to increase fitness at least partly by reducing this cost. Therefore, in analogy to the contributions to fitness by a single enzyme (17), we developed a mathematical model that partitions fitness into two phenotypes: a "benefit" component  $b_0$ , analogous to a single conglomerate "enzyme activity" that sets the rate of energy extracted from the substrate to generate biomass; and a cost  $c_0$ , encompassing a fixed amount of energy diverted to deal with overexpression of the foreign pathway (3). Thus, the fitness of the ancestral strain can be written, as  $W_0 = b_0 - c_0 = 1$ . We hypothesize that a new allele  $i$  could modify the benefit and the cost of the ancestral background by certain multiplicative factors ( $\lambda_i$  and  $\theta_i$ , respectively), giving rise to a fitness  $W_i = \lambda_i b_0 - \theta_i c_0$ . A successive allele  $j$ , on top of the background of mutant  $i$ , is similarly assumed to act multiplicatively on the benefit and cost components, yielding a fitness  $W_{ij} = \lambda_i \lambda_j b_0 - \theta_i \theta_j c_0$ .

If we could determine experimentally the values of  $b_0$ ,  $c_0$ , and the  $\lambda_i$  and  $\theta_i$  for each allele, then the above model should provide predictions for the fitness of any multiallele strain, computable as

$$W_{\text{mutant}} = \prod_{i \in \text{alleles}} \lambda_i b_0 - \prod_{i \in \text{alleles}} \theta_i c_0$$

(3). We estimated these parameters: Cost was determined by expressing the foreign pathway in

WT, where its metabolic function was fully redundant ( $c_0 = 0.141$ ) (17). Setting  $W_0 = 1$ , results in  $b_0 = 1.141$ . The lowered cost of expression,  $\theta_i$ , for each allele was approximated as the decreased relative proportion of morphological defects (table S3) (3). Factors  $\lambda_i$  could then be estimated using the single-allele benefit-cost model.

Without specifying further information, this simple model partitioning fitness into benefit and cost outperformed the standard null model in predicting fitness values of multiallele combinations [coefficient of determination ( $R^2$ ) = 0.97 versus  $R^2 = 0.64$ ] (figs. S9 and S10) (3). It also recapitulated the antagonistic trend of epistasis among the three alleles affecting cell morphology and correctly predicted the consistent magnitude of benefit from *pntAB<sup>EVO</sup>* (Fig. 3). The agreement between our experimental data and model predictions supports our model assumptions and thus our hypothesis as to why diminishing returns epistasis was observed: Proportional reductions of a cost became successively less beneficial as the cost itself was alleviated.

Diminishing returns has been predicted (18) but because of different assumptions. The non-linearity of fitness increase in these models arises because it is assumed that a given trait is under stabilizing selection for an intermediate optimum, which explicitly considers fitness as being displaced from a fixed adaptive peak. Although the assumption of intermediate optimality holds well for many traits like body weight and length, fitness rises monotonically with increasing growth rate or decreasing protein expression burden. In this study, we considered a higher-level phenotype (growth rate) as the sum of two constituent phenotypes (metabolic rate and protein expression burden), which allowed us to generate a precise expectation for the fitness of multiallele strains without explicitly assuming stabilizing selection. The success of this approach suggests that it may be possible to generalize the idea of expressing higher-level phenotypes (such as fitness) as combinations of multiple underlying traits to provide quantitative predictions of epistasis.

An analogous study (19) of the interactions between beneficial mutations in *E. coli* evolved in minimal glucose medium found similar epistatic trends: four of five new alleles exhibit significant diminishing returns. The fifth such mutation, and a mutation present as a component of our *GB<sup>EVO</sup>* allele that is beneficial only in metal-poor media (15), showed the opposite trend: an increase in selective advantage with higher background fitness. Thus, across these two distinct model systems 7 of 10 alleles consistently showed antagonism, whereas only 2 exhibited synergy. This tendency toward diminishing returns between beneficial mutations was predicted from trajectories of fitness increase and substitution rate (12) but had never been tested directly. Furthermore, these results are in stark contrast to the epistatic effects seen among mutations within single proteins, which are varying and unpredictable

in their effect with regard to background activity (5, 7). This distinction between results from within- and between-gene epistasis suggests that the underlying causes of epistasis at different physiological scales (i.e., within-gene protein biophysics versus between-gene physiological networks) lead to categorically distinct, but reproducible, trends in genetic interactions that affect both the speed of adaptation and the degree to which possible trajectories are limited.

*Note added in proof:* Kvitek and Sherlock (20) recently reported an additional experimental system, evolution of *Saccharomyces cerevisiae* in a glucose-limited chemostat, that exhibited a general trend of diminishing returns for epistasis between pairs of beneficial mutations in different loci.

## References and Notes

1. P. C. Phillips, *Nat. Rev. Genet.* **9**, 855 (2008).
2. H. J. Cordell, *Hum. Mol. Genet.* **11**, 2463 (2002).
3. Materials and methods are available as supporting material on Science Online.
4. D. Segrè, A. Deluna, G. M. Church, R. Kishony, *Nat. Genet.* **37**, 77 (2005).
5. D. M. Weinreich, N. F. Delaney, M. A. Depristo, D. L. Hartl, *Science* **312**, 111 (2006).
6. M. Lunzer, S. P. Miller, R. Felsheim, A. M. Dean, *Science* **310**, 499 (2005).
7. J. T. Bridgham, S. M. Carroll, J. W. Thornton, *Science* **312**, 97 (2006).
8. R. Sanjuán, A. Moya, S. F. Elena, *Proc. Natl. Acad. Sci. U.S.A.* **101**, 15376 (2004).
9. M. K. Applebee, M. J. Herrgård, B. O. Palsson, *J. Bacteriol.* **190**, 5087 (2008).
10. S. F. Elena, R. E. Lenski, *Nat. Rev. Genet.* **4**, 457 (2003).
11. J. E. Barrick *et al.*, *Nature* **461**, 1243 (2009).
12. S. Kryazhinskiy, G. Tkacik, J. B. Plotkin, *Proc. Natl. Acad. Sci. U.S.A.* **106**, 18638 (2009).
13. L. Chistoserdova, J. A. Vorholt, R. K. Thauer, M. E. Lidstrom, *Science* **281**, 99 (1998).
14. C. J. Marx, L. Chistoserdova, M. E. Lidstrom, *J. Bacteriol.* **185**, 7160 (2003).
15. H. H. Chou, J. Berthet, C. J. Marx, *PLoS Genet.* **5**, e1000652 (2009).
16. C. G. Kurland, H. Dong, *Mol. Microbiol.* **21**, 1 (1996).
17. E. Dekel, U. Alon, *Nature* **436**, 588 (2005).
18. G. Martin, S. F. Elena, T. Lenormand, *Nat. Genet.* **39**, 555 (2007).
19. A. I. Khan, D. M. Dinh, D. Schneider, R. E. Lenski, T. F. Cooper, *Science* **332**, 1193 (2011).
20. D. J. Kvitek, G. Sherlock, *PLoS Genet.* **7**, e1002056 (2011).

**Acknowledgments:** We thank S. Kryazhinskiy, D. Weinreich, J. Weitz, C. Wilke, R. Whitaker, and members of the Marx and Segrè labs for suggestions and discussions. Supported by NIH grant R01 GM078209, and NSF grant DEB-0845893. The resulting single-end 36-bp read data have been deposited in the NCBI Short Read Archive with accession no. SRA030695.1.

## Supporting Online Material

www.sciencemag.org/cgi/content/full/332/6034/1190/DC1  
Materials and Methods  
SOM Text  
Figs. S1 to S10  
Tables S1 to S3  
References

3 February 2011; accepted 25 April 2011  
10.1126/science.1203799

# Negative Epistasis Between Beneficial Mutations in an Evolving Bacterial Population

Aisha I. Khan,<sup>1\*†</sup> Duy M. Dinh,<sup>1\*</sup> Dominique Schneider,<sup>2,3</sup> Richard E. Lenski,<sup>4</sup> Tim F. Cooper<sup>1‡</sup>

Epistatic interactions between mutations play a prominent role in evolutionary theories. Many studies have found that epistasis is widespread, but they have rarely considered beneficial mutations. We analyzed the effects of epistasis on fitness for the first five mutations to fix in an experimental population of *Escherichia coli*. Epistasis depended on the effects of the combined mutations—the larger the expected benefit, the more negative the epistatic effect. Epistasis thus tended to produce diminishing returns with genotype fitness, although interactions involving one particular mutation had the opposite effect. These data support models in which negative epistasis contributes to declining rates of adaptation over time. Sign epistasis was rare in this genome-wide study, in contrast to its prevalence in an earlier study of mutations in a single gene.

Evolutionary theory predicts that epistatic interactions between mutations can play an important role in determining patterns of adaptation (1–5). Nevertheless, despite many studies of mutational interactions, little is known about the distribution of their fitness effects. Do most mutations combine additively, or are epistatic interactions widespread? When mutations interact epistatically, are their combined fitness effects usually greater or less than expected from their separate effects? Do the prevalence and form of epistasis depend on how the mutations are generated—for example, whether the mutations are random and therefore usually deleterious or, alternatively, ones that have been fixed by selection? Recent studies have examined epistatic interactions by measuring the relative fitness of genotypes with known numbers and combinations of mutations (6–14). These studies have typically found that epistasis is common, although there is often no consistent directional effect. Nevertheless, some general patterns have been suggested. For example, synergistic epistasis may be more common in organisms with complex genomes (15). However, most studies have examined deleterious mutations, and few data exist on interactions among beneficial mutations that arose during a population's evolution.

The difficulty of identifying and precisely manipulating beneficial mutations has meant that the role of epistasis in adaptive evolution has usually been inferred indirectly from its effects on evolutionary dynamics and outcomes (16–21).

A common observation in microbial evolution experiments is that the rate of fitness increase tends to decelerate over time (21–25). Negative epistasis, in which the combined effect of beneficial mutations is smaller than would be expected from their separate effects, could explain that tendency. However, such deceleration might instead occur simply because beneficial mutations of large effect will tend to be incorporated earlier owing to their faster spread and greater success in the face of competing beneficial mutations (26), and this explanation does not require epistasis. The capacity to sequence experimentally evolved genomes, as well as to enumerate beneficial mutations over time, adds another dimension to evolutionary dynamics that can inform efforts to understand the role of epistasis in adaptive evolution (24). Kryazhinskiy *et al.* (4) recently proposed that trajectories for fitness and accumulated beneficial mutations could be jointly analyzed to infer the nature of epistasis among the beneficial mutations. By analyzing these com-

bined data for the same experimental population that is the focus of our study, they inferred that interactions between beneficial mutations were predominantly negative in form. Here we will directly test that inference.

To that end, we constructed all possible combinations of the first five beneficial mutations that were fixed in one population of *Escherichia coli* from a long-term evolution experiment. In that experiment, 12 replicate populations were started from a common ancestor and independently evolved in a defined environment supplemented with glucose as the limiting resource (22). Fitness increased in all populations, relative to the ancestor, in that same environment (22, 27). This experiment was designed, in part, to examine the repeatability of adaptive evolution, and subsequent studies have documented many examples of both phenotypic and genetic parallelism (24, 27–30). Nevertheless, replicate populations have diverged in other phenotypic and genetic traits (24, 31, 32). A striking example of divergence is the ability to grow on citrate that evolved in only 1 of the 12 populations (32). Aside from that case, all of the populations show a strong tendency toward decelerating rates of fitness increase (27, 28).

Whole-genome sequencing of a clone that was isolated after 20,000 generations from one of the populations (designated Ara-1) identified 45 mutational differences from the ancestor (24). Many other mutations appeared in the population, of course, but most were eliminated by random drift or negative selection. Other beneficial mutations also arose, including some that reached detectable frequencies, but these were lost by interference from superior beneficial mutations (24, 26) and, in at least one case, because they were less able to evolve than the eventual winners (33). Here we focus on the first five mutations that fixed in this population and whose spread coincided with the period of fastest adaptation. These mutations together produced

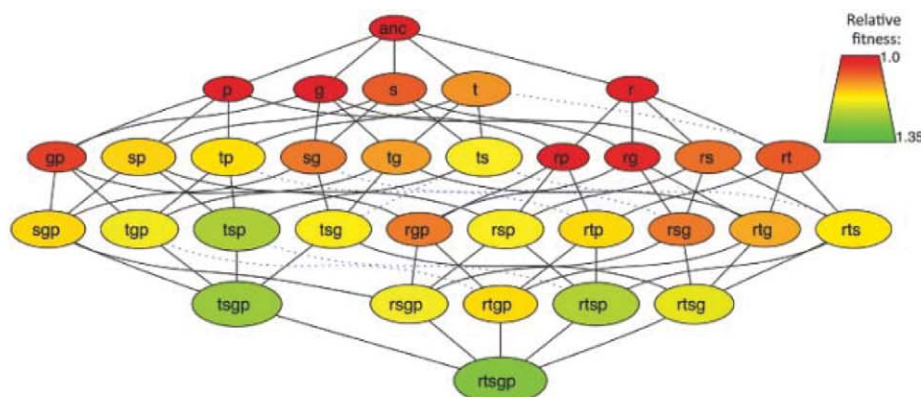


**Fig. 1.** Mutational network connecting constructed genotypes. Each node represents one of 32 possible combinations of five mutations. Anc indicates the ancestral strain. Other labels indicate mutations affecting these genes: *r*, *rbs*; *t*, *topA*; *s*, *spoT*; *g*, *glmUS*; and *p*, *pykF*. Node colors and sizes reflect the genotype's fitness relative to the ancestor. Edges show all one-step mutations. Solid and dotted lines indicate whether the additional mutation caused an increase or decrease in fitness, respectively.

<sup>1</sup>Department of Biology and Biochemistry, University of Houston, Houston, TX 77204, USA. <sup>2</sup>Laboratoire Adaptation et Pathogénie des Microorganismes, Université Joseph Fourier, Institut Jean Roget, F-38041 Grenoble, France. <sup>3</sup>CNRS UMR5163, F-38041 Grenoble, France. <sup>4</sup>Department of Microbiology and Molecular Genetics, Michigan State University, East Lansing, MI 48824, USA.

\*These authors contributed equally to this work.

†Present address: University of Texas Medical Branch, Galveston, TX 77555, USA.

‡To whom correspondence should be addressed. E-mail: tfcooper@uh.edu

a fitness increase of ~30% relative to the ancestor, and thus they account for much of the ~80% increase in mean fitness that this population achieved by 20,000 generations (24, 34). These mutations, listed in the order they arose, are in these genes or gene regions: *rbs* operon, *topA*, *spoT*, *glmUS* promoter, and *pykF*.

The five beneficial mutations were moved into the ancestral chromosome to produce a set of 32 ( $= 2^5$ ) genotypes representing all possible combinations of those mutations (table S1). This approach follows previous studies that examined combinations of mutations underlying focal traits in single genes or gene regions (7, 9, 12). The fitness of each constructed genotype was then estimated in direct competition against a marked variant of the ancestor, which enabled us to describe the local fitness landscape for this full set of genotypes (Fig. 1 and fig. S1). Note that each mutational step that was followed in the evolving population produced an increase in fitness relative to the immediate progenitor. Therefore, each of these mutations was beneficial on the genetic background in which it arose.

To test for epistasis between the focal beneficial mutations, we first used a multiplicative null model that gave the expected fitness of a genotype as the product of the individual fitness effects of the relevant mutations (35). The absolute epistatic deviation was then calculated as the difference between observed and expected fitness values (fig. S2). We also calculated the relative epistatic deviation as the log ratio of observed and predicted fitness values (35). In both cases, positive (or negative) deviations indicated that the observed fitness of a genotype was greater (or less) than expected under the null model.

We found no overall trend in the contribution of either absolute or relative deviations to the fitness of the 26 constructed genotypes with two or more mutations {mean absolute epistatic deviation =  $0.006 \pm 0.021$  [95% confidence interval (CI)],  $t_{25} = 0.553$ ,  $P = 0.585$ ; mean relative deviation =  $0.002 \pm 0.008$  (95% CI),  $t_{25} = 0.670$ ,  $P = 0.510$ } (Fig. 2). The nonsignificant average deviations might mean that epistatic effects were small, rare, or both; alternatively, nonsignificance may indicate that positive and negative effects tended to offset one another (6). Consistent with the latter possibility, epistasis was common in the constructed genotypes. The absolute epistatic deviation was significantly positive in seven genotypes and negative in five ( $P < 0.05$ ) (table S2).

There were seven cases in which the addition of a mutation appeared to reduce fitness (Fig. 1), but only one was significant ( $P < 0.05$ ) when analyzed in isolation, and it became nonsignificant with a Bonferroni correction for multiple tests. In any case, even if all seven cases of apparent marginal declines were real, the local adaptive landscape has only one fitness peak, because it is possible to reach the most-fit genotype by uphill trajectories from any starting point. Moreover, 86 of the 120 possible mutational trajectories

connecting the ancestor and the most-fit genotype are monotonically increasing for fitness (fig. S1 and table S3). Although not all of the step-wise changes are significant, the paucity of even nonsignificant declines supports the inference that most steps are individually positive. The preponderance of monotonically increasing fitness trajectories in our study stands in sharp contrast to a previous study of five mutations in a  $\beta$ -lactamase gene, where only 18 of the 120 trajectories gave strictly increasing levels of antibiotic resistance (9).

What factors might explain the observed variation in the direction and strength of epistasis in our study? One possibility is that epistasis depends on the magnitude of the fitness effects of the contributing mutations. To test this hypothesis, we examined the relation between epistasis and the expected fitness of each genotype in the absence of any epistatic effect. We observed an overall negative relation, indicating that epistatic effects became more negative as the expected fitness rose [absolute epistasis: correlation coefficient ( $r$ ) =  $-0.578$ ; relative epistasis:  $r = -0.586$ ], although this relation appeared to obscure some underlying genetic complexity (Fig. 3). Henceforth, we will focus on the relation between expected fitness and relative epistatic deviation because it provides a measure of the influence of epistasis on the strength of selection for a new beneficial mutation.

The negative relation between epistasis and expected fitness could reflect a consistent effect, such as saturating the potential improvement in some underlying physiological process. Alternatively, the presence or absence of specific mutations might produce groups of genotypes that have different average fitness and epistasis values. For example, if one particular mutation conferred a large benefit in the ancestor but interacted negatively with the other mutations, then it might drive an overall correlation that would not be typical of most mutational interactions. To distinguish between these possibilities, we used analysis of covariance to test whether the presence of any single mutation, or any combination of

**Fig. 2.** Distributions of estimated epistatic fitness deviations for 26 genotypes with at least two mutations. (A) Absolute epistatic deviations. (B) Relative epistatic deviations. Red lines indicate mean values. Note that the *pykF* mutation drives almost all of the positive values of epistasis (Fig. 3 and table S2).

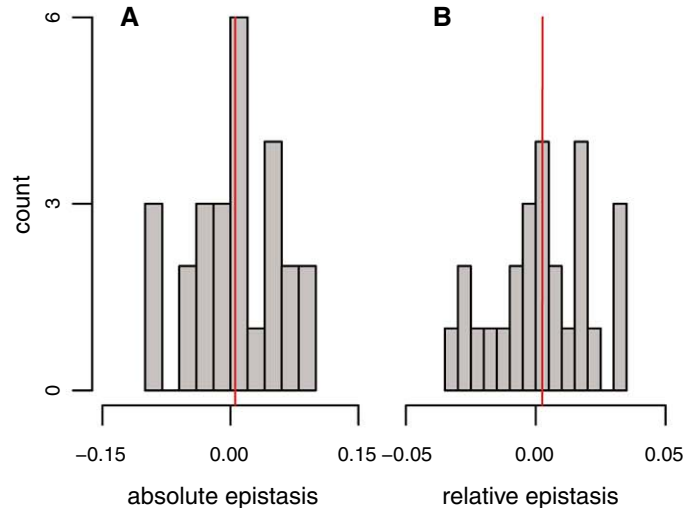
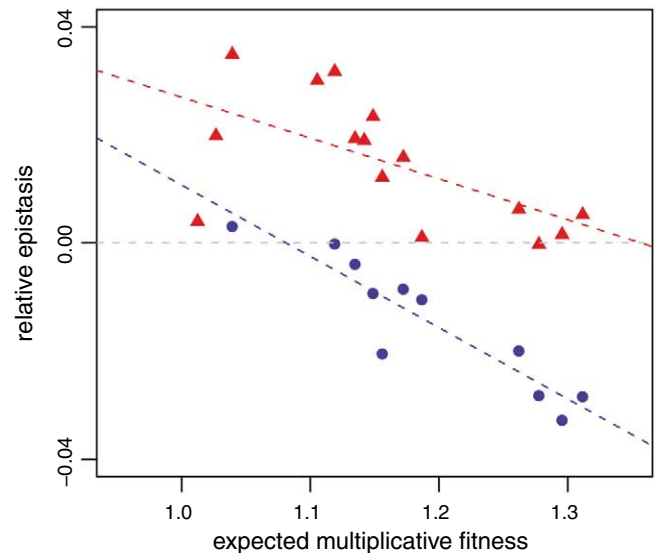


**Fig. 3.** Relation between relative epistasis and expected fitness under a null model without epistasis. Blue circles and red triangles show genotypes with the ancestral and evolved *pykF* alleles, respectively.





two mutations, explained a significant fraction of the variation in the relation between epistasis and expected fitness. The only gene that showed a significant effect was *pykF* (Fig. 3 and fig. S3) ( $F_{1,23} = 61.93$ ,  $P < 0.001$ ) (table S4). The mean epistatic deviation was significantly negative among genotypes with the ancestral allele (mean =  $-0.014$ ,  $t_{10} = -3.942$ ,  $P = 0.003$ ), whereas it was significantly positive among those with the evolved allele (mean =  $0.015$ ,  $t_{14} = 4.913$ ,  $P < 0.001$ ) (fig. S4). Thus, the *pykF* mutation enhances fitness through its epistatic interactions with the other evolved mutations. However, the sets of genotypes with ancestral and evolved *pykF* alleles both exhibit negative correlations between relative epistasis and expected fitness values (ancestral *pykF*:  $r = -0.923$ ; evolved *pykF*:  $r = -0.610$ ) (Fig. 3 and fig. S5). As a consequence, the slope

of the major axis regression (35) of the observed and expected fitness values is less than unity in both cases, although only marginally so for those genotypes with the evolved *pykF* allele (ancestral *pykF*: slope =  $0.628$ , 95% CI of  $0.519$  to  $0.748$ ; evolved *pykF*: slope =  $0.850$ , 95% CI of  $0.698$  to  $1.029$ ) (fig. S6). These data thus indicate a strong negative relation between expected fitness and epistatic deviations, although the details of this relation also clearly depend on the particular beneficial mutations involved.

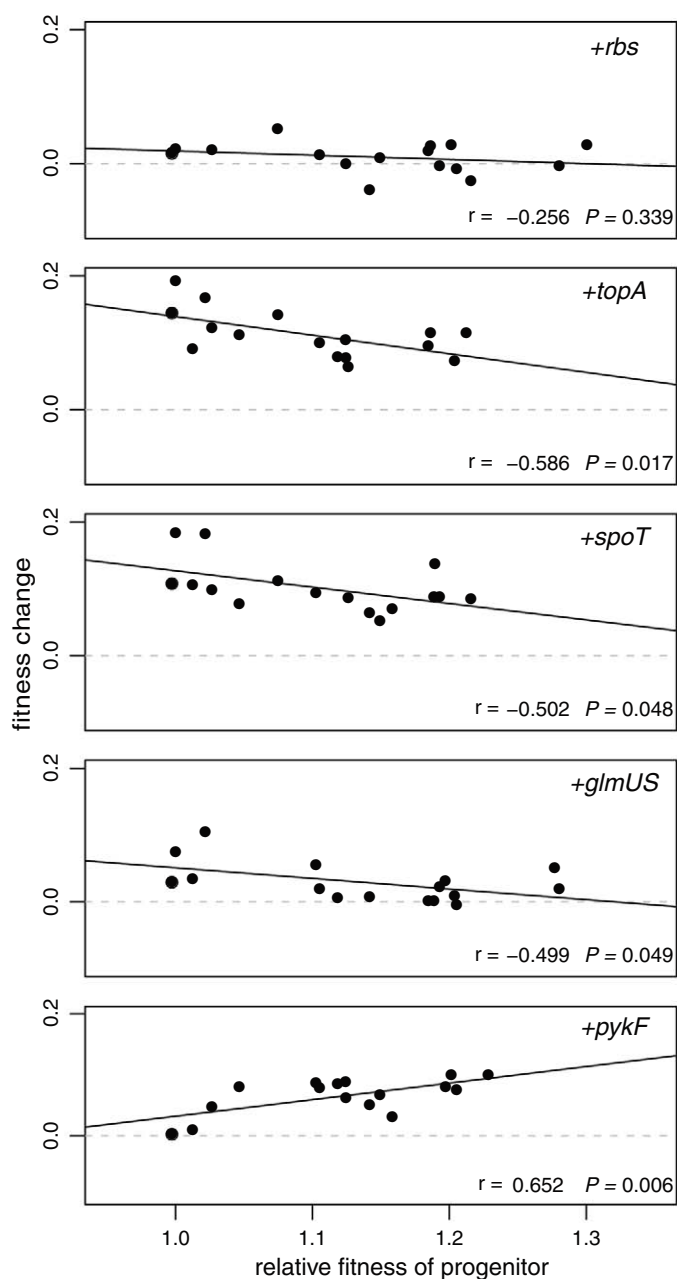
We also examined the relation between fitness and epistasis by arranging the 32 genotypes into 16 pairs, such that each pair differed only by the presence or absence of a particular mutation. This pairing allowed us to quantify how the marginal fitness effect of each mutation varied with the fitness of the progenitor background in

which the mutation was placed. The benefits conferred by the first four mutations that fixed in the population (*Δrbs*, *topA*, *spoT*, and *glmUS*) tended to decline as the fitness of the progenitor increased, and that correlation was significant ( $P < 0.05$ ) in three of those cases (Fig. 4). Notably, the relation was reversed for the *pykF* mutation, such that it tended to confer a greater benefit in the more-fit genetic backgrounds. In fact, the *pykF* mutation was selectively neutral in the ancestral background, unlike the earlier beneficial mutations. Thus, the effect of background fitness on the strength of epistasis depended on the specific mutation, which suggests that these mutations conferred their beneficial effects through different underlying physiological processes.

A conspicuous feature of the mean-fitness trajectory for this population—and indeed for most experimental populations evolving in a constant environment—is that the rate of adaptation declined over time (21–25). Mechanisms that may explain this deceleration include reductions in the number and effect-size of beneficial mutations as a population becomes better adapted to its environment (21, 22, 36). The strong negative relation between epistasis and the expected fitness of a genotype in the absence of epistasis (Fig. 3) suggests that epistatic interactions contribute greatly to this deceleration by reducing the effect-size of the remaining beneficial mutations as a population approaches a fitness peak. In other words, epistasis acts as a drag that reduces the contribution of later beneficial mutations. Note that similar trends were seen by Chou *et al.* (37), who examined the fitness interactions among five beneficial mutations that occurred during adaptation of an engineered strain of *Methylobacterium extorquens* AM1. That study, like ours, found that four mutations interacted to yield diminishing fitness returns, whereas one mutation had the opposite effect.

Our results are also consistent with a recent theoretical study that used population-genetic models to infer that negative epistasis between beneficial mutations could explain the fitness trajectory in the same experimental population that we have studied (4). Although we observed widespread epistatic interactions among beneficial mutations in this study, and there was strong epistasis with another beneficial mutation that arose but did not fix in the same population (33), we did not observe the extreme constraints on possible mutational paths to higher fitness seen in an earlier study of the  $\beta$ -lactamase gene (9). More generally, our results suggest that a relatively simple epistasis function might be incorporated into models that seek to predict the dynamics of adaptation, at least for asexual haploid populations evolving under constant conditions. However, our results also caution that there will be exceptions to any simple function, as evidenced by the finding that the *pykF* mutation greatly affected the magnitude, although not the trend, of the relation between epistasis and fitness.

**Fig. 4.** Relation between the marginal fitness effect of adding a particular mutation and the fitness of the progenitor background to which it was added for each one of five focal mutations. Each panel includes the Pearson correlation coefficient and its significance. The open symbols show the effects of adding each focal mutation to the ancestral strain.



## References and Notes

1. A. S. Kondrashov, *Nature* **369**, 99 (1994).
2. H. A. Orr, M. Turelli, *Evolution* **55**, 1085 (2001).
3. D. M. Weinreich, R. A. Watson, L. Chao, *Evolution* **59**, 1165 (2005).
4. S. Kryazhimskiy, G. Tkacik, J. B. Plotkin, *Proc. Natl. Acad. Sci. U.S.A.* **106**, 18638 (2009).
5. J. A. Draghi, T. L. Parsons, G. P. Wagner, J. B. Plotkin, *Nature* **463**, 353 (2010).
6. S. F. Elena, R. E. Lenski, *Nature* **390**, 395 (1997).
7. M. Lunzer, S. P. Miller, R. Felsheim, A. M. Dean, *Science* **310**, 499 (2005).
8. R. Sanjuán, J. M. Cuevas, A. Moya, S. F. Elena, *Genetics* **170**, 1001 (2005).
9. D. M. Weinreich, N. F. Delaney, M. A. Depristo, D. L. Hartl, *Science* **312**, 111 (2006).
10. L. Jasnos, R. Korona, *Nat. Genet.* **39**, 550 (2007).
11. J. A. G. M. de Visser, S. C. Park, J. Krug, *Am. Nat.* **174** (suppl. 1), S15 (2009).
12. J. da Silva, M. Coetzer, R. Nedellec, C. Pastore, D. E. Mosier, *Genetics* **185**, 293 (2010).
13. K. M. Pepin, H. A. Wichman, *Evolution* **61**, 1710 (2007).
14. L. Jasnos, K. Tomala, D. Paczesniak, R. Korona, *Genetics* **178**, 2105 (2008).
15. R. Sanjuán, S. F. Elena, *Proc. Natl. Acad. Sci. U.S.A.* **103**, 14402 (2006).
16. R. Korona, C. H. Nakatsu, L. J. Forney, R. E. Lenski, *Proc. Natl. Acad. Sci. U.S.A.* **91**, 9037 (1994).
17. C. L. Burch, L. Chao, *Nature* **406**, 625 (2000).
18. F. B.-G. Moore, D. E. Rozen, R. E. Lenski, *Proc. Biol. Sci.* **267**, 515 (2000).
19. R. Montville, R. Froissart, S. K. Remold, O. Tenaillon, P. E. Turner, *PLoS Biol.* **3**, e381 (2005).
20. R. Sanjuán, J. M. Cuevas, V. Furió, E. C. Holmes, A. Moya, *PLoS Genet.* **3**, e93 (2007).
21. O. K. Silander, O. Tenaillon, L. Chao, *PLoS Biol.* **5**, e94 (2007).
22. R. E. Lenski, M. R. Rose, S. C. Simpson, S. C. Tadler, *Am. Nat.* **138**, 1315 (1991).
23. M. R. Goddard, H. C. J. Godfray, A. Burt, *Nature* **434**, 636 (2005).
24. J. E. Barrick *et al.*, *Nature* **461**, 1243 (2009).
25. S. E. Schoustra, T. Bataillon, D. R. Gifford, R. Kassen, *PLoS Biol.* **7**, e1000250 (2009).
26. P. J. Gerrish, R. E. Lenski, *Genetica* **102-103**, 127 (1998).
27. V. S. Cooper, R. E. Lenski, *Nature* **407**, 736 (2000).
28. R. E. Lenski, M. Travisano, *Proc. Natl. Acad. Sci. U.S.A.* **91**, 6808 (1994).
29. T. F. Cooper, D. E. Rozen, R. E. Lenski, *Proc. Natl. Acad. Sci. U.S.A.* **100**, 1072 (2003).
30. R. Woods, D. Schneider, C. L. Winkworth, M. A. Riley, R. E. Lenski, *Proc. Natl. Acad. Sci. U.S.A.* **103**, 9107 (2006).
31. M. Travisano, F. Vasi, R. E. Lenski, *Evolution* **49**, 189 (1995).
32. Z. D. Blount, C. Z. Borland, R. E. Lenski, *Proc. Natl. Acad. Sci. U.S.A.* **105**, 7899 (2008).
33. R. J. Woods *et al.*, *Science* **331**, 1433 (2011).
34. J. A. G. M. de Visser, R. E. Lenski, *BMC Evol. Biol.* **2**, 19 (2002).
35. Materials and methods are available as supporting material on Science Online.
36. H. A. Orr, *Genetics* **163**, 1519 (2003).
37. H.-H. Chou, H.-C. Chiu, N. F. Delaney, D. Segrè, C. J. Marx, *Science* **332**, 1190 (2011).

**Acknowledgments:** This work was supported by grants from the NSF (DEB-1019989 to R.E.L. and DEB-0844355 to T.F.C.), the James S. McDonnell Foundation (220020174 to T.F.C.), the Agence Nationale de la Recherche (Program Génomique, Grant ANR-08-GENM-023-001 to D.S.) and the Defense Advanced Research Projects Agency "Fun Bio" Program (HR0011-09-1-0055 to R.E.L. and T.F.C.). We thank R. Azevedo, T. Paixão, and D. Stoebel for valuable discussions and helpful comments on the manuscript. R.E.L. will make the ancestral and evolved strains used in this study available to qualified recipients, subject to completion of a material transfer agreement that can be found at <http://technologies.msu.edu/forms.html>. T.F.C. will make the strains constructed in this study available to qualified recipients. Competition experiment counts, summary input data, and analysis scripts that pertain to the experiments and analyses reported in this paper have been deposited at <http://dx.doi.org/10.5061/dryad.5rv40>.

## Supporting Online Material

[www.sciencemag.org/cgi/content/full/332/6034/1193/DC1](http://www.sciencemag.org/cgi/content/full/332/6034/1193/DC1)

Materials and Methods

Figs. S1 to S6

Tables S1 to S4

References and Notes

3 February 2011; accepted 25 April 2011

10.1126/science.1203801

# Scaling Up Digital Circuit Computation with DNA Strand Displacement Cascades

Lulu Qian<sup>1</sup> and Erik Winfree<sup>1,2,3\*</sup>

To construct sophisticated biochemical circuits from scratch, one needs to understand how simple the building blocks can be and how robustly such circuits can scale up. Using a simple DNA reaction mechanism based on a reversible strand displacement process, we experimentally demonstrated several digital logic circuits, culminating in a four-bit square-root circuit that comprises 130 DNA strands. These multilayer circuits include thresholding and catalysis within every logical operation to perform digital signal restoration, which enables fast and reliable function in large circuits with roughly constant switching time and linear signal propagation delays. The design naturally incorporates other crucial elements for large-scale circuitry, such as general debugging tools, parallel circuit preparation, and an abstraction hierarchy supported by an automated circuit compiler.

The power and mystery of life is entangled within the information processing at the heart of all cellular machinery. Engineering molecular information processing systems may allow us to tap into that power and elucidate principles that will help us to understand and appreciate the mystery.

DNA is an excellent engineering material for biochemical circuits because its biological nature supports technological applications in vivo, its easy chemical synthesis facilitates practical experiments in vitro, its combinatorial structure provides sufficient sequence design space, and the Watson-Crick complementarity principle enables predictable molecular behavior.

DNA has been used as a computing substrate since the first demonstration of solving a seven-city Hamiltonian path problem in 1994 (1) and has evolved away from competing with silicon to embedding control within molecular systems. Although DNA automata can be built

with deoxyribozymes (2, 3) or with restriction enzymes (4), the introduction of toehold-mediated DNA strand displacement enabled enzyme-free DNA machinery that is automated by hybridization alone (5–8). A DNA strand can serve as a signal when it is free, but is inhibited when it is bound to a complementary strand. A single-stranded DNA signal can first bind to a partially double-stranded complex by a single-stranded domain called a toehold, then release the originally bound strand after branch migration has occurred. Thus, an output signal can be activated upon the arrival of an input signal, and the reaction rate can be controlled by the length of the toehold. This principle has inspired the development of a rich theory (9, 10) and practice (11–13) of DNA strand displacement circuits, resulting in a wide range of applications such as medical therapeutics in vivo (14), molecular instruments in situ (15), and biomedical diagnostics in vitro (16). To date, the largest digital circuit built with DNA strand displacement cascades involved 12 initial DNA species (17). However, their logic gates were constructed with multistranded DNA complexes, challenging sequence design constraints were required, and signal restoration occurred only at the circuit output, perhaps explaining why the performance decayed surprisingly with scale.

To create a scalable DNA circuit architecture, we proposed (17) a simple DNA gate motif—a “seesaw” gate—that makes use of a reversible strand displacement reaction based on the principle of toehold exchange (8, 12). In this context, seesawing is the reversible reaction that exchanges

<sup>1</sup>Bioengineering, California Institute of Technology, Pasadena, CA 91125, USA. <sup>2</sup>Computer Science, California Institute of Technology, Pasadena, CA 91125, USA. <sup>3</sup>Computation and Neural Systems, California Institute of Technology, Pasadena, CA 91125, USA.

\*To whom correspondence should be addressed. E-mail: winfree@caltech.edu

the activity of DNA signals; a pair of seesawing steps completes a catalytic cycle, allowing signal amplification and signal isolation. A pair of seesaw gates can perform AND or OR operation, sufficient for universal Boolean function evaluation using dual-rail logic (18). A robust digital abstraction is maintained by embedding thresholding and catalysis into every logic operation to clean up signal degradation. With the use of plug-and-play molecular components, gates can be

easily wired into circuits with arbitrary numbers of inputs (fan-in) and outputs (fan-out) at each gate, and they can be reconfigured to perform an AND or OR logic function through simple concentration adjustments. DNA sequence design is straightforward because of the independence of strand domains. The simplicity of gate structures makes parallel DNA synthesis and circuit preparation plausible. We present all circuits using a formal abstraction that concisely defines the DNA

species and their initial states, thus determining the circuit wiring, logical function, and temporal behavior. The size of the circuits implemented here with the seesaw architecture is larger than any previous strand displacement circuit, as measured by the number of initial DNA species in the circuit, by at least a factor of 5.

In the seesaw abstraction, each DNA gate is represented by a two-sided node (Fig. 1A and fig. S1, A and B). Each DNA signal is

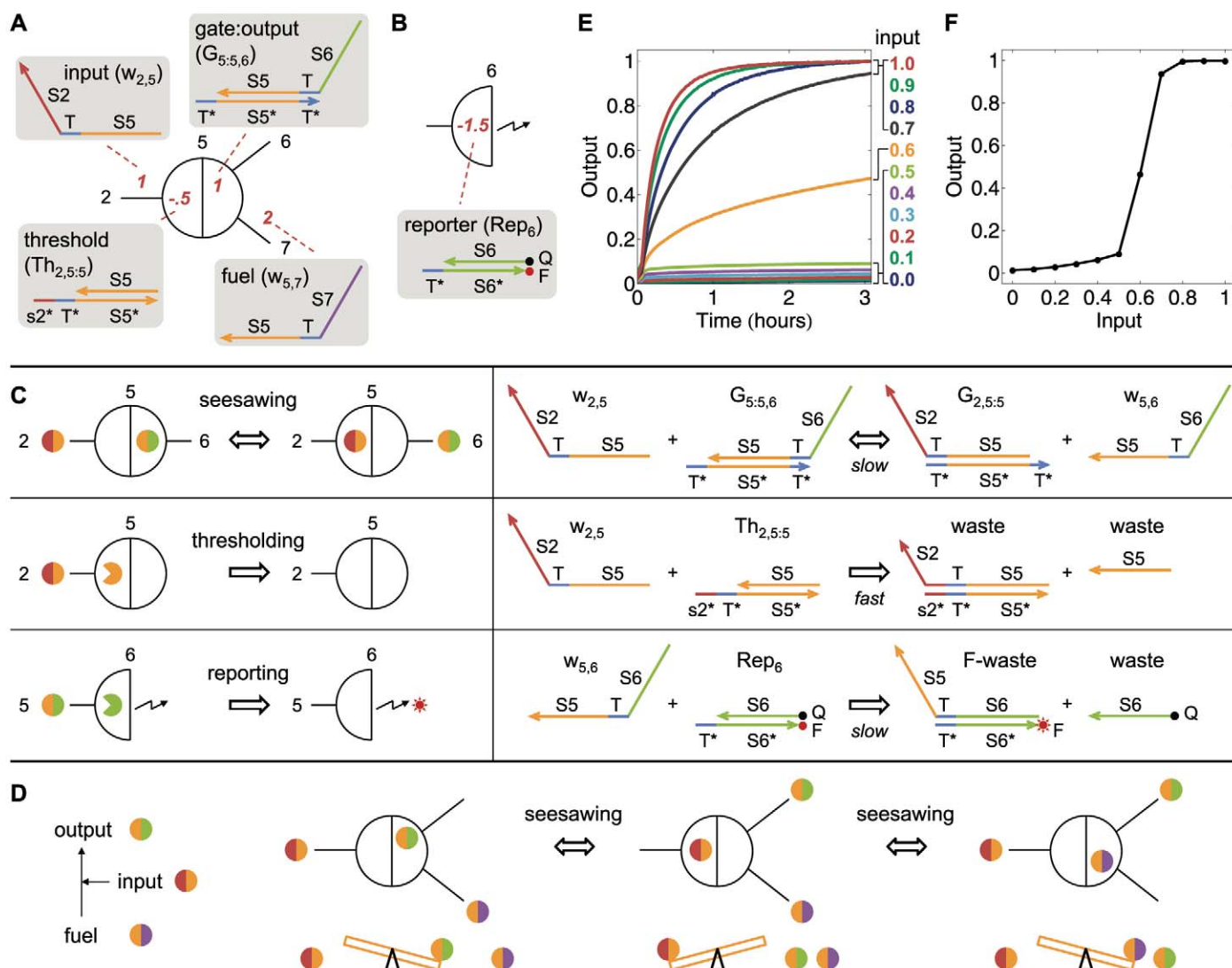


**Fig. 1.** The seesaw gate motif and its DNA implementation. **(A)** Abstract diagram for a gate. Black numbers indicate identities of nodes (or interfaces to those nodes in a network). Red numbers within the nodes or on the wires indicate relative concentrations of different initial DNA species. Each species plays a specific role (e.g., input) within a gate and has a unique name (e.g., w<sub>2,5</sub>) within a network. Colored lines represent DNA strands at the domain level, with arrowheads marking their 3' ends and colors indicating distinct DNA sequences. S2, S5, and S6 are long (15-nucleotide) recognition domains corresponding to nodes 2, 5, and 6; S7 does not interact with other nodes in the network but preserves the uniform format of a signal strand. T is a short (5-nucleotide) toehold domain; T\* is the Watson-Crick complement of T, etc.; s2\* is the first few nucleotides of S2\* from the 3' end. **(B)** Abstract diagram for a reporter; F and Q denote fluorophore and quencher, respectively. **(C)** Three basic reaction mechanisms involved in a seesaw network: seesawing, thresholding, and reporting. Solid circles with

two colors indicate signal strands that have two sides. Colored pac-men indicate threshold or reporter complexes. w<sub>2,5</sub> is the signal strand that connects gates 2 and 5; G<sub>5,5,6</sub> is signal strand w<sub>5,6</sub> bound to gate 5; Th<sub>2,5,5</sub> is the threshold that absorbs w<sub>2,5</sub> when it arrives at gate 5; and Rep<sub>6</sub> is the reporter that absorbs w<sub>5,6</sub> and generates fluorescence signal for any *i*. **(D)** One cycle of a seesaw catalytic reaction. **(E)** Kinetics experiments of the seesaw DNA catalyst with a threshold. Threshold complex, gate:output complex, fuel strand, and reporter complex were mixed in solution with relative concentrations of 0.5×, 1×, 2×, and 1.5×, respectively (standard concentration 1× = 100 nM). Input strands were then added at 0.0× to 1.0× in increments of 0.1×. Sequences of strands are listed in tables S2 and S3, circuit 2. Experiments were performed at 20°C in Tris-acetate-EDTA buffer containing 12.5 mM Mg<sup>2+</sup>. Output signals were inferred by fluorescence signals normalized to the maximum completion level. **(F)** Input versus output plot of (E). The output at ~3 hours is replotted against the initial input.



represented by a wire. Each side of the node can be connected to any number of wires. Each wire connects two different sides of two nodes. Each red number indicates one DNA species with its initial relative concentration: Each number on a wire corresponds to a free signal strand; each number within a node at the end of a wire corresponds to a bound signal strand (positive number) or a threshold that absorbs a signal when it arrives at the gate (negative number). A reporter that transforms a DNA signal into a fluorescence signal is represented by half a node with a zigzag arrow (Fig. 1B), with its initial relative concentration written similar to a threshold.

Each signal is a single-stranded DNA molecule that has two recognition domains identifying the two gates it connects, one on either side of a central toehold domain. Each gate is associated with a gate base strand that has (the complement of) one recognition domain flanked by two toehold domains. When a signal strand is bound to a gate, it forms a gate:signal complex with the gate's base strand. At any given moment (not counting the transient states during reactions shown in fig. S1C), a gate base strand always has a signal strand bound to one side, leaving the toehold on the other side uncovered.

There are three basic reactions involved in a seesaw network (Fig. 1C and fig. S1C). The first one is seesawing: A free signal on one side of a gate can release a signal bound on the other side of the gate by toehold-mediated strand displacement. The process starts with the free signal strand (e.g.,  $w_{2,5}$ ) hybridizing to the gate:signal complex (e.g.,  $G_{5,5,6}$ ) at the uncovered toehold domain (e.g.,  $T^*$ ) and then undergoing branch migration through the recognition domain (e.g.,  $S5$ ). The previously bound signal will fall off when it is attached to the gate base strand only by the short toehold. The resulting gate:signal complex (e.g.,  $G_{2,5,5}$ ) will have an uncovered toehold on the other side, and therefore the now-free signal (e.g.,  $w_{5,6}$ ) can reverse the process symmetrically. The second reaction is thresholding: A threshold species associated with a gate and an impinging signal can react with the signal by means of a longer toehold (e.g.,  $s2^*T^*$ ), producing only inert waste species that have no exposed toehold. Thresholding is much faster than seesawing because the toehold-mediated strand displacement rate grows exponentially with toehold length for short toeholds (7, 8). As a result, seesawing effectively only happens when the input signal exceeds the threshold. The third reaction is reporting: A reporter species similar to a threshold, but modified with a fluorophore and quencher pair, can absorb an impinging signal while generating a fluorescence signal. Unlike thresholding, reporting does not compete with seesawing, and it therefore does not require a longer toehold.

DNA signals can play different roles such as input (signals that arrive at a gate), output (signals that are produced by a gate), and fuel (signals that help to catalytically produce the output). One seesaw gate with a few wires can create a catalytic cycle in which input transforms free fuel into free output without being consumed in the process (Fig. 1D and fig. S1, B and C). Initially, the output signal is bound to the right side of the gate; the input and fuel signals are free (in our analogy, the output is riding on the right side of the seesaw board; the input and fuel are wandering around). The input signal first releases the output signal and binds to the gate instead (the input jumps onto the left side of the board and makes the output jump off). The fuel signal then displaces the input signal by binding to the gate in the same way (the fuel pushes off the input). A catalytic cycle has been completed. In general, a free signal on one side of a seesaw gate can catalyze the exchange of signals on the other side, and this exchange will not happen without the catalyst. These reactions are driven forward by the entropy of equilibration for the seesawing reactions. A small amount of free input can catalyze the release of a large amount of free output (fig. S2).

Thresholding can be directly combined with a seesaw catalyst to support a digital abstraction—which is the basic principle underlying digital

logic in electronics—by pushing the intrinsically analog signal toward either the ideal ON or OFF value. Fluorescence kinetics experiments (Fig. 1E) demonstrated the circuit in Fig. 1A connected to the reporter in Fig. 1B. The input-versus-output relationship (plotted in Fig. 1F) reveals a sharp threshold, ideal for signal restoration.

A cascade of two seesaw gates can compute the logic function OR or AND. To explain this, we introduce two composable seesaw components for digital circuits. We first define the gross production of signal  $X$  as the total amount eventually released from the gate:

$$\langle X \rangle = \int_0^{+\infty} X^{\text{prod}}(t) dt \quad (1)$$

Motivated by sequence design constraints (figs. S3 and S4), we then define two types of feedforward seesaw gates, each assuming an irreversible downstream drain. The first type is called an amplifying gate. It has a threshold and fuel. If the gross production of its input is greater than the initial amount of threshold, the output will keep being released catalytically until it reaches the maximum, which is the initial amount of bound

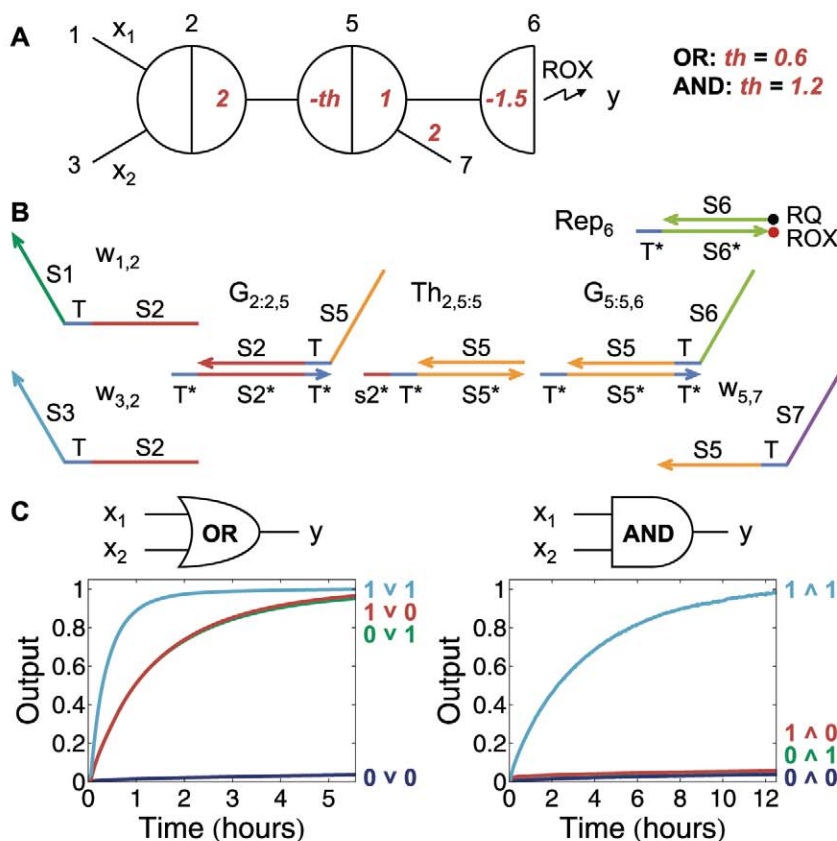


**Fig. 2.** Digital logic gates implemented with the seesaw DNA motif. (A) Abstract diagram of a seesaw circuit that computes either OR or AND, depending on the initial concentration of the threshold. Input signals  $x_1$  ( $w_{1,2}$ ) and  $x_2$  ( $w_{3,2}$ ) are summed together at gate 2 and, if they exceed the threshold, are amplified by gate 5 to generate output signal  $y$  ( $w_{5,6}$ ), which is reported by the ROX fluorophore in reporter 6. (B) Domain-level DNA implementation of the two-input AND or OR gate. (C) Kinetics experiments. Input strands were at  $0.1 \times$  (0, logic OFF) or  $0.9 \times$  (1, logic ON), where  $1 \times = 100$  nM. Sequences of strands are listed in tables S2 and S3, circuit 3. Experiments were performed at  $20^\circ\text{C}$ .

output; otherwise, the output remains at zero. An amplifying gate can support multiple outputs. This is simply done by adding one bound output signal for each output wire. These gate:output complexes will have the same gate base strand bound by signal strands with different right-side recognition domains to connect to different downstream gates. To sufficiently drive the release of all outputs, the initial amount of free fuel will be twice the sum of all initially bound outputs:

$$\langle \text{output}_1 \rangle = \begin{cases} w_1 & \text{if } \langle \text{input} \rangle > th \\ 0 & \text{if } \langle \text{input} \rangle \leq th \end{cases}$$

$$\langle \text{output}_2 \rangle = \begin{cases} w_2 & \text{if } \langle \text{input} \rangle > th \\ 0 & \text{if } \langle \text{input} \rangle \leq th \end{cases}$$

$$th \geq 0, w_i > 0$$

side recognition domain but different left-side recognition domains to connect to different upstream gates. With multiple inputs, the output will be the sum of all inputs. To ensure that all free inputs can be transformed into free output, the initial amount of bound output must be at least the maximum sum of all inputs that can possibly arrive:

$$w \geq \max(\sum \langle \text{input}_i \rangle)$$

An integrating gate followed by an amplifying gate can compute either OR or AND (Fig. 2A). A two-input OR gate will have an integrating gate that outputs the sum of the two inputs. The downstream amplifying gate will output 1 when the sum is greater than 0.6 and will output 0 otherwise. In practice, the outputs will not be exactly 0 or 1 because of spurious or incomplete reactions, so we must ensure that logic gates will function correctly even with imperfect inputs.

Assuming a digital abstraction where OFF signals may be in the range 0 to 0.2 and ON signals in the range 0.8 to 1, we see that only when both inputs are OFF can the output remain OFF. Changing the threshold from 0.6 to 1.2 computes AND. In this case, only when both inputs are ON can the sum exceed the threshold and catalyze the output to be ON.

In kinetics experiments, a reporter gate was used to provide an irreversible drain and to transform the output into a fluorescence signal. With exactly the same set of molecules (Fig. 2B) but different initial concentrations of the threshold, OR and AND computations were demonstrated (Fig. 2C). The AND gate behaved slower than the OR gate because the initial concentration of the threshold was higher, so it took longer for the upstream signal to exceed the threshold. Thanks to the thresholding and catalysis, even when the inputs were imperfect (0.1 was used for OFF inputs and 0.9 for ON inputs), the outputs still achieved ideal OFF and ON signal levels, preserving the digital abstraction.

Two-layer cascading was demonstrated with OR-OR, AND-OR, OR-AND, and AND-AND

**Fig. 3.** Digital logic composition implemented with the seesaw DNA motif.

(A) Circuit layer versus delay in OR cascades. Half completion times of seven selected experiments with a single input being ON in OR cascade circuits (Fig. 2 and figs. S5 and S6) are plotted against the depth of the activated input. (B) Circuit layer versus switching time in OR cascades. The time intervals between 20% and 80% completion of the above seven experiments are plotted against the depth of the activated input. (C) A circuit with four layers and five AND or OR gates. Numbers aligned with six input wires are logic values of respective inputs from 12 different experiments. Rectangles indicate the experiments where the output stayed OFF. Trajectories and their corresponding inputs have matching colors. (D) A circuit with a four-input OR gate. (E) A circuit with a four-output OR gate. Outputs from top to bottom in the circuit diagram correspond to plotted data of left top, right top, left bottom, and right bottom. Abstract diagrams of seesaw circuits in (C), (D), and (E) are included in figs. S7, S8, and S9, respectively. Sequences of strands are listed in tables S2 and S3, circuits 7, 8, and 9, respectively. Experiments were performed at 20°C, 1× = 100 nM, and 0.1× was used for OFF and 0.9× for ON inputs.

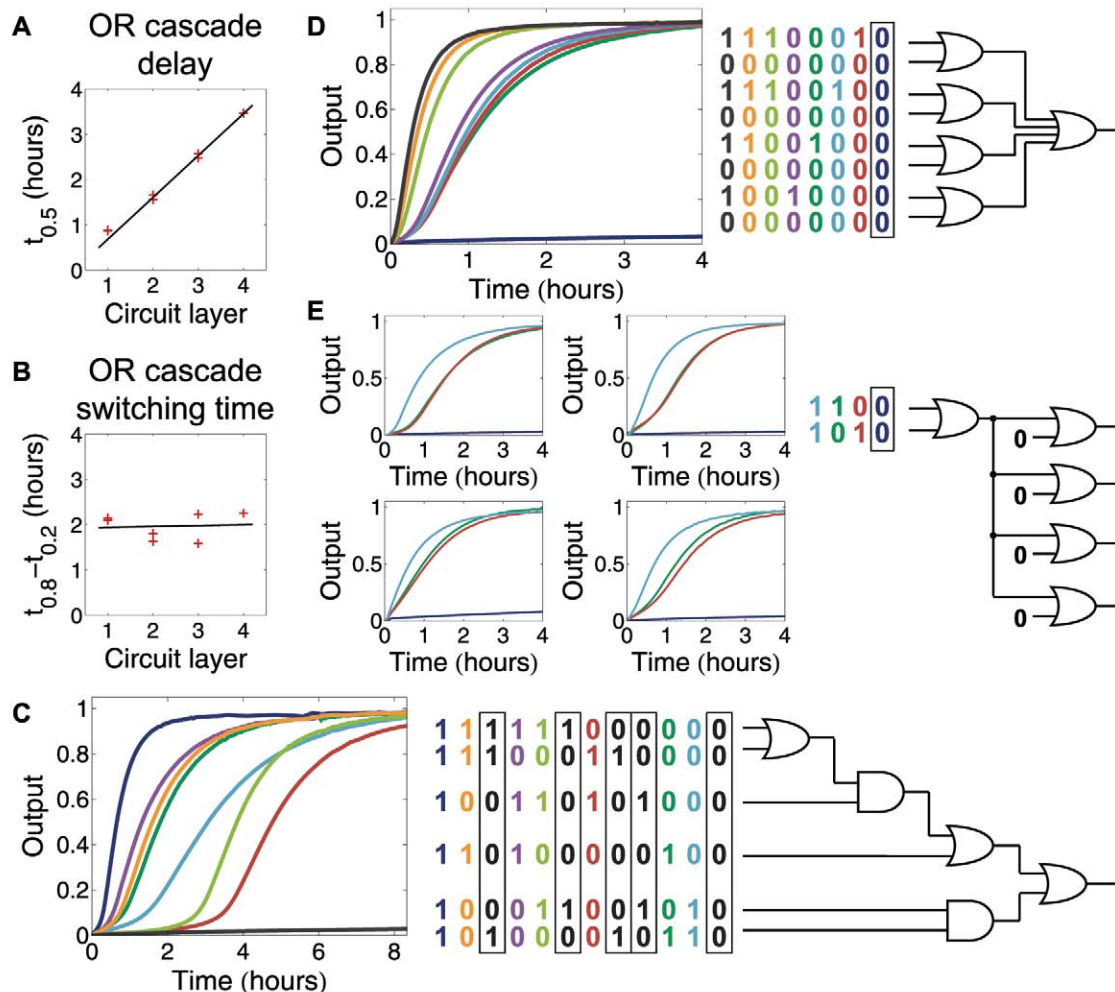


(fig. S5). In all tested cases, the output went to the correct ON or OFF state. A three-OR cascade (fig. S6, A and B) and a four-OR cascade (fig. S6, C and D) also worked. The delay time required for circuit computation increased linearly with the number of layers (Fig. 3A). However, once the threshold for the output gate was exceeded, the signal increased at roughly the same rate as in the smaller circuit (Fig. 3B). In a circuit with four layers, two AND gates, and three OR gates, with 12 different combinations of inputs, the output went to clear and correct ON or OFF states in 8 hours (Fig. 3C).

Because integrating gates support multiple inputs and amplifying gates support multiple outputs, logic gates built from a pair of them can easily support fan-in and fan-out. In a circuit with a four-input OR gate, only when all inputs from the upstream OR gates were OFF did the output

stay OFF (Fig. 3D). In a circuit with a four-output OR gate, each output copied the correct logic from the upstream OR gate (Fig. 3E). Circuits with a four-input AND gate and a four-output AND gate are shown in fig. S8C and fig. S9C, respectively.

To demonstrate a digital circuit with an interesting function, we built a circuit that computes the floor of the square root of a four-bit binary number (Fig. 4A). It is not an optimized digital logic circuit; it is designed to showcase AND, OR, NOT, NAND, NOR, fan-in, and fan-out of logic gates, as well as fan-out of input signals. NOT gates are difficult to implement directly using representations where the ON or OFF state of an input is determined by the presence or absence of a single DNA species: A circuit might compute a false output before all input strands are added, because NOT gates already produce ON signals in the

absence of their inputs, and for use-once circuits (such as seesaw circuits), computations cannot be undone. Therefore, we use dual-rail logic (fig. S10B). Each input is replaced by a pair of inputs, representing logic ON and OFF separately. Each logic gate is replaced by a pair of AND or OR gates. (Taking the NOR gate as an example, output being OFF is the OR of both inputs being ON; output being ON is the AND of both inputs being OFF.) Initially, the pair of inputs is absent, indicating that the logic value of this signal is unknown. At the beginning of computation, one input of the pair will be added, indicating either logic ON or OFF. In this way, no computation will take place before the input signals arrive. With dual-rail logic, any AND-OR-NOT circuit can be transformed into an equivalent circuit with AND or OR gates only. Then, any AND-OR circuit can be further transformed into an equivalent seesaw

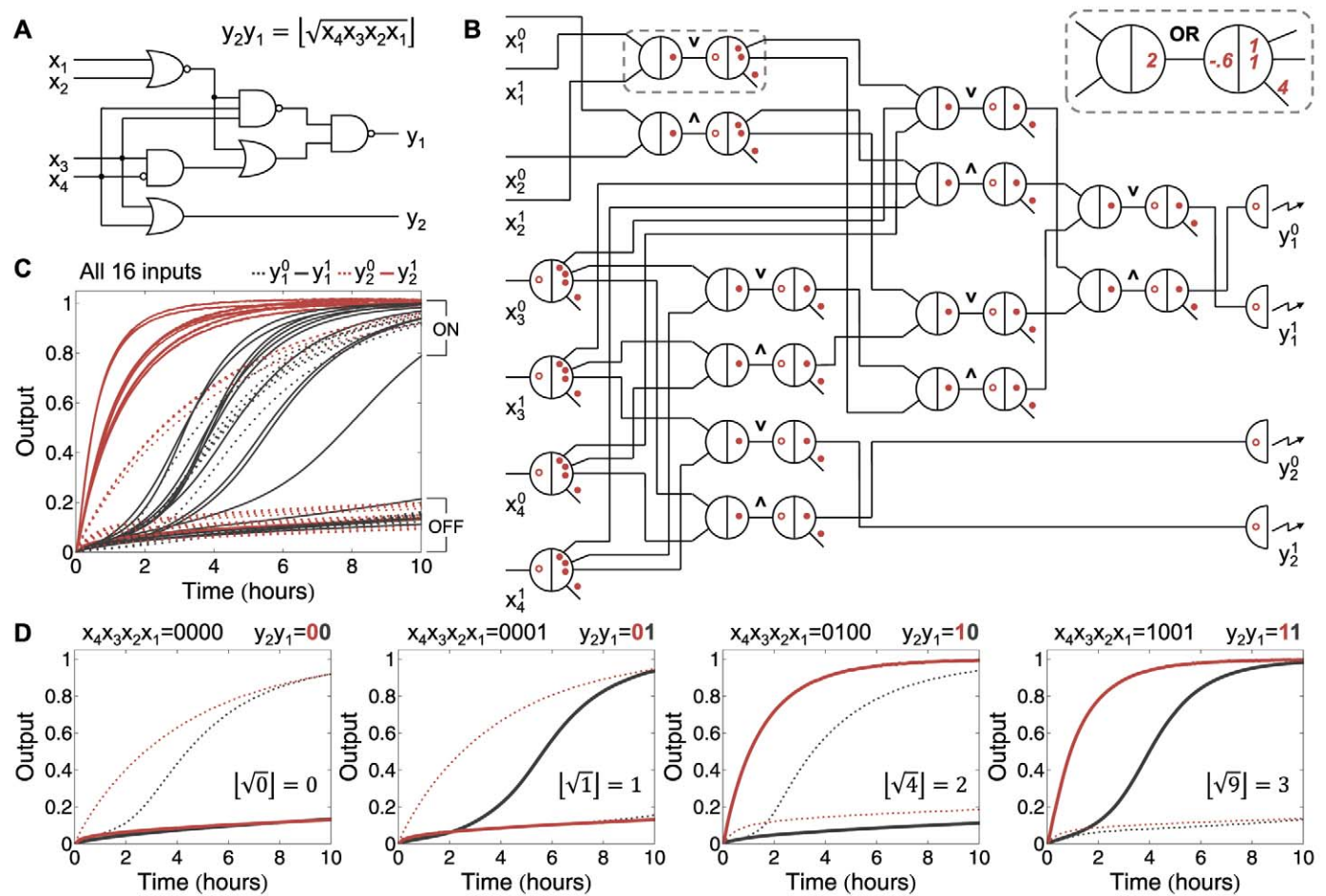


**Fig. 4.** A square-root circuit implemented with the seesaw DNA motif. **(A)** A digital logic circuit that computes the floor of the square root of four-bit binary numbers. **(B)** Abstract diagram of the seesaw circuit that is equivalent to the square-root digital logic circuit.  $x_i^0$  and  $x_i^1$  are dual-rail inputs of  $x_i$ , and they represent logic OFF and ON, respectively (the same rule applies to the outputs). Each pair of seesaw gates implements an AND ( $\wedge$ ) or OR ( $\vee$ ) gate. Each pair of dual-rail AND or OR gates implements one ANDNOT, OR, NAND, or NOR gate. Red dots indicate positive red numbers, specifying initial relative concentrations of free or bound signals; red circles indicate negative red numbers, specifying initial relative concentra-

tions of thresholds or reporters. An example of a two-input, two-output OR gate is highlighted; full details are provided in fig. S10. **(C)** Kinetics experiments of the square-root circuit with all combinations of inputs from 0000 to 1111. All 16 plots are shown separately in fig. S11. **(D)** Kinetics experiments that compute the square roots of 0, 1, 4, and 9. Trajectories and their corresponding outputs have matching colors. Dotted and solid lines indicate dual-rail outputs that represent logic OFF and ON, respectively. Sequences of strands are listed in tables S4 to S7. Experiments were performed at 25°C,  $1\times = 50$  nM, and  $0.1\times$  was used for OFF and  $0.9\times$  for ON inputs.



circuit, with the construction we described above, and translated into DNA. The seesaw circuit that is equivalent to the square-root circuit in Fig. 4A is shown in Fig. 4B. This circuit has 74 initial DNA species, excluding inputs. When it runs, there are 130 different DNA strands—consisting of 15 to 33 nucleotides each—interacting within one test tube. With all possible inputs from 0000 to 1111, outputs went to the correct ON state or OFF state. The 16 plots are superimposed in Fig. 4C, and four selected examples are shown separately in Fig. 4D.

As circuits grow in size, a general debugging tool would be useful. In addition to the four output reporters for the square-root circuit, we had a fifth reporter to read one arbitrary internal output at a time (fig. S12). To do so, only one extra wire that connects the target gate to the fifth reporter needed to be added to the circuit. This corresponds to a single bound signal strand as an additional output from the target gate. Internal outputs from an OR gate, an AND gate, and an ANDNOT gate were observed without disturbing the functioning of the square-root circuit (fig. S13).

In our experiments, especially as the circuit size increased, we encountered issues related to sequence design and experimental conditions. For example, we added “clamps” to eliminate one type of leaky reaction (figs. S14 to S16), chose an optimal toehold length (fig. S17), selected the synthesis procedure for DNA strands (fig. S18), and adjusted the running temperature (fig. S19).

All components in seesaw circuits can be easily obtained from single-stranded DNA precursors (fig. S20), which facilitates parallel synthesis using DNA microarrays and parallel circuit preparation (19). During annealing, intramolecular hairpins form first and become kinetically trapped before other intermolecular reactions occur (20). Then, the undesired stem-loop fragments can be removed by restriction enzyme digestion or photocleavage. Kinetics experiments showed that thresholding and catalysis by a single seesaw gate worked well with DNA complexes prepared from hairpins (fig. S21).

The simple and systematic architecture for seesaw circuits made it possible to build quantitative models and to compile digital logic networks all the way to their DNA implementations. With just five rate constant parameters, our models fit single-gate data well (figs. S22 and S23) and semiquantitatively reproduced all other experimental data (figs. S24 to S31). The compiler [figs. S32 and S33; see also (21)] automatically translates any feedforward logic circuit into its equivalent seesaw circuit and DNA sequences, generates Mathematica and Systems Biology Markup Language (SBML) (22) code for simulations at the chemical reaction level, and generates DNA strand displacement calculus (DSD) (10) code for visualization and simulation at the domain level.

Three general principles guided us in successfully scaling up the complexity of DNA strand displacement circuitry. *Simplicity*: With just three

basic reactions (seesawing, thresholding, and reporting) involving just four types of active species (free or bound signal, threshold, and reporter) comprising no more than two short strands, it is possible to develop a detailed understanding that generalizes to all units in a complex network. *Abstraction*: With five levels of hierarchical abstraction (DNA sequence, DNA domain, seesaw circuit, dual-rail logic, and AND-OR-NOT logic), design and analysis can take place at a higher level while neglecting irrelevant details. *Tolerance*: Signal restoration within every logic operation ensures that the digital abstraction is maintained even when synthesis and operational defects are inevitable.

Despite the speed, robustness, and straightforward sequence design of seesaw circuits, further scaling up will encounter challenges such as increased spurious binding that slows down the desired reaction rates and decreases the effectiveness of the thresholds. We expect that these challenges can be partially addressed by improved sequence design and by running reactions at lower concentrations (see supporting online material). However, a better solution would be to transition from solution-phase circuitry to circuitry organized on a surface, such as DNA origami (23–25), where adjacent DNA gates can interact without diffusion, spurious interactions are limited to immediate neighbors, and sequences can be safely reused in spatially separated locations.

A picture is now emerging for the future of DNA strand displacement circuitry. Proposals for systematic design of circuits with analog behavior (9) and systems that exploit spatial structures (26) make use of DNA complexes only moderately more complex than those used here. The problems of making reusable DNA gate components (27) powered by a single universal fuel (28) are being tackled. It is not yet clear what limits the amount of intelligence (29) that purely nucleic acid systems can exhibit.

As with other DNA strand displacement cascades, seesaw circuits can be applied to the embedded sensing and control of various molecular events by adapting biological signals such as microRNAs (11), small molecules (30), and proteins (31) as inputs or outputs. Moreover, the seesaw motif is structurally similar to microRNAs and small interfering RNAs (32, 33)—all are short duplex nucleic acids with single-stranded overhangs processed from hairpins—hinting at the possibility that strand displacement circuitry may play an important, although still obscure, regulatory role within biological cells.

#### References and Notes

1. L. M. Adleman, *Science* **266**, 1021 (1994).
2. M. N. Stojanovic, D. Stefanovic, *Nat. Biotechnol.* **21**, 1069 (2003).
3. J. Elbaz et al., *Nat. Nanotechnol.* **5**, 417 (2010).
4. Y. Benenson, B. Gil, U. Ben-Dor, R. Adar, E. Shapiro, *Nature* **429**, 423 (2004).

5. B. Yurke, A. J. Turberfield, A. P. Mills Jr., F. C. Simmel, J. L. Neumann, *Nature* **406**, 605 (2000).
6. A. J. Turberfield et al., *Phys. Rev. Lett.* **90**, 118102 (2003).
7. B. Yurke, A. P. Mills Jr., *Genet. Program. Evolvable Mach.* **4**, 111 (2003).
8. D. Y. Zhang, E. Winfree, *J. Am. Chem. Soc.* **131**, 17303 (2009).
9. D. Soloveichik, G. Seelig, E. Winfree, *Proc. Natl. Acad. Sci. U.S.A.* **107**, 5393 (2010).
10. A. Phillips, L. Cardelli, *J. R. Soc. Interface* **6** (suppl. 4), S419 (2009).
11. G. Seelig, D. Soloveichik, D. Y. Zhang, E. Winfree, *Science* **314**, 1585 (2006).
12. D. Y. Zhang, A. J. Turberfield, B. Yurke, E. Winfree, *Science* **318**, 1121 (2007).
13. P. Yin, H. M. T. Choi, C. R. Calvert, N. A. Pierce, *Nature* **451**, 318 (2008).
14. S. Venkataraman, R. M. Dirks, C. T. Ueda, N. A. Pierce, *Proc. Natl. Acad. Sci. U.S.A.* **107**, 16777 (2010).
15. H. M. T. Choi et al., *Nat. Biotechnol.* **28**, 1208 (2010).
16. G. Eckhoff, V. Codrea, A. D. Ellington, X. Chen, *J. Systems Chem.* **1**, 13 (2010).
17. L. Qian, E. Winfree, *J. R. Soc. Interface* **10**, 1098/rsif.2010.0729 (2011).
18. D. E. Muller, in *Symposium on the Application of Switching Theory to Space Technology* (Stanford Univ. Press, Stanford, CA, 1963), pp. 289–297.
19. J. Tian, K. Ma, I. Saaem, *Mol. Biosyst.* **5**, 714 (2009).
20. J. S. Bois, thesis, California Institute of Technology (2007).
21. [www.dna.caltech.edu/SeesawCompiler](http://www.dna.caltech.edu/SeesawCompiler).
22. M. Hucka et al., *Bioinformatics* **19**, 524 (2003).
23. P. W. K. Rothmund, *Nature* **440**, 297 (2006).
24. H. Gu, J. Chao, S. J. Xiao, N. C. Seeman, *Nature* **465**, 202 (2010).
25. K. Lund et al., *Nature* **465**, 206 (2010).
26. L. Qian, D. Soloveichik, E. Winfree, in *DNA Computing and Molecular Programming, Lecture Notes in Computer Science*, Vol. 6518, Y. Sakakibara, Y. Mi, Eds. (Springer, New York, 2011), pp. 123–140.
27. E. Chiniforooshan, D. Doty, L. Kari, S. Seki, in *DNA Computing and Molecular Programming, Lecture Notes in Computer Science*, Vol. 6518, Y. Sakakibara, Y. Mi, Eds. (Springer, New York, 2011), pp. 25–36.
28. A. Goel, M. Ibrahimi, in *DNA Computing and Molecular Programming, Lecture Notes in Computer Science*, Vol. 5877, R. Deaton, A. Suyama, Eds. (Springer, New York, 2009), pp. 67–77.
29. E. B. Baum, *Science* **268**, 583 (1995).
30. R. M. Dirks, N. A. Pierce, *Proc. Natl. Acad. Sci. U.S.A.* **101**, 15275 (2004).
31. W. U. Dittmer, A. Reuter, F. C. Simmel, *Angew. Chem. Int. Ed.* **43**, 3550 (2004).
32. V. N. Kim, *Nat. Rev. Mol. Cell Biol.* **6**, 376 (2005).
33. R. W. Carthew, E. J. Sontheimer, *Cell* **136**, 642 (2009).

**Acknowledgments:** We thank D. Y. Zhang for providing useful comments on the manuscript. Supported by NSF grants 0728703 and 0832824 (Molecular Programming Project) and Human Frontier Science Program award RGY0074/2006-C.

#### Supporting Online Material

[www.sciencemag.org/cgi/content/full/332/6034/1196/DC1](http://www.sciencemag.org/cgi/content/full/332/6034/1196/DC1)  
Materials and Methods  
Figs. S1 to S34  
Tables S1 to S9  
References (34–43)

16 November 2010; accepted 15 April 2011  
10.1126/science.1200520

# Crystal Structure of the Maltose Transporter in a Pretranslocation Intermediate State

Michael L. Oldham and Jue Chen\*

Adenosine triphosphate (ATP)–binding cassette (ABC) transporters convert chemical energy from ATP hydrolysis to mechanical work for substrate translocation. They function by alternating between two states, exposing the substrate-binding site to either side of the membrane. A key question that remains to be addressed is how substrates initiate the transport cycle. Using x-ray crystallography, we have captured the maltose transporter in an intermediate step between the inward- and outward-facing states. We show that interactions with substrate-loaded maltose-binding protein in the periplasm induce a partial closure of the MalK dimer in the cytoplasm. ATP binding to this conformation then promotes progression to the outward-facing state. These results, interpreted in light of biochemical and functional studies, provide a structural basis to understand allosteric communication in ABC transporters.

**A**ctive transport systems transfer substrates across a membrane against a concentration gradient by coupling to a thermodynamically “downhill” reaction. In the prevailing alternating access model, the transporter cycles between two conformations, alternately exposing a substrate-binding site to either side of the membrane (1). Crystal structures of homologous transporters in multiple conformations provide insights into the changes that mediate alternating access (2–8). It is becoming clear that the two-state model may be an oversimplification of active transport-

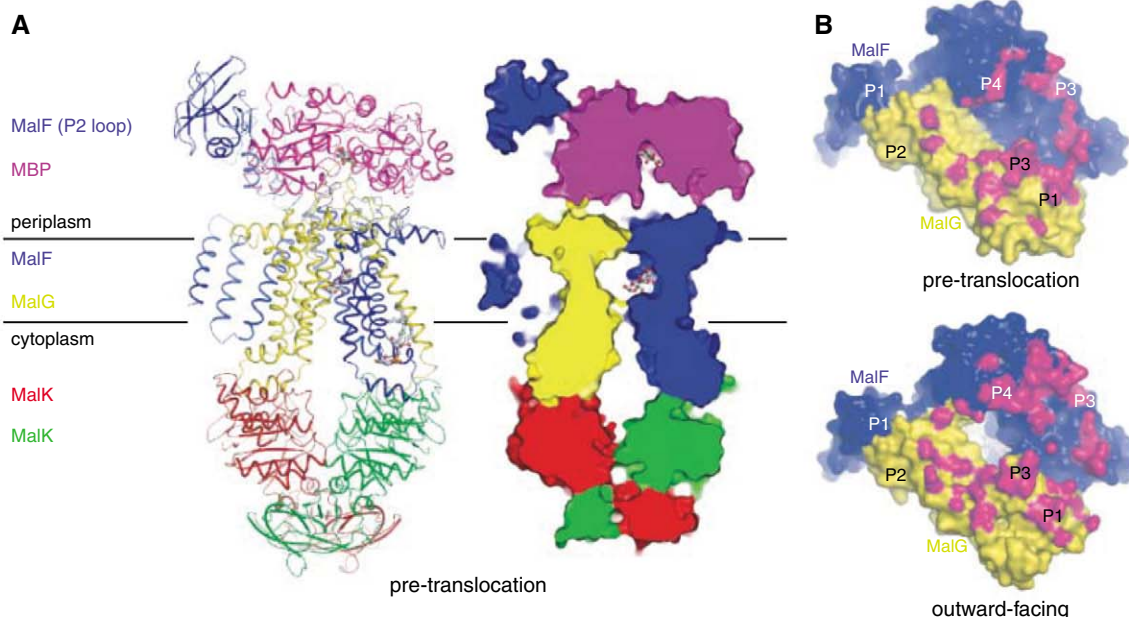
ers; intermediate steps are likely to be involved to channel energy from internal and external sources to enable the transition between the inward- and outward-facing states.

Adenosine triphosphate (ATP)–binding cassette (ABC) transporters offer an opportunity to elucidate a detailed mechanism of active transport. Crystal structures of many isolated nucleotide-binding domains (NBDs) [reviewed in (9)], as well as full-length transporters, have been reported (2, 10–16). Together, these structures show that all ABC transporters contain two cytosolic NBDs attached to two transmembrane domains (TMDs). While the various conformations adopted by these different structures indicate how rigid-body rotations of the TMDs can coincide with closing and opening of the NBD interface [reviewed in

(17)], our understanding of how the presence of transport substrate is communicated to the NBDs to initiate the transport cycle remains incomplete (18).

We used the maltose transporter (MalFGK<sub>2</sub>) from *Escherichia coli* as a model system to analyze the molecular events that couple ATP hydrolysis to substrate translocation. The maltose transporter is an importer composed of two TM subunits, MalF and MalG, and two subunits of a cytoplasmic adenosine triphosphatase (ATPase), MalK. Like many uptake systems in Gram-negative bacteria, a periplasmic maltose-binding protein (MBP), is required to stimulate the ATPase activity of the transporter (19). In the absence of maltose, MBP exists in equilibrium between an open and closed conformation (20–24), and binding of maltose stabilizes the closed conformation. Two structures of MalFGK<sub>2</sub> were determined by x-ray crystallography (2, 3). In the absence of MBP, MalFGK<sub>2</sub> forms an inward-facing conformation with the TM maltose-binding site exposed to the cytoplasm (3). An outward-facing conformation, crystallized in complex with open MBP and ATP, shows that closure of the NBDs of MalK is concomitant with the transfer of maltose from MBP to the TM subunits (2). These structures capture two states in the transport cycle: The inward-facing conformation represents the resting state where the transporter has a very low ATPase activity (19), and the outward-facing conformation represents a catalytic intermediate where ATP is poised for hydrolysis. Because MBP stimulates ATP hydrolysis and initiates the transport process (19), it must interact with the resting state conformation to form a “pretranslocation” (pre-T) complex that is metastable in order to advance to the outward-facing conformation in the presence of ATP (25). Here, we

**Fig. 1.** Structure of the maltose transporter in a pretranslocation conformation. **(A)** Ribbon representation (left) and a surface slab view (right) of the pretranslocation conformation. Maltose molecules are shown in stick model (red, O atom; gray, C atom). **(B)** Surface representation of MalF and MalG viewed from MBP, showing the fingerprint of MBP at the membrane surface in both the pretranslocation and outward-facing states. Atoms of MalFG within 5 Å of MBP are colored in magenta. Periplasmic loops are labeled; the MalF P2 loop is removed for clarity.



present the crystal structure of the initial complex formed between closed MBP and MalFGK<sub>2</sub> (Fig. 1A). As an essential intermediate between the inward- and the outward-facing conformations, this structure suggests a mechanism by which substrate bound on the periplasmic surface influences the conformation of the NBDs at the intracellular surface.

The pre-T complex was obtained by co-crystallizing MalFGK<sub>2</sub> in the presence of maltose with either wild-type (WT) MBP or the MBP<sub>(G69C/S337C)</sub> mutant [see supporting online material (26)]. The MBP<sub>(G69C/S337C)</sub> mutant contains two cysteines that form an interdomain disulfide bond, stabilizing the closed, substrate-bound conformation (27). The two pre-T complex structures are identical, with an overall root mean square deviation (RMSD) less than 1.0 Å (fig. S1). Crystals obtained using the MBP<sub>(G69C/S337C)</sub> mutant diffracted anisotropically to a slightly higher resolution of 3.1 Å (tables S1 and S2), and thus are used here to describe the pre-T state.

The crystal structure of the pre-T complex contains five subunits: MBP in a maltose-bound, closed conformation; the two transmembrane subunits MalF and MalG encapsulating an occluded maltose-binding pocket; and a semi-open MalK dimer with no nucleotide bound (Fig. 1A). The configuration of the pre-T state lies between the inward- and outward-facing states, thus repre-

senting an intermediate in the alternating access model (fig. S2 and movies S1 and S2).

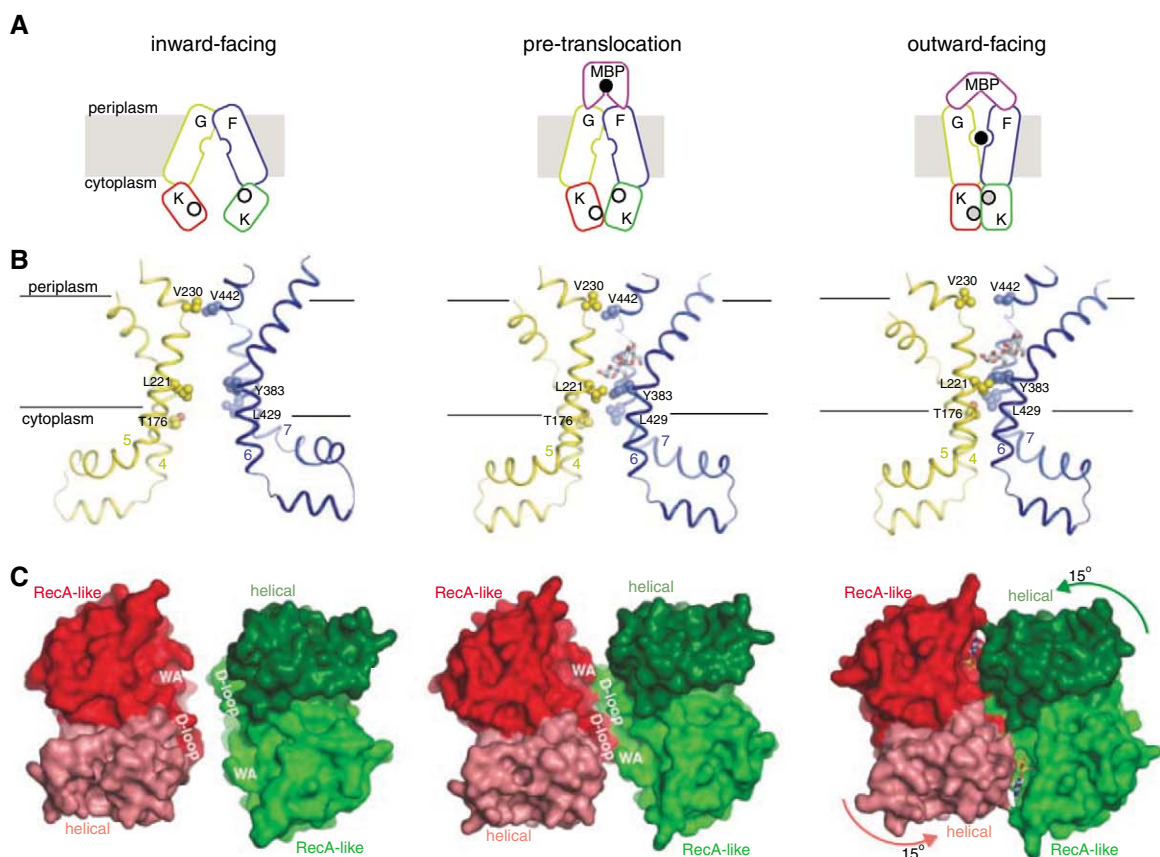
The structure of MBP is very similar to that of isolated MBP in the closed form (23) (RMSD of 0.48 Å for 370 Cα), indicating that neither interactions with MalFGK<sub>2</sub> nor the introduced disulfide bond alter the conformation of the binding protein (fig. S3). At the membrane surface, the two lobes of MBP interact with MalF and MalG, and the circular interface is smaller than that observed in the open MBP, outward-facing structure (Fig. 1B). The total buried surface at the interface is 2438 Å<sup>2</sup> in the pre-T complex and 2872 Å<sup>2</sup> in the outward-facing complex (2), which also contains 15 more hydrogen bonds or salt bridges, consistent with the higher affinity shown in biochemical studies (28).

The TM region of the transporter can be divided into two units, one consisting of MalF TM1-3 and MalG TM2-6, and the other consisting of MalG TM1 and MalF TM4-8 (Fig. 1A and fig. S4). During the transition between different conformational states, these two TM units move relative to each other as rigid bodies. In addition to the maltose molecule present in the closed MBP, a second maltose molecule was identified in the TM site of the pre-T structure (Fig. 2). This TM-bound maltose is likely nonphysiological in the pre-T state, caused by the high concentration of maltose used in crystallization, but it shows that

residues contacting maltose can adopt the same conformation as observed in the outward-facing structure. Access to the binding site in the pre-T state is restricted from both sides of the membrane. The periplasmic gate, similar to that in the inward-facing structure, is formed by residues at the intersection of kinked TM helices, including V230, P231 of MalG and F441, V442 of MalF (Fig. 2B and fig. S5A). However, the configuration of the cytoplasmic gate is different than in either the inward- or outward-facing structures. In contrast to the outward-facing structure, in which MalG TM 4, 5 and MalF TM 6, 7 form a tightly packed helix bundle near the membrane inner leaflet, in the pre-T state these helices are separated, except for residues T176, L221 of MalG and Y383, L429 of MalF, which create van der Waals interactions to shield the TM maltose-binding site from the cytoplasm (Fig. 2B and fig. S5B).

The structure of the MalK dimer resembles a pair of tweezers with a fulcrum point formed by the two regulatory domains and pincers formed by the two NBDs that open and close depending on the ATP hydrolysis state (fig. S2) (29). The outward-facing TMDs coincide with a closed MalK dimer, in which two ATP molecules are bound at the dimer interface (Fig. 2C). In the inward-facing, resting state, the MalK dimer relaxes to an open configuration, in which the NBDs are well

**Fig. 2.** The pretranslocation state is an intermediate conformation between the inward- and outward-facing states. (A) Cartoon representation of three different states of the transport cycle. Maltose is shown as a black ball. The open and filled circles in MalK represent empty and occupied ATP binding sites, respectively. (B) Structure of transmembrane maltose-binding site observed in the three states. For clarity, only two helices from each TM subunit are shown. Residues forming the periplasmic and cytoplasmic gates are shown in space-filling model. Maltose is shown in ball-and-stick model. (C) Surface representations of the nucleotide-binding domains (NBDs) in the three states. The RecA-like and the helical subdomains are differentiated by color and shade. The D loop and the Walker A (WA) motifs are labeled. The rotation of the helical subdomain with respect to the RecA-like domain during transition from the pretranslocation state to the outward-facing conformation is indicated.





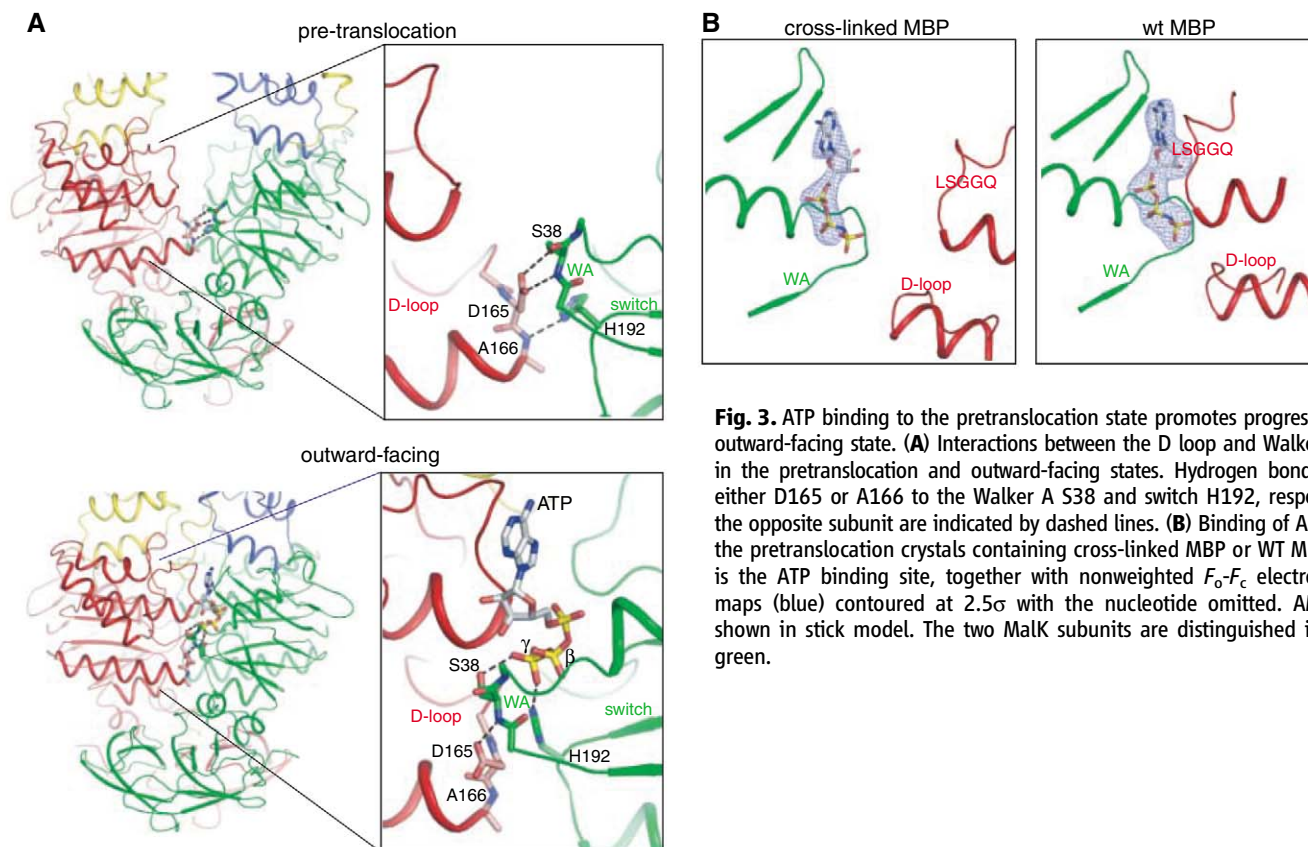


**Fig. 3.** ATP binding to the pretranslocation state promotes progression to the outward-facing state. **(A)** Interactions between the D loop and Walker A motifs in the pretranslocation and outward-facing states. Hydrogen bonds between either D165 or A166 to the Walker A S38 and switch H192, respectively, of the opposite subunit are indicated by dashed lines. **(B)** Binding of AMP-PNP to the pretranslocation crystals containing cross-linked MBP or WT MBP. Shown is the ATP binding site, together with nonweighted  $F_o - F_c$  electron density maps (blue) contoured at  $2.5\sigma$  with the nucleotide omitted. AMP-PNP is shown in stick model. The two MalK subunits are distinguished in red and green.

separated from each other. In the pre-T state, the MalK dimer is semi-open, as the distance between the two NBDs is between those of the open and the closed forms (Fig. 2C and fig S2). The structure of a NBD monomer can be divided into two subdomains: a RecA-like subdomain containing the Walker A/B motifs that are found in many ATPases and a helical subdomain that is specific to ABC transporters. The relative orientations between the RecA-like and the helical subdomains are similar in the resting state and pre-T state. In contrast, transition from the pre-T state to the outward-facing state involves a  $15^\circ$  rotation of the helical subdomain in addition to the movement of the entire NBD (Fig. 2C). Consistently, EPR studies demonstrated that in detergent solutions and in lipid bilayers, the helical subdomain rotation occurs only in the presence of both adenylyl-imidodiphosphate (AMP-PNP) and maltose-MBP (30).

One key feature of the pre-T state is that the D loops are located at the MalK dimer interface (Figs. 2C and 3A). D165 of the D loop is highly conserved among members of the ABC transporter family, and mutations at this position substantially reduce ATPase activity (31). In the pre-T complex, D165 and A166 make H-bonds to the Walker A S38 and H192 of the opposite subunit, respectively (Fig. 3A). In the closed-dimer form of the outward-facing state, both S38 and H192 interact with the  $\gamma$ -phosphate of ATP (Fig. 3A). ATP binding would perturb the pre-T structure

by causing local conformational changes of S38, H192 and the D loop, thereby initiating progression toward the outward-facing conformation. In contrast, in the inward-facing resting state, where MBP is absent, the Walker A/B motifs are distant from the dimer interface (Fig. 2C); thus, ATP binding would not induce such a global structural rearrangement necessary for hydrolysis.

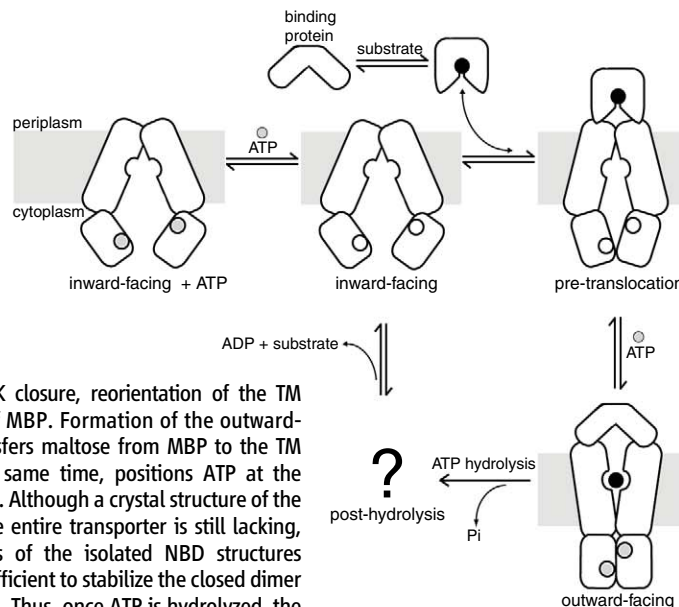
To further investigate the effect of ATP binding, we took advantage of the fact that pre-T crystals were obtained using both maltose-loaded WT MBP and the locked closed MBP mutant. After soaking with the nonhydrolysable ATP analog, AMP-PNP, both the WT and the mutant crystals diffracted anisotropically to about  $3 \text{ \AA}$  resolution (tables S1 and S2); however, the resulting structures were different. AMP-PNP soaking of the WT MBP-MalFGK<sub>2</sub> resulted in a complete conversion to the outward-facing conformation, with clear density for the entire AMP-PNP molecule (Fig. 3B and fig. S6). In contrast, crystals with the MBP<sub>(G69C/S337C)</sub> mutant remained in the pre-T conformation, with AMP-PNP bound to the Walker A motif of each MalK subunit (Fig. 3B and fig. S6). The electron-density map showed density corresponding to the adenoside, the  $\alpha$ - and  $\beta$ -phosphates, and the  $\text{Mg}^{2+}$  ion, but not the  $\gamma$ -phosphate of the nucleotide (Fig. 3B), suggesting that the  $\gamma$ -phosphate is disordered in the semi-open MalK configuration. These data suggest that the formation of the closed NBD dimer in

the outward-facing state is necessary to orient the  $\gamma$ -phosphate for hydrolysis. Consistently, in high-resolution structures of monomeric NBDs, although densities were observed for the  $\gamma$ -phosphate, its position varies among different structures (32–35).

Upon closing the NBD dimer, the LSGGQ motif from the opposing subunit is located at the ATP binding site (Fig. 3B). The LSGGQ motif, also known as the signature motif, is highly conserved in ABC transporters and is essential for ATPase function (36, 37). Its role in orienting the  $\gamma$ -phosphate is reminiscent of the “arginine finger” in many RecA-like ATPases (38). For example, in the structure of  $F_1$ -ATPase, the arginine finger (R373) from the  $\alpha$  subunit inserts into the catalytic  $\beta$  subunit in a position equivalent to that of the LSGGQ motif (39) (fig. S7). In  $F_1$ -ATPase, ATP binding and hydrolysis modulate the interface between the  $\alpha$  and  $\beta$  subunits (40). Analogously, in ABC transporters, ATP hydrolysis is coupled to opening and closure of the NBD dimer interface, which in turn are linked to the orientations of the substrate-binding site relative to the membrane.

Electron paramagnetic resonance (EPR) studies demonstrated that in detergent solutions in the presence of MBP, AMP-PNP induces formation of the outward-facing conformation (41). Here, the same conformational changes occurred inside the crystal lattice. The structural rearrangements are substantial, including opening of the two lobes of

**Fig. 4.** An extended alternating access model for ABC importers. When maltose diffuses into the periplasm through the outer-membrane channel maltoporin, it binds to MBP and stabilizes a closed conformation that interacts with the resting state MalFGK<sub>2</sub>. Binding of MBP to MalFGK<sub>2</sub> brings the NBDs closer such that ATP would promote a concerted motion of MalK closure, reorientation of the TM subunits, and opening of MBP. Formation of the outward-facing conformation transfers maltose from MBP to the TM binding site and, at the same time, positions ATP at the catalytic site for hydrolysis. Although a crystal structure of the posthydrolysis state of the entire transporter is still lacking, EPR studies and analysis of the isolated NBD structures suggest that ADP is not sufficient to stabilize the closed dimer conformation (41, 43, 44). Thus, once ATP is hydrolyzed, the TMDs will likely reorient toward the cytoplasm and the substrate will be released into the cell through diffusion.



MBP, rotations of the TM domains, and closure of the MalK dimer. Usually such large-scale conformational changes would destroy a crystal; however, in this case, both conformational states crystallize in the same triclinic space group with similar packing arrangements (fig. S8), fortuitously allowing the conversion within the crystal. Prevention of MBP opening by an introduced disulfide between its two lobes (G69C/S337C) effectively locks the crystals in the pre-T state, suggesting that the conformational changes involved in the transition are tightly coupled.

The crystal structure of the pre-T conformation extends our knowledge of how coordinated motions in the maltose transporter are communicated more than 80 Å across the membrane to allow active transport (Fig. 4). In the absence of MBP, the resting state MalFGK<sub>2</sub> has little ATPase activity (19), indicating that there is an energetic barrier between the inward- and outward-facing conformations that cannot be overcome by ATP binding alone. EPR studies have shown that binding of both MBP and ATP are required to form the outward-facing conformation (41). The crystal structure of the pre-T state shows that MBP induces rotations of the transmembrane subunits and a partial closure of the MalK dimer, bringing two catalytic residues, the Walker A S38 and switch H192, to the dimer interface. In contrast to the resting state, ATP binding to the pre-T state drives progression to the outward-facing state, indicating that MBP binding lowers the energy barrier for closure of the MalK dimer necessary for ATP hydrolysis. MBP binds in the closed form to induce the pre-T state, thus explaining the well-known enhancement of ATP hydrolysis by maltose (19). This property of the maltose transporter and MBP emphasizes the important role of the sub-

strate in regulating the ATPase activity by stabilizing a specific conformation of the binding protein that productively interacts with the transporter. Genetic data have shown that the requirement of MBP to activate ATP hydrolysis can be bypassed by mutations in the transmembrane subunits (42). Mapping these mutations into the structure suggests that they destabilize the resting state, equivalent to lowering the energy barrier between the inward- and outward-facing states (3).

#### References and Notes

- O. Jardetzky, *Nature* **211**, 969 (1966).
- M. L. Oldham, D. Khare, F. A. Quijcho, A. L. Davidson, J. Chen, *Nature* **450**, 515 (2007).
- D. Khare, M. L. Oldham, C. Orelle, A. L. Davidson, J. Chen, *Mol. Cell* **33**, 528 (2009).
- S. K. Singh, C. L. Piscitelli, A. Yamashita, E. Gouaux, *Science* **322**, 1655 (2008).
- P. L. Shaffer, A. Goehring, A. Shankaranarayanan, E. Gouaux, *Science* **325**, 1010 (2009).
- O. Boudker, R. M. Ryan, D. Yernool, K. Shimamoto, E. Gouaux, *Nature* **445**, 387 (2007).
- D. Yernool, O. Boudker, Y. Jin, E. Gouaux, *Nature* **431**, 811 (2004).
- N. Reyes, C. Ginter, O. Boudker, *Nature* **462**, 880 (2009).
- C. Oswald, I. B. Holland, L. Schmitt, *Naunyn-Schmiedeberg's Arch. Pharmacol.* **372**, 385 (2006).
- K. Hollenstein, D. C. Frei, K. P. Locher, *Nature* **446**, 213 (2007).
- R. N. Hvorup *et al.*, *Science* **317**, 1387 (2007).
- H. W. Pinkett, A. T. Lee, P. Lum, K. P. Locher, D. C. Rees, *Science* **315**, 373 (2007).
- R. J. P. Dawson, K. P. Locher, *Nature* **443**, 180 (2006).
- N. S. Kadaba, J. T. Kaiser, E. Johnson, A. Lee, D. C. Rees, *Science* **321**, 250 (2008).
- S. G. Aller *et al.*, *Science* **323**, 1718 (2009).
- A. Ward, C. L. Reyes, J. Yu, C. B. Roth, G. Chang, *Proc. Natl. Acad. Sci. U.S.A.* **104**, 19005 (2007).
- M. L. Oldham, A. L. Davidson, J. Chen, *Curr. Opin. Struct. Biol.* **18**, 726 (2008).

- P. M. Jones, M. L. O'Mara, A. M. George, *Trends Biochem. Sci.* **34**, 520 (2009).
- A. L. Davidson, H. A. Shuman, H. Nikaido, *Proc. Natl. Acad. Sci. U.S.A.* **89**, 2360 (1992).
- C. Tang, C. D. Schwieters, G. M. Clore, *Nature* **449**, 1078 (2007).
- J. Evenäs *et al.*, *J. Mol. Biol.* **309**, 961 (2001).
- J. A. Hall, T. E. Thorgeirsson, J. Liu, Y. K. Shin, H. Nikaido, *J. Biol. Chem.* **272**, 17610 (1997).
- J. C. Spurlino, G. Y. Lu, F. A. Quijcho, *J. Biol. Chem.* **266**, 5202 (1991).
- A. J. Sharff, L. E. Rodseth, J. C. Spurlino, F. A. Quijcho, *Biochemistry* **31**, 10657 (1992).
- B. H. Shilton, *Biochim. Biophys. Acta* **1778**, 1772 (2008).
- Materials and methods are available as supporting material on Science Online.
- Y. Zhang, D. E. Mannering, A. L. Davidson, N. Yao, M. D. Manson, *J. Biol. Chem.* **271**, 17881 (1996).
- J. Chen, S. Sharma, F. A. Quijcho, A. L. Davidson, *Proc. Natl. Acad. Sci. U.S.A.* **98**, 1525 (2001).
- J. Chen, G. Lu, J. Lin, A. L. Davidson, F. A. Quijcho, *Mol. Cell* **12**, 651 (2003).
- C. Orelle *et al.*, *Proc. Natl. Acad. Sci. U.S.A.* **107**, 20293 (2010).
- S. Hunke, H. Landmesser, E. Schneider, *J. Bacteriol.* **182**, 1432 (2000).
- L. W. Hung *et al.*, *Nature* **396**, 703 (1998).
- G. Verdon, S. V. Albers, B. W. Dijkstra, A. J. Driessen, A. M. Thunnissen, *J. Mol. Biol.* **330**, 343 (2003).
- H. A. Lewis *et al.*, *EMBO J.* **23**, 282 (2004).
- M. Haffke, A. Menzel, Y. Carius, D. Jahn, D. W. Heinz, *Acta Crystallogr. D Biol. Crystallogr.* **66**, 979 (2010).
- P. C. Smith *et al.*, *Mol. Cell* **10**, 139 (2002).
- A. L. Davidson, J. Chen, *Annu. Rev. Biochem.* **73**, 241 (2004).
- J. Ye, A. R. Osborne, M. Groll, T. A. Rapoport, *Biochim. Biophys. Acta* **1659**, 1 (2004).
- M. W. Bowler, M. G. Montgomery, A. G. Leslie, J. E. Walker, *J. Biol. Chem.* **282**, 14238 (2007).
- J. P. Abrahams, A. G. Leslie, R. Lutter, J. E. Walker, *Nature* **370**, 621 (1994).
- C. Orelle, T. Ayvaz, R. M. Everly, C. S. Klug, A. L. Davidson, *Proc. Natl. Acad. Sci. U.S.A.* **105**, 12837 (2008).
- K. M. Covitz *et al.*, *EMBO J.* **13**, 1752 (1994).
- N. Karpowich *et al.*, *Structure* **9**, 571 (2001).
- G. Lu, J. M. Westbrook, A. L. Davidson, J. Chen, *Proc. Natl. Acad. Sci. U.S.A.* **102**, 17969 (2005).

#### Supporting Online Material

www.sciencemag.org/cgi/content/full/science.1200767/DC1  
Materials and Methods  
SOM Text  
Figs. S1 to S8  
Tables S1 and S2  
References  
Movies S1 and S2

22 November 2010; accepted 14 April 2011  
Published online 12 May 2011;  
10.1126/science.1200767

# Residue-Specific Vibrational Echoes Yield 3D Structures of a Transmembrane Helix Dimer

Amanda Remorino,<sup>1</sup> Ivan V. Korendovych,<sup>2</sup> Yibing Wu,<sup>2</sup> William F. DeGrado,<sup>2</sup> Robin M. Hochstrasser<sup>1\*</sup>

Two-dimensional (2D) vibrational echo spectroscopy has previously been applied to structural determination of small peptides. Here we extend the technique to a more complex, biologically important system: the homodimeric transmembrane dimer from the  $\alpha$  chain of the integrin  $\alpha_{IIb}\beta_3$ . We prepared micelle suspensions of the pair of 30-residue chains that span the membrane in the native structure, with varying levels of heavy ( $^{13}\text{C}=^{18}\text{O}$ ) isotopes substituted in the backbone of the central 10th through 20th positions. The constraints derived from vibrational coupling of the precisely spaced heavy residues led to determination of an optimized structure from a range of model candidates: Glycine residues at the 12th, 15th, and 16th positions form a tertiary contact in parallel right-handed helix dimers with crossing angles of  $-58^\circ \pm 9^\circ$  and interhelical distances of  $7.7 \pm 0.5$  angstroms. The frequency correlation established the dynamical model used in the analysis, and it indicated the absence of mobile water associated with labeled residues. Delocalization of vibrational excitations between the helices was also quantitatively established.

Two-dimensional infrared spectroscopy (2D-IR) has been used to obtain conformations of small peptides (2–6) from the strength and polarization characteristics of the spectral crosspeaks using principles analogous to those of 2D nuclear magnetic resonance (NMR) (7). Nevertheless, it remains a major challenge to apply 2D-IR to obtain structures of larger systems, such as proteins, where many more constraints are needed. We have now successfully used 2D-IR to determine the tertiary structure of a homodimeric transmembrane (TM) dimer from the  $\alpha$  chain of the integrin  $\alpha_{IIb}\beta_3$ , which mediates the binding of fibrinogen to platelets. The TM domain from this integrin, which preserves the native state, forms homodimers in micelles and bacterial membranes (8), facilitating its study in isolation from the rest of the protein.

The high degeneracy of the amide transitions in helical proteins complicates efforts aimed at extracting structural constraints with the use of vibrational spectroscopy. This difficulty is overcome by carbon and oxygen isotope replacements in the carbonyl groups of amide units, which shift the vibrational frequencies beyond the natural bandwidths in the infrared, enabling resolution of individual and pairs of residues. Therefore, a residue-level set of constraints is achievable even for a large system. In addition, 2D-IR reveals the dynamics of the frequency distributions of the vibrations of each residue, which are sensitive to the presence of water molecules (9, 10). Protein conformations that interchange more slowly than  $\sim 1$  ps and that are averaged in NMR become accessible as discrete, exchanging transitions in 2D-IR spectroscopy, which can become a stan-

dard method to determine structures and structural dynamics (11).

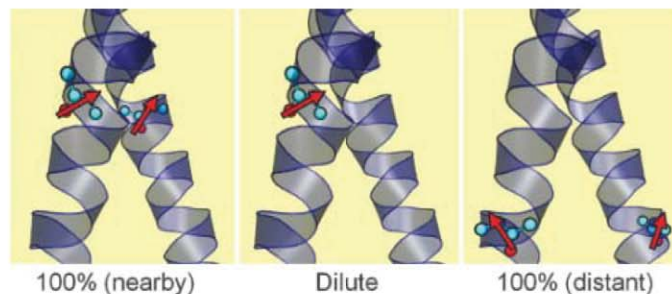
Our experimental concept relies on the fact that molecular vibrational excitation creates an oscillating dipole that is sensed by nearby molecules through electrostatic interactions. The oscillatory transfer of the vibrational excitation to a near resonant vibrator depends on the inverse cube of the separation and on the absolute square and orientation of the vibrational transition dipoles. This quantum mechanical effect delocalizes the vibrational excitations of the peptide on (12) or between (13) backbones. The microscopic situation prevailing in the present experiments is illustrated schematically in Fig. 1. The relatively large isotope shift ( $\sim 65\text{ cm}^{-1}$ ) from substitution of  $^{13}\text{C}=^{18}\text{O}$  into the peptide backbone strongly localizes the amide vibration. If there is also a  $^{13}\text{C}=^{18}\text{O}$  label on the same residue of the neighboring helix of a transmembrane dimer, the vibrational mode may become delocalized over the pair of isotopically isolated vibrational states on the different helices. However, if only one helix of the dimer has the isotopic substitution or if the resonance pair separation is too large, the mode will remain localized. Therefore, if made

from mixtures of isotopically substituted and unsubstituted peptides, the TM dimers will consist of structures having both localized and delocalized pair modes, depending on the residue and isotope dilution. The spectral differences between the diluted and undiluted samples provide constraints to determine the 3D structure of the dimer. These differences arise only from electrostatic interactions, because the amide I modes on different helices have vanishingly small charge overlap.

Interhelical contacts between nearby amides were detected in the NMR structure of the TM domain of the homodimeric protein glycoporphin A by MacKenzie *et al.* (14). This finding suggested that it might be possible to solve structures of membrane proteins by 2D-IR if two methodological and theoretical challenges could be met. First, methods of sample preparation and spectroscopic measurements would have to be sufficiently well optimized to process multiple labels scanned through the interaction site of the TM helices. Second, the coupling between the amide oscillators would be needed for input into computations of protein structures. Here we provide the spectroscopic and theoretical underpinnings necessary to allow deconvolution of the 2D-IR spectra into static versus dynamic components, and then we derive spectral parameters to guide de novo structure determination of the weakly interacting  $\alpha_{IIb}$  homodimer (8).

We prepared this peptide with varying degrees of  $^{13}\text{C}=^{18}\text{O}$  incorporation (15) at each of the residues in the central L10 to L20 span (16). Based on knowledge of the typical sequences of interacting regions of TM dimers (14) and mutagenesis studies of the  $\alpha_{IIb}$  homodimer (8), we anticipated that this region would encompass some amides on different helices undergoing measurable interactions. We then applied 2D-IR spectroscopy to micelle-embedded samples of these peptides in solution. The 2D-IR spectra (6) displayed in Fig. 2 are plots of the coherence frequency  $\omega_c$  introduced by the pump laser versus the coherence frequency  $\omega_l$  probed for various waiting times ( $T$ ) between the second and third infrared pulses of the three-pulse echo experiment. The two overlapping regions with opposite signs correspond to the  $\nu = 0 \rightarrow 1$  transition (red)

**Fig. 1.** Schematic depiction of three possible situations present in the isotope dilution experiment. The nearby and distant cases depict 100%  $^{13}\text{C}=^{18}\text{O}$  substituted samples and their localized transition dipoles (red arrows). In the nearby case, the dipoles interact considerably through space to cause tertiary delocalization of the vibrational excitation. In the dilute case, a  $^{13}\text{C}=^{18}\text{O}$  residue experiences a localized excitation. In the distant case, the excited residues are not close enough to interact, so the spectrum does not depend on isotope dilution.



<sup>1</sup>Department of Chemistry, University of Pennsylvania, Philadelphia, PA 19104–6323, USA. <sup>2</sup>Department of Biochemistry and Biophysics, University of Pennsylvania School of Medicine, Philadelphia, PA 19104–6059, USA.

\*To whom correspondence should be addressed E-mail: hochstra@sas.upenn.edu



and to the  $\nu = 1 \rightarrow 2$  transition (blue) (where  $\nu$  is the vibrational quantum number). The elongation along the diagonal of the 2D axes indicates the distribution of vibrational frequencies exhibited by the distribution of dimer structures.

The data for G12 and L14 in Fig. 2 illustrate the residue dependence of the 2D-IR line shapes at different isotope dilutions. The spectra for the mixtures of the nine remaining residues are presented in fig. S6. These 2D-IR spectra were taken at  $T = 300$  fs. The 2D-IR spectral shapes, as judged by the diagonal and antidiagonal widths and the slopes (17), were found to be identical at  $T = 300$  and 1500 fs. The shapes were constant during these  $T$  intervals. This result, which cannot be obtained from linear spectroscopy, completely specifies the dynamical picture needed to compute the spectra. The decay of the 2D-IR signal of the  $^{13}\text{C}=^{18}\text{O}$  amide-I band yielded population decay time,  $T_1$ , of  $800 \pm 100$  fs for all residues [see the supporting online material (SOM)].

The  $^{13}\text{C}=^{18}\text{O}$  amide I transition of each residue is indicated in Fig. 2 with a dashed horizontal yellow line at  $\omega_t$  between  $1582$  and  $1602\text{ cm}^{-1}$ . Two main features are central: (i) The line shape for the 100%  $^{13}\text{C}=^{18}\text{O}$  sample is broader than that for the 10% sample in the case of G12, but the corresponding line shapes are almost the same for L14. (ii) In spectra of the 10% samples, G12 shows a circular 2D-IR peak, whereas L14 shows a more diagonally elongated peak. The spectral broadening of G12 in the 100%  $^{13}\text{C}=^{18}\text{O}$  sample spectrum is a result of the through-space coupling between the resonant pair of isotopically replaced residues. The interactions were evaluated from the trace of the 2D-IR spectra along the line  $\omega_t = \omega_i + c$  where  $c = 2.5\text{ cm}^{-1}$  is the frequency difference between the maxima of the  $^{13}\text{C}=^{18}\text{O}$  peaks and the diagonal line. The results for G12,

where the isotopomer concentration effect is evident, and L14, where it is not, are shown in Fig. 2, C and D (see fig. S6 for the other nine residues).

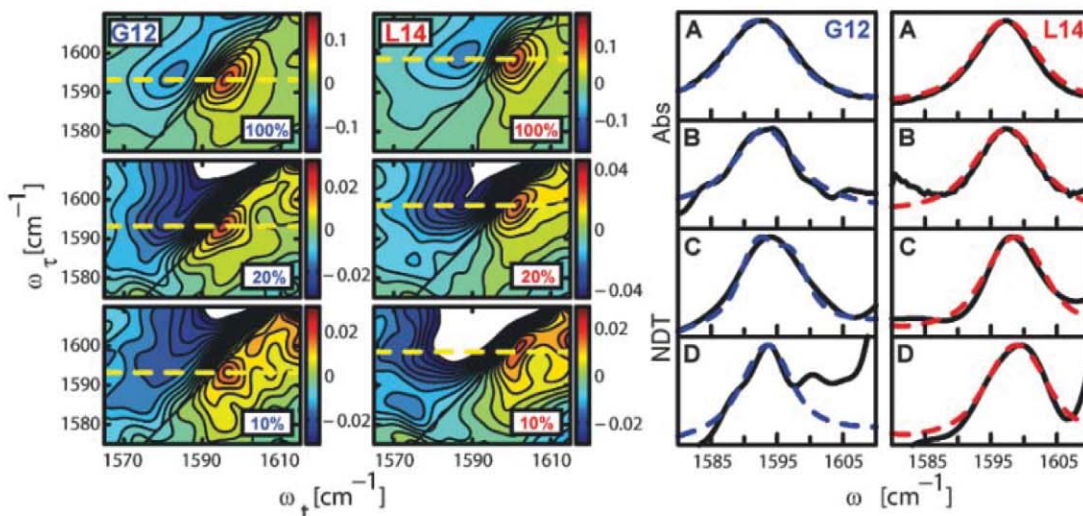
The  $^{13}\text{C}=^{18}\text{O}$  transitions in the diluted samples, which are so clearly visible in the 2D-IR spectra of all the isotopomers, are not directly obtainable from the 1D Fourier transform infrared (FTIR) spectra, in which optical densities are less than  $\sim 0.001$ . The 2D-IR spectral signals depend on the fourth power of the transition dipole moment so that, for a given absorbance, they are proportional to the extinction coefficient of the transition. These factors cause considerable suppression of signals with low extinction coefficients like  $\text{D}_2\text{O}$  and the tail of the main-band amide I absorption. The FTIR spectra shown in Fig. 2, A and B, for G12 and L14 were processed using information from the 2D-IR spectra, as explained in more detail in the text accompanying figs. S2 to S4, where FTIR data for the remaining nine residues are given.

An important result is the variation of nonlinear and linear spectral properties with the position of the residue along the sequence. For example Fig. 3, A and B, shows the alternation with residue number of the spectral widths of the 2D-IR diagonal traces and FTIR spectra of the  $^{13}\text{C}=^{18}\text{O}$  transitions. The repeat separation is three to four residues. The amplitude of the alternation effect is caused mainly by the excitonic coupling between the labeled sites of a dimeric helix. A smaller amplitude alternation is also seen in the 10% samples, which indicates that, even when free from coupling, the signals are sequence-location sensitive. The dilute (10%) 2D-IR spectral widths in Fig. 3A alternate one helix turn out of phase with the other signals (see SOM). Already, without quantitative analysis, we can posit

that the residues V11 to L17 are bracketing the main crossing interactions between the two helices. However, to proceed further, it is necessary to develop a quantitative description of these spectra to obtain the through-space coupling constants needed as structure constraints.

The residue positional dependence of the differences between 2D-IR spectra at different isotope dilutions is essential to the determination of the coupling constants. The peptide links in different helices of a dimer are always separated by more than  $\sim 4\text{ \AA}$ , which is the shortest separation seen in the very stable dimer of glycoporphin A (GPA) (14). Hence, the differences between the 100% and 10% shapes must be solely caused by the electrostatic interaction of the transition charge distributions associated with the excitation of the amide I mode. Therefore, an exciton model, in which two local  $^{13}\text{C}=^{18}\text{O}$  sites on each helix couple through space to form new states that are linear combinations of the local ones, was used to describe them. The dynamics of these delocalized states are determined by their population and pure dephasing relaxation. The  $T$  invariance of the 2D-IR spectral shapes implies that the distribution of vibrational frequencies constituting the band shapes of the spectra remains constant. This result prompts the use of a dynamical model in which the frequency-frequency correlation function  $C(T)$  has two components, one of which decays more quickly and the other much more slowly than the inverse bandwidth of the IR spectrum. The quickly decaying component gives rise to a homogeneous dephasing,  $T_2^*$ , of each of the transitions, and the ultraslow decay introduces an inhomogeneous width,  $\sigma$ . Hence, the signals are represented by Lorentzian functions averaged over fixed distributions of the frequency. The few-picosecond decay that occurs

**Fig. 2.** 2D-IR correlation spectra and FTIR spectra with different concentrations of  $^{13}\text{C}=^{18}\text{O}$  isotopic substitution on residues G12 and L14. The mixtures of  $^{13}\text{C}=^{18}\text{O}$  labeled and unlabeled ( $^{12}\text{C}=^{16}\text{O}$ ) helices are given as the percentage of the sample that is  $^{13}\text{C}=^{18}\text{O}$ . (Left) Contour plots showing 2D-IR correlation spectra of peptides substituted to the extent indicated (10 to 100%) with  $^{13}\text{C}=^{18}\text{O}$  at the G12 and L14 residues. The spectra were taken at  $T = 300$  fs and a  $\tau$  range of  $-2800$  to  $3200$  fs. The dashed yellow lines indicate the peak frequency assigned to the  $^{13}\text{C}=^{18}\text{O}$  amide I transition. The corresponding 2D-IR diagonal traces for the 100 and 10% samples are shown in (C) and (D), respectively. (Right) Subtracted FTIR spectra of (A) 100% and (B) 10%  $^{13}\text{C}=^{18}\text{O}$  substituted samples at G12 and L14 are shown. The normalized experimental results (black solid lines) were fitted with the model explained in the text (blue dashed lines). For G12, the 100% sample peaks are broader than the 10% sample peaks in the FTIR [(A) versus (B)] and in the 2D-IR [(C) versus



(D)] spectra, whereas the data for L14 show no significant difference in peak widths for different isotopic dilutions. The peak at  $\sim 1601\text{ cm}^{-1}$  in panel (D) of G12 is a weak transition that becomes evident in the 10% samples where the signal-to-background ratio is reduced. It is definitely not related to the  $^{13}\text{C}=^{18}\text{O}$  amide I transition, so it was readily subtracted and removed from the analysis (see SOM and fig. S7). Abs, absorbance; NDT, normalized diagonal trace.

when  $C(T)$  is influenced by water molecules near the amide groups is absent in the signals, from which we conclude there is no mobile associated water in the sense of (9, 10) for any residue.

Each isotopically selected dimer in the ensemble contributes two site transitions to the inhomogeneous distribution of frequencies. Deviations of these frequencies from their means are assumed to be uncorrelated on the basis that they are caused by independent, local forces on modes of different helix backbones. The exciton states (here referred to as  $|+\rangle$  and  $|-\rangle$ ) originate from the perturbation of the  $\nu = 1$  states by intersite, dipole-dipole electrostatic interactions of  $\nu = 0 \rightarrow 1$  transitions. For the computation of the spectra, the linear and nonlinear (18) response functions are calculated in the basis of these eigenstates. The exciton eigenfrequencies and transition dipole vectors are readily expressed in terms of the pair state variables  $\theta$  and  $\phi$ , where  $\tan\theta = 2|\beta|/\omega_{12}$  and  $\beta = |\beta|e^{i\phi}$ , where  $\omega_{12}$  is the site frequency gap,  $\beta$  is the coupling, and  $i^2 = -1$ . Equation 1 is the linear infrared spectral shape,  $S_{\text{FTIR}}(\omega)$ , of the amide I transitions of the  $^{13}\text{C}=^{18}\text{O}$  labeled residues involving components at  $\omega_{0\pm}$  between the ground state and the resonance pair states  $|\pm\rangle$ , with  $\vec{\mu}_{0\pm}$  being the transition dipoles and  $\gamma_{0\pm}$  the homogeneous dephasing rates

$$S_{\text{FTIR}}(\omega) = \frac{1}{3} \text{Re} \left\langle \frac{|\vec{\mu}_{0+}|^2}{i(\omega_{0+} - \omega) + \gamma_{0+}} + \frac{|\vec{\mu}_{0-}|^2}{i(\omega_{0-} - \omega) + \gamma_{0-}} \right\rangle \quad (1)$$

The 2D-IR spectra (Eq. 2 and SOM) are constructed from different Liouville pathways (18) that involve all the exciton one and two quantum excitations (19) at  $T = 300$  fs. Equation 2 shows the contribution to the spectrum from one typical 2D-IR response function in the frequency domain, with all the broad bandwidth incident fields sharing the same polarization and transitions between the same exciton levels involved in each step of the nonlinear interaction (the Liouville diagrams and analytical forms for the others are shown in the SOM). In Eqs. 1 and 2, the joint average denoted by angle brackets is taken over the two-site frequency distributions assumed to be uncorrelated Gaussians having width  $\sigma$

$$R_1(\omega_\tau = \omega_d, \omega_r = \omega_d + c) = \frac{1}{5} \text{Re} \left\langle \frac{e^{-T/T_1} |\vec{\mu}_{0+}|^4}{[i(\omega_{0+} - \omega_d) + \gamma_{0+}][i(\omega_{0+} - \omega_d - c) + \gamma_{0+}]} \right\rangle \quad (2)$$

The frequency  $\omega_d$  is the diagonal trace; the Lorentz parameter  $\gamma_{mn}$  represents the homogeneous widths: for example,  $2\gamma_{mn} = 1/2T_1 + 1/T_2^*(m, n; \beta, \omega_{12})$ , where  $T_2^*(m, n; \beta, \omega_{12})$  is the pure dephasing time of the  $mn$  transition, which, in turn, depends on the degree of localization of the excitation determined (20) by  $\beta$  and  $\omega_{12}$ .

For reference, the dipolar coupling between typical amide I oscillators with  $\mu = 0.35$  debye is  $610\kappa(\Omega)/R^3 \text{ cm}^{-1}$ , where  $\kappa(\Omega)$  is a geometric parameter  $-1 < \kappa(\Omega) < 2$ , and  $R$  is the point dipole separation in angstrom units. For two-fold symmetry,  $\kappa(\Omega) = 1 + (\cos\theta_{12} - 1)P_2(\cos\phi)$ , where  $P_2$  is the second Legendre polynomial, the angle between the dipoles is  $\theta_{12}$ , and  $\phi$  or  $\phi + \pi$  are their azimuths.

Therefore at  $R = 5.7 \text{ \AA}$ , we find  $-3.3 < \beta < 6.6 \text{ cm}^{-1}$ ; this is the approximate range of expected couplings. Their magnitudes are comparable with typical linewidths, so the exciton transitions are expected to be overlapped. However, such exciton interactions should cause substantial broadening of the transitions, which is exactly what is observed and characterized quantitatively in our data.

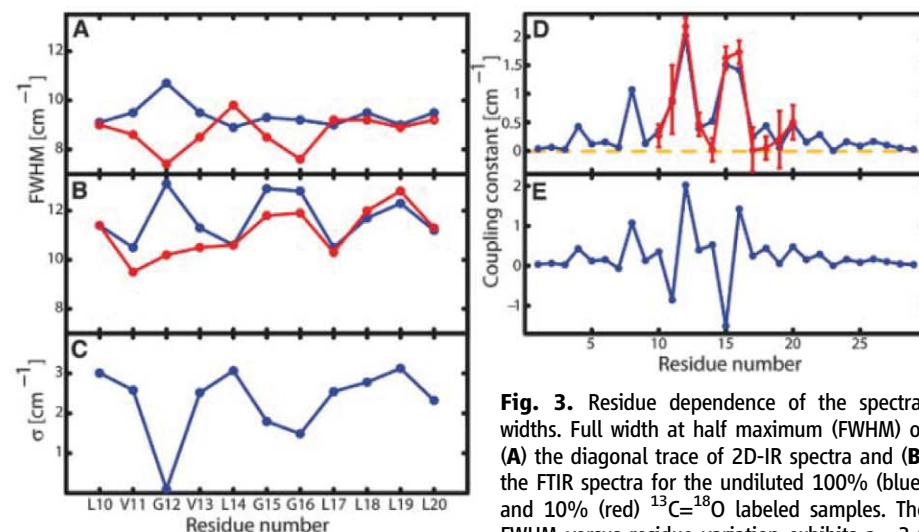
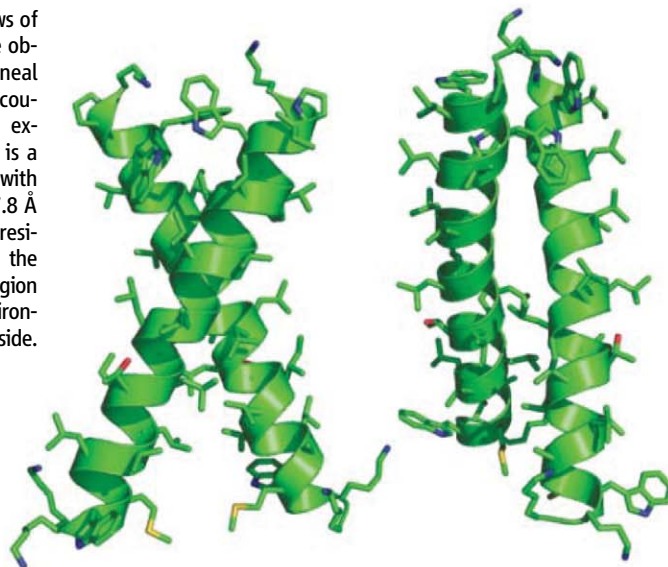


**Fig. 3.** Residue dependence of the spectral widths. Full width at half maximum (FWHM) of (A) the diagonal trace of 2D-IR spectra and (B) the FTIR spectra for the undiluted 100% (blue) and 10% (red)  $^{13}\text{C}=^{18}\text{O}$  labeled samples. The FWHM versus residue variation exhibits a  $\sim 3.6$  residue repeat corresponding to the helicity of

the monomers. The 2D-IR traces of the 10% samples show a change in phase in this oscillation resulting from the higher homogenous component of the residues facing the inside of the dimer (see SOM for discussion of this point). The overall smaller widths of the 2D-IR traces compared with the FTIR spectra make the determination of the coupling constant more accurate. (C) The inhomogeneous component  $\sigma$  defines the Gaussian average. It is obtained by varying  $\sigma, T_2^*$  and the zero order frequencies (see SOM) in fits of the FTIR and 2D-IR traces to the model explained in the text. This result is consistent with the noticeable elongation of the peaks of the 2D-IR spectra, and it suggests that the residues involved in the tertiary contact experience a narrower distribution of structures. (D) The absolute value of the coupling constants for the final structure (red) and those obtained from the fit of the experiment (blue) also present a periodicity of  $\sim 3.6$  residues. G12, G15, and G16 form the tertiary contact and present the highest coupling magnitudes. The error bar corresponds to a change in  $\chi^2$  of 0.5. The dashed yellow line indicates zero coupling. (E) The signed coupling constant of the final structure. G15, L19, and V11 have negative coupling constants.

**Fig. 4.** Front and side views of the lowest-energy structure obtained from simulated anneal using the through-space coupling constants from the experiment as constraints. It is a right-handed helix dimer with a  $-55^\circ$  crossing angle and  $7.8 \text{ \AA}$  interhelical distance. The residues facing the inside of the dimer in the investigated region experience a different environment than those on the outside.





The structural information can be obtained exclusively from the 2D-IR traces, but we included the FTIR to further constrain the analysis. In contrast, the coupling constants could not be obtained from FTIR data alone. In the first place, the vibrational frequency dynamics would be undetermined. Furthermore, the enhanced signal-to-background ratio results in the 2D-IR diagonal trace having better resolution and diminished background interference, permitting a robust calculation of the coupling constants. The 2D-IR width is intrinsically more sensitive to coupling than the linear IR in the range of our parameters (see SOM), but incorporation of both provides a better set of results than does either one.

The FTIR and 2D-IR spectra of the 10 and 100% samples were simultaneously fit by least-squares minimization to the foregoing model to yield the absolute values of the coupling constants and dynamical parameters that are mutually consistent with four data sets for each of the 11 residues. The peaks in the residue dependence of the coupling in Fig. 3D show clearly that G12, G15, and G16 have the closest tertiary proximity. The periodicity of this pattern of peaks in the experiment is  $\sim 3.6$  residues, matching the repeat of the  $\alpha$  helix. The fits generate values for the inhomogeneous broadening parameter whose residue positional dependence is shown in Fig. 3C. The alternation of  $\sigma$  (21, 22) is consistent with the observed trend in the extent of elongation along the diagonal of the 2D-IR spectra of the 10% samples. It indicates that those residues in the dimer interface—namely G12, G15, and G16—present significantly narrower static distributions of structures than do the other residues. The results imply that there are specific interactions causing local ordering of the residues forming the tertiary contacts, resulting in a narrowing of their frequency distributions such as would occur in a crystal.

A key factor in the structure simulation is the direction of the  $^{13}\text{C}=\text{O}$  amide transition dipole in the frame of the peptide link. A perturbation theory estimate using the method described in (23), based on the isotope shift being large compared with coupling, shows that the coupling of a  $^{13}\text{C}=\text{O}$  amide with the remaining  $^{12}\text{C}=\text{O}$  residues of a typical helix does not cause its transition dipole to rotate in the peptide frame by more than  $3^\circ$  (see SOM). Therefore, the transition dipole for an isolated amide unit from (12, 24) was used in the simulation.

To find a family of structures consistent with the experiments, we first sampled the whole space of interacting two-fold symmetric ideal helices to identify the pose most consistent with the 2D-IR coupling constants. A  $\chi^2$  test revealed 48 structures that were consistent with the experiment within a 75% confidence interval. They were all right-handed parallel dimers with an average crossing angle of  $-63^\circ \pm 13^\circ$  and interhelical distance  $8.5 \pm 0.3$  Å. The structure with an interhelical distance of 8.5 Å and crossing angle of  $-60^\circ$  showed the best agreement with the experiments. The model was further refined with the appropri-

ate side chains by a constrained simulated anneal with Xplor-NIH (25, 26). A new module was written for Xplor-NIH (25, 26) to account for the deviation from the vibrational dipole-dipole coupling constants obtained from the experiment (see SOM). The 48 preselected structures were each taken as starting points for 100 structures. Every structure was first minimized by 500 steps to remove bad contacts, bathed at a high temperature (3000 K) for 1000 steps, followed by cooling to a low temperature (10 K) for another 1000 steps and was subjected to Powell minimization for final 2000 steps. More details on the constraints can be found in the SOM. This simulated annealing using vibrational through-space coupling constants as constraints minimizes the energy and accommodates the side chains and the backbone to find a better agreement with the experiment. This procedure yielded 20 parallel right-handed helix dimers with crossing angles of  $-58^\circ \pm 9^\circ$  and interhelical distances of  $7.7 \pm 0.5$  Å. The absolute values of the coupling constants for the structure that presented the lowest energy ( $-55^\circ$  crossing angle and 7.8 Å interhelical distance) and the experimental results are compared in Fig. 3D. The residues G12, G15, and G16 form the tertiary contact and present the highest coupling magnitudes. The residues G15, L19, and V11 have negative coupling constants. The view of the final energy-minimized structure is shown in Fig. 4.

The peptide studied here belongs to the overall class of G-XXX-G motifs that drive dimerization in cell membranes and lipid micelles (14). Within this sequence motif, the affinity, specificity, and precise geometric details of the interaction depend critically on the surrounding primary sequence (27). The computed structural model for the  $\alpha_{\text{IIb}}$  homodimer differs from the original canonical motif seen in glycophorin, which has a somewhat smaller crossing angle, interhelical distance, and rotation of each helix about its axis (helical phase). Instead, the computed structure fits to a related right-handed motif, cluster #10 of (28), which has an average crossing angle of  $-60^\circ \pm 15^\circ$  and interhelical distances of  $8.6 \pm 1.0$  Å. A previous site-directed mutagenesis study showed a somewhat surprising phase-shift in the distribution of the residues that contribute to homodimerization in  $\alpha_{\text{IIb}}$  versus GPA, consistent with a rotation of the helix by  $50^\circ$  (8). The difference was attributed to the fact that  $\alpha_{\text{IIb}}$  has a GxxGG sequence with a third Gly residue that contributes to the interface in this homodimer but not in GPA. This interaction is now clearly seen in the spectral widths and couplings at positions 15 and 16 in Fig. 3, D and E. Moreover, the computed structure shows the  $50^\circ$  helical phase shift and the larger crossing angle inferred from site-directed mutagenesis. Thus, these results provide direct structural information that explains the previous mutagenesis study, illustrating the power of 2D-IR as a structural tool.

The 2D-IR method is introduced here as a viable approach to protein structure determina-

tion. A selection of tertiary constraints are used, which could be enlarged and also incorporate secondary interactions (23). These constraints can be obtained by 2D-IR equally well for populations that are transient, undergoing either equilibrium or nonequilibrium (29) kinetics.

## References and Notes

- P. Hamm, M. Lim, R. M. Hochstrasser, *J. Phys. Chem. B* **102**, 6123 (1998).
- S. Sul, D. Karaickaj, Y. Jiang, N.-H. Ge, *J. Phys. Chem. B* **110**, 19891 (2006).
- I. V. Rubtsov, R. M. Hochstrasser, *J. Phys. Chem. B* **106**, 9165 (2002).
- P. Hamm, M. Lim, W. F. DeGrado, R. M. Hochstrasser, *Proc. Natl. Acad. Sci. U.S.A.* **96**, 2036 (1999).
- S. Woutersen, P. Hamm, *J. Phys. Chem. B* **104**, 11316 (2000).
- Y. S. Kim, J. Wang, R. M. Hochstrasser, *J. Phys. Chem. B* **109**, 7511 (2005).
- R. R. Ernst, G. Bodenhausen, A. Wokaun, *Principles of Nuclear Magnetic Resonance in One and Two Dimensions* (Oxford Univ. Press, Oxford, 1987).
- R. Li et al., *J. Biol. Chem.* **279**, 26666 (2004).
- Y. S. Kim, L. Liu, P. H. Axelsen, R. M. Hochstrasser, *Proc. Natl. Acad. Sci. U.S.A.* **106**, 17751 (2009).
- A. Ghosh, J. Qiu, W. F. DeGrado, R. M. Hochstrasser, *Proc. Natl. Acad. Sci. U.S.A.* **108**, 6115 (2011).
- W. Zhuang, T. Hayashi, S. Mukamel, *Angew. Chem. Int. Ed. Engl.* **48**, 3750 (2009).
- S. Krimm, J. Bandekar, *Adv. Protein Chem.* **38**, 181 (1986).
- C. Fang, A. Senes, L. Cristian, W. F. DeGrado, R. M. Hochstrasser, *Proc. Natl. Acad. Sci. U.S.A.* **103**, 16740 (2006).
- K. R. MacKenzie, J. H. Prestegard, D. M. Engelman, *Science* **276**, 131 (1997).
- J. Marecek et al., *Org. Lett.* **9**, 4935 (2007).
- Single-letter abbreviations for the amino acid residues are as follows: G, Gly; L, Leu; V, Val.
- K. Kwac, M. Cho, *J. Chem. Phys.* **119**, 2256 (2003).
- S. Mukamel, *Principles of Nonlinear Optical Spectroscopy* (Oxford Univ. Press, New York, 1995).
- J. Wang, R. M. Hochstrasser, *Chem. Phys.* **297**, 195 (2004).
- R. Wertheimer, R. Silbey, *Chem. Phys. Lett.* **75**, 243 (1980).
- P. Mukherjee, I. Kass, I. T. Arkin, M. T. Zanni, *Proc. Natl. Acad. Sci. U.S.A.* **103**, 3528 (2006).
- A. M. Woys et al., *J. Am. Chem. Soc.* **132**, 2832 (2010).
- C. Fang, *Chem. Phys. Lett.* **382**, 586 (2003).
- H. Torii, M. Tasumi, *J. Chem. Phys.* **96**, 3379 (1992).
- C. Schwieters, J. Kuszewski, G. Mariusclore, *Prog. Nucl. Magn. Reson. Spectrosc.* **48**, 47 (2006).
- C. D. Schwieters, J. J. Kuszewski, N. Tjandra, G. M. Clore, *J. Magn. Reson.* **160**, 65 (2003).
- B. W. Berger et al., *Proc. Natl. Acad. Sci. U.S.A.* **107**, 703 (2010).
- R. F. S. Walters, W. F. DeGrado, *Proc. Natl. Acad. Sci. U.S.A.* **103**, 13658 (2006).
- C. Kolano, J. Helbing, M. Kozinski, W. Sander, P. Hamm, *Nature* **444**, 469 (2006).

**Acknowledgments:** The research was supported by grants NIH-GM12592, NIH-RR01348, and NSF-CHE (to R.M.H.) and NIH-GM54616, NIH-GM60610, NSF-MRSEC, and NIH-GM56423 (to W.F.D.). We thank C. Schwieters and M. Clore for providing us with the Xplor-NIH source code.

## Supporting Online Material

www.sciencemag.org/cgi/content/full/332/6034/1206/DC1

Materials and Methods

SOM Text

Figs. S1 to S10

Tables S1 and S2

References (30–32)

18 January 2011; accepted 20 April 2011

10.1126/science.1202997



# Interaction Between Notch and Hif- $\alpha$ in Development and Survival of *Drosophila* Blood Cells

Tina Mukherjee,<sup>1</sup> William Sang Kim,<sup>1</sup> Lolitika Mandal,<sup>1\*</sup> Utpal Banerjee<sup>1,2†</sup>

A blood cell type termed crystal cell in *Drosophila* functions in clotting and wound healing and requires Notch for specification and maintenance. We report that crystal cells express elevated levels of Sima protein orthologous to mammalian hypoxia-inducible factor- $\alpha$  (Hif- $\alpha$ ) even under conditions of normal oxygen availability. In these platelet-like crystal cells, Sima activates full-length Notch receptor signaling via a noncanonical, ligand-independent mechanism that promotes hemocyte survival during both normal hematopoietic development and hypoxic stress. This interaction initiates in early endosomes, is independent of Hif- $\beta$  (Tango in *Drosophila*), and does not activate hypoxia response targets. Studies in vertebrate myeloid cells have shown a similar up-regulation of Hif- $\alpha$  protein in well-oxygenated environments. This study provides a mechanistic paradigm for Hif- $\alpha$ /Notch interaction that may be conserved in mammals.

The *Drosophila* lymph gland (hematopoietic organ) gives rise to myeloid blood cells: plasmotocytes, crystal cells, and lamellocytes (1). A majority of these cells are macrophages; a small fraction become crystal cells that function during wound healing (2, 3). Hemolymph (Hml) is the earliest marker expressed as cells initiate differentiation. The Runt-domain protein Lozenge (Lz) (4, 5) is essential for commitment

to crystal-cell fate (6), and its expression initiates in these Hml<sup>+</sup> precursors, which then discontinue Hml expression (6). Mature crystal cells express prophenol oxidase (ProPO), essential for melanization (5), whereas macrophages remain Hml<sup>+</sup>.

Sima is the *Drosophila* ortholog of hypoxia-inducible factor- $\alpha$  [Hif- $\alpha$  (7)], the key mediator of responses to hypoxia (8). Sima is stably expressed in mature crystal cells even under normal

oxygen tension (Fig. 1A). Overexpression of *sima* in the lymph gland causes dramatic expansion of crystal cells (Fig. 1B and fig. S1A), whereas single-copy loss of *sima* reduces their number (Fig. 1C and fig. S1A). These phenotypes are similar to phenotypes resulting from *Notch* gain and loss of function (5) (Fig. 1, D and E, and fig. S1A). Furthermore, altering Sima can change Notch reporter [12xSu(H)lacZ] expression (Fig. 1, F to H, and fig. S1B), and a single mutant allele of *sima* suppresses the excess crystal-cell phenotype caused by *Notch*<sup>activated</sup> (*N<sup>act</sup>*) (Fig. 1I and fig. S1A). Thus, Sima and Notch signaling appear to function in the same pathway in this tissue.

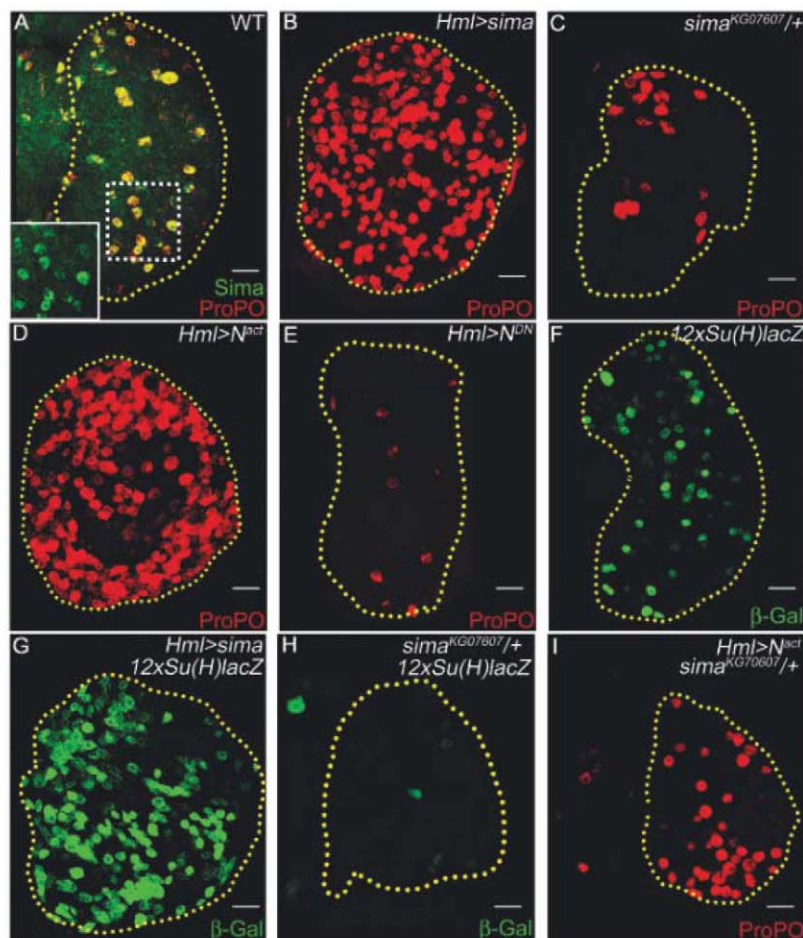
We examined the temporal requirement of Sima during crystal-cell development. Hph (hydroxy prolyl hydroxylase), which marks Sima for degradation (9), or *sima* RNA interference (*sima*<sup>RNAi</sup>) was expressed in Hml<sup>+</sup> precursors by

<sup>1</sup>Department of Molecular, Cell and Developmental Biology, University of California, Los Angeles, CA 90095, USA. <sup>2</sup>Molecular Biology Institute, Department of Biological Chemistry, and Eli and Edythe Broad Center of Regenerative Medicine and Stem Cell Research, University of California, Los Angeles, CA 90095, USA.

\*Present address: Indian Institute of Science Education and Research, Mohali, MGSIPAP Complex, Sector 26, Chandigarh 160019, India.

†To whom correspondence should be addressed. E-mail: banerjee@mbi.ucla.edu

**Fig. 1.** Sima functions with Notch during crystal-cell development. Crystal cells marked with ProPO (red). Scale bars indicate 20  $\mu$ m. (A) Wild-type lymph gland, crystal cells show elevated levels of Sima (green; yellow because of ProPO co-localization). (Inset) Magnified view of crystal cells expressing Sima (green). (B) Overexpression or (C) single-copy loss of *sima* causes crystal-cell expansion or reduction, respectively. (D) Overexpression of activated Notch (*N<sup>act</sup>*) that functions as a gain of function Notch or (E) dominant-negative Notch (*N<sup>DN</sup>*) that functions as a loss of function Notch causes crystal-cell expansion and reduction, respectively. (F) Wild-type *Notch* reporter activity [12xSu(H)lacZ, green] (G) increases with *sima* gain of function and (H) decreases with single-copy loss of *sima*.  $\beta$ -Gal,  $\beta$ -galactosidase. (I) Single-copy loss of *sima* suppresses *N<sup>act</sup>*-driven crystal-cell expansion. Compare with (D).



using *Hml-gal4* as the driver that is switched off once a cell becomes  $Lz^+$  (10). Neither has any effect on crystal-cell number (Fig. 2, A, C, and E, and fig. S1C). However, expression of *Hph* or *sima*<sup>RNAi</sup> later in  $Lz^+$  crystal-cell precursors causes a significant reduction in crystal-cell number (Fig. 2, B and D to F, and fig. S1C,  $P < 0.0001$ ). This loss is associated with bursting (compare Fig. 2, D' with B') of these cells, visualized by membrane green fluorescent protein (GFP) expression, a phenomenon (3) important for crystal cell-mediated blood clotting because of release of enzymes (3).

Crystal cell-fate specification requires canonical Notch signaling (6, 11). Expressing *Notch*<sup>RNAi</sup> in early differentiating *Hml*<sup>+</sup> cells causes loss of crystal cells (Fig. 2, G and I). Additionally, late loss of Notch from already-specified crystal-cell precursors by either expressing *N*<sup>RNAi</sup> or *Ofut*<sup>RNAi</sup> [modification of Notch by *Ofut* is required for proper Notch function (12)] causes a bursting phenotype (Fig. 2, H to J) as seen with loss of *Sima* (Fig. 2D'). Thus, Notch function is required continuously: first in specifying the  $Lz^+$  precursor and then in expansion and maintenance of crystal cells.

High endogenous Notch expression in crystal cells (Fig. 2K) is further increased upon *Sima*

overexpression (Fig. 2L), without change in *Notch* RNA (fig. S2, A to C). The majority of Notch protein in crystal cells is seen in intracellular vesicles (Fig. 2, M and N). In live trafficking assays (13), surface-labeled Notch internalized from the plasma membrane is rapidly degraded in all cells (Fig. 2, O and P) except in mature crystal cells, where Notch persists in Hepatocyte growth factor regulated tyrosine kinase substrate (Hrs)-positive early endocytic vesicles (Fig. 2, P and Q) and co-localizes with *Sima* (fig. S2, D to D''').

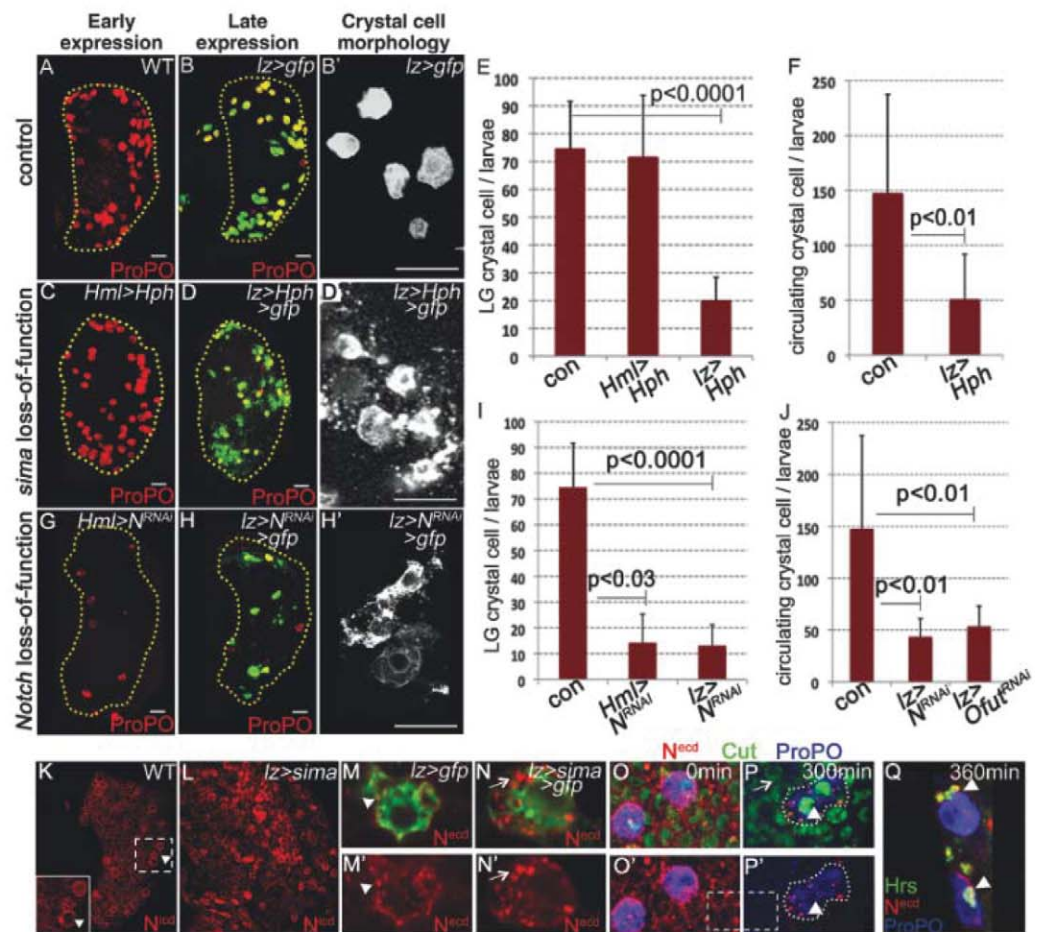
Canonical Notch signaling requires the interaction of Notch with its membrane-bound ligand on an adjacent signaling cell (14, 15). Crystal cell-fate specification requires ligand-Serrate (*Ser*) (6, 11), but at late stages *Ser* is expressed in a restricted number of cells (6), not adjacent to a *Ser*-positive cell. This issue is even more acute for individualized circulating crystal cells, not in direct contact with a neighbor, that continue to require Notch function for their maintenance (Fig. 2J). The circulating crystal cells are of embryonic origin (16) and are not derived from the larval lymph gland (17). The other Notch ligand, Delta, lacks any obvious role in crystal-cell development (6, 11) (fig. S2E). Removal of *Ser* early prevents crystal cell-fate specification (Fig. 3,

A and B), but unlike Notch and *Sima*, removing *Ser* after crystal cell-fate specification does not affect crystal-cell number or morphology (Fig. 3, A and C), suggesting that *Sima*-mediated Notch activation occurs independent of its ligand.

We addressed the question of ligand independence by using additional genetic criteria. Overexpression of *Fng*, a glycosyl transferase that inhibits *Ser*-Notch signaling (18) by using *Hml-gal4*, dramatically reduces crystal-cell number (Fig. 3, D and F), whereas late expression using *lz-gal4* has no effect (Fig. 3, D, E, and G). *Mib1* (19) and *neuralized* (20), which encode E3 ubiquitin ligases necessary for ligand endocytosis and promotion of ligand-dependent Notch signaling, have no role in crystal-cell development (fig. S2, F to I). We conclude that in  $Lz^+$  cells, Notch activation is *Ser*-independent but *Sima*-dependent for its intracellular stabilization.

Full-length Notch ( $N^{\text{fl}}$ ) can accumulate in endocytic vesicles in a ligand-independent manner (13, 21). This is also seen in hemocytes expressing *Sima* (fig. S3A), and  $N^{\text{fl}}$  is sufficient to increase crystal-cell number (Fig. 3I). This increase is not suppressed by *mib1* (Fig. 3J), but *Rab5* co-expression, expected to enhance turnover of

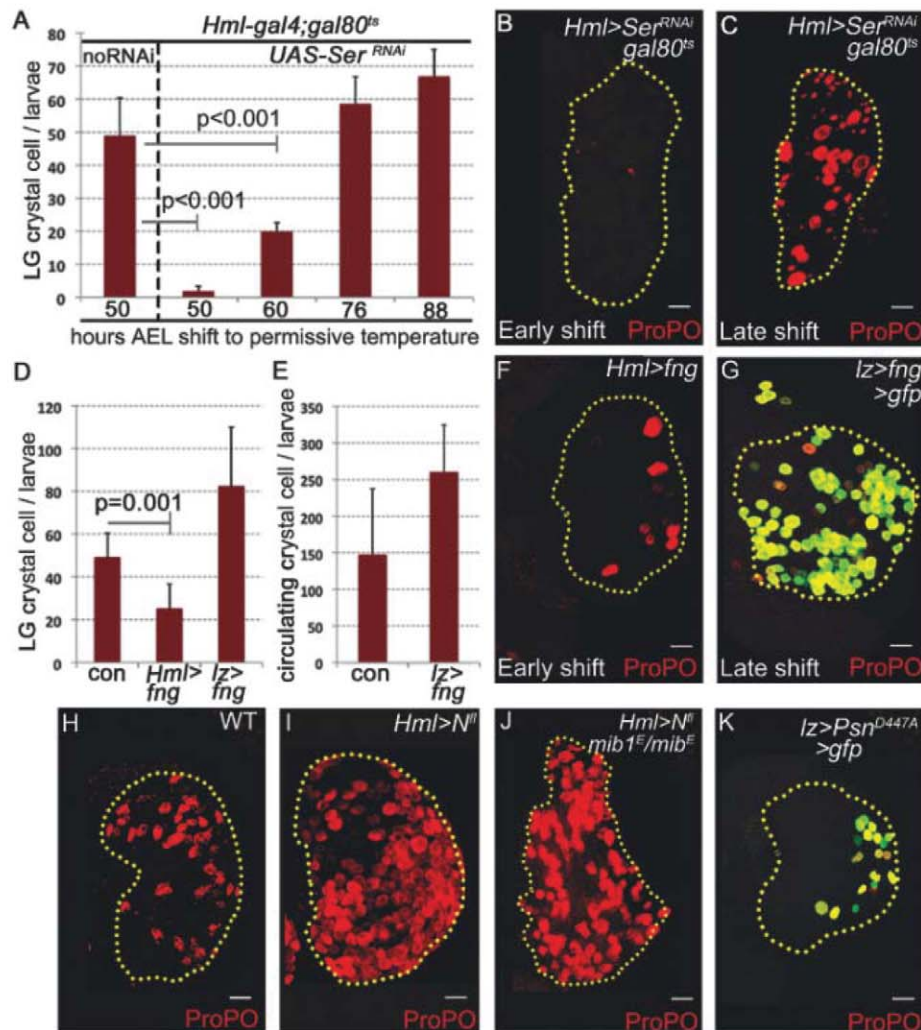
**Fig. 2.** *Sima* stabilizes Notch in mature crystal cells, which is necessary for their maintenance and survival. Crystal cells marked with ProPO (red). Scale bars, 20  $\mu\text{m}$ . (A) Wild-type (WT) lymph gland. (B) Control lymph glands expressing membrane GFP in crystal cells. Magnified in (B'). Overexpression of *Hph* (C) early does not affect crystal cells [compare with (A)]; (D) late expression in crystal cells causes their reduction and (D') rupturing [compared with (B')]. Quantification of (E) lymph gland ( $n = 8$ ) and (F) circulating crystal-cell ( $n = 8$ ) data. Error bars indicate standard deviation. Expressing *N*<sup>RNAi</sup> (G) early and (H) late causes reduction in crystal cells [compared with (A) and (B)]. Loss of Notch late from crystal cells causes their rupturing [(H') similar to (D')] compared with (B'). Quantification of (I) lymph gland ( $n = 12$ ) data and (J) circulating crystal-cell data expressing *N*<sup>RNAi</sup> ( $n = 8$ ) and *Ofut*<sup>RNAi</sup> ( $n = 8$ ). (K) Wild-type lymph glands with elevated Notch protein [Notch intracellular domain ( $N^{\text{icd}}$ ), red] in crystal cells (arrowheads, magnified in inset). (L) *sima* overexpression causes further Notch ( $N^{\text{icd}}$ , red) accumulation. Antibody against the extracellular domain of Notch ( $N^{\text{ecd}}$ , red) antibody detects (M and M') Notch in vesicles (arrowheads) in crystal cells from control lymph glands expressing GFP and (N and N') overexpressing *sima* further increases Notch ( $N^{\text{ecd}}$ , red) accumulation in vesicles (arrows, compare with M and M'). (O to Q) Live endocytic trafficking assay: Notch antibody-recognizing epitope on  $N^{\text{ecd}}$  (red) in wild-type lymph glands marked with nuclear (Cut, green) and crystal-cell (ProPO, blue) markers. (O and O') Notch protein is detected on all



membranes at 0 min. (P) and (P') At 300 min, endocytosed Notch is degraded from surrounding cells [compare  $N^{\text{ecd}}$  levels in the dashed areas in (O') and (P')] except in crystal cells (arrowheads) (Q) that retain Notch (red) in Hrs-positive (green, arrowheads) early endosomes.  $N^{\text{ecd}}$  (red) and Hrs (green) co-localize (yellow).



**Fig. 3.** Sima promotes ligand-independent stabilization of full-length Notch protein for crystal-cell maintenance. (A to C) *Ser<sup>RNAi</sup>* in signaling cells affects crystal cell [(A) and (B)] early [ $n = 5, 50$ , and 60 hours after egg laying (AEL)] but not [(A) and (C)] late ( $n = 5, 76$  and 88 hours AEL). Crystal cells marked with ProPO (red). Scale bars, 20  $\mu\text{m}$ . (D to F) *fng* overexpression [(D and (F)] early in signaling cells ( $n = 7$ ) causes crystal-cell reduction but not [(D), (E), and (G)] late ( $n = 4$ ). (H) Wild-type lymph gland. (I) Overexpressing *N<sup>fl</sup>* increases crystal cells [compare with (H)]. (J) Expressing *N<sup>fl</sup>* in *mib1* background shows no reduction in crystal cells [compare with (I) and (H)]. (K) Expressing dominant-negative presenilin (*Psn<sup>D447A</sup>*) in crystal cells causes reduction.



endocytic *N<sup>fl</sup>* (22), causes strong suppression of Sima excess crystal-cell phenotype (fig. S3, B to D), confirming the involvement of endocytic vesicles in *N<sup>fl</sup>/Sima* interaction. Although ligand-independent, the signaling entity is still cleaved Notch because expressing a dominant-negative form of presenilin (*Psn<sup>D447A</sup>*, Fig. 3K) necessary for S3 cleavage of Notch (23) or feeding larvae with a  $\gamma$ -secretase inhibitor, DAPT {N-[N-(3,5-difluorophenacetyl)-l-alanyl]-S-phenylglycine t-butyl ester} (fig. S3E), causes bursting of crystal cells. Also, expressing a dominant-negative form of Su(H) in *Lz<sup>+</sup>* cells causes bursting of crystal cells (fig. S2J).

In the context of hypoxia, Hif- $\alpha$  (Sima) functions as a heterodimer with Hif- $\beta$  [Tango in *Drosophila* (24)]. However, *tgo* mutants or *tgo<sup>RNAi</sup>* do not cause reduction but increase in crystal cells (Fig. 4, A to C). Crystal cells do not express the Sima/Tgo heterodimer-dependent hypoxia reporter (24) in wild-type (fig. S3F) and in Sima overexpression (fig. S3G) backgrounds. We hypothesize that in this context Tgo functions as a cytosolic sink to sequester Sima and prevents it from interacting with Notch.

Although normoxic Sima/Notch function does not require Tgo, the system responds to hypoxia

by coopting the same developmental strategy. Conditions that stabilize Sima from degradation, such as blocking Hph (Fig. 4D) or exposing larvae to hypoxic stress (Fig. 4E), are sufficient to mediate an expansion of crystal cells. Under these conditions, the hypoxia-stabilized Sima further enhances Notch signaling independent of Tgo, causing an expansion of crystal cells.

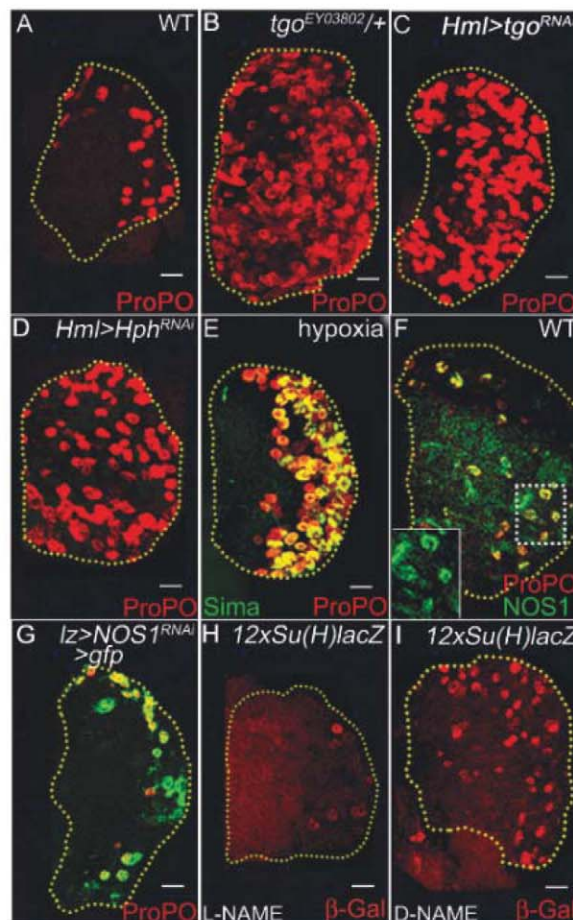
Stimuli reported to stabilize Hif- $\alpha$  under normoxia include nitric oxide (NO) (25), reactive oxygen species (ROS) (26), and cations (27) that inhibit Hph (27) or stabilize Sima (28). Mature crystal cells express high levels of nitric oxide synthase1 (NOS1) (Fig. 4F), and expressing *NOS1<sup>RNAi</sup>* causes bursting of crystal cells (Fig. 4G). Additionally, feeding larvae NO inhibitor [L-NAME (NG-nitro-L-arginine methyl ester)] diminishes Notch reporter expression (Fig. 4, H compared to I). Lastly, clones expressing *NOS1<sup>RNAi</sup>* have low Sima protein and do not form crystal cells (fig. S3, H and H'). Thus, maturing crystal cells express NOS1, which raises NO level, stabilizing Sima, which then functions with Notch to promote crystal cell maintenance and survival (fig. S4).

Earlier biochemical studies have established direct binding of Notch to Hif- $\alpha$  (29). Here, we

describe a hypoxia and Notch ligand-independent developmental role for such an interaction. Normally a cell requiring continuous Notch signal needs to be in constant contact with a ligand-bearing cell, and a circulating cell will be unable to maintain active Notch signal. Crystal cells circumvent this need through noncanonical Notch activation via stabilization of *N<sup>fl</sup>* receptor in the endocytic pathway mediated by Hif- $\alpha$ , even in the absence of ligand binding. Once stabilized, cleavage by presenilin creates an active signaling moiety, likely to be a *N<sup>act</sup>/Hif- $\alpha$ /Su(H)* complex essential for crystal-cell maintenance. The Sima/Notch-dependent phase is a two-step process: the first is an expansion of *Hml<sup>+</sup> Lz<sup>+</sup>* crystal-cell precursors, followed by maintenance of *Lz<sup>+</sup> ProPO<sup>+</sup>* mature crystal cells (see fig. S4 for a summary of all the data presented here). Circulating crystal cells in the larvae originate from the embryonic mesoderm (16) and not the lymph gland (17), and they show a similar Sima-mediated Notch requirement for their maintenance. Circulating T cells also require Notch function to respond to pathogens (30) and express elevated levels of Hif- $\alpha$  (31). The source of ligand is the antigen-presenting cell, but additional alternate mechanisms are worth investigating.



**Fig. 4.** Sima function in mature crystal cells is independent of Tgo. ProPO (red) marks crystal cells (red). Scale bars, 20  $\mu$ m. (A) Wild-type lymph gland. (B) Single-copy loss of *tgo*<sup>EY03802</sup> or (C) expressing *tgo*<sup>RNAi</sup> causes an increase in crystal cells. (D) Expressing *Hph*<sup>RNAi</sup> or (E) exposing second instar wild-type larvae to 5% hypoxic stress increases Sima (green) stabilization and crystal-cell expansion. (F) Crystal cells from third instar WT lymph glands show elevated NOS1 (green, yellow because of overlap with ProPO; see inset). (G) *NOS1*<sup>RNAi</sup> in crystal cells causes bursting [compare with (A)]. (H and I) Feeding larvae with (H) L-NAME (NO inhibitor) shows reduction in *Notch* reporter activity (red), whereas (I) D-NAME (inactive isomer) has no effect.



Sima stabilization is important both for normal development and during response to hypoxia. A similar dual use of a signaling scenario is seen with ROS (32). At low levels, ROS functions as a signaling molecule in the stemlike progenitors, and scavenging ROS retards their differentiation. Under oxidative stress, the sensitized progenitors differentiate rapidly (32). Thus, the *Drosophila* myeloid system makes dual use of the same ROS/c-Jun N-terminal kinase and Sima/Notch signaling pathways for development and stress responses. Interestingly, vertebrate myeloid cells also maintain high Hif- $\alpha$  in normoxic environments to maintain their cellular energy pools and ability to mount an inflammatory response (33). Because *Drosophila* hemocytes are functionally most similar to mammalian myeloid cells, the concepts presented here are worthy of further investigation in mammalian systems.

#### References and Notes

1. S. H. Jung, C. J. Evans, C. Uemura, U. Banerjee, *Development* **132**, 2521 (2005).
2. R. R. Rizki, T. M. Grell, *Roux's Arch. Dev. Biol.* **188**, 91 (1980).
3. G. Bidla, M. S. Dushay, U. Theopold, *J. Cell Sci.* **120**, 1209 (2007).
4. R. R. Rizki, *Genetics* **97**, s90 (1981).
5. T. Lebestky, T. Chang, V. Hartenstein, U. Banerjee, *Science* **288**, 146 (2000).
6. T. Lebestky, S. H. Jung, U. Banerjee, *Genes Dev.* **17**, 348 (2003).

10. Materials and methods are available as supporting material on Science Online.
11. B. Duvic, J. A. Hoffmann, M. Meister, J. Royet, *Curr. Biol.* **12**, 1923 (2002).
12. T. Okajima, A. Xu, K. D. Irvine, *J. Biol. Chem.* **278**, 42340 (2003).
13. T. Vaccari, D. Bilder, *Dev. Cell* **9**, 687 (2005).
14. S. Artavanis-Tsakonas, M. D. Rand, R. J. Lake, *Science* **284**, 770 (1999).
15. E. M. Hansson, U. Lendahl, G. Chapman, *Semin. Cancer Biol.* **14**, 320 (2004).
16. C. J. Evans, V. Hartenstein, U. Banerjee, *Dev. Cell* **5**, 673 (2003).
17. R. Märkus et al., *Proc. Natl. Acad. Sci. U.S.A.* **106**, 4805 (2009).
18. V. M. Panin, V. Papayannopoulos, R. Wilson, K. D. Irvine, *Nature* **387**, 908 (1997).
19. W. Wang, G. Struhl, *Development* **132**, 2883 (2005).
20. C. Pitsouli, C. Delidakis, *Development* **132**, 4041 (2005).
21. K. H. Moberg, S. Schelble, S. K. Burdick, I. K. Hariharan, *Dev. Cell* **9**, 699 (2005).
22. R. Jaekel, T. Klein, *Dev. Cell* **11**, 655 (2006).
23. G. Struhl, I. Greenwald, *Proc. Natl. Acad. Sci. U.S.A.* **98**, 229 (2001).
24. S. Lavista-Llanos et al., *Mol. Cell. Biol.* **22**, 6842 (2002).
25. K. B. Sandau, J. Fandrey, B. Brüne, *Blood* **97**, 1009 (2001).
26. D. Gerald et al., *Cell* **118**, 781 (2004).
27. C. J. Schofield, P. J. Ratcliffe, *Biochem. Biophys. Res. Commun.* **338**, 617 (2005).
28. F. Li et al., *Mol. Cell* **26**, 63 (2007).
29. M. V. Gustafsson et al., *Dev. Cell* **9**, 617 (2005).
30. H. R. MacDonald, A. Wilson, F. Radtke, *Trends Immunol.* **22**, 155 (2001).
31. H. Nakamura et al., *J. Immunol.* **174**, 7592 (2005).
32. E. Owusu-Ansah, U. Banerjee, *Nature* **461**, 537 (2009).
33. T. Cramer et al., *Cell* **112**, 645 (2003).

**Acknowledgments:** We thank H. Bellen, C. Frei, S. Artavanis-Tsakonas, C. Delidakis, M. Guo, M. Reguluski, B. Shilo, G. Struhl, P. Wappner, National Institute of Genetics, Vienna Drosophila RNAi Center, Flybase, and Bloomington for reagents and D. Walker, G. Weinmaster, and C. Evans for helpful discussion. Supported by NIH grant R01HL067395.

#### Supporting Online Material

www.sciencemag.org/cgi/content/full/332/6034/1210/DC1

Materials and Methods

Figs. S1 to S4

References

27 October 2010; accepted 26 April 2011

10.1126/science.1199643

## Increased Structure and Active Learning Reduce the Achievement Gap in Introductory Biology

David C. Haak,<sup>1\*</sup> Janneke HilleRisLambers,<sup>1</sup> Emile Pitre,<sup>2</sup> Scott Freeman<sup>1†</sup>

Science, technology, engineering, and mathematics instructors have been charged with improving the performance and retention of students from diverse backgrounds. To date, programs that close the achievement gap between students from disadvantaged versus nondisadvantaged educational backgrounds have required extensive extramural funding. We show that a highly structured course design, based on daily and weekly practice with problem-solving, data analysis, and other higher-order cognitive skills, improved the performance of all students in a college-level introductory biology class and reduced the achievement gap between disadvantaged and nondisadvantaged students—without increased expenditures. These results support the Carnegie Hall hypothesis: Intensive practice, via active-learning exercises, has a disproportionate benefit for capable but poorly prepared students.

Since the 1970s, policy-makers have been calling for an increase in the number of underrepresented minority (URM) students

who complete science-related degrees at the undergraduate, graduate, and professional levels (1–3). In response, educators and administrators

have created programs focused on recruiting and retaining minorities in the STEM (science, technology, engineering, and mathematics) disciplines. In some cases these programs also target students from socioeconomically disadvantaged backgrounds, irrespective of ethnicity. At the college level, most of these efforts fall into two broad categories: (i) comprehensive programs that recruit promising students and provide financial aid, supplementary instruction, mentoring, social support, and research opportunities (2, 4–6) or (ii) less-intensive programs that offer supplementary instruction or peer-led workshops associated with introductory courses that have high failure rates (7–9). Many of the latter programs have increased the success of the target populations in the STEM disciplines; some of the former have succeeded in reducing or eliminating the achievement gap that exists between URM and non-URM students—a gap that starts in K-12 and continues through undergraduate education (10, 11). Unfortunately, both approaches are expensive and have therefore rarely been permanently incorporated into the traditional funding structure of host institutions (2). When external funding has run out, participation and success rates have dropped dramatically (7).

Changing introductory STEM courses for undergraduates from traditional lecturing to active learning designs has been advocated as an alternative solution to the achievement gap problem (3, 12). This call has trickled up from research on K-12 programs, where the implementation of active learning (13) and culturally responsive teaching (14) has had a profound impact on the achievement gap. Some reformed introductory courses at the college level have also reported success in boosting achievement by disadvantaged students, although these course designs required increased investment by external funders and host institutions (15, 16).

We asked the following: Can an existing STEM course be modified to improve performance by students from disadvantaged educational and socioeconomic backgrounds who are at high risk of failing, without requiring increased resources in the way of staffing or external funding? In essence, our work addresses what Benjamin Bloom called the “2 Sigma Problem”: the need to create teaching-learning conditions under large-group instruction that allow students to achieve at the level they would under individual instruction by a skilled tutor (10, 17). The question has taken on added urgency as faculty-to-student ratios worsen in response to the global economic crisis.

We worked with a large-enrollment introductory biology course for undergraduate majors

called Biology 180 and studied changes in the performance of students in the University of Washington’s Educational Opportunity Program (EOP) (18). Individuals in the EOP are from educationally or economically disadvantaged backgrounds; most are first in their family to attend college. Although EOP students are not identified on the basis of ethnicity, most URM students at the University of Washington (UW) (76.5%, in the present study) are also in the EOP category. Analyzing individuals in the EOP captures most URM students while broadening the analysis to include all students from disadvantaged backgrounds.

Previous work showed that we can predict student performance in this course a priori, on the basis of college grade point average at the time of entering the course and SAT verbal score (18–20). Failure in this course is defined as a final grade under 1.5, the threshold required to continue in the UW introductory biology series; students who are at high risk of failing include a disproportionate number of students in the EOP (Fig. 1A). Actual failure rates are consistent with the predicted-grade analysis: From 2003 to 2008, the mean failure rate for EOP students was 21.9%, whereas the failure rate for non-EOP students was 10.1%.

As a comparison, we also analyzed 111,227 records on students taking introductory STEM courses at the University of Washington from 2003 to 2008. We calculated means and 95% confidence intervals for the achievement gaps between EOP and non-EOP students, calculated as the difference in final grade on a 4.0 point scale, for the first course in these multicourse sequences designed for prospective majors in the STEM disciplines. The achievement gaps in Biology 180 are among the highest on our campus (Fig. 1B). We hypothesized that the large gaps occur because Biology 180 final grades depend largely on short-answer midterm and final exams that test higher-order cognitive skills (19) and be-

cause EOP students are underprepared for this type of assessment relative to non-EOP students.

Previous work on four quarters of Biology 180, taught by the same instructor, showed that incorporating a moderate level of required (graded) active-learning exercises increased performance by all students compared with performance in lecture-intensive courses where active-learning exercises were absent or optional (19). The active-learning exercises were daily, multiple-choice “clicker questions” implemented in a peer instruction format (21) and a weekly practice exam comprising five short-answer questions that were peer-graded (18, 19). Recent analyses combined these data with data from two additional quarters taught by the same instructor in a third course design: a lecture-free format that added preclass reading quizzes (18, 20–22) and extensive informal group work in class (18, 20, 23, 24). This course design was considered highly structured because it required students to (i) prepare for class sessions, (ii) use clickers or random-call responses to participate in class sessions that were focused entirely on active-learning exercises, and (iii) complete a weekly low-risk assessment in the form of a practice exam. The highly structured approach resulted in another increase in overall performance by all students, compared with the low-structure, lecture-intensive course with no required active learning and the moderate-structure design based on clickers and a weekly practice exam (20).

To reduce the achievement gap, however, interventions must have a disproportionate benefit for disadvantaged students. To test whether EOP students disproportionately benefit from high-structure versus low-structure courses, we analyzed grades achieved by students in 29 quarters of Biology 180 by using their predicted grades to control for among-quarter variation in student ability and preparation (18). Comparing student performance in the two highly structured quar-

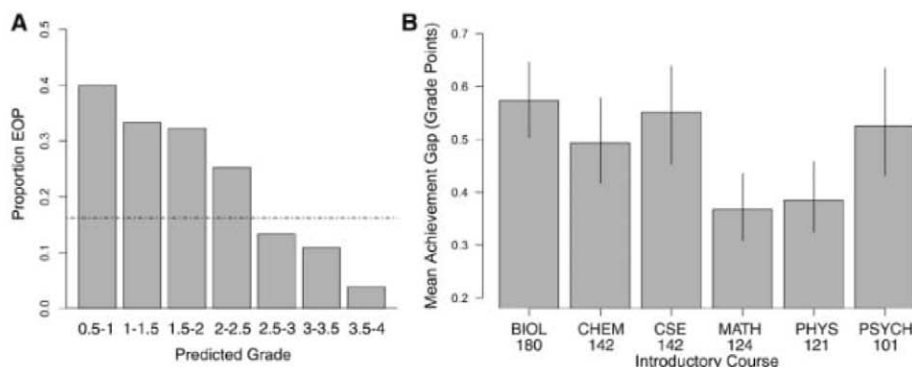


**Fig. 1.** Students from disadvantaged backgrounds are at high risk for failure in introductory STEM courses. **(A)** Frequency distribution of students in Biology 180, binned by predicted grade. The horizontal line indicates the overall proportion of EOP students in this course (16). EOP students are overrepresented at the low end of the distribution of predicted grades relative to non-EOP students (generalized linear model with binomial error distribution,  $P < 0.001$ ). **(B)** Achievement gaps between EOP and non-EOP students in introductory STEM courses at the University of Washington. Means were calculated for gaps in each quarter, academic years 2003 to 2008; error bars represent bootstrapped 95% confidence intervals.

<sup>1</sup>Department of Biology, Box 351800, University of Washington, Seattle, WA 98195, USA. <sup>2</sup>Office of Minority Affairs and Diversity, Box 352835, University of Washington, Seattle, WA 98195, USA.

\*Present address: Department of Biology, Indiana University, Bloomington, IN 47405–3700, USA.

†To whom correspondence should be addressed. E-mail: srf991@uw.edu

ters versus 27 quarters with little or no active learning, we find that, although all students benefit from structure, EOP students experience a disproportionate benefit. The generalized linear mixed model with the most power to explain the actual grades received by students included active learning, predicted grade, EOP status, and their interaction as explanatory variables, with quarter as a random effect to control for instructor differences (likelihood ratio test,  $P = 0.0023$ , Table 1). Our highly structured course significantly improved student performance in this broad-based comparison—but did so disproportionately for EOP students (Fig. 2).

To verify that these results are robust to instructor differences, we reexamined the achievement gap between EOP and non-EOP students but restricted the analysis to the six quarters taught by the same instructor: two in the lecture-intensive, low-structure format; two in the moderately structured format that included in-class clicker questions and weekly practice exams; and two in the highly structured format that added daily reading quizzes and in-class group exercises and nearly eliminated lecturing (18, 20). The highly structured format reduced the raw achievement gap for EOP versus non-EOP students from 0.80 to 0.44 grade points—a 45% drop from both the moderate-structure and the low-structure formats. This decline in achievement gap exceeded the 95% confidence intervals from the low- and moderate-structure quarters (Fig. 3). We found a similar decrease in achievement gap over these six quarters when accounting for incoming achievement (fig. S2). Overall, course structure has a significant impact on the achievement gap, controlling for instructor identity and student ability (table S2).

The change from low to moderate to high structure did not require additional financial resources, smaller class sizes, or more class time. In fact, the second iteration of the highly structured course (in autumn 2009) took place when class size had increased from a maximum of 345 in the earlier five quarters analyzed to 700, labs had been cut from 3 hours per week to 2, and the number of graduate teaching assistants had been reduced from one for every 49 students to one for every 87.5 students.

Our results raise two related questions: Did EOP students actually learn more or simply perform better on assessments? And were their performance gains due to benefits derived from active learning or frequent testing (25)? Ranking exam questions on Bloom's taxonomy of educational objectives (26, 27) provides a standardized framework for assessing the level of learning (28). A recent analysis of the exams given in the six quarters taught by the same instructor shows that (i) an average exam question, weighted by points available, is at the application level of Bloom's taxonomy and (ii) the Bloom's level and difficulty of exams actually increased during the transition from low- to medium- to highly structured course designs (20). The application level subsumes mastery of vocabulary and strong conceptual understanding and demands that students apply concepts in new situations. The high level of exam questions in this course suggests that the performance gains we document here reflect actual learning gains. Further, active-learning exercises have been shown to increase performance on exam questions that demand higher-order cognitive skills, while having no effect on exam questions focused on lower-order cognitive skills [levels 3 to 6 versus 1 and 2 on Bloom's taxonomy; e.g., (29)]. These results suggest that active learning does not help with information transfer, only with problem-solving and other types of higher-order learning. Thus, student gains in performance in our highly structured design should reflect a deeper understanding of the content and not result simply from increased frequency of assessment.

An intriguing next step is to explore the mechanisms responsible for the disproportionate change in EOP student performance in a large-enrollment, highly structured course design. The success of other interventions at the K-12 (13) and college (7) levels suggests that many students from educationally disadvantaged backgrounds are capable of succeeding in the STEM disciplines but simply lack exposure to the challenge of integrating concepts to solve new problems. We propose that almost all students arrive on college campuses with 12 years of practice at Bloom's levels 1 and 2, but that most students from deprived educational backgrounds have had mini-

mal exposure to higher-order thinking [Bloom's levels 3 and above (30)]. Highly structured course designs provide practice with problem-solving and reasoning skills that may be new to high-risk students in introductory college STEM courses. Specifically, active learning that promotes peer interaction makes students articulate their logic and consider other points of view when solving problems, leading to learning gains [e.g., (31)].

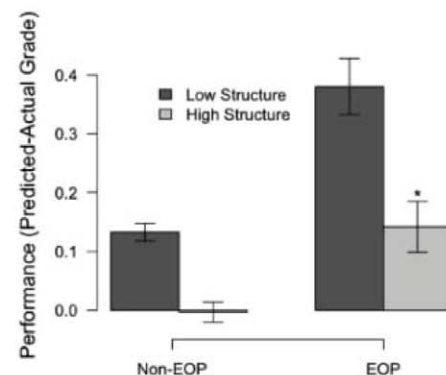


**Fig. 2.** Highly structured course designs benefit all students, but especially disadvantaged students. The difference between predicted performance and actual performance is significantly decreased for all students, and EOP students in particular, in two highly structured courses relative to 27 low-structure versions of the same course with little to no active learning. The best-fit generalized linear mixed-effects models of performance include EOP as a fixed effect, likelihood ratio test,  $df = 13$ ,  $\chi^2 = 10.997$ ,  $P = 0.0027$ ; see Table 1. Error bars indicate  $\pm 1$  SE.

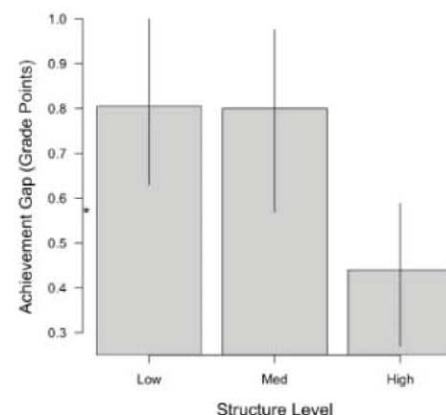


**Fig. 3.** For quarters with a common instructor, the achievement gap is halved with increased structure. Across six quarters of low, medium, and high structure (two quarters each), the achievement gap is the smallest under high structure. Controlling for differences in predicted student ability, we find a drop under the medium-structure course design as well (fig. S2). Means were calculated from 10,000 bootstrap iterations; error bars represent 95% bootstrapped confidence intervals. The asterisk near the vertical axis represents the average achievement gap across all instructors, 2003 to 2008 (Fig. 1B).

**Table 1.** Ability of alternative models, containing different combinations of explanatory variables (such as predicted grades, structure, and EOP status), to explain observed grades students receive in introductory biology. Only a subset of all possible models are shown here for clarity; for a full list see table S2, and see (18) for a description of the models.  $k$  is the number of parameters in the model; AIC, Akaike's information criterion;  $\omega$ , the weighted AICs.  $P = 0.0023$  for a likelihood ratio test between Structure\*Predicted+EOP and Predicted+EOP models.  $P = 2.2 \times 10^{-16}$  for a likelihood ratio test between Predicted+EOP and Structure+Predicted+EOP.  $P = 0.074$  for likelihood ratio test between Structure and Null models.

Model	$k$	log-likelihood	AIC	$\Delta$ AIC	$\omega$
Structure*Predicted+EOP	13	-2532.176	5090.353	0	0.75
Predicted+EOP	9	-2537.675	5093.350	3.00	0.17
Structure+Predicted+EOP	9	-2538.696	5095.392	5.04	0.06
Structure	7	-2573.406	5160.812	70.46	0.00
Null	6	-2575.005	5162.01	71.66	0.00



We call this proposal the Carnegie Hall hypothesis on the basis of the story of a tourist who asks a New Yorker how to get to Carnegie Hall. The answer? "Practice." The hypothesis is a direct extension of constructivist theory (32, 33), a cornerstone of classical explanations for why active learning works (29, 34). Constructivism maintains that individuals incorporate new information into their previous conception and that they only change ideas when they realize that the new information conflicts with their previous understanding, creating cognitive dissonance. Constructivism defines the types of practice that are valuable for underprepared students in introductory courses: not drilling, but exercises that challenge previous conceptions and require students to explain their thinking.

Traditional approaches to reducing the achievement gap have produced disproportionate benefits for disadvantaged students by focusing an influx of resources on them. If the Carnegie Hall hypothesis is correct, highly structured courses may be able to reduce the achievement gap while raising the performance of all students without requiring additional resources because of a disproportionate benefit of increased practice for capable students who have grown up lacking exposure to higher-order cognitive skills.

#### References and Notes

1. S. M. Malcom, *Science* **271**, 1817 (1996).
2. A. Tekian, L. Hruska, *Teach. Learn. Med.* **16**, 28 (2004).
3. F. A. Hrabowski 3rd, *Science* **331**, 125 (2011).
4. P. Gándara, J. Maxwell-Jolly, *Priming the Pump: Strategies for Increasing the Achievement of Underrepresented Minority Undergraduates* (College Board, New York, 1999).
5. J. Matsui, R. Liu, C. M. Kane, *Cell Biol. Educ.* **2**, 117 (2003).
6. M. F. Summers, F. A. Hrabowski 3rd, *Science* **311**, 1870 (2006).
7. R. E. Fullilove, P. U. Treisman, *J. Negro Educ.* **59**, 463 (1990).
8. C. Dirks, M. Cunningham, *CBE Life Sci. Educ.* **5**, 218 (2006).
9. K. A. Rath, A. R. Peterfreund, S. P. Xenos, F. Bayliss, N. Carnal, *CBE Life Sci. Educ.* **6**, 203 (2007).
10. T. R. Guskey, *J. Adv. Acad.* **19**, 8 (2007).
11. C. Alexander, E. Chen, K. Grumbach, *Acad. Med.* **84**, 797 (2009).
12. J. Mervis, *Science* **330**, 306 (2010).
13. R. E. Slavin, N. E. Madden, B. Chambers, B. Haxby, *Two Million Children: Success for All* (Corwin, Thousand Oaks, CA, 2009).
14. W. L. Bainbridge, T. J. Lasley II, *Educ. Urban Soc.* **34**, 422 (2002).
15. R. J. Beichner et al., in *Research-Based Reform of University Physics*, E. F. Redish, P. J. Cooney, Eds. (American Association of Physics Teachers, College Park, MD, 2007).
16. R. W. Preszler, *CBE Life Sci. Educ.* **8**, 182 (2009).
17. B. S. Bloom, *Educ. Res.* **13**, 4 (1984).
18. Materials and methods are available as supporting material on *Science* Online.
19. S. Freeman et al., *CBE Life Sci. Educ.* **6**, 132 (2007).
20. S. Freeman, D. Haak, M. P. Wenderoth, *CBE Life Sci. Educ.* **10**, 175 (2011).
21. C. H. Crouch, E. Mazur, *Am. J. Phys.* **69**, 970 (2001).
22. G. M. Novak, E. T. Patterson, A. D. Gavrin, W. Christian, *Just-in-Time Teaching* (Prentice Hall, Upper Saddle River, NJ, 1999).
23. J. J. Farrell, R. S. Moog, J. N. Spencer, *J. Chem. Educ.* **76**, 570 (1999).
24. T. Eberlein et al., *Biochem. Mol. Biol. Educ.* **36**, 262 (2008).
25. D. P. Larsen, A. C. Butler, H. L. Roediger 3rd, *Med. Educ.* **43**, 1174 (2009).
26. B. S. Bloom, D. R. Krathwohl, B. B. Masia, *Taxonomy of Educational Objectives: The Classification of Educational Goals* (McKay, New York, 1956).
27. D. R. Krathwohl, *Theory Prac.* **41**, 212 (2002).
28. A. Crowe, C. Dirks, M. P. Wenderoth, *CBE Life Sci. Educ.* **7**, 368 (2008).
29. T. R. Lord, *Innovative Higher Educ.* **21**, 197 (1997).
30. J. Oakes, J. Rogers, M. Lipton, *Learning Power: Organizing for Education and Justice* (Teachers College Press, New York, 2006).
31. M. K. Smith et al., *Science* **323**, 122 (2009).
32. J. Piaget, *The Language and Thought of the Child* (Harcourt Brace, New York, 1926).
33. L. S. Vygotsky, *Mind in Society* (Harvard Univ. Press, Cambridge, MA, 1978).
34. S. L. Stockdale, R. L. Williams, *J. Behav. Educ.* **13**, 37 (2004).

**Acknowledgments:** We thank the University of Washington Biology Education Research Group, Bio-Grads Organizing Opportunities for Diversity and Development, and P. Haak for helpful discussion and A. Arquiza, R. Moreno, and S. Fernandes for assembling the achievement gap data across introductory STEM courses from the Office of Minority Affairs and Diversity. Data are archived with the study authors and may be obtained by contacting S.F. The work was funded by grants from the University of Washington's College of Arts and Sciences as part of the Foundations Course program, the University of Washington-Howard Hughes Medical Institute Undergraduate Science Education Programs (grant 52003841), and an NSF predoctoral fellowship to D.C.H. The research was conducted under Human Subjects Review no. 07-8483-J01.

#### Supporting Online Material

[www.sciencemag.org/cgi/content/full/332/6034/1213/DC1](http://www.sciencemag.org/cgi/content/full/332/6034/1213/DC1)  
Materials and Methods  
Figs. S1 and S2  
Tables S1 to S3  
References (35–47)

25 February 2011; accepted 27 April 2011  
10.1126/science.1204820

### BIOMOLECULAR INTERACTION DETECTION

The Octet RED96 system can rapidly measure protein and other biomolecule concentrations as well as determine kinetics, affinity, and specificity of protein-protein and protein-small molecule interactions. It extends the capabilities of the company's premier Octet RED platform by featuring biosensor reracking, which enables more efficient workflow, reduces amounts of capture molecule use, and lowers assay-running costs. The system enables life science researchers to perform analyses that have traditionally been conducted with SPR, HPLC, ELISA, and other single-purpose microfluidics instruments. Researchers can run a suite of assays in a multiplexed panel format using ForteBio's Protein A, Protein G, and new Protein L biosensors. The Octet platform is based on BioLayer Interferometry (BLI) technology, which uses optical biosensors to measure multiple interactions in parallel, without the use of detection agents. The Octet platform consists of 8- and 16-channel instruments that accommodate 96- and 384-well assay formats.

ForteBio

For info: 650-322-1360 | [www.fortebio.com](http://www.fortebio.com)



### WATER PURIFICATION SYSTEM

The Elix Gulfstream Clinical water purification system will provide up to 100 liters per hour and 2000 liters of clinical laboratory reagent water (CLRWW) daily. The system includes EMD Millipore's well-known Elix electrodeionization technology as well as improved reverse osmosis cartridges. These complementary technologies help to extend the lifetime of the purification cartridges, thus reducing running costs. Biomedical labs need to avoid costly downtime; problems that occur due to inconsistent pure water quality, however, can disrupt sample processing, halting or reducing a lab's output and incurring unforeseen expenses. The Elix Gulfstream Clinical system provides biomedical labs with a reliable, constant source of pure water for their analyzers. Water produced by the system meets the stringent standards of the Clinical and Laboratory Standards Institute (CLSI) for CLRWW. The all-in-one design and small footprint let users install the system in limited space.

EMD Millipore

For info: 800-645-5476 | [www.millipore.com](http://www.millipore.com)

### MICROPLATE HANDLER

The BenchBot robot is a new mid-sized microplate handler designed to meet the automation workflow needs of diverse laboratories. The BenchBot incorporates the robust functionality of Agilent Automation's larger automated microplate handlers into a compact design for use in small lab spaces, enabling automation of a wide variety of changing, science-driven workflows. The robot has the capability to easily integrate with an expansive list of laboratory equipment increasing its utility for applications from next generation sequencing and microarray sample preparation to high throughput LC/MS sample management and numerous cell-based assays. The power of the BenchBot comes from its flexibility, accessibility, and ease of use. The compact size of the BenchBot enables it to be used right where it is needed most—on a bench, in a fume hood, or on a docking table. With the BenchBot robot, automated solutions move from large, specialized machines to compact, flexible robots that any scientist can use.

Agilent Automation Solutions

For info: +44-(0)-1763-850230 | [www.agilent.com](http://www.agilent.com)

### BLUE LIGHT TRANSILLUMINATOR

The Blue Light Transilluminator light box can be used for safe, precise viewing of fluorescently labeled DNA and proteins. The new light box does not need to be used in a darkroom, although it can easily fit into any Syngene image capture system. The transilluminator can illuminate dyes that emit light at 420 to 480 nm, so is excellent for visualizing nanogram amounts of nontoxic DNA stains including: SYBR Safe, SYBR Green, SYBR Gold, and GelGreen as well as protein stains such as SYPRO Ruby and ProQ Diamond. Because visible blue light is not damaging to the human eye and does not photo-nick DNA as ultraviolet light does, scientists can view, image, and cut out DNA or protein bands from gels without worrying about harmful effects. The Blue Light Transilluminator comes either with a 20 cm x 20 cm gel viewing area or a 25 cm x 30 cm viewing plate.

Syngene

For info: +44-(0)-1223-727123 | [www.syngene.com](http://www.syngene.com)

### NORMAL PRIMARY CARDIOMYOCYTES

The American Type Culture Collection (ATCC) now offers primary cardiomyocytes isolated from adult human tissue. Unlike cardiomyocytes derived from human ES or iPS cells, these heart muscle cells propagate in culture with high viability and plating efficiency. ATCC Normal Primary Cardiomyocytes are one part of ATCC Primary Cell Solutions, a system of matched components that include cryopreserved cells, optimized media, growth factors, and reagents for cell culture. The kit is composed of several purified recombinant human (rh) growth factors, including rh FGF-basic, rh insulin, and rh EGF/rh TGF- $\beta$ 1, in addition to FBS and fetuin. Normal Primary Cardiomyocytes are cryopreserved in the second passage, assuring the highest purity. The cells have undergone sterility testing for bacteria, yeast, fungi, and mycoplasma and shown to be negative for HIV-1, HIV-2, HBV, and HCV. Scientists can expect cell cultures with functional expression of relevant biomarkers, normal morphology, and superior growth and proliferation.

ATCC

For info: 800-638-6597 | [www.atcc.org](http://www.atcc.org)

Electronically submit your new product description or product literature information! Go to [www.sciencemag.org/products/newproducts.dtl](http://www.sciencemag.org/products/newproducts.dtl) for more information.

Newly offered instrumentation, apparatus, and laboratory materials of interest to researchers in all disciplines in academic, industrial, and governmental organizations are featured in this space. Emphasis is given to purpose, chief characteristics, and availability of products and materials. Endorsement by *Science* or AAAS of any products or materials mentioned is not implied. Additional information may be obtained from the manufacturer or supplier.

## Science Careers

From the journal *Science*



### Science Careers Advertising

For full advertising details, go to [ScienceCareers.org](http://ScienceCareers.org) and click For Employers, or call one of our representatives.

#### Tracy Holmes

Worldwide Associate Director  
Science Careers  
Phone: +44 (0) 1223 326525

#### UNITED STATES & CANADA

E-mail: [advertise@sciencecareers.org](mailto:advertise@sciencecareers.org)  
Fax: 202-289-6742

#### Tina Burks

Midwest/West Coast/  
South Central/Canada  
Phone: 202-326-6577

#### Elizabeth Early

East Coast & Industry  
Phone: 202-326-6578

#### Marci Gallun

Sales Administrator  
Phone: 202-326-6582

#### Online Job Posting Questions

Phone: 202-326-6577

#### EUROPE & REST OF WORLD

E-mail: [ads@science-int.co.uk](mailto:ads@science-int.co.uk)  
Fax: +44 (0) 1223 326532

#### Alex Palmer

Phone: +44 (0) 1223 326527

#### Susanne Kharraz

Phone: +44 (0) 1223 326529

#### Dan Pennington

Phone: +44 (0) 1223 326517

#### Lisa Patterson

Phone: +44 (0) 1223 326528

#### JAPAN

#### ASCA Corporation

Jie Chin  
Phone: +81-3-6802-4616  
Fax: +81-3-6802-4615  
E-mail: [careerads@sciencemag.jp](mailto:careerads@sciencemag.jp)

#### CHINA & TAIWAN

#### Ruolei Wu

Phone: +86-1367-1015-294  
E-mail: [rwu@aaaas.org](mailto:rwu@aaaas.org)

All ads submitted for publication must comply with applicable U.S. and non-U.S. laws. *Science* reserves the right to refuse any advertisement at its sole discretion for any reason, including without limitation for offensive language or inappropriate content, and all advertising is subject to publisher approval. *Science* encourages our readers to alert us to any ads that they feel may be discriminatory or offensive.



深圳大学  
Shenzhen University

## Opening Positions for Full-time Distinguished Professors

Shenzhen University (SZU) invites applications for Full-time Distinguished Professor positions for highly qualified candidates with special expertise in one of the following academic areas listed below.

#### The University

The university, founded in 1983, is located in Shenzhen and has been a comprehensive university with fundamental influence. We are now aggressively seeking highly qualified international scholars to join us as we continue towards our mission of becoming a top-class research institution in China.

#### Areas of Interest

01. Mathematics and Computational Science, 02. Material Science and Engineering, 03. Communication and Information Processing, 04. Computer and Software, 05. Civil Engineering, 06. Manufacturing and Automation, 07. Marine Biology and Marine Ecology, 08. Micro-nano Photon-electronics and its Devices, 09. Biophotonics, X-ray Optics, 10. Molecular Biology, Molecular Target based Anticancer Drugs, Cancer Biology, Stem Cell and Immunity Allergic Reaction, 11. Comparative Literature, Western Philosophy, 12. Economics, 13. Management, 14. Industrial Design, Animation Design, Environmental Design

#### Qualifications

1. Have an earned doctorate in a closely related discipline with a track record of extraordinary accomplishment in teaching, research / scholarship, and professional service judged by peers to be outstanding;
2. Have assistant-professor or above academic experience in world-renowned universities;
3. Have been recognized nationally or internationally for the importance of their achievements and are expected to bring distinction to SZU and serve as a key contributor to achieving its strategic goal of becoming a World-Class university.
4. Have great academic potential and be able to anticipate the development tendency of their field.
5. Have a strong organizing and communicating ability to lead their research team to reach world leading level.

#### Salary/Benefits

Salary and benefits are very competitive; yearly salary starting from 100,000 to 200,000 US Dollars and will be commensurate with qualifications and experience.

#### To Apply

Interested candidates should submit all application documents to the below contacts or submit all information to <http://szuhr.szu.edu.cn>. For more information please visit <http://www.szu.edu.cn/szu2007/indexe.asp>

#### Contact

Ms. Samantha ZENG, ([zengsa@szu.edu.cn](mailto:zengsa@szu.edu.cn), 0086-755-26732890) or Ms. Yun LI ([liyun@szu.edu.cn](mailto:liyun@szu.edu.cn), 0086-755-26536111)



## Joint Department of Biomedical Engineering The University of North Carolina at Chapel Hill and North Carolina State University at Raleigh



152 MacNider Hall, Chapel Hill, NC 27599 7575  
(919) 966-1175; (919) 966-2963 fax  
<http://www.bme.unc.edu>

911 Oval Drive, 4130 EB3, CB7115, Raleigh, NC 27695-7115  
(919) 515-5252; (919) 513-3814 fax  
<http://www.bme.ncsu.edu>

### Professor of Biomedical Engineering Director of Center for Rehabilitation Engineering

The Joint Department of Biomedical Engineering at the University of North Carolina at Chapel Hill and North Carolina State University is seeking a Professor to direct the Center for Rehabilitation Engineering in Biomedical Engineering Department. Candidates should have experience in bringing teams of individuals together, working across disciplines and, in particular, working with individuals in the clinical sciences. The NC State College of Engineering and the UNC School of Medicine are making substantial investments in space, funds and FTE positions to establish the new Center. Applicants are expected to have earned doctoral degrees in biomedical engineering or related engineering sciences. Successful candidates will be expected to have a demonstrated track record of sustained extramural funding and an internationally acclaimed research program. The candidate is expected to possess a clear commitment to the academic programs of the Department.

The individual sought for this position should currently be a tenured full professor or associate professor or equivalent in rehabilitation engineering, biomedical engineering, or a closely related field. The successful candidate will need to build interdisciplinary and inter-institutional research teams and have the ability to forge collaborations/interactions with individuals in the clinical sciences within and outside of the Research Triangle area.

The Director of this Center will report to the Chair of the Joint Department of Biomedical Engineering. The Director will be expected to take a lead role in strategic planning and program development efforts of the newly created Center. The Director will be responsible for the oversight and management of all aspects of the Center's resources. The Director in coordination with the Department Chair will be responsible for the recruitment of new faculty hires within the Center.

**Application procedure:** Applicants should complete an online application at <http://jobs.ncsu.edu/> for position #04-07-0704.

**Application deadline:** Applications will be accepted until suitable candidates are found.

**Joint Department of Biomedical Engineering:** <http://www.bme.unc.edu/> or <http://www.bme.ncsu.edu/>

**Inquiries:** Contact Rick Segal, PT, PhD, FAPTA at 919-843-8660 or [rsegal@med.unc.edu](mailto:rsegal@med.unc.edu)

*NCSU is an Equal Opportunity and Affirmative Action Employer. Also, NC State welcomes all persons without regard to sexual orientation. In its commitment to diversity and equity, NCSU seeks applications from women, minorities and persons with disabilities. Individuals with disabilities desiring accommodations in the application process should contact Rekha Balasubramanyam, Administrative Manager, [srbalasu@ncsu.edu](mailto:srbalasu@ncsu.edu), ph/vm 919-513-7622, fax 919-513-3814.*





## Plant Biochemistry

The Division of Biochemistry (biochem.missouri.edu) and the Interdisciplinary Plant Group (ipg.missouri.edu) at the University of Missouri invite applications for appointment as a tenure-track Assistant or Associate Professor. Applicants should apply biochemical and molecular approaches to the study of plant metabolism. The successful candidate will have or will establish a research program that complements and enhances our existing strengths in plant biochemistry. The successful candidate will contribute to departmental teaching in areas of undergraduate, graduate, or medical education. The University is noted for interdisciplinary research programs including the Interdisciplinary Plant Group of > 50 faculty members in five Departments. Position qualifications include a Ph.D. in biochemistry or related field and postdoctoral training.

We offer a competitive salary and start-up package, an active doctoral program and a highly interactive, multidisciplinary faculty.

Cover letter, vitae, a description of research plans and teaching interests, and a list of three references and their affiliation required for application. Apply electronically at: <http://hrs.missouri.edu/find-a-job/academic/index.php>. Job Opening ID #4903. Application review will begin **July 15, 2011**.

*MU is an Equal Opportunity-Affirmative  
Action Employer To request ADA  
accommodation contact Human Resource  
Services at 573-882-7976.*



**UNIVERSITY AT ALBANY**  
State University of New York

## Director, Atmospheric Science Research Center

The University at Albany, State University of New York is seeking a Director of the Atmospheric Sciences Research Center. The Director serves as the chief administrative officer of the Center and provides strategic planning and direction in the initiation and integration of the research enterprise at the Center. The Director provides guidance to Center members in the development and coordination of academic affiliations and research projects and is expected to maintain a significant research portfolio and contribute to the graduate program (i.e., mentoring graduate students and teaching graduate course) of the Director's host academic appointment. The Director is responsible for the development and implementation of the Center's strategic research plan and the management of its research infrastructure and operations to assure a productive research environment. The Director reports directly to the Vice President for Research.

For a complete position description and application instructions, please see **P11-23398** at: <http://albany.interviewexchange.com/jobofferdetails.jsp?JOBID=24495>

*UAlbany is an EO/AA/IRCA/ADA employer.*



**DEAKIN**  
UNIVERSITY AUSTRALIA

MELBOURNE GEELONG WARRNAMBOOL

## Lecturer / Senior Lecturer in Marine Science

**Faculty** Science and Technology  
**School** Life and Environmental Sciences  
**Reference number** 110231  
**Applications close** Sunday 3 July 2011  
**Salary range** Lecturer \$74,918 – \$88,964 p.a.  
(plus 17% superannuation)  
Senior Lecturer \$91,772 – \$105,820 p.a.  
(plus 17% superannuation)  
**Position status** Full-time and continuing  
**Location** Warrnambool Campus  
**Contact** Professor Gerry Quinn on +61 3 5563 3268

## Lecturer / Senior Lecturer in Forensic Science

**Faculty** Science and Technology  
**School** Life and Environmental Sciences  
**Reference number** 110233  
**Applications close** Sunday 3 July 2011  
**Salary range** Lecturer \$74,918 – \$88,964 p.a.  
(plus 17% superannuation)  
Senior Lecturer \$91,772 – \$105,820 p.a.  
(plus 17% superannuation)  
**Position status** Full-time and continuing  
**Location** Geelong Waurn Ponds Campus  
**Contact** Professor Guang Shi on +61 3 9251 7619

## Lecturer in Biomedical Science

**Faculty** Science and Technology  
**School** Life and Environmental Sciences  
**Reference number** 110226  
**Applications close** Sunday 3 July 2011  
**Salary range** Lecturer \$74,918 – \$88,964 p.a.  
(plus 17% superannuation)  
**Position status** Full-time and continuing  
**Location** Melbourne Burwood Campus  
**Contact** Professor Guang Shi on +61 3 9251 7619

## Lecturer in Physiology

**Faculty** Science and Technology  
**School** Life and Environmental Sciences  
**Reference number** 110229  
**Applications close** Sunday 3 July 2011  
**Salary range** Lecturer \$74,918 – \$88,964 p.a.  
(plus 17% superannuation)  
**Position status** Full-time and continuing  
**Location** Geelong Waurn Ponds Campus  
**Contact** Professor Guang Shi +61 3 9251 7619

Apply online at [www.deakin.edu.au/jobs](http://www.deakin.edu.au/jobs)

*The difference is Deakin*

**Human Resources +61 3 9246 8139**



Equal Opportunity is  
University Policy

# Positions @ NIH

## THE NATIONAL INSTITUTES OF HEALTH

### ***The Eunice Kennedy Shriver* National Institute of Child Health and Human Development National Children's Study Program Director**

The National Children's Study is an unprecedented complex high profile Congressionally mandated longitudinal observational study to determine the effects of environmental exposure, as broadly defined, and genetics on the growth, development and health of a national cohort of 100 000 children from before birth through age 21 years. The position of Program Director offers a unique and exciting opportunity for a leader to execute and manage daily operations in support of the National Children's Study strategic vision and mission. More than one position may be available. The Program Director works with a team of federal employees and contractors, collaboratively across the NIH, throughout the federal government and with other key stakeholders and organizations to coordinate and direct the protocol implementation to achieve the objectives of the Study. The Program Director is responsible for managing people and financial resources with integrity and fairness, utilizing state of the art tools and processes with frequent refresh cycles to maintain high quality cost effective research and coordinate and harmonize the methods and process of the Study with other international cohort studies. The Program Director is a key member of the senior leadership team for a system of integrated activities in an active learning community.



Applicants must possess a Ph.D., M.D., or comparable doctorate degree in the health sciences field plus senior-level scientific experience and knowledge of research program operations in one or more scientific areas related to clinical research. Candidates should have demonstrated expertise in study implementation, organizational management and a proven record of achieving goals and deliverables. They should have demonstrated leadership and ability to engage others to execute complex projects; optimize organizational performance, setting and communicating clearly defined expectations, promoting accountability for results and resolving operational problems and issues. Candidates should have demonstrated management acumen, including identification and management of financial and human resource needs; proven ability to make complex and strategic decisions to optimize resource usage, mitigate risks, and achieving desired results; and, the ability to build, mentor, motivate, and maintain a culturally diverse staff.

**Salary/Benefits:** The Program Director will be appointed GS-15 level plus a Physician's Compatibility Allowance if qualified. Full Federal benefits will be provided including leave, health and life insurance, long-term care insurance, retirement, and savings plan (401k equivalent).

**How To Apply:** Applicants must submit a current CV and bibliography electronically to Ms. Josephine Evans, [evansjo@mail.nih.gov](mailto:evansjo@mail.nih.gov). In addition, applicants must also submit a supplemental narrative statement that addresses the qualifications requirements (not to exceed a total of two pages), and provide the names, titles, and telephone numbers of 4-5 references. Information on the National Children's Study including a Concept of Operations is located at its website (<http://www.nationalchildrensstudy.gov>). The NIH encourages the application and nomination of qualified women, minorities, and individuals with disabilities.

**Standards of Conduct/Financial Disclosure:** The National Institutes of Health inspires public confidence in our science by maintaining high ethical principles. NIH employees are subject to Federal government-wide regulations and statutes as well as agency-specific regulations described at the NIH Ethics website. We encourage you to review this information. The position requires the incumbent to complete a public financial disclosure report prior to the effective date of the appointment. Selection for this position will be based solely on merit, with no discrimination for non-merit reasons such as race, color, religion, gender, sexual orientation, national origin, political affiliation, marital status, disability, age, or membership or non-membership in an employee organization.

**Reasonable Accommodation:** NIH provides reasonable accommodations to applicants with disabilities. If you require reasonable accommodation during any part of the application and hiring process, please notify us. The decision on granting reasonable accommodation will be made on a case-by-case basis.





WWW.NIH.GOV

# Help Us Help Millions

## Computational Biologist

The Dale and Betty Bumpers Vaccine Research Center (VRC) at the National Institute of Allergy and Infectious Diseases (NIAID), National Institutes of Health (NIH), is dedicated to improving global human health through the rigorous pursuit of effective vaccines for human diseases, including HIV and emerging infectious disease. The VRC translates the latest concepts in disease pathogenesis and immunology into new vaccine strategies, providing safe and effective means to prevent and control human diseases.

We are seeking a computational structural biologist interested in protein design. Candidates should have experience with a broad range of computational tools associated with protein structure and protein-protein interactions and have an interest in applying these tools to an exciting series of problems associated with vaccine design. The successful applicant will join a computational biology team that is integrated with VRC scientists working on the development of an effective HIV-1 vaccine. This team currently consists of several staff mentoring two postdoctoral fellows.

The major goal of the computational biology team at the VRC is to enhance current HIV-1 vaccine design efforts. These efforts involve 1) crystallographic definition of a site of vulnerability on the HIV-1 env to antibody-mediated neutralization, 2) design of immunogens based on the vulnerable site, and 3) design of select binding ligands to decipher the elicited response. In addition to assisting with structure-based HIV-1 vaccine efforts, successful applicants will be encouraged to pursue independently other avenues of computational vaccine-design efforts for other viral diseases, including Ebola, Marburg, and influenza viruses. Interactions with graduate students and postdoctoral fellows related to protein production and computational design will also be encouraged.

See more about the computational biology team at [www.niaid.nih.gov/labsandresources/labs/aboutlabs/vrc/structuralbioinform](http://www.niaid.nih.gov/labsandresources/labs/aboutlabs/vrc/structuralbioinform).

Salary will be based on the individual's qualifications and experience, in the range of \$80,000 – \$100,000. This position is subject to a background investigation.

### Specific Requirements

- Ph.D. in biophysics or related field with experience in computational biology and with protein design
- Excellent oral and written communication skills



# NIAID

National Institute of Allergy and Infectious Diseases

### Application Information

Submit a current curriculum vitae and three letters of reference.

### Contact

To apply or for more information, contact NIAID/VRC, c/o Vaccine Research Center Administrative Support Branch, Attn: Mrs. Renita Farrington, Building 40, Room 1118, 40 Convent Drive, Bethesda, MD 20892-3013 or [brookr@mail.nih.gov](mailto:brookr@mail.nih.gov).

### Deadline

Applications are due by close of business **July 31, 2011**.

For more information about NIAID and our available opportunities, visit us on the Web at [www.niaid.nih.gov/careers/vcb](http://www.niaid.nih.gov/careers/vcb).

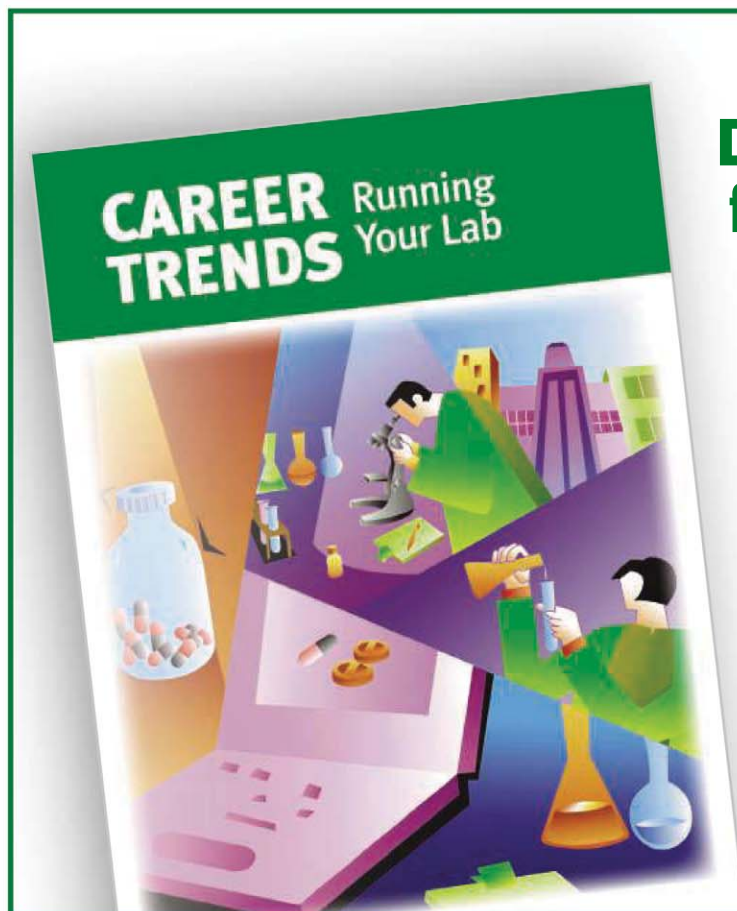


US DEPARTMENT OF HEALTH AND HUMAN SERVICES  
National Institutes of Health



National Institute of Allergy and Infectious Diseases  
Proud to be Equal Opportunity Employers





## Download your free copy today.

**ScienceCareers.org/booklets**

- **Business Sense:** Starting an Academic Lab
- **Lab Management:** The Human Elements
- **Mind Matters:** In Defense of Downtime
- **Funding Your Future:** Publish or Perish
- **If at First You Don't Succeed,** Cool Off, Revise, and Submit Again
- **Your Research in the Headlines:** Dealing with the Media

**Science Careers**

From the journal *Science*



Brought to you by the AAAS/Science Business Office

### Chair, Department of Biological Chemistry and Molecular Pharmacology (BCMP)

Harvard Medical School seeks a scientist of the highest distinction to serve as Chair, Department of Biological Chemistry and Molecular Pharmacology (BCMP). Candidates must have a MD and/or a PhD degree, a record of sustained scientific accomplishment in an area related to the department, and a demonstrated commitment to academic and educational leadership. The Chair will be charged with building upon and reshaping an already strong department based on a clearly articulated scientific vision, and will have the opportunity to play a key role in overall scientific leadership at HMS, including a planned cross-department initiative in translational science and therapeutics. Formed in 1987 by the merger of historic Biochemistry and Pharmacology Departments, BCMP is the largest preclinical department of HMS, with core and affiliated faculty. Department research focuses on the molecular mechanisms of fundamentally important life processes, including structure and function of proteins; control of gene expression; mechanisms of DNA replication, recombination, and repair; organization and regulation of chromatin structure; biosynthesis of membrane lipids, carbohydrates, and proteins; chemical biology; principles of antibiotic and natural product synthesis, and morphological and biochemical differentiation of cells. Faculty are also deeply engaged in technology development, including new methods for single-molecule studies, optical microscopy, nuclear magnetic resonance and x-ray crystallographic approaches for atomic resolution, protein analysis using mass spectroscopy, use of natural or synthetic organic molecules in biological studies, and high throughput methods for functional studies. This recruitment is a rare opportunity for an exceptional scientist to lead a great department, in an outstanding and highly collaborative school and university, and at a time of unusual scientific progress. The Chair will have access to resources and space appropriate to the goals for the future of the department. HMS offers a competitive salary and benefits package.

Please send a letter of application or nomination, with curriculum vitae, to:

Chair, BCMP Chair Search Committee  
Gordon Hall-Suite 101  
25 Shattuck Street, Boston MA 02115  
email: [BCMP\\_Chair\\_Search@hms.harvard.edu](mailto:BCMP_Chair_Search@hms.harvard.edu)

Harvard Medical School is an equal opportunity/affirmative action employer. We recognize the power and importance of a diverse employee population and strongly encourage applicants with various experiences and backgrounds.



HARVARD MEDICAL SCHOOL



### Yamada Research Grant 2011

Yamada Research Grant aims to promote the latest and highly original studies from multiple points of view in the fields of preventive medicine or cosmetic dermatology using bee products and honeybee science.

#### 1. Eligible researchers:

- 1) Grant for Young researchers: Under 45 years old on April 1, 2011.
- 2) Grant for Specific areas: No age restriction.

#### 2. Subject for research:

- 1) Young researchers:
  - Preventive medical research on Anti-metabolic syndrome, Brain science, Anti-aging and Anti-locomotive syndrome.
  - Basic research on honeybees
  - Beekeeping technology research
- 2) Specific areas:
  - Prevention of diabetes (focusing on insulin resistance)
  - Prevention of dementia
  - (Urgent theme) Prevention of radiation damage

#### 3. Grant amount:

- 1) Grant for Young researchers: Between 1,000,000 and 3,000,000 Japanese Yen (approx.\$10,000 - \$30,000) per theme.
- 2) Grant for Specific areas: Up to 10,000,000 Japanese yen (approx.\$100,000) per theme, (Urgent theme) Total amount :4,000,000 Japanese yen.

#### 4. Language: English or Japanese

#### 5. How to apply: Applications should be filled out the specified format on the following website according to application guideline for this grant.

#### The official website of Application for Yamada Research Grant 2011:

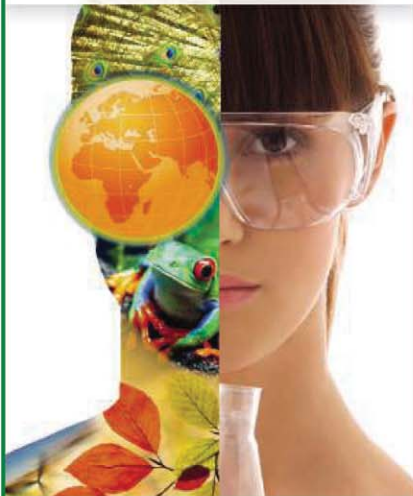
[http://grant.bee-lab.jp/grant/grant\\_2011/guideline\\_eng.html](http://grant.bee-lab.jp/grant/grant_2011/guideline_eng.html)

#### 6. Application period: From May 1 to June 30, 2011 at 5:00 p.m. (in Japan) (Urgent theme) From May 13 to May 31 at 5:00 p.m. (in Japan)

#### 7. How to inquire: Please send your questions to the secretaries of this grant, Yamada Apiculture Center, Inc. by e-mail: [bee-lab@yamada-bee.com](mailto:bee-lab@yamada-bee.com)

# WOMEN IN SCIENCE

forging  
new pathways in  
green  
science



Read inspiring stories  
of women working in  
"Green Science"  
who are blending  
a unique combination of  
enthusiasm for science  
and concern for others  
to make the world  
a better place.

Download this  
free booklet  
[ScienceCareers.org/  
LOrealWiS](http://ScienceCareers.org/LOrealWiS)



This booklet is brought to you by the  
AAAS/Science Business Office  
in partnership with the  
L'Oreal Foundation



## Department of Health and Human Services National Institutes of Health National Institute on Aging Intramural Research Program



### Staff Scientist - Animal Program Director

The National Institute on Aging (NIA), a major research component of the National Institutes of Health (NIH) and Department of Health and Human Services (DHHS), is recruiting for a Staff Scientist-Facility Head who will serve as the Animal Program Director for the NIA Intramural Research Program (IRP). The incumbent will be responsible for an AAALAC accredited animal care and use program and for support of the animal research programs in the Institute, studying animal models of development and aging, and interventions to prevent or alleviate aging-related deficits. The supervisory and regulatory responsibilities of this position require the applicant to hold a veterinary degree (D.V.M., V.M.D., or equivalent degree) with certification or eligibility for board certification in laboratory animal medicine or veterinary pathology.

Applicants must have a proven record of management of an animal research program and demonstrated experience with the regulatory aspects of animal welfare. The expertise and experience should include, but not be limited to interaction and cooperation with scientific staff in a manner that promotes and facilitates their scientific programs. Duties will include cost-effective breeding and maintaining numerous transgenic and knockout lines (currently in excess of 600) including "difficult" lines, collaboration with scientific staff in effective production and import of new genetically manipulated lines, and, especially, in maintaining a current and accurate database on the colony status. The incumbent will take primary responsibility for the clinical aspects of the animal program and will oversee animal health surveillance and maintain both a barrier facility and a quarantine area. The incumbent will perform animal surgery and teach appropriate procedures to animal care and technical staff.

Salary is commensurate with experience and accomplishments. The salary range for Staff Scientists is \$89,033 - \$173,826. A full Civil Service package of benefits (including retirement, health, life and long term care insurance, Thrift Savings Plan, etc.) is available. Additional information regarding the NIA, IRP is available at <http://www.grc.nia.nih.gov>. To apply: Please send a cover letter, curriculum vitae, bibliography, statement of research interests, and three letters of recommendation electronically or by mail to: Peggy Grothe, Intramural Program Specialist; Office of the Scientific Director; National Institute on Aging, 251 Bayview Boulevard, Suite 100-Room 04C232, Baltimore, MD 21224-6825. Email: [grothep@mail.nih.gov](mailto:grothep@mail.nih.gov). Position will remain open until filled; however, application reviews will begin on **August 1, 2011**. Please include the following vacancy number in all correspondence: Vacancy # NIA-IRP-11-02.



DHHS and NIH are Equal Opportunity Employers



Careers with **Mass Appeal**

### Associate Professor Positions Department of Biological Sciences

The University of Massachusetts Lowell is a comprehensive university with a national reputation in science, engineering and technology, committed to educating students for lifelong success in a diverse world and conducting research and outreach activities that sustain the economic, environmental and social health of the region. In February 2009, a campus-wide strategic planning initiative was launched to reposition UMass Lowell as a world-class institution over the next decade. A major component of that initiative is to ensure that diversity and inclusion are in every aspect of our strategic plan. We seek a diverse talented candidate pool to be part of our mission and achievements.

**Position Description:** The University of Massachusetts Lowell Department of Biological Sciences invites applications for full-time tenure-track faculty positions, rank negotiable, to start September 2012 or thereafter. The successful candidates will be expected to have a vigorous, externally funded research program, and collaboration within this and other departments is encouraged.

Current faculty research interests include genetics, neurobiology, cancer biology, invertebrate biology, developmental biology, virology, microbial ecology, evolution, and biogeochemistry. Our campus is located very near the vibrant academic and commercial biotechnology centers of Boston, Cambridge and Worcester.

We are seeking established mid-career individuals with expertise in one or more of the following areas: molecular/cell biology, plant science, integrative zoology, vertebrate physiology, comparative vertebrate structure/biomechanics, and/or evolutionary developmental biology. Teaching obligations include development of upper level undergraduate/graduate courses in his/her area of expertise and participation in the teaching of core undergraduate courses as needed.

**Minimum Qualifications:** earned doctorate (must have at the time of application); demonstrated teaching ability at the undergraduate and graduate levels; evidence of a sustainable externally funded research program; demonstrated publication record in scholarly journals; excellent communication and interpersonal skills; and demonstrated ability to work with diverse student and faculty population.

**How to apply:** Interested applicants should apply online at <https://jobs.uml.edu>. Candidates should submit a curriculum vitae, copies of several recent research publications, a statement of research and teaching interests, not to exceed three pages, and names and contact information of three references. Thank you for considering the University of Massachusetts Lowell as an employer of choice. We look forward to receiving your application.

*The University of Massachusetts Lowell is committed to increasing diversity in its faculty, staff, and student populations, as well as curriculum and support programs, while promoting an inclusive environment. We seek candidates who can contribute to that goal and encourage you to apply and to identify your strengths in this area.*



# Get a Career Plan that Works.

An exceptional career requires insightful planning and management. That's where *Science Careers* comes in. From job search to career enhancement, *Science Careers* has the tools and resources to help you achieve your goals. Get yourself on the right track today and get a real career plan that works. Visit [ScienceCareers.org](http://ScienceCareers.org).

**Science Careers**

From the journal *Science*



[ScienceCareers.org](http://ScienceCareers.org)





National Aeronautics and Space Administration

## NASA AMES RESEARCH CENTER Research Scientist Position



### WORK WITH NASA AMES TO DEFINE THE FIELD OF SPACE SYNTHETIC BIOLOGY

Building on decades of cutting edge scientific achievements, NASA Ames Research Center is creating a new, interdisciplinary, research effort to use synthetic biology as an enabling technology to explore our solar system.

As a recognized expert and leader, you will establish a Center for Space Synthetic Biology and play a key role in defining the field. You will direct start-up funds (subject to appropriation) intended to fund your salary, lab equipment, graduate students, and post-doctoral students, and grow research capabilities to build this center into a world-renowned establishment. You will recruit and lead research teams, compete for grants, and collaborate with others within and outside of NASA.

The Center for Space Synthetic Biology at NASA Ames Research Center is being created to harness biology in reliable, robust, engineered systems to support NASA's exploration and science missions, to improve life on Earth, and to help shape NASA's future.

At NASA, your research could change the world, and enable exploration of new ones.

#### US Citizenship is required.

Interested applicants should apply directly to USAJobs to vacancy number AR11B0066 at

<http://jobsearch.usajobs.gov/fvtva.asp?opmcontrol=2240258>

*NASA Ames Research Center does not discriminate in employment on the basis of race, color, religion, sex, national origin, political affiliation, sexual orientation, gender identity, marital status, disability and genetic information, age, membership in an employee organization, or other non-merit factor.*



南京医科大学基础医学院

School of Basic Medical Sciences,  
Nanjing Medical University, CHINA

### Full /Associate Professor Positions

The School of Basic Medical Sciences, Nanjing Medical University, China was ranked No. 9 in the overall ranking in the nationwide discipline evaluation (basic medical sciences) of academic degree and graduate education carried out in China in 2009. Now we sincerely invite applications for full-time faculty positions, at academic ranks of Associate or Full Professor. Individuals with demonstrated accomplishments in, but not limited to, the following areas are encouraged to apply:

Research Areas	Number
Areas of Human Anatomy	2~3
Areas of Reproductive Medicine	2~3
Areas of Pathology	2~3
Areas of Pathophysiology	2~3
Areas of Human Parasites and Vector Biology	2~3
Areas of Medical Microbiology	2
Areas of Immunology	2
Areas of Pharmacology	2
Areas of Forensic Medicine	1~2
Areas of Oncology	1~2
Areas of Human Physiology	1~2
Areas of Cell Biology	1~2
Areas of Development and Genetics	1~2
Areas of Neurobiology	1~2
Areas of Bioinformatics	1~2

Interested individuals, regardless of their nationalities, should submit a detailed letter of interest, curriculum vitae, PDFs of three of their best publications, and two letters of recommendation to: **Jicheng Guo ([jcdw@njmu.edu.cn](mailto:jcdw@njmu.edu.cn)) or Changliang Zhu Ph.D. ([clzhu@njmu.edu.cn](mailto:clzhu@njmu.edu.cn)), School of Basic Medical Sciences, Nanjing Medical University, 140 Hanzhong Road, Nanjing, Jiangsu 210029, China.** The positions are available immediately. Applications will be evaluated by faculty search committee upon receipt until the positions are filled.

### Associate Chief of Staff (ACOS) for Research and Development

The Department of Veterans Affairs Medical Center (VAMC), Syracuse, New York seeks an ACOS for Research and Development. The Syracuse VAMC is an active teaching hospital affiliated with the State University of New York Upstate Medical University (SUNY UMU). We are seeking the right individual to further develop and grow our research program. Current research areas include Infectious Disease, Medical Oncology, Vascular Biology, Neuroscience and Physiology, Behavioral Health, Traumatic Brain Injury and Post Traumatic Stress Disorder. The Syracuse VAMC is nearing completion of a 150,000 square foot clinical addition that will house a state of the art 30 bed Spinal Cord and Traumatic Brain Injury Center. We are especially interested in expanding our research activities in this emerging area.

The ACOS for Research and Development is expected to have a strong record of funded research and experience in fostering inter-institutional relationships and building regional research programs. This position involves strong administrative leadership for continued program compliance and development. Interactions with the leadership at the affiliate SUNY UMU is an important element of the incumbent's duties. The successful candidate will be responsible for programmatic growth including recruitment of clinical and basic scientists, faculty development, research mentorship, and planning the design and renovation of research facilities. Applicants must be United States citizens, possess an M.D. and/ or Ph.D., and qualify for a corresponding academic appointment at the Associate or full Professor rank at the SUNY UMU College of Medicine.

Interested candidates should submit a cover letter and current CV to **Deborah Collins, Administrative Officer, Research Service (151), Syracuse VA Medical Center, 800 Irving Avenue, Syracuse, New York 13210 or fax to (315) 425-4871.** CVs will be accepted until the position is filled. Information on Upstate New York VISN 2 VA Healthcare Network can be found at [www.visn2.va.gov](http://www.visn2.va.gov).

*The Syracuse VAMC is an Equal Opportunity Employer.*

### Dean Search, Bilkent University, Ankara

Bilkent University, Ankara, invites applications or nominations for the position of Dean of Faculty of Science, which comprises Departments of Chemistry, Mathematics, Molecular Biology and Genetics, and Physics. All the departments have both undergraduate and graduate programs.

The primary goals of the Faculty of Science are (1) educating future leaders of Science in an environment that fosters "cultures of creativity," (2) conducting cutting-edge research with worldwide impact in several sub-disciplines, and (3) providing an exemplary research environment for faculty.

The Dean is expected to have a broad understanding of the Sciences along with the following qualities and qualifications:

- Scholarly stature, credentials, and intellectual acumen;
- Academic vision and leadership;
- Readiness to pursue a flexible strategy to foster excellence in teaching and research;
- Adequate qualifications for an appointment as (full) professor in one of the departments of the Faculty;
- Administrative experience to manage a complex and research oriented Faculty.

Bilkent University is recognized and ranked internationally as the premier institution of higher education in Turkey. The medium of instruction at Bilkent is English. Its international community of scholars and students forms an essential component of academic programs, research activities, and social life. The university campus is located 12 kilometers from the city center and offers easy access to the city's parks, shopping centers, cultural activities, museums, and entertainment venues ([www.bilkent.edu.tr](http://www.bilkent.edu.tr)).

Applications or nominations should include a CV and a letter outlining the applicant's philosophy of being a dean of a faculty of Science in a prominent research university, and should be sent to Ms. Birgül Bulut ([bbulut@bilkent.edu.tr](mailto:bbulut@bilkent.edu.tr)). The deadline for applications is November 1, 2011. The new Dean will be appointed as of September 1, 2012.

## POSITIONS OPEN



### RESEARCH LEADER

Commodity Protection and Quality Research Unit  
Parlier, CA

Supervisory Research Entomologist/Supervisory  
Research Geneticist/Supervisory Research  
Chemist/Supervisory Research Plant Pathologist/  
Supervisory Research Plant Physiologist Salary  
Range of \$96,690 to \$147,857 USD

Announcement Open: May 24, 2011 to June 21,  
2011

The U.S. Department of Agriculture (USDA), Agricultural Research Service (ARS), Commodity Protection and Quality Research Unit in Parlier, California is seeking a permanent, full-time scientist to lead a dynamic/diverse research group and to conduct personal research targeted at developing strategies to effectively manage insect and plant pathogen pests associated with fresh and stored horticultural commodities postharvest while maintaining the quality of these commodities. This position provides an exciting leadership opportunity to contribute to development of strategies to meet requirements that ensure, maintain, and expand domestic and foreign export markets for U.S. commodities, and to promote a sustainable, safe, and nutritious food supply for consumers in the U.S. and around the world. The Research Unit is part of the San Joaquin Valley Agricultural Sciences Center, a state-of-the-art research facility (since 2001) on 125 acres in the agriculturally diverse heartland of Central California. The unit enjoys stable annual funding and excellent collaborations with the University of California at Berkeley, Davis, and Riverside researchers as well as several commodity groups. The city of Parlier offers a small-town, rural atmosphere within a short distance from Fresno. Yosemite and Sequoia National Parks, as well as Pacific Ocean beaches along the central coast of California, are within short-distance drives from the surrounding Fresno-Parlier areas. A Ph.D. is highly desirable.

For details and application directions, a full-text vacancy announcement may be obtained via the Internet at website: <http://www.afm.ars.usda.gov/divisions/hrd/index.html> with announcement number ARS-X11W-0190. U.S. Citizenship is required. Questions about the position may be directed to Dr. Edwin Civerolo, center director, telephone: 559-596-2702 or e-mail: [edwin.civerolo@ars.usda.gov](mailto:edwin.civerolo@ars.usda.gov). An attractive Federal benefits package is available. Applications must be received by June 21, 2011.

USDA/ARS is an Equal Opportunity Employer and Provider.

The Department of Radiation Oncology at the University of Pennsylvania's School of Medicine seeks candidates for an **ASSISTANT PROFESSOR** position in the non-tenure research track. Applicants must have a Ph.D. or equivalent degree and have demonstrated excellent qualifications in research.

The candidate must have evidence of research experience in the study of biological materials including cells in culture or isolated organs and knowledge of free radical chemistry and anti-oxidant defense. Expertise in enzymology and protein chemistry is desirable.

The successful candidate will be expected to develop an independent research program in related to signaling by oxygen radicals, will be responsible for the direction of a funded research program in mechanisms of NADPH oxidase activation, and will supervise the immunobiological reagents and participate in the collaborative research programs of the Institute for Environmental Medicine.

The University of Pennsylvania is an Equal Opportunity/Affirmative Action Employer. Women and minority candidates are strongly encouraged to apply. Please submit curriculum vitae, a brief statement of research interests and three letters through the website: [http://www.med.upenn.edu/apps/faculty\\_ad/index.php/d2654](http://www.med.upenn.edu/apps/faculty_ad/index.php/d2654).

## POSITIONS OPEN



### MICROBIOLOGY FACULTY POSITION-Mercer University School of Medicine Savannah, GA Campus

Mercer University School of Medicine invites applications for a full-time tenure-track (rank open) microbiology faculty position in the Department of Biomedical Sciences at the Savannah, Georgia campus on the site of Memorial Health University Medical Center. The basic science curriculum at Mercer University School of Medicine is presented in an interdisciplinary, clinically relevant, problem-based learning format. Candidates must have a doctoral degree (Ph.D., MD, or equivalent) and postgraduate experience in medical microbiology. A demonstrated ability to develop an independent research program capable of attracting extramural funding is strongly desired. Suitable laboratory facilities and startup package will be provided. For a full description, qualifications, and to apply, please go to website: <https://www.mercerjobs.com>. Affirmative Action/Equal Opportunity Employer/ADA.

### FACULTY POSITION Department of Neurology Columbia University

The Department of Neurology at Columbia University and NewYork-Presbyterian Hospital are recruiting a new faculty member at the **ASSISTANT PROFESSOR** level to engage in clinical activities and clinical research at the Allen Pavilion. Qualified applicants must have completed residency training in neurology, a fellowship in vascular neurology, and possess relevant research experience and demonstrated potential as an independent investigator. Protected research time and appropriate resource support will be provided.

M.D., board certified in neurology, with specialty training in vascular neurology (fellowship or equivalent). Faculty rank is expected to be at the Assistant Professor level, commensurate with experience and achievement. External research funding is preferred.

Qualified candidates should send a letter of interest and curriculum vitae in Word format to:

Richard Mayeux, M.D., M.Sc.  
622 West 168th Street, P&S Box 16  
New York, NY 10032  
E-mail: [rpm2@columbia.edu](mailto:rpm2@columbia.edu)

Apply online at website: <https://academicjobs.columbia.edu/applicants/Central?quickFind=54785>.

Columbia University is an Equal Opportunity/Affirmative Action Employer.

**CAREER OPPORTUNITY**—Doctor of Optometry (O.D.) degree in 27 months for Ph.D.s in science and M.D.s. Excellent career opportunities for O.D.-Ph.D.s and O.D.-M.D.s in research, education, industry, and clinical practice. This unique program starts in March of each year, features small classes, and 12 months devoted to clinical care.

Contact the Admissions Office, telephone: 800-824-5526 at: The New England College of Optometry, 424 Beacon Street, Boston, MA 02115. Additional information at website: <http://www.neco.edu>, or by e-mail: [admissions@neco.edu](mailto:admissions@neco.edu).

Find your  
future here.



Science Careers

From the journal Science



[www.ScienceCareers.org](http://www.ScienceCareers.org)



## Nontraditional Careers: Opportunities Away From the Bench Webinar

Want to learn more about exciting and rewarding careers outside of academic/industrial research? View a roundtable discussion that looks at the various career options open to scientists and strategies you can use to pursue a nonresearch career.

Now Available  
On Demand

[www.sciencecareers.org/webinar](http://www.sciencecareers.org/webinar)

Produced by the  
Science/AAAS Business Office.

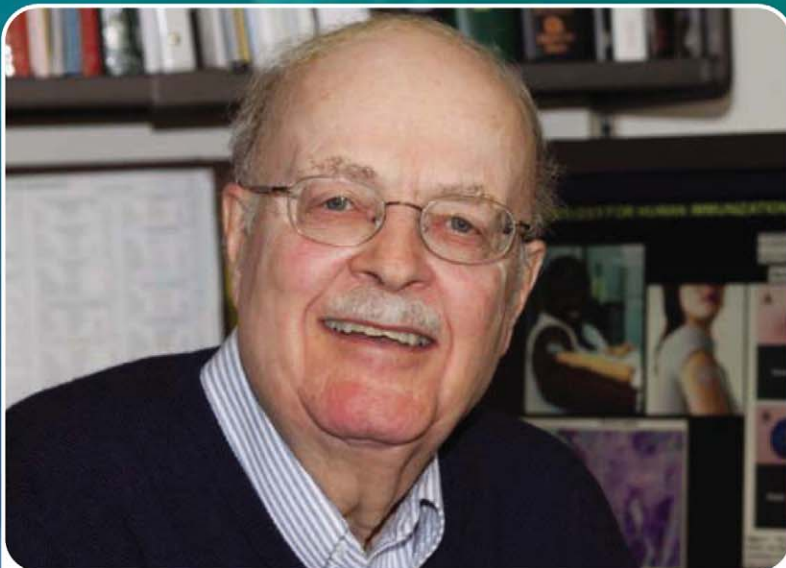
Science Careers

From the journal Science



# “A dream told me to do it.”

*Dr. Carl Alving  
on his inspiration  
for inventing  
the vaccine patch.*



Carl R. Alving, M.D.  
Chief of the Department of Adjuvant & Antigen Research,  
Division of Retrovirology  
at the Walter Reed Army Institute of Research  
AAAS member

**MemberCentral** is the new website that looks at science through the eyes of AAAS members. It celebrates their achievements—like Dr. Alving’s vaccine patch—and their shared belief in the transformative power of science. Use **MemberCentral** to connect with other members, learn about work being done in other fields, and get fresh perspectives on issues ranging from speciation to STEM education.

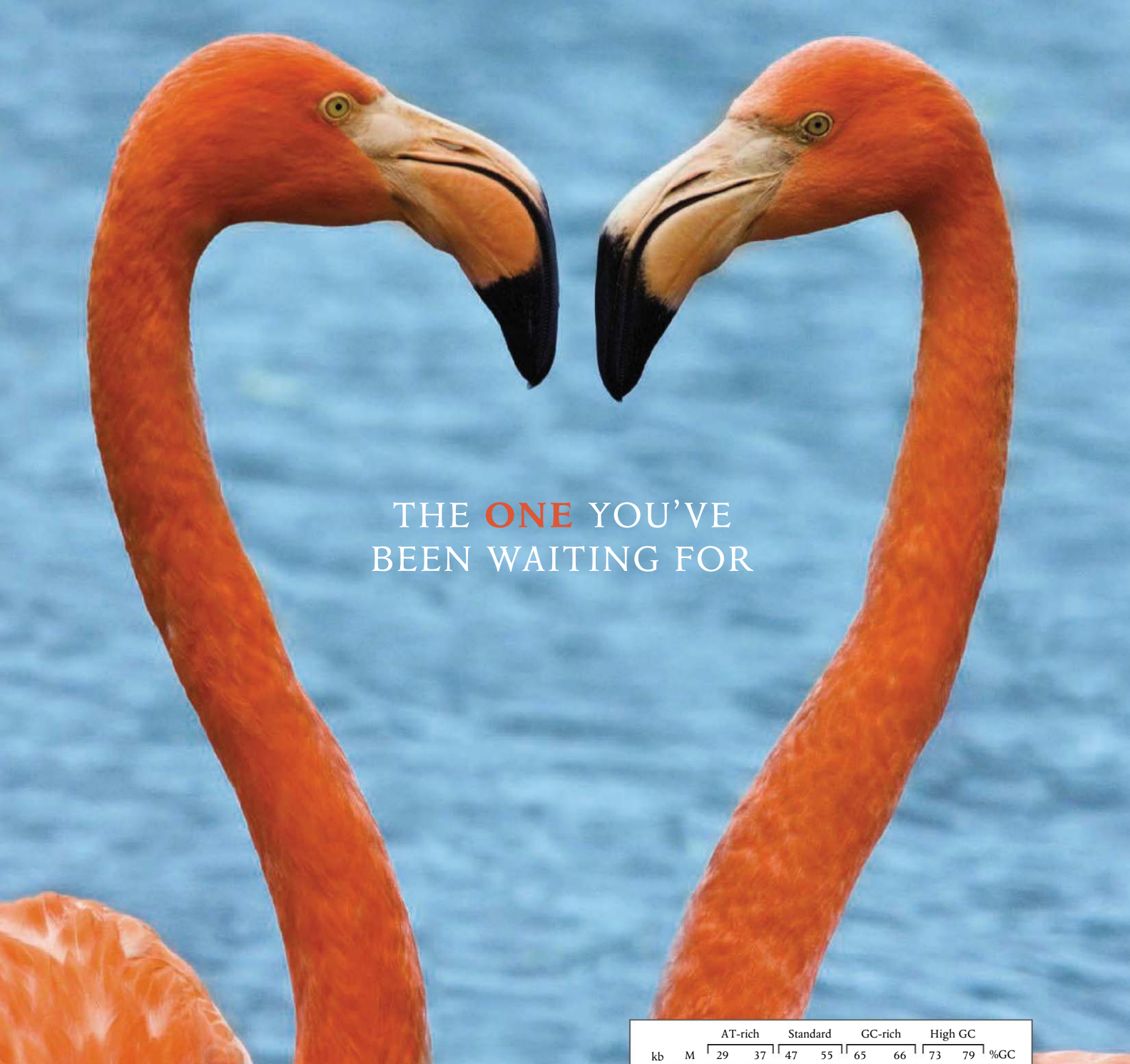
Visit **MemberCentral** today and get to know the  
AAAS member community in a whole new way.



## MemberCentral.aaas.org

Blogs | Videos | Webinars | Discounts | Downloads | Community





THE **ONE** YOU'VE  
BEEN WAITING FOR

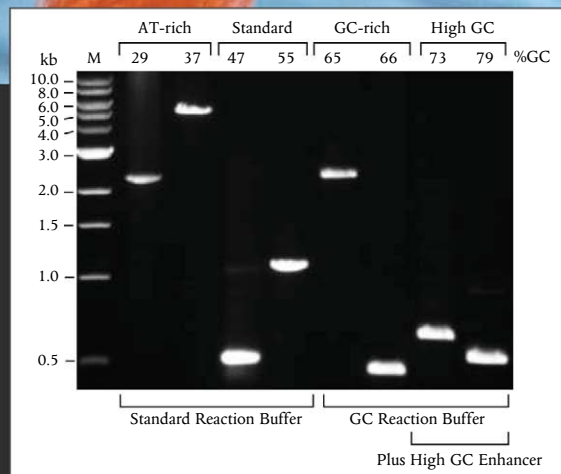
## OneTaq™ DNA Polymerase

*The ONE polymerase for your endpoint PCR needs*

- Robust yield with minimal optimization
- Ideal for routine, AT- or GC-rich templates
- Hot start and master mix versions available



Request a sample at  
[www.neb.com/OneTaq](http://www.neb.com/OneTaq)



*Amplification of a selection of sequences with varying AT and GC content from human and C. elegans genomic DNA, using OneTaq DNA Polymerase.*